TECHNISCHE
UNIVERSITÄT
WIEN
Vienna University of Technology

DISSERTATION

SURFACE SCIENCE STUDIES OF IRON OXIDES AS MODEL CATALYST SUPPORTS

Ausgeführt zum Zwecke der Erlangung des akademischen Grades eines
Doktors der technischen Wissenschaften unter der Leitung von

Assoc. Prof. Gareth S. Parkinson, PhD
und
Univ.Prof. Dr.techn. Ulrike Diebold
Institut für Angewandte Physik E134

eingereicht an der Technischen Universität Wien
Fakultät für Physik

von

Ing. Zdeněk Jakub
01429434
Mohsgasse 26/55
1030 Wien

Wien, Mai 2020

Acknowledgements

I take this opportunity to express my gratitude to everyone who supported me during my PhD studies.

First of all, I'd like to thank Gareth S. Parkinson for giving me the opportunity to work on his exciting research project, for his supervision and guidance, and for always being interested in what's going on in the lab. I thank Ulrike Diebold for setting up such a great research group and giving me a chance to be part of it. The everyday discussions I've had with my supervisors, both about science or life in general, made my time as a PhD student very enjoyable. I also thank Michael Schmid for his invaluable help when solving technical problems, for sharing his knowledge of image processing, and for always being a very thorough internal reviewer of our publications.

I'm very grateful to all the people in the surface science research group, who created a very friendly and stimulating atmosphere. It has been great to share our everyday problems, achievements and failures while sitting in the data-analysis room or later in a pub. In times of need, each member of the group was always willing to help regardless of whether the issue was related to work or not, I value this very much. Scientifically, I have collaborated the most closely with Florian Kraushofer, Jan Hulva and Matthias Meier; it's been fun and it's been very fruitful.

I gracefully acknowledge the financial support which I recieved from the doctoral college TU-D and from Austrian Science Fund (FWF) Start-prize Y847-N20.

Finally, I thank my wife Anna for always supporting me during my studies, even when it meant moving to a small boring town of Břeclav and enduring tiresome commutes to work for almost three years.

Abstract

The performance of heterogeneous catalysts often depends on the properties of the supporting substrate. The surface stability, its ability to support the active species, the structural evolution upon heating or upon interaction with adsorbates can all affect the catalytic activity of the whole system. This thesis deals with surface science studies of two iron oxide surfaces: hematite α-Fe_2O_3 and magnetite Fe_3O_4, both of which are commonly used as catalyst supports or as catalysts themselves.

The first part of the thesis deals with the interaction of three dominant iron oxide surfaces with water. The $(1\bar{1}02)$ surface of hematite (α-Fe_2O_3) was studied both as a pristine surface in and after exposure to water vapor and liquid water. Two surface reconstructions with (1×1) and (2×1) symmetries were observed and studied by scanning tunneling microscopy (STM), noncontact atomic force microscopy (ncAFM), x-ray photoemission spectroscopy (XPS) and low-energy electron diffraction (LEED). The results confirm a bulk-truncated model of the (1×1) surface. Water adsorption on this surface was studied using temperature programmed desorption (TPD), STM, ncAFM, XPS and LEED, which in combination with density functional theory computations clearly show that water adsorbs in the form of partially dissociated water dimers at all coverages prior to multilayer formation. The same spectroscopy and diffraction results acquired in ultrahigh vacuum (UHV) after exposure of the surface to liquid water indicate that the surface survives immersion, and that similar partially-dissociated species still form on the surface. Based on the UHV results it cannot be said whether such species are present even during the actual immersion in liquid water, but such scenario is consistent with previously published in-situ diffraction studies.

Water adsorption in UHV was also studied on the (001) and (111) surface of magnetite (Fe_3O_4) using the same approach. NcAFM imaging with a CO-terminated tip was used as the main method to image the individual water species. On both of these surfaces, water first adsorbs as small partially dissociated water agglomerates, but at slightly higher water coverages complex hydrogen-bonded networks are observed. While the water TPD spectra show desorption features at similar temperatures on both surfaces, the initial water agglomerate formation mechanisms are quite different. On the (001) surface, partially-dissociated water dimers and trimers were clearly identified, which are formed at specific sites of the surface. At higher water coverage, these anchor a hydrogen-bonded network. On the (111) surface, the smallest water agglomerates were clearly identified as trimers in experiments, but their observed shape in ncAFM images was inconsistent with the supporting computational results. This discrepancy can be explained if the water adsorption modifies the surface by pulling out an additional Fe cation from the bulk to the surface. The same mechanism could stabilize highly specific water hexamers which were experimentally observed at higher water coverage. These results suggest, that

the Fe_3O_4(111) surface might be surprisingly dynamic even at cryogenic temperatures.

The last chapter of this thesis deals with Ni, Rh and Ir adatoms and small clusters on the Fe_3O_4(001) surface. Depending on sample preparation, all these adatoms can occupy multiple sites on Fe_3O_4(001) and it was studied how the different local environment affects the adsorption properties and reactivity. The interaction of the Ni/Fe_3O_4(001) system with water was studied with a view towards the enhanced performance of NiFe compounds for the water-gas shift and oxygen-evolution reactions. It was found that Ni adatoms can coordinate multiple water molecules above room temperature, but the water adsorbed on Ni incorporated in the octahedral sites of the support has similar characteristics as water adsorbed on intrinsic surface defects.

The Ir and Rh/Fe_3O_4(001) systems were studied to understand the high activity of Ir and Rh-based catalysts for CO oxidation. It was found that both Rh_1 and Ir_1 adatoms can coordinate either a single CO molecule or two CO molecules, and in both cases a square-planar coordination geometry is formed. In the monocarbonyl case, this is achieved by forming an additional bond to a subsurface oxygen atom. On both Ir and Rh, CO adsorption significantly stabilizes the single adatoms, which is explained by the analogy to rules from coordination chemistry and the availability of the preferred coordination geometry on the surface. Both Rh and Ir systems were found to catalyze CO oxidation via a Mars-van-Krevelen mechanism at elevated temperatures, but are deactivated by adatom incorporation once the adsorbed molecules desorb. Additional experiments on Rh/Fe_3O_4(001) were carried out to find whether the Rh_1 species could catalyze CO oxidation via a Langmuir-Hinshelwood mechanism. TPD experiments with isotopically-labeled gases have shown that the system is active for such CO oxidation mechanism at low temperature if O_2 is dosed before the CO, but it is not the single Rh_1 species which are responsible for this activity. Instead, it was found that the O_2 adsorption mobilizes the Rh which then agglomerates to form small oxidized Rh_xO_y with weakly bound oxygen which acts as the oxidizing agent. If CO is dosed prior to O_2, the highly stable carbonyls are formed and the system is blocked for O_2 adsorption. The mechanism of CO oxidation on this system is therefore determined by the order in which the system is exposed to the two reactants.

Overall, the results presented in this thesis provides significant fundamental insights into the surface structures, stability and reactivity of clean and modified iron oxide surfaces. On all the studied systems, previously unforeseen phenomena were observed, which highlights the importance of detailed surface science studies carried out on a case-by-case basis.

Kurzfassung

Die Leistung heterogener Katalysatoren hängt häufig von den Eigenschaften des Trägermaterials ab. Die Struktur der Oberfläche, ihre Stabilität, ihre Fähigkeit, die aktive Spezies zu beherbergen, sowie ihre strukturelle Evolution während der Interaktion mit Adsorbaten können die katalytische Aktivität des gesamten Systems beeinflussen. Diese Arbeit behandelt oberflächenphysikalische Studien auf zwei Eisenoxid-Oberflächen, Hämatit α-Fe_2O_3 und Magnetit Fe_3O_4, die beide verbreitet als Trägermaterialen sowie selbst als Katalysatoren in Verwendung sind.

Der erste Teil dieser Arbeit behandelt die Interaktion dreier dominanter Eisenoxid-Oberflächen mit Wasser. Die $(1\bar{1}02)$-Oberfläche von Hämatit (α-Fe_2O_3) wurde sowohl als unberührte Oberfläche als auch nach Interaktion mit Wasserdampf und flüssigem Wasser untersucht. Zwei Oberflächen-Rekonstruktionen mit (1×1)- und (2×1)-Symmetrien wurden beobachtet und mit Rastertunnelmikroskopie (STM), Nicht-Kontakt-Rasterkraftmikroskopie (ncAFM), Röntgenphotoelektronenspektroskopie (XPS) und Beugung niederenergetischer Elektronen (LEED) untersucht. Die Ergebnisse bestätigen ein Volumens-terminiertes Modell der (1×1)-Oberfläche. Adsorption von Wasser auf dieser Oberfläche wurde mittels Temperatur-programmierter Desorption (TPD), STM, ncAFM, XPS und LEED untersucht, die in Kombination mit Dichtefunktionaltheorie-Rechnungen klar zeigen, dass Wasser bis zur Bildung von Multilagen bei allen Bedeckungen in Form teilweise dissoziierter Dimere adsorbiert. Die gleichen Spektroskopie- und Beugungs-Ergebnisse wurden in Ultrahochvakuum (UHV) aufgenommen, nachdem die Oberfläche flüssigem Wasser ausgesetzt wurde. Dies weist darauf hin, dass die Oberfläche durch den Kontakt mit Wasser nicht modifiziert wird, und dass ähnliche teilweise dissoziierte Spezies auf der Oberfläche gebildet werden. Aufgrund der UHV-Ergebnisse kann nicht festgestellt werden, ob solche Spezies sogar während des Kontakts mit flüssigem Wasser vorhanden sind. Dies wäre allerdings im Einklang mit bereits publizierten in-situ Diffraktions-Studien.

Wasser-Adsorption in UHV wurde mit dem gleichen Ansatz auch auf den (001)- und (111)-Oberflächen von Magnetit (Fe_3O_4) untersucht. NcAFM mit einer CO-terminierten Spitze wurde als hauptsächliche Methode benutzt, um die individuellen Wasser-Spezies abzubilden. Auf beiden Oberflächen adsorbiert Wasser zunächst in Form von kleinen, teilweise dissoziierten Agglomeraten, während bei etwas höheren Bedeckungen komplexe, mit Wasserstoffbrückenbindungen verbundene Netzwerke beobachtet werden. Obwohl die TPD-Spektren von Wasser auf beiden Oberflächen Desorptions-Charakteristika bei ähnlichen Temperaturen aufweisen, sind die Mechanismen der anfänglichen Bildung vom Wasser-Agglomeraten sehr verschieden. Auf der (001)-Oberfläche können Wasser-Dimere und -Trimere klar identifiziert werden, die sich an spezifischen Stellen der Oberfläche bilden. Bei höherer Wasser-Bedeckung verankern diese ein Wasserstoff-gebundenes Netzwerk. Auf der (111)-Oberfläche kon-

nten die kleinsten Wasser-Agglomerate im Experiment klar als Trimere identifiziert werden, aber ihre im ncAFM beobachtete Form ist unvereinbar mit den computergestützten Resultaten. Diese Diskrepanz kann erklärt werden, wenn die Wasser-Adsorption die Oberfläche modifiziert, indem sie ein zusätzliches Eisen-Kation vom Volumen an die Oberfläche zieht. Der gleiche Mechanismus könnte höchst spezifische Wasser-Hexamere stabilisieren, die experimentell bei höheren Wasser-Bedeckungen beobachtet wurden. Diese Ergebnisse suggerieren, dass die $Fe_3O_4(111)$-Oberfläche selbst bei kryogenen Temperaturen überraschen dynamisch sein könnte.

Das letzte Kapitel dieser Arbeit beschäftigt sich mit Ni-, Rh- und Ir-Adatomen und kleinen Clustern auf der $Fe_3O_4(001)$-Oberfläche. Je nach Vorbehandlung der Probe können diese Adatome auf $Fe_3O_4(001)$ verschiedene Plätze besetzen, und es wurde untersucht, wie die verschiedenen Umgebungen die Adsorptions-Eigenschaften und die Reaktivität beeinflussen. Die Interaktion des $Ni/Fe_3O_4(001)$-Systems mit Wasser wurde in Hinblick auf erhöhte Leistungsfähigkeit von NiFe-Verbindungen für die Wassergas-Shift-Reaktion und die Sauerstoff-Bildungsreaktion untersucht. Es wurde festgestellt, dass Ni-Adatome über Raumtemperatur mehrere Wasser-Moleküle koordinieren können, aber dass Wasser, das auf in oktaedrischen Gitterplätzen inkorporiertem Nickel adsorbiert, ähnliche Eigenschaften hat wie Wasser, das auf intrinsischen Oberflächendefekten adsorbiert.

Die Ir und $Rh/Fe_3O_4(001)$-Systeme wurden untersucht, um die hohe Aktivität bei CO-Oxidation von Ir- und Rh-basierten Katalysatoren zu verstehen. Es wurde festgestellt, dass sowohl Rh_1- als auch Ir_1-Adatome entweder ein einzelnes oder zwei CO-Moleküle koordinieren können, und dass in beiden Fällen eine quadratisch planare Koordinationsgeometrie gebildet wird. Im Fall des Monocarbonyls wird dies erreicht, indem eine zusätzliche Bindung mit einem Sauerstoff-Atom unter der Oberfläche gebildet wird. Sowohl auf Ir als auch auf Rh stabilisiert CO-Adsorption die einzelnen Adatome auf der Oberfläche signifikant, was durch eine Analogie zu den Regeln der Koordinationschemie und die Verfügbarkeit der bevorzugten Koordinations-Geometrie auf der Oberfläche erklärt wird. Sowohl Rh- als auch Ir-Systeme katalysieren CO-Oxidation über einen Mars-van-Krevelen-Mechanismus bei erhöhten Temperaturen, werden dann jedoch durch Aufnahme der Adatome in die Oberfläche deaktiviert, sobald die Moleküle desorbieren. Weitere Experimente auf Rh/Fe_3O_4 wurden durchgeführt, um herauszufinden, ob Rh_1-Spezies CO-Oxidation durch einen Langmuir-Hinshelwood-Mechanismus katalysieren können. TPD-Experimente mit isotopisch markierten Gasen haben gezeigt, dass das System bei niedrigen Temperaturen aktiv für diese Art der CO-Oxidation ist, wenn O_2 vor CO aufgetragen wird, aber dass nicht die einzelnen Rh_1-Spezies für diese Aktivität verantwortlich sind. Stattdessen zeigte sich, dass O_2-Adsorption das Rh mobilisiert, das sich dadurch zu Rh_xO_y ansammelt, mit schwach gebundenem Sauerstoff als Oxidationsmittel. Wenn CO vor dem Sauerstoff aufgetragen wird, werden stattdessen höchst stabile Monocarbonyle gebildet, was die O_2-Adsorption blockiert. Der Mechanismus der CO-Oxidation auf diesem System wird daher durch die Reihenfolge bestimmt, in der das System den beiden Reaktanden ausgesetzt wird.

Insgesamt bieten die Ergebnisse, die in dieser Arbeit präsentiert werden, signifikante, fundamentale Erkenntnisse zur Oberflächenstruktur, Stabilität und Reaktivität von sauberen und modifizierten Eisenoxid-Oberflächen. Auf allen betrachteten Systemen wurden vorher unbekannte Phänomene beobachtet, was die Wichtigkeit detaillierter oberflächenphysikalischen Studien unterstreicht.

Contents

1 Introduction

Studies of materials reactivity often resemble a black box, where we know the ingredients coming in, we can measure the products coming out, but how exactly the process happens remains a secret. By a trial and error approach people have initially classified some materials as reactive and others as inert, but it became clear very soon that there's more than just bulk chemical composition which defines these properties. The field of surface science came about as an attempt to minimize the number of variables that can affect the reaction outcome and to gain understanding of the reaction pathways at an atomic level. Such knowledge is highly relevant for a wide range of applied fields including catalysis, electrochemistry, corrosion studies, geochemistry, hydrogen production, fuel-cell design and many others.

The properties of surfaces differ dramatically from the properties of the bulk. Bonds are broken upon cleavage and top surface layers relax towards the bulk. Undercoordinated atoms on the surface tend to saturate their dangling bonds by reconstructing to different patterns than found in the bulk. The reactivity is thus not only specific to the bulk material, but also to the exposed crystallographic facets, and even to each individual type of surface reconstruction on these facets. Some surfaces are energetically much more favorable than others, which leads to their prevalence both in natural crystals and in nanomaterial utilized in industrial processes; these dominant surfaces are then the typical research topics of surface science studies. The importance of such approach has been universally recognized in 2007 by the Nobel Prize in Chemistry awarded to G. Ertl for his work on well-characterized metal surfaces [1]. Another layer of complexity is added by many different types of defects, from step edges and domain boundaries to missing or excess atoms and impurities, which are often responsible for the relevant chemistries [2–4].

Surface science studies typically take place in conditions very different from the environment of a typical working catalyst or a corroding electrode. In atmospheric pressure it only takes a fraction of a microsecond to form a monolayer of adsorbates on the surface. Therefore, the detailed understanding of the atomic positions on the bare surface, its adsorption properties and reactivity requires ideal conditions of ultrahigh vacuum ($P \leq 10^{-10}$ mbar), where the monolayer formation time extends to days, and individual adsorption or reaction events can be controllably induced and observed. Additionally, because many of the techniques needed for surface structure analysis require extended surfaces of the same crystallographic orientation, the majority of surface science studies are conducted on single crystals or thin films grown on suitable substrates. The price that's being paid for the atomic-scale understanding is the wide gap between the idealized conditions and the real world outside the vacuum chambers. Latest trends in surface science therefore aim to bridge the gap by transferring the concepts developed in vacuum to more realistic systems [5], either by developing similar analytical instruments working in near-ambient pressures [6–9] or by analyzing the well-defined surfaces in vacuum after controlled exposure to high pressures or liquid environment [10–12].

Heterogeneous and “Single-Atom” Catalysis

One of the main motivations and applications of surface science is heterogeneous catalysis, where identification of active sites and reaction mechanisms presents a crucial step in the optimization of catalyst activity and stability. The most catalytically active elements such as Pt, Pd, Rh or Ir belong to the rarest and most expensive materials on Earth, which drives the search for ways to minimize the used amount while maintaining the activity.

The widely used method to increase the per-atom reactivity of heterogeneous catalysts is to use the precious material in the form of nanoparticles dispersed on a cheap support [13, 14]. Increasing the surface-to-volume ratio of the active phase is highly desirable, because the catalyzed reaction takes place on the surface of the catalyst and the atoms buried in the bulk are essentially “wasted”. Downsizing the nanoclusters can be a nontrivial task, however, because the small clusters are often unstable against formation of bigger nanoparticles, which reduces the surface free energy. This process, called sintering, presents one of the bigger challenges in supported nanocatalyst design as it can lead to a complete deactivation of the catalyst [15, 16].

Assuming the same reaction mechanism, the total activity of the catalyst should scale monotonically with the number of active sites and thus with the size of the catalyst nanoparticles. This generally works for “large” nanoparticles, but it has been known since 1980s that clusters smaller than a few nm diverge from this rule and their catalytic properties differ dramatically from their bigger counterparts [17, 18]. Clusters containing only several atoms can show significant changes of catalytic activity with the addition or removal of as little as a single atom, leading to a whole new field of size-selected nanocatalysts [19–21]. “Magic-sized” clusters have been identified for different metals, where the given atomic arrangement can allow lowering of the rate-limiting reaction step [22–24]. Importantly, the properties of the small clusters do not always correlate with the reactivity trends known for bulk metals [25], and thus there is a real prospect of not only minimizing the used amount of rare metals, but maybe even replacing them completely with cheaper materials [26, 27].

Downsizing of the nanoparticles has a natural limit at the single atom level. In early 2000s it has been shown by several groups that single atoms on surfaces can be catalytically active [28–30]. The interest for the “single-atom catalysis” (SAC) as a field of its own was further reinforced in 2011 when a Pt_1/FeO_x single atom catalyst was prepared by wet chemical approach with extremely low loading of Pt on a high surface area iron oxide support, and this catalyst showed very high activity for CO oxidation [31]. Since then, various approaches to synthesize single-atom catalysts have been developed [31–38] and now it seems generally accepted than single atoms can, indeed, effectively catalyze selected reactions.

However, it is not just the potentially increased per-atom activity that’s exciting about SACs. Heterogeneous catalysis, in general, allows high throughput and easy product separation, but typically suffers from limited selectivity due to a high number of different active sites. If a SAC can be engineered, in which the majority of adatoms resides in the same site on the support surface, this could lead to dramatic improvements in the selectivity. In fact, such a SAC would resemble coordination complexes used as the active species in homogeneous catalysis: In both cases the metal is typically cationic and is stabilized by chemical bonds to the surroundings (see Fig. 1.1). This has led researches to the idea that SACs could combine the best of the two fields and “bridge” heterogeneous and homogeneous catalysis [39–41]. There has been early success on that front recently, and SACs tailored to catalyze reactions typically performed in solution show selectivity levels comparable to the homogeneous processes [42–44].

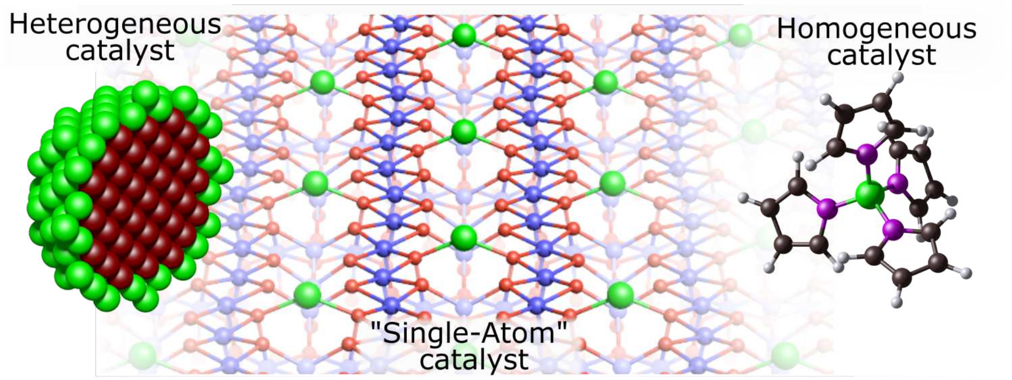

Figure 1.1: Single-atom catalyst as a bridge between heterogeneous and homogeneous catalysis. Supported nanoparticles (shown on the left) allow high throughput, but only the atoms on the surface are utilized which leads to lower per-atom reactivity and lower selectivity. Homogeneous catalysts (right) are typically coordination complexes with a metal stabilized by ligands. These reach excellent levels of selectivity, but are hard to separate from the product. Single-atom catalyst can combine the characteristics of both. Figure adapted from [40].

The typical tools used to characterize SACs include aberration-corrected transmission electron microscopy (TEM), which provides 2D projections of the cationic lattice and thus allows identification of foreign single atoms residing on a powder support. This is corroborated by X-ray adsorption spectroscopy (XAS) which gives information about the number of metal-metal bonds; the absence of such bonds serves as a proof of the isolated nature of the active species. X-ray photoelectron spectroscopy (XPS) and XAS are used to probe the chemical state of the active species. Infrared reflection absorption spectroscopy (IRAS) with a CO probe molecule is a widely used method to characterize the properties and uniformity of the sites active for adsorption. The reactivity of the catalyst is measured in a reactor cell either in a steady state or as a function of temperature, and the reaction pathways are modelled by density functional theory (DFT) computations. This approach has yielded significant success in SAC research, but one of its limitations is the weak link between experimental data and theory. None of these techniques used can firmly determine the exact local coordination of the adatom, a crucial starting parameter for the computations. Additionally, identification of the adatom charge state and active site geometry by XPS and IRAS is only possible by comparison to a suitable reference, and such references are often missing or are very difficult to interpret. These issues lead to significant controversies in SAC research and groups have drawn directly opposite conclusions from similar datasets, casting doubt on the very concept of single atom reactivity [37, 39, 45]. Such controversies illustrate the need for well-defined model systems, which can establish a firm link between the theory and experiment and provide reliable reference data for studies of working catalysts.

Utilizing a surface science approach, a model system is first thoroughly described in ultrahigh vacuum (UHV), both as a bare support surface and with the deposited catalytically active species. The next important step is to find out how the system changes upon controlled exposures to species expected to be present in applied studies. A prime example of such species is water, some amount of which is omnipresent in all the potential applications of the studied materials. Water is a relatively simple molecule, but exhibits a range of non-trivial phenomena on surfaces: On some surfaces it readily dissociates, on others it stays intact, it can form hydrogen-bonded agglomerates of various shapes and at higher coverages it forms hydrogen-bonded networks with long-range order. When a surface is exposed to liquid water, its atomic scale structure can affect the ordering of water molecules even a few layers into the liquid phase [46]. Conversely, a water film on top of the surface can induce structural changes to the surface itself [12, 47]. Since in almost any application the surfaces are covered with a thin layer of water, great effort has been invested into understanding the water adsorption properties on well-defined surfaces, both in UHV and at ambient conditions [48–50]. However, especially on oxide surfaces with complicated unit cells, a thorough understanding of water adsorption behavior is missing.

Scope of this thesis

This thesis deals with the surfaces of two iron oxides, magnetite (Fe_3O_4) and hematite (α-Fe_2O_3). Both are commonly used as supports for nanocatalysts, therefore a thorough understanding of their structure and reactivity presents relevant knowledge for the field of heterogeneous catalysis. The first part of this thesis deals with the interaction of the α-$Fe_2O_3(1\bar{1}02)$, $Fe_3O_4(001)$ and $Fe_3O_4(111)$ surfaces with water vapor in UHV, and in the case of α-$Fe_2O_3(1\bar{1}02)$ also with liquid water. The main research question is how does water interact with these surfaces, what are the specifics of stable water structures on these surfaces, and in what way can this be relevant to applications. The results described in this part were published in the following peer-reviewed papers:

- Kraushofer, F., Jakub, Z., Bichler, M., Hulva, J., Drmota, P., Weinold, M., Schmid, M., Setvin, M., Diebold, U., Blaha, P. & Parkinson, G. S. **Atomic-Scale Structure of the Hematite α-$Fe_2O_3(1\bar{1}02)$ "R-Cut" Surface**. *The Journal of Physical Chemistry C* **122**, 1657–1669 (2018).
- Jakub, Z., Kraushofer, F., Bichler, M., Balajka, J., Hulva, J., Pavelec, J., Sokolović, I., Müllner, M., Setvin, M., Schmid, M., Diebold, U., Blaha, P. & Parkinson, G. S. **Partially Dissociated Water Dimers at the Water–Hematite Interface**. *ACS Energy Letters* **4**, 390–396 (2019).
- Meier, M., Hulva, J., Jakub, Z., Pavelec, J., Setvin, M., Bliem, R., Schmid, M., Diebold, U., Franchini, C. & Parkinson, G. S. **Water agglomerates on $Fe_3O_4(001)$**. *Proceedings of the National Academy of Sciences* **115**, E5642–E5650 (2018).
- Zaki, E., Jakub, Z., Mirabella, F., Parkinson, G. S., Shaikhutdinov, S. & Freund, H.-J. **Water Ordering on the Magnetite Fe_3O_4 Surfaces**. *The Journal of Physical Chemistry Letters* **10**, 2487–2492 (2019).

The second part of this thesis focuses on the $Fe_3O_4(001)$ "subsurface cation vacancy" reconstruction, which was previously shown to stabilize dense arrays of single metal adatoms up to elevated temperatures. The question addressed in this part is how the presence of Ni, Rh and Ir species affects the adsorption properties of the system towards water and CO, and how does the local coordination environment of the single adatoms affect their presumed catalytic performance. The results described in this part were published in the following peer-reviewed papers:

- Jakub, Z., Hulva, J., Mirabella, F., Kraushofer, F., Meier, M., Bliem, R., Diebold, U. & Parkinson, G. S. **Nickel Doping Enhances the Reactivity of $Fe_3O_4(001)$ to Water**. *The Journal of Physical Chemistry C* **123**, 15038–15045 (2019).

- Jakub, Z., Hulva, J., Meier, M., Bliem, R., Kraushofer, F., Setvin, M., Schmid, M., Diebold, U., Franchini, C. & Parkinson, G. S. **Local Structure and Coordination Define Adsorption in a Model Ir_1/Fe_3O_4 Single-Atom Catalyst**. *Angewandte Chemie Internation Edition* **58**, 13961–13968 (2019).
- Jakub, Z., Hulva, J., Ryan, P. T. P., Duncan, D. A., Payne, D. J., Bliem, R., Ulreich, M., Hofegger, P., Kraushofer, F., Meier, M., Schmid, M., Diebold, U. & Parkinson, G. S. **Adsorbate-induced structural evolution changes the mechanism of CO oxidation on a $Rh/Fe_3O_4(001)$ model catalyst**. *Nanoscale* **12**, 5866–5875 (2020).

A full list of publications I have co-authored is given at the end of this thesis, along with the statement of contributions.

2 Iron oxides

Iron oxides are highly abundant minerals in the Earth's crust, which makes them very cheap and thus appealing for technological applications [51]. Apart from the already mentioned use as catalyst supports or catalysts themselves, iron oxides are currently utilized in various other fields such as contrast agents or drug delivery systems in biomedicine [52, 53], as electrode materials in photoelectrochemistry [54], as energy storing media [55, 56], as pollutant sinks in groundwater remediation [57], and obviously as the main source of iron in steel production.

Looking at the Fe-O_2 phase diagram (Fig. 2.1), at ambient conditions the lowest energy form of iron oxide is hematite (α-Fe_2O_3), which leads to its very high abundance. Magnetite (Fe_3O_4) is preferred at slightly reducing conditions, but due to the high energetic cost of recrystallization between the structures of magnetite and hematite it is also stable at ambient conditions. Maghemite (γ-Fe_2O_3) is the intermediate step between the two, being isostructural to magnetite but having a number of randomly distributed point defects leading to overall Fe_2O_3 stoichiometry. The most reduced form of iron oxide is wüstite ($Fe_{1-x}O$). Wüstite is rare in nature and can typically be found only in places exposed to highly reducing conditions, such as on meteorites or rocks struck by lightning.

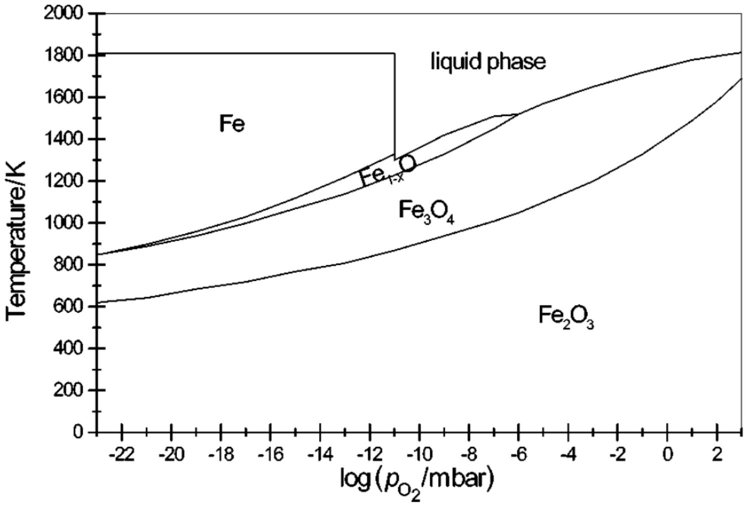

Figure 2.1: Calculated Fe-O_2 phase diagram, reprinted from [58].

2.1 Magnetite Fe_3O_4

Magnetite crystallizes in the inverse spinel structure, which is based on the face centered cubic lattice of O^{2-} in which 1/8 of thetetrahedral sites and 1/2 of the octahedral sites is occupied by iron cations, see Fig.2.2. The general formula of the spinel structure is $A^{2+}B_2^{3+}O_4^{2-}$ and we distinguish between a normal spinel and an inverse spinel depending on the distribution of A^{2+} and B^{3+} cations in the octahedral and tetrahedral sites. In an inverse spinel, the tetrahedral sites are occupied by the X^{3+} cations and the octahedral sites are filled with a 50:50 mixture of X^{2+} and X^{3+}. In the case of magnetite, the coexistence of Fe^{2+} and Fe^{3+} in the octahedral sites enables easy electron transfer between the two, leading to relatively high electrical conductivity at room temperature. Below the so-called Verwey transition temperature of 120 K, the rate of electron hopping between the Fe atoms in octahedral sites is significantly reduced and the conductivity abruptly drops by two orders of magnitude [59], which is accompanied by a distortion of the cubic crystal symmetry into monoclinic. In the further text, the Fe cations in tetrahedral and octahedral sites are labeled by a subscript, Fe_{tet} and Fe_{oct}.

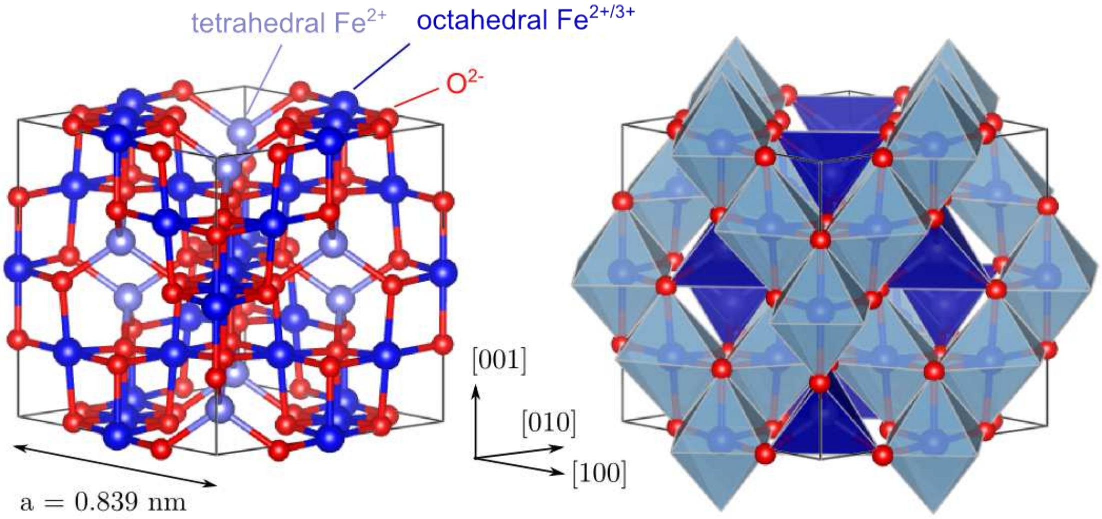

Figure 2.2: Ball-and-stick and polyhedral models of magnetite. The spinel structure is based on face centered cubic lattice of O^{2-}. Cations occupy 1/8 of the tetrahedral sites and 1/2 of the octahedral sites. Cations in the tetrahedral sites are Fe^{3+}, the octahedral sites are filled with with 50:50 mixture of Fe^{2+} and Fe^{3+}.

Magnetite owes its name to its magnetic properties at ambient temperatures. After it was long considered a ferromagnet, Neel used magnetite as a prototype material for his theory of ferrimagnetism, proposing the Fe_{oct} and Fe_{tet} are antiferromagnetically coupled [60]. That means the unit cell magnetic moment of the Fe^{3+} is zero and all the magnetization comes from the Fe^{2+}. The Curie temperature for magnetite is 858 K, above which it is paramagnetic.

The natural magnetite single crystals are most commonly octahedrons enclosed by {111} surfaces. The {100} facets are less frequent, but still common on natural crystals and can be grown on synthetic single crystals [61]. The energetic preference for {111} and {100} surfaces is supported by most of the theoretical DFT studies [62], [63] although some studies show different results [64]. Understandably, those two surfaces are the most extensively studied experimentally. Recently it was shown that the remaining low-index magnetite surface, the {110}, commonly reconstructs to expose {111} nanofacets [65].

2.1.1 The (001) Surface

In the [001] direction, magnetite consists of alternating planes of Fe_{tet} and $(Fe_{oct})_2O_4$. At the (001) surface, terminated by the $(Fe_{oct})_2O_4$ plane, the most stable phase over a wide range of chemical potentials is the well documented $(\sqrt{2} \times \sqrt{2})R45°$ surface reconstruction. In the Scanning Tunneling Microscopy (STM) image, characteristic undulating Fe_{oct} rows are present, creating the so-called "narrow" and "wide" sites (see figure 2.3a). On neighboring terraces, the Fe_{oct} rows are rotated by 90° due to the spinel structure. Such images were reported already in the early 1990s and several surface structure models were proposed over the years [66–68]. Nevertheless, none of these models could explain all the experimentally observed phenomena, such as the remarkable stability of single metal atoms on the surface (Fig. 2.3b and [69]) and facile incorporation of transition metals into the surface upon mild thermal annealing [70, 71].

The Subsurface Cation Vacancy (SCV) structure, published in 2014, introduces interstitial Fe_{int} atoms sitting between the two Fe_{tet}, effectively blocking the "wide" side for adatom adsorption. The origin of those Fe_{int} is in the third layer, where there are two octahedrally coordinated Fe_{oct} missing for every Fe_{int} (see Fig. 2.4B), resulting in a net reduction of one Fe atom per unit cell in comparison to the previously accepted distorted bulk truncation (DBT) model (see Fig. 2.4A). According to DFT+U calculations and spectroscopic data, the top three layers of the SCV-reconstructed surface feature only Fe^{3+} cations. The surface is thus oxidised with respect to the bulk Fe_3O_4, in agreement with the thermodynamic preference for Fe_2O_3 at the relevant conditions (see Fig. 2.1.) The SCV structure was convincingly confirmed by quantitative LEED IV measurements showing excellent agreement with the model [72].

The defect commonly present on as-prepared SCV surfaces are well documented, and most of them well understood. Commonly observed defects include surface hydroxyls, boundaries between phase-shifted domains and unreconstructed unit cells [51]. There is some evidence for the presence of oxygen vacancies on the surface [75], but these are commonly not observed using the typical surface characterization tools such as STM or XPS.

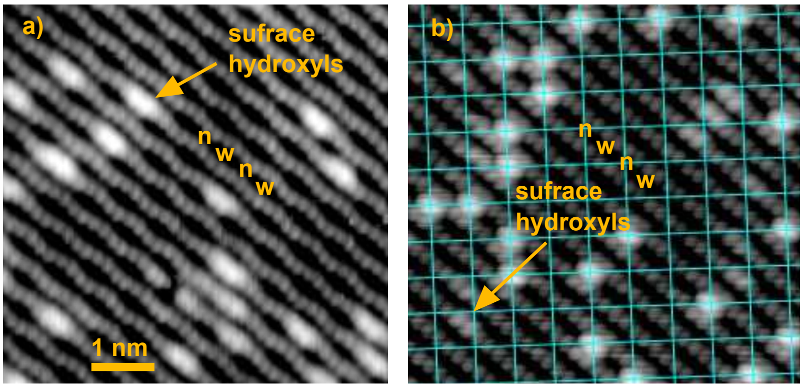

Figure 2.3: (a) Scanning Tunneling Microscopy images of $Fe_3O_4(001)$ after typical surface preparation feature Fe_{oct} rows. The undulation pattern of these rows results in the $(\sqrt{2} \times \sqrt{2})R45°$ symmetry of the surface, and forms distinguishable "narrow" and "wide" sites (highlighted by the "n" and "w" letters). At normal scanning conditions (bias voltage between 1 and 3 V), the "n" and "w" sites are reversed from the real undulations of the surface Fe atoms, see Fig. 2.4C and ref. [72]. The bright protrusions on the row are surface hydroxyls [73] (b) When metal atoms are deposited on the surface, they reside exclusively in the "narrow" sites as highlighted by the grid. This figure shows Ni adatoms, but the behaviour seems to be universal for all the tested metals [74].

The SCV reconstruction is thermodynamically the most stable phase of the $Fe_3O_4(001)$ surface over a wide range of chemical potentials, but its stability is not unlimited. Upon harsh reductive treatment an Fe_{tet}-terminated surface can be prepared [76]. Also, it was shown recently that contact with liquid water induces heavy hydroxylation and structural changes to the surface, which were interpreted as growth of an Fe(OH) phase [12].

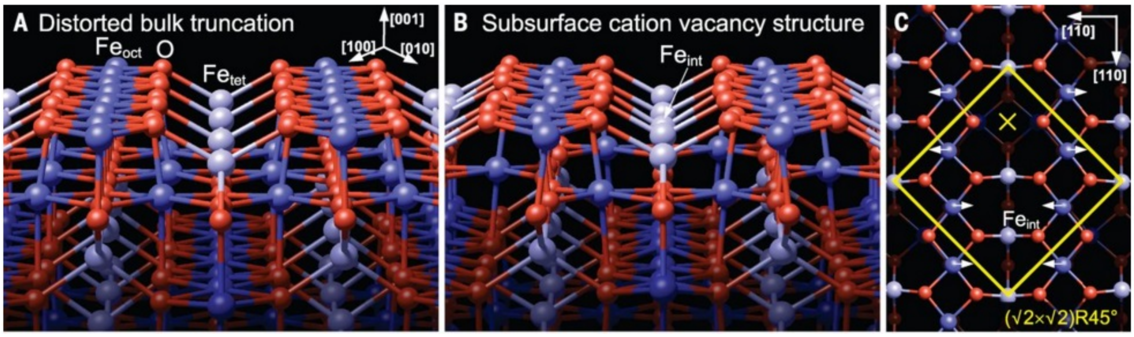

Figure 2.4: Magnetite (001) surface structure models: (a) distorted bulk truncation, (b) subsurface cation vacancy. The subsurface cation vacancy features interstitial Fe_{int} effectively blocking one of the two available adsorption sites (c). The yellow cross marks the preferred adsorption site. Two Fe_{oct} in the third layer are missing under every Fe_{int}. Picture reprinted from [72].

$Fe_3O_4(001)$ as an Adatom Template

Magnetite (001) can stabilize single metal atoms up to coverages of 0.8 ML and temperatures around 700 K (a monolayer (ML) is defined as one adatom per $(\sqrt{2}\times\sqrt{2})R45^\circ$ surface unit cell). Upon evaporation, almost all the adatoms reside in the same site on the surface (the so-called "narrow" site, highlighted by the yellow "×" in Fig. 2.4), as was demonstrated for various metals including Au, Ag, Pt, Pd, Rh, Ir, Cu, Ni and others [69, 70, 72, 74, 77–81]. In this adsorption site, the adatoms are 2-fold coordinated to the surface oxygen atoms, and essentially reside in the bulk-continuation site.

It is important to note that the adatom stabilizing ability of the SCV surface does not stem from the thermodynamic preference for the single atoms. In many of the cases analyzed by DFT+U calculations, the adsorption energy of the adatom is lower than the cohesive energy of the metal. Nevertheless, there are kinetic barriers that prevent the agglomeration process at the relevant temperatures. It was shown for Ag adatoms that even though the diffusion of single Ag_1 was observed at room temperature, the Ag_1 did not agglomerate [78]. This was explained by the instability of Ag_2 dimers, which can be formed, but immediately break up back into single Ag_1. This, combined with the facile diffusion of Ag_1 monomers, allows stabilization of unusally high coverages of Ag_1 adatoms up to 0.8 monolayer. Neverthess, the the Ag_3 trimers are stable, and once they are formed, further agglomeration process soon follows due to the Ag_1 diffusion [78]. Rh and Ir present another special case, where the dimers are observed to be metastable at room temperature, but the agglomeration is limited by immobility of monomers [74]. For almost all other metals on the SCV surface it is a combination of both described stabilizing mechanisms; the dimers are unstable and adatom diffusion does not occur at room temperature. It can be thus said that all of the single-atom/$Fe_3O_4(001)$ systems are stabilized by kinetics, but the specific rate limiting step differs case to case. Some adatoms remain isolated up to ≈ 700 K, where the SCV reconstruction is lifted [69].

The agglomeration is however not the only deactivation mechanism of single-atom/$Fe_3O_4(001)$ systems. It was observed that metals such as Ti, Ni or Co readily incorporate into the surface already after mild thermal annealing [70, 71, 82]. This is in accordance with the existence of subsurface cation vacancies in the SCV reconstructed surface, which can accommodate additional cations. Upon incorporation of foreign metal atom into one of those octahedral vacancies, the Fe_{int} is pushed down into the other of the two vacancies in the SCV unit cell, and this arrangement of cations resembles the unreconstructed (1×1) surface. Upon further annealing, the metal atoms can diffuse further into the bulk, recovering the clean SCV-reconstructed surface. This behaviour is rationalized by analogy to nickel-, titanium- or cobalt-ferrites ($X_1Fe_2O_4$), which are minerals commonly found in nature.

Lastly, the single-atom/Fe_3O_4(001) systems can be destabilized by interaction with adsorbates. It was shown for Pd and Pt that adsorption of a CO molecule weakens the interaction of the adatom with the substrate, which leads to the adatom mobility at room temperature [77, 80]. In this thesis, this concept will be elaborated on further and it will be shown that the interaction with molecules can have both destabilizing or stabilizing effect, and this can be rationalized by analogies to coordination chemistry.

2.1.2 The (111) surface

The (111) surface is prevalent on natural magnetite crystals, and it has also been intensively studied using the surface science approach. In the [111] direction the repeat unit consists of six atomic planes, commonly labelled Fe_{tet1}, O_1, Fe_{oct1}, O_2 Fe_{oct2} and Fe_{tet2} (see Fig. 2.5). The surface reconstruction most commonly observed in UHV is a surface exhibiting a (2 × 2) periodicity with respect to the O-plane, which corresponds to a (1 × 1) periodicity with respect to the Fe_{tet} plane. For a long time it was debated whether this "regular" surface is terminated by Fe_{tet} or Fe_{oct}, as there has been reported evidence for both [83–86]. Now it seems accepted that a surface terminated by Fe_{tet} can be routinely prepared in UHV, which was confirmed by LEED-IV, STM, DFT+U and adsorption studies of various probe molecules [84, 87–89]. Nevertheless, the Fe_{oct} terminated surface can also be prepared in slightly reducing conditions, and small patches of this termination often appear among the Fe_{tet} when the surface is not oxidized enough during preparation [90]. In even more reducing conditions, multiple competing surface reconstructions are observed whose exact atomic arrangement is unknown [91–93]. The main issue with studying those is that it is nearly impossible to prepare a monophase surface and thus area-averaging spectroscopic techniques always show data corresponding to multiple phases. In oxidizing conditions (cooling down in O_2 after the sputter/anneal cycles), growth of yet another phase was observed, appearing as trianglular islands on top of the Fe_{tet} termination [87]. The model for this phase is also missing.

The sensitivity of the surface termination to small changes in surface preparation conditions makes the (111) surface challenging to study. Nevertheless, after years of research there are preparation recipes that reproducibly lead to high quality Fe_{tet} surfaces on both thin films or single crystal surfaces. This provides a valuable basis for more complex fundamental studies of the surface reactivity. It is highly interesting, for example, to compare the adsorption properties of molecules on the well-defined Fe_3O_4(111) and Fe_3O_4(001) surfaces to find out whether there are any universal characteristics underlying the reactivity of magnetite surfaces.

Modifications of the Fe_3O_4(111) by various metals were extensively studied both experimentally and computationally, mostly focusing on the reactivity of metal clusters [51, 94, 95]. The majority of the deposited metals readily forms nanoparticles

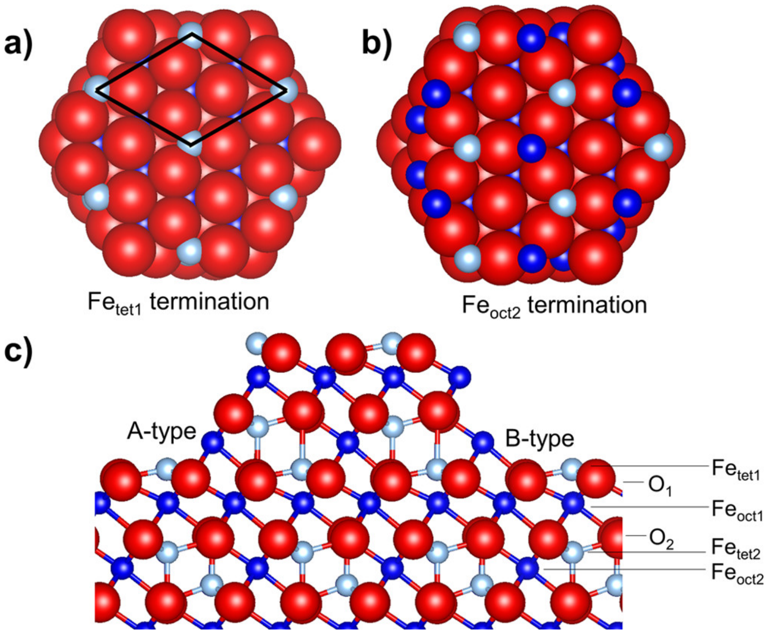

Figure 2.5: Models of the Fe_{tet} (a) and Fe_{oct} (b) terminations considered as the ”regular” surface reconstructions of $Fe_3O_4(111)$. Panel (c) shows bulk stacking of atoms in the [111] direction and two types of step edges possible on the Fe_{tet} surface. Figure reprinted from [88].

on this surface at room temperature [51]. Some metal adatoms were observed, but there is no clear consensus on the exact site which these adatoms occupy. Isolated Au adatoms were reportedly observed as minority species after deposition of more than 1 ML of Au and heating to 500 °C, and the STM images suggested the Au_1 to be atop surface O atoms [96]. Computational studies of the same system favor Au_1 adsorption atop the Fe_{te1} atoms or in the Fe_{te1} vacancies [97, 98]. In the case of Pd, computational studies report Pd binding preferentially to oxygen in three fold hollow site [98], but experimental works show that Pd is clustered already at room temperature [99]. Pt was reported to form small single-layer islands upon deposition at cryogenic temperatures and heating to room temperature [100]. The $Cu_1/Fe_3O_4(111)$ system was studied computationally and the most stable Cu_1 site was found to be three fold hollow site binding to surface oxygen [101]. However, no experimental evidence of such Cu_1 adsorption is available.

2.2 Hematite α-Fe_2O_3

Hematite is the most oxidized form of iron oxide. The structure of hematite is based on a hexagonal close packed (hcp) anion O^{2-} lattice stacked along the [0001] direction. All the Fe^{3+} cations are octahedrally coordinated; along the [0001] directions there are always two occupied octahedral sites followed by one empty (see figure 2.6). The pairs of occupied-face sharing octahedra are slightly distorted from the ideal packing of the cation sub-lattice, as the cations repell each other and shift towards the unshared faces [102]. As a consequence of this distortion, two different Fe-O bond lengths are present in the hematite structure.

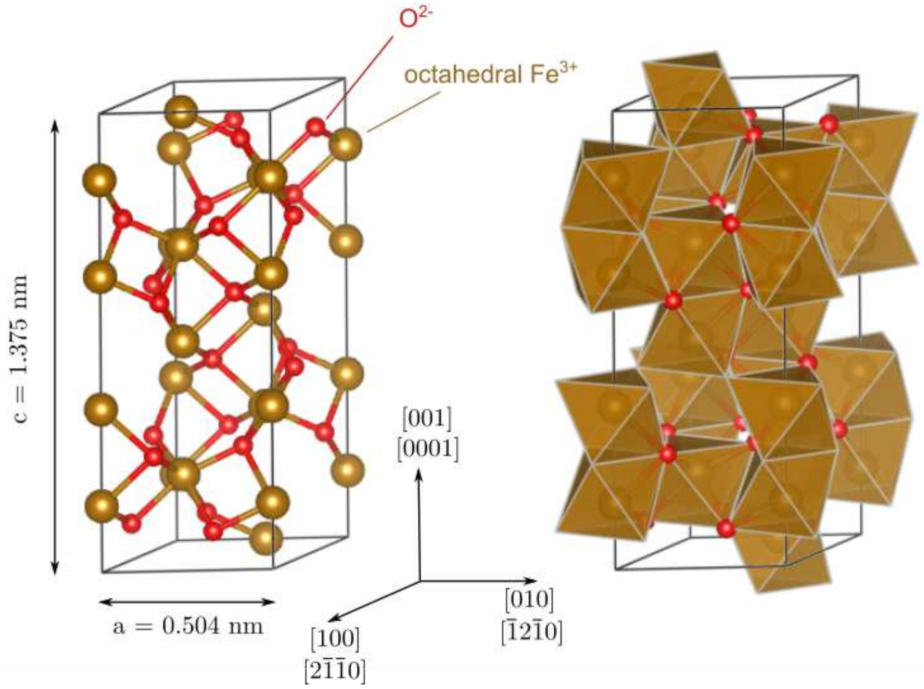

Figure 2.6: Ball-and-stick and polyhedral models of hematite unit cell. The oxygen forms a slightly distorted hcp lattice. Two thirds of the octahedral sites are filled with iron, which can be seen on the polyhedral model - in the [0001] direction there are always two face-sharing octahedra followed by one missing. Note the coordinate system is trigonal, the directions are given in both three-index and four-index notations.

Hematite is perfectly antiferromagnetic at temperatures below 260 K (referred to as Morin the temperature), when the spins are oriented perfectly perpendicular to the (0001) plane. At the Morin temperature, a 90° spin-flip occurs and the spins are oriented in the (0001) planes. The antiferromagnetic ordering is not ideal above the Morin temperature and the spins are slightly canted, causing hematite to be weak (parasitic) ferromagnet [102, 103]. The Neel temperature for hematite is 950 K, above which it is paramagentic.

In the absence of doping or impurities, the conductivity of α-Fe_2O_3 is poor and highly anisotrophic [104] - up to several orders of magnitude higher along the (0001) plane than perpendicular to it [105]. That phenomenon can be explained considering the magnetic structure of hematite; the spins of the Fe are ferromagnetically coupled along the (0001) planes and antiferromagnetically coupled along the [0001] direction, which creates an environment where the electrons can move within the Fe layers but are forbidden to hop across the oxygen planes to another Fe layer [106].

Natural crystals of hematite often expose the (0001) or the $(1\bar{1}02)$ facets, and these are also favoured by DFT calculations [51, 107]. In the literature, these facets are often referred to by the three-index notation equivalents or by the common names in corundum structure. In the case of the (0001) the three index equivalent is (001) and the common name is C-cut. The $(1\bar{1}02)$ is equivalent to $(01\bar{1}2)$ and $(\bar{1}012)$ in the four-index notation, to (012), $(\bar{1}02)$ and $(1\bar{1}2)$ in the three-index notation and the surface is commonly known as the R-cut. Visualization of the relevant surfaces on the corundum structure unit cell is shown in Fig. 2.7.

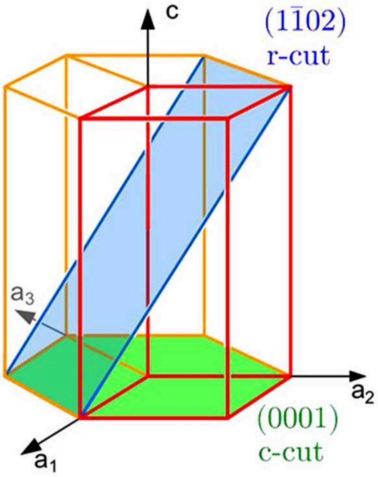

Figure 2.7: Visualization of he (0001) and $(1\bar{1}02)$ planes in corundum structure. The hexagonal unit cell shown in Fig. 2.6 is highlighted by red. Figure adapted from [108].

2.2.1 The (0001) surface

By far the most experimental work on hematite has been done on the (0001) surface. However, in UHV conditions this surface is easily reduced and forms a number of competing surface reconstructions which makes its atomic-scale structural studies very difficult to interpret. For these reasons the system has been described as "the most challenging and controversial among iron oxides" in a recent review of model oxide surfaces [109]. On a polished α-Fe_2O_3(0001) single crystal, the typical cleaning procedure of sputtering and annealing results in significant reduction of the surface, and this change is irreversible in UHV conditions [110]. The exact stoichiometry of the reduced phases was long debated and various models featuring coexistence of $Fe_{1-x}O$ or Fe_3O_4 phases with the α-Fe_2O_3 have been proposed [109, 111]. On thin hematite films, the redox behavior strongly depends on the substrate, and the substrate effects can lead to complex and highly counter-intuitive results [112]. Reportedly stoichiometric α-Fe_2O_3(0001) surfaces have only been observed after preparation in near-ambient partial pressures of oxygen [113, 114], after annealing in atomic oxygen [115] or after ozone treatment [116]. Nevertheless, it is still discussed how some of these are terminated [109, 117]. Thus, any studies that intend to provide atomic-scale understanding of the processes happening on the α-Fe_2O_3(0001) are extremely challenging and require surface characterization by multiple techniques in each step of the experiment.

2.2.2 The $(1\bar{1}02)$ surface

With the well-documented struggles in preparation of well-defined α-Fe_2O_3(0001) surfaces, it is surprising that the other dominant facet of hematite $(1\bar{1}02)$ stayed mainly out researchers' focus. The literature on this surface is scarce, but all the studies suggest that well-defined monophase surfaces are achievable on the α-$Fe_2O_3(1\bar{1}02)$ [118–126]. It has been known since 1988 that two surface reconstructions are stable on the $(1\bar{1}02)$ surface, and these have a (1×1) and a (2×1) symmetry. Both are easily preparable in UHV conditions and can be interconverted by annealing in UHV or in a low partial pressure of oxygen [118]. The ratio of distances in the Low Energy Electron Diffraction (LEED) pattern and ratio of intensities in of the O and Fe Auger lines in the Auger Electron Spectroscopy (AES) are consistent with a simple bulk-truncation model for the (1×1) surface (see Fig. 2.8) [119]. Such a surface termination is also plausible from the view of surface polarity, as the atomic arrangement can be classified as Tasker type 2 "non-polar" surface [127].

No imaging study of the α-$Fe_2O_3(1\bar{1}02)$ has ever been published, and the structures are proposed solely on the spectroscopic and diffraction data. The (2×1) symmetry implies that the reconstruction takes place in the direction perpendicular to the zig-zag rows formed by surface oxygen atoms in the bulk-truncated (1×1) surface. Electron Energy Loss Spectroscopy (EELS) spectra shows the (2×1) has Fe^{2+} cations on the surface. The proposed models for the (2×1) feature a partially or completely missing oxygen row on the bulk terminated surface (see Fig. 2.8) [120, 128, 129].

Both the (1×1) and (2×1) surface have been studied using Temperature Programmed Desorption (TPD) with various probe molecules [120–122, 129]. It was shown that both recostructions adsorb water both dissociatively and molecularly, although different amounts and with different strengths [120]. The (2×1) surface has also been studied by O_2 TPD and it was found to adsorb oxygen both dissociatively and molecularly. In a model of the (2×1) surface based on surface oxygen vacancies (such as the one illustrated in Fig. 2.8), adsorption of dissociated oxygen would hint on reparation of the oxygen vacancies and recovery of the stoichiometric (1×1) surface. This was however not observed and a new structure with $c(2 \times 2)$ symmetry in LEED was reported, suggesting that the (2×1) structure might be more complex [129].

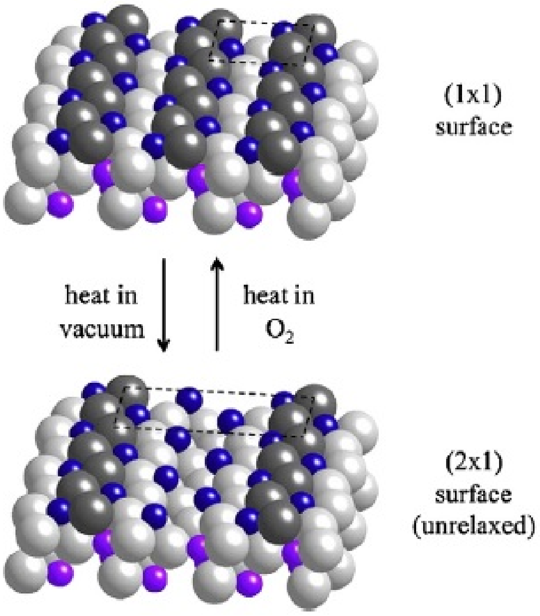

Figure 2.8: Surface reconstructions of hematite $(1\bar{1}02)$. The (1×1) surface is bulk terminated, it features oxygen (gray) rows (highlighted by dark gray) straddled by iron (blue). The surface structure of the (2×1) in unknown. One of the proposed models is bulk termination with missing row. Picture reprinted from [129].

The α-$Fe_2O_3(1\bar{1}02)$ surface has also been studied by in-situ surface X-Ray diffraction and molecular dynamics simulations [123, 124, 130, 131] in dry and humid atmospheres. It was first concluded that surfaces prepared by chemical-mechanical polishing exhibit a dominant phase with an incomplete occupancy of the topmost iron layer (so-called half-layer termination). This was further supported by DFT calculations showing the hydrated half-layer model being thermodynamically the most stable in humid environment [126]. Nevertheless, using the same techniques the same group later showed that a stoichiometric surface (regarded as a “full-layer” in this context) can be prepared by annealing the half-layer terminated surface in air [124, 130], and that the topmost iron-layer can also be filled by exposure to solutions containing Fe(II) ions which become oxidized to Fe(III) upon adsorption [132]. These results raise the question whether the half-layer termination really presents a global thermodynamic minimum, or whether it is just a consequence of the rough surface preparation by chemical-mechanical polishing. A recent DFT study comparing the terminations of the α-$Fe_2O_3(1\bar{1}02)$ surface shows that hydroxylated stoichiometric (full-layer) surface is at the very least energetically comparable to the Fe-deficient (half-layer) surface, and in a relatively wide window of relevant O_2 and H_2O chemical potentials, the hydroxylated stoichiometric (full-layer) termination is the most stable of the tested phases [133]. Very recently it was proposed that the Fe-deficient (half-layer) surface is stabilized by continuous ultrafast oxygen exchange of the topmost oxygen layer with the water adsorbed on top [134].

3 Methods

This chapter gives a brief description of the general principles of the techniques, and the specific experimental apparatus used throughout this thesis.

3.1 Scanning Tunneling Microscopy (STM)

Scanning Tunneling Microscopy (STM) is one of the most popular real space imaging techniques in surface science. Invented in 1981 and awarded a Nobel prize five years later, STM can image well-prepared surfaces with atomic resolution to provide information about surface topography and electronic structure [135]. STM belongs to the family of Scanning Probe Microscopes (SPM), which means the imaging takes place by scanning a sharp tip line-by-line in close vicinity to the studied surface. A schematic image of a typical STM setup is shown in Fig. 3.1A. In all SPM techniques, a precision piezo drive is used to move the tip to the typical tip-sample distance of units of nm to units of Å. Different SPM techniques then vary by the type of signal that is being recorded and by the feedback mechanism that keeps the tip close to the surface. In the case of STM, a small bias voltage (a few mV to several V) is applied between the tip and the sample, and the quantum tunneling current is measured. This tunneling current is then either used as a process value of the feedback mechanism in the so-called constant current mode, or is recorded as the measured signal in the so-called constant height mode (see Fig. 3.1B).

The concept of tunneling

Quantum tunneling can be explained using a simple model of a particle approaching a rectangular potential barrier. In the simplest case, the wave function of the particle must satisfy the time-independent, one-dimensional Schrödinger equation:

$$-\frac{\hbar^2}{2m}\Delta\psi(x) + V(x)\psi(x) = E\psi(x), \tag{3.1}$$

where $\hbar$ is the reduced Planck constant ($h/2\pi$), Δ is the Laplacian operator, V is the potential barrier and E is the sum of potential and kinetic energy of the particle.

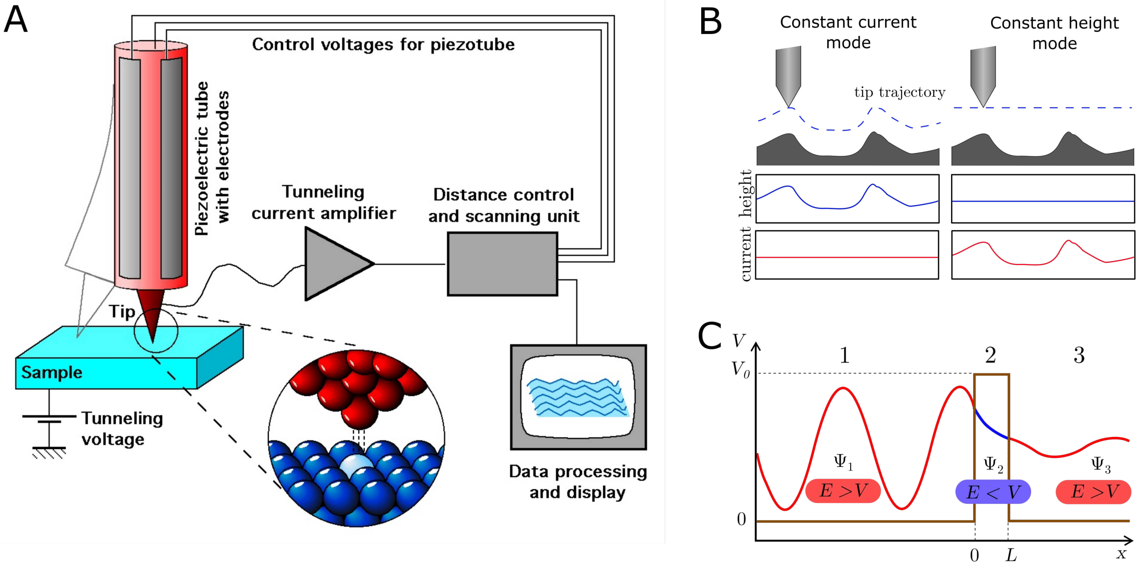

Figure 3.1: A) Schematic illustration of the experimental STM setup. Image courtesy of Michael Schmid. B) The two basic modes of STM imaging. Either the current is kept constant and the information is recorded in the height channel, or the other way around. C) Illustration of a tunneling effect on a potential barrier. An electron with wave function Ψ_1 hits a potential barrier. Even though the potential barrier is higher than the energy of an electron, the wave function continues in the form of exponential decay. In the region behind the barrier, the wave function Ψ_3 has much lower, but still non-zero amplitude.

The solution of equation 3.1 can be expressed as a linear combination of harmonic functions

$$\psi(x) = A\exp(\mathrm{i}kx) + B\exp(-\mathrm{i}kx), \tag{3.2}$$

where k is the length of the wave vector defined as

$$k = \frac{\sqrt{2m(E - V(x))}}{\hbar}. \tag{3.3}$$

Assuming a rectangular potential barrier with height $V_0 > E$ and width L as shown in Fig. 3.1C , the solutions to equation 3.1 outside of the barrier are propagating waves. Inside the barrier, however, the wave vector is an imaginary number and the solution is an exponentially decaying wave function.

To find the probability P of detecting the particle on the other side of the barrier, we compare the squared modulus of the wave function in front of the barrier and behind it. After expressing the A and B coefficients using the continuity conditions of the wave function and its first derivative, we find that the probability is proportional to $\exp(-2k_2L)$

$$P = \frac{|\Psi_3|}{|\Psi_1|} = \frac{A_3^2}{A_1^2} \cong \exp(-2k_2L). \tag{3.4}$$

Contrast in STM images

Even though the real case of STM tip-substrate problem is much more complex than a free particle approaching a rectangular barrier, the general principle of stays the same. For typical STM scanning parameters and substrates, the tunneling current decreases by roughly an order of magnitude per every Åincrease in distance. This is the reason of the high resolution achievable by STM and its surface sensitivity: The atoms located higher on the tip or lower in the surface contribute negligibly to the tunneling current, because the of the exponentially decaying tunneling probability.

The information about topopgraphy is always convoluted with the information about electronic structure in the STM data. A more rigorous model of tunneling between the STM tip and the substrate was developed by Tersoff and Hamann [136], taking into account the local density of states of the surface and the geometry of the tip. This model shows that the tunneling probability is proportional to the local density of states (LDOS) close to the Fermi energy, and thus in the constant-current mode of STM scanning the tip follows the contours of constant LDOS. The apparent height in STM therefore does not always correlate with the real dimensions of the surface features, and especially on systems consisting of several chemically distinct species the data must be interpreted very carefully.

3.2 Noncontact Atomic Force Microscopy (ncAFM)

Atomic Force Microscopy (AFM) is one of the most powerful and versatile imaging and manipulation tools in current micro- and nanoscale studies. AFM is a Scanning Probe Microscopy technique invented only four years after the STM with the motivation to develop a technique capable of imaging insulating surfaces [137]. This was accomplished relatively early on, and even though the achievable resolution was initially inferior to STM, the ability to image almost any surface in any environment made the AFM very popular in many different fields. Since then, the dynamic noncontact AFM (ncAFM) was developed, and current state-of-the-art ncAFM tools not only surpass the resolution of STM, [138, 139] but can also be used to measure phenomena unaccessible by STM, such as charge states of single atoms, [140, 141] bond orders in organic molecules [142, 143] or single electron injection events [144, 145]. There are many types of AFM instruments for various applications differing mostly by the mode of operation and working environment. In this thesis, a frequency-modulated noncontact AFM (ncAFM) instrument operating in ultra-high vacuum at low temperature was used, and only this type is described in the following subsection.

Forces between the tip and sample

AFM relies on the measurement of forces acting between the tip and the measured surface. In ncAFM, the tip is attached to an oscillating cantilever and the resonant frequency of the cantilever is monitored. The resonant frequency shifts when an external force acts on the tip, and this shift is recorded as the primary signal in constant-height ncAFM imaging.

Generally, the overall force between the tip and the surface (F_{tot}) consists of several components [146]

$$F_{\mathrm{tot}} = F_{\mathrm{el}} + F_{\mathrm{vdW}} + F_{\mathrm{chem}}, \tag{3.5}$$

where F_{el} is the electrostatic force, F_{vdW} is the van der Waals force and F_{chem} is the chemical interaction force. The electrostatic and van der Waals forces are weakly dependent on distance in comparison to chemical forces, and are therefore regarded as long-range. To maximize the relative contribution of the short-range F_{chem}, which is the relevant component for high resolution imaging, the tip has to be brought very close ($< 1\,\mathrm{nm}$) to the sample.

The qPlus sensor

To avoid snapping of the tip to contact due to long range attractive forces, the stiffness and amplitude of the cantilever/tuning fork must fulfill the condition [147]

$$k \cdot A > \max\left(\frac{\delta V_{\mathrm{ts}}}{\delta z}\right), \tag{3.6}$$

where k is the stiffness of the cantilever, A is the oscillation amplitude, V_{ts} is the potential energy between the tip and the sample and z is the distance between the tip and the sample. From eq. 3.6 it is clear that for the noncontact scanning to be stable, either the cantilever must be very stiff, or the oscillation amplitude must be very high. The latter is not desirable, because at larger amplitudes the contribution of F_{chem} diminishes and the long range forces dominate. It is much more convenient to use sensors with high stiffness, and as of today the two widely used high-stiffness ncAFM sensors are the qPlus and KolibriSensor.

The qPlus sensor was developed by F. Giessibl, and is based on a quartz tuning fork [148]. One of the prongs is fixed to a ceramic plate, while the other has a tip attached and is free to oscillate. A schematic picture of a qPlus sensor is shown in Fig. 3.2A. In the first qPlus sensors the oscillation was induced by adding a small signal to the z-piezo voltage of the scanner. The oscillation of the prong is then measured by the two electrodes collecting the deflection current induced by the piezoelectric effect on the surface of the prong. A separate electrode is then connected to the tip to collect tip-sample tunneling current and thus allow STM measurements. The latest qPlus sensors have another electrode for the oscillation excitation. The sensors used in this thesis (photo shown in Fig. 3.2B) have a resonance frequency ≈ 31 kHz, stiffness ≈ 2000 N/m and Q factor between 10000 and 20000.

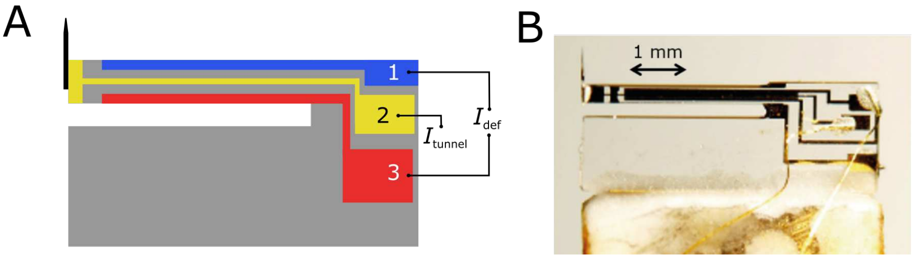

Figure 3.2: A) Schematic illustration of a qPlus sensor. Electrodes 1 and 3 are used to measure the deflection current induced by the piezoelectric effect. Electrode 2 is connected to the tip to provide the STM capability. B) A photo of a real qPlus sensor used in this work (provided by Martin Setvin).

Contrast in ncAFM images

Pioneering ncAFM works on oxide surfaces identified two basic types of ncAFM contrast with the determining factor being the tip termination [149]. Tips terminated with a cation were referred to as “positive”, and these showed attractive interaction with surface anions and repulsive with surface cations. The opposite was observed with the “negative” tips terminated by an anion. The contrast changes were relatively frequently observed during scanning due to mild contact of the tip with the surface.

These days, the highest resolution ncAFM images are typically acquired with a “functionalized” tip, meaning a tip with a known termination that can be prepared in a known and reproducible way. By far the most popular tip functionalization is by a CO molecule, which is relatively easily picked up and remains stable at the tip at 4 K. The big advantage of a CO-terminated tip is that it is chemically very stable and thus does not form a chemical bond to the measured substrate, which would result in a tip change. It is therefore easy to scan very close to the surface, where a significant force is measured due to overlap of the orbitals of the tip and the substrate. The resulting Pauli repulsion is highly localized and thus its detection leads to ultrahigh resolution [138]. Another equally important asset of a CO-terminated tip is that the contrast is relatively straightforward to simulate computationally [150].

In this work, the tip was functionalized by picking up a CO molecule from Pt, Rh or Ir species on Fe_3O_4 surfaces. CO adsorbs very strongly on these species (temperature programmed desorption studies show that CO desorbs at 500-600 K) and the tip likely becomes terminated by these metals during scanning. Therefore, the CO-terminated tips prepared this way are stable even at temperatures significantly higher than 4 K. While an increase of measurement temperature is generally not desirable in ncAFM imaging due to higher thermal noise, in this thesis performing the measurements at 78 K enabled valuable comparison to the simultaneously acquired STM data, which are impossible to get at 4 K when the studied samples are insulating.

3.3 X-Ray Photoelectron Spectroscopy (XPS)

X-Ray Photoelectron Spectroscopy, also known as Electron Spectroscopy for Chemical Analysis (ESCA), is a surface-sensitive technique for measuring the elemental composition of the sample. XPS data can be used to identify elements on the surface, distinguish between the same elements bonded in different chemical states, and determine the depth profiles of different species.

The technique is based on the photoelectric effect. A photoelectron can be excited if the incident photon energy is larger than work function of the material and the binding energy of the electron. The detected kinetic energy of the emitted electron is given by the equation

$$E_{kin} = h\nu - E_b - \Phi_{spec}, \tag{3.7}$$

where $h\nu$ is the energy of the incident beam, E_b is the binding energy of the atomic orbital from which the electron originates and Φ_{spec} is the work function of the spectrometer, see figure 3.3A.

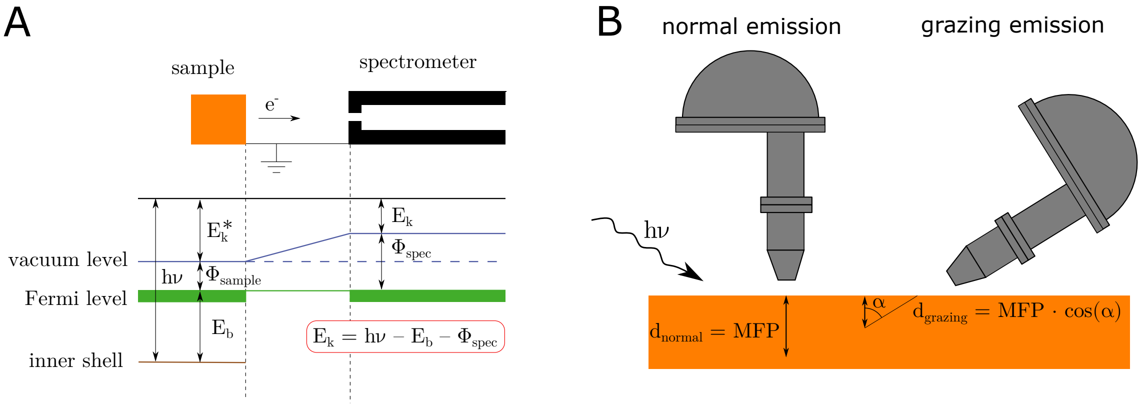

Figure 3.3: A) Energy levels of the sample and the analyzer in an XPS experiment, see eq. 3.7. B) Measurements in grazing emission geometry are more surface sensitive due to the probing depth scaling with the cosine of the emission angle.

In XPS, the sample is irradiated by monoenergetic x-rays and photoelectron counts at different energies are taken. In the resulting spectra, peaks can be assigned to electrons emitted from specific orbitals or originating from other inelastic processes.

Although the photons travel micrometers deep into the sample, only the electrons from several top atomic layers are detected in XPS. That is due to the inelastic mean free path (IMFP) of the excited electrons, which is in the range of units to tens of Ångströms for the relevant energies [151]. The surface sensitivity can be enhanced by measuring in grazing emission geometry, where the probing depth scales with the cosine of the emission angle (see Fig. 3.3B)

Information in XPS spectra

The XPS spectra are usually plotted on the binding energy scale, not kinetic energy scale. That is convenient, because the binding energy of photoelectrons stays constant irrespective of the excitation energy and thus XPS data acquired with different x-ray source anodes are easily comparable. Many processes take place during XPS measurements, and peaks of different origins are observed in XPS spectra; the most common phenomena are summarized in the following text.

The most prominent peaks in an XPS spectrum are the photoelectron peaks. Every element has a specific set of photoelectron peaks that can be assigned to electron emission from its core levels. The position of the peaks can change within a few eV depending on the chemical state of the atoms. XPS can thus be used not only to detect the presence of a given element, but also provides information about its charge state if suitable reference data are available.

When an electron from an outer shell fills an electron vacancy in an inner shell, another electron from an outer shell can be emitted. This process called the Auger effect (see figure 3.4) and the Auger peaks are commonly present in XPS spectrum. The Auger process is intrinsic to the atom, therefore the kinetic energy of Auger electrons originating from the same levels is constant, and on the binding energy scale the Auger positions will shift if a different anode is used. This is one of the reasons why dual-anode x-ray sources are usually used - in case an Auger peak overlaps with a photoelectron peak, changing the anode separates them in the spectrum.

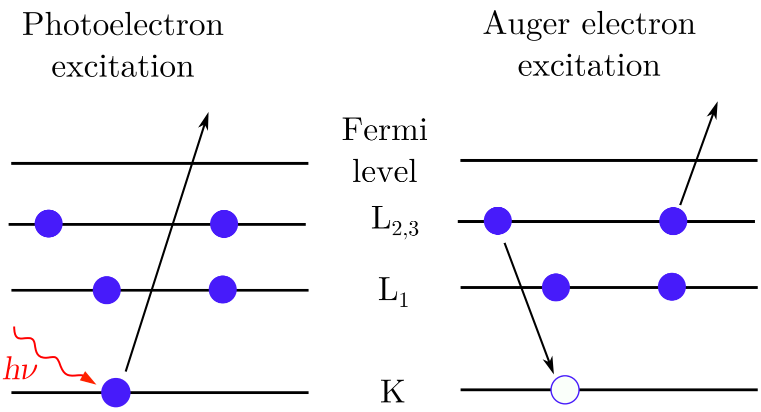

Figure 3.4: Illustration of photoelectron and Auger processes.

The emitted photoelectrons can take part in multiple inelastic processes, which can lead to specific photoelectron energy losses. These are detected as well-defined “satellite” peaks at the higher binding energy (lower kinetic energy) with respect to the photoelectron peaks. Typical well-defined inelastic processes include plasmon excitation (“plasmon” peaks) or interaction with an outer shell electron (“shake-up” peaks). Other photoelectrons that get inelastically scattered and still reach the analyzer contribute to the background signal, which significantly increases at low kinetic energies.

For quantitative analysis, the photoemission peaks are typically fitted with Gaussian-Lorentzian functions to deconvolute the individual components. In some cases the interpretation can be relatively straightforward (for $1s$ peaks and a known number of components, for example), but some peaks can be very complicated to quantify due to various multiplet splitting contributions. A typical example of a non-trivial peak shape is the Fe $2p$ [152].

3.4 Temperature Programmed Desorption (TPD)

Temperature programmed desorption is a spectroscopic technique for studying the interaction of molecules with surfaces. Information about desorption energies and mechanisms can be extracted from the TPD spectra, along with information about chemical reactivity of molecules with the surface or with other molecules on the surface. The TPD data provide a quintessential basis for surface reactivity studies that is ideally complemented by other experimental techniques and density functional theory (DFT) caluclations to determine the exact reaction pathways.

A typical TPD experiment consists of several steps: First, the sample is cooled to a temperature low enough to adsorb the molecules of interest. Then the molecules are dosed on the surface and the sample is moved in front of a quadrupole mass spectrometer (QMS). The sample is heated with a constant heating rate and the QMS is used to monitor the relevant molecular masses. Because of the constant heating rate the data can easily be plotted on the temperature scale, and the output from a TPD experiment is a plot of desorption rate versus temperature. Usually, this is repeated multiple times for different molecular doses, so that a typical TPD plot shows multiple lines for different coverages of molecules on the surface, as shown in Fig. 3.5.

The desorption kinetics is mathematically described by the Polanyi-Wigner equation:

$$-\frac{\mathrm{d}\Theta}{\mathrm{d}t} = -\beta\frac{\mathrm{d}\Theta}{\mathrm{d}T} = \nu\Theta^n \exp\left(-\frac{E_d}{k_B T}\right), \tag{3.8}$$

where $-\frac{\mathrm{d}\Theta}{\mathrm{d}t}$ is the desorption rate, β is the heating rate, ν is the pre-exponential factor, Θ is the coverage, n is the order of desorption, E_d is the desorption energy, k_B is the Boltzmann constant and T is the temperature.

In the experiment, the heating rate β is an experimental parameter, and the desorption rate $-\frac{\mathrm{d}\Theta}{\mathrm{d}T}$ is measured. The desorption order n describes the dependence of the desorption rate on coverage. In most cases relevant for surface science, $n =$ $= 0, 1$, or 2. Desorption order of zero is expected when the molecules are desorbing from an effectively infinite reservoir, a typical example is desorption from multilayers. Then the measured desorption rate follows the exponential dependence on temperature until all the species are desorbed and the desorption rate sharply drops to zero. The leading edges of TPD spectra with different initial coverage overlap perfectly and the desorption maximum shift to higher temperatures with increasing coverage, see Fig. 3.5A. A first-order process is expected for desorption of species molecularly adsorbed on the surface. Here, the desorption rate is modulated by the decreasing coverage. TPD spectra of a first order desorption process show the desorption maximum being independent on initial coverage, see Fig. 3.5B. A second order desorption occurs when the species adsorb dissociatively on the surface. In order to desorb, the components of the molecule must first meet and recombine on the surface. The probability of this happening strongly depends on coverage, and therefore in the TPD spectra the desorption rate maximum shifts to lower temperature with increasing initial coverage (see Fig. 3.5C). The peak shape and desorption rate maximum dependence on coverage can be also affected by the lateral interactions of the adsorbed molecules. Repulsive interactions cause the desorption rate maximum to shift to lower temperatures with increasing initial coverage, attractive interactions do the opposite.

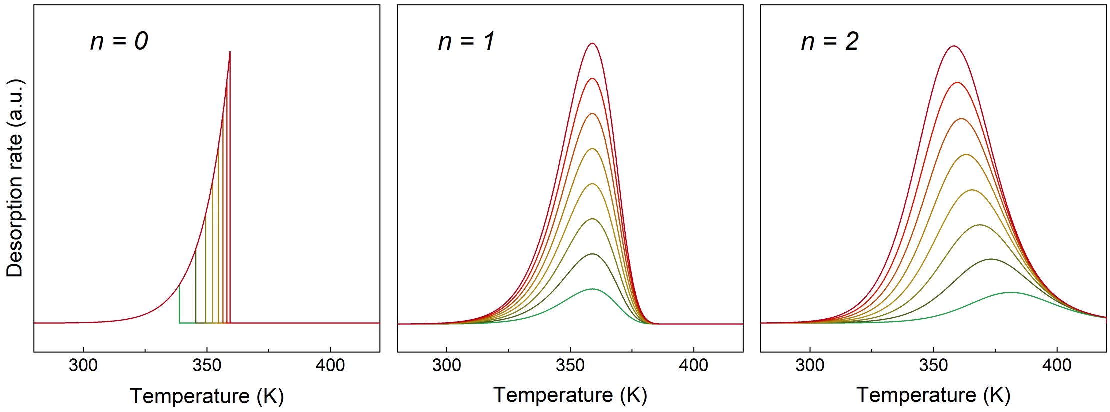

Figure 3.5: Simulated temperature programmed desorption (TPD) spectra for the most common orders of desorption $n = 0, 1, 2$. Spectra are normalized to desorption rate maximum. In all three cases, the desorption energy E_d is 1 eV and the prefactor ν is $1 \cdot 10^{13}\,\mathrm{s}^{-1}$.

The prefactor ν for a non-activated reversible first order desorption can be expressed using the transition state theory as

$$\nu = \frac{k_B T}{h} \exp\left(\frac{\Delta S^{\#}}{k_B}\right), \tag{3.9}$$

where h is the Planck constant and $\Delta S^{\#}$ is the entropy difference between the adsorbed state and the transition state. From this it is clear that the more confined the molecule is on the surface, the higher the desorption prefactor is. Often, a prefactor value of $\nu = 10^{13}\,\mathrm{s}^{-1}$ is assumed without any further comment, but this value is only valid for simple molecules with translational and rotational degrees of freedom. A more rigorous way of determining a prefactor value is to either calculate it for a given molecule from transition state theory, or to extract it from a TPD dataset using a suitable method (one such method, inversion analysis, is described below). It is not unusual that the prefactor values found this way are several orders of magnitude higher than the "typical" value of $10^{13}\,\mathrm{s}^{-1}$.

Limiting the background signal

In TPD experiment it is important to ensure that the only measured signal comes from desorption of molecules intentionally and controllably adsorbed on the surface. Thus, the signal corresponding to molecules adsorbed from the background and/or adsorbed on the sample mount should be limited to an absolute minimum. A common way to achieve this is to use a QMS equipped with a cooled differentially pumped inlet, which moves very close to the sample. This way, the molecules can be dosed by backfilling the whole chamber, but only those desorbing in direct line-of-sight to the QMS ionizer are measured. Alternatively, the molecules can be dosed on the sample by a focused molecular beam, so that they only adsorb on the sample surface. The latter setup is utilized in the chamber used in this thesis, and it was shown before that 99.9 % of the molecules dosed by the beam impinge a well-defined area on the sample surface (see reference [153] and Fig. 3.6). When the molecules of interest are also present in the background pressure of the chamber, it is advisable to use isotopically-labeled versions of these (i.e., D_2O instead of H_2O or ^{13}CO instead of ^{12}CO, etc.) to limit the signal background.

Analysis of the TPD data

This subsection describes three methods of TPD data analysis used in this thesis: the Arrhenius plot $\ln r/\nu\Theta^n$ vs. $1/T$ analysis, the Redhead analysis and the inversion analysis. For a comprehensive review of other methods to analyze TPD data, the interested reader is referred to [154–156].

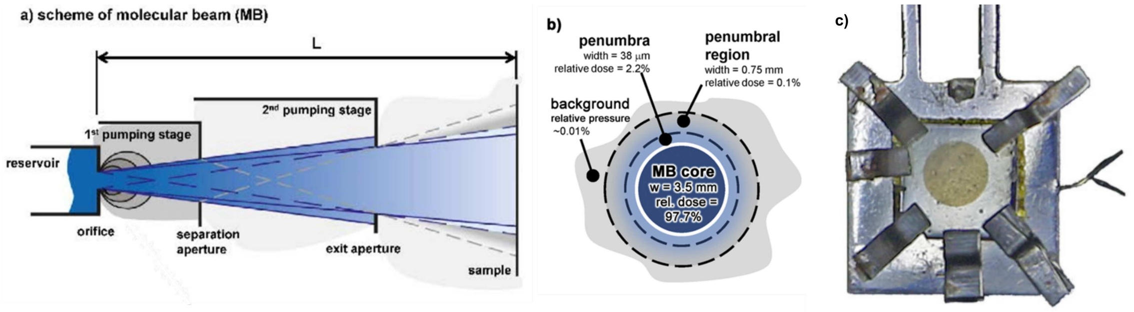

Figure 3.6: Schematic picture of the effusive molecular beam used for gas dosing in TPD experiments described in this thesis. The beam is formed by expansion of the gas through two differentially-pumped stages (a), and results in a well-defined spot on the sample surface, which contains $\approx 99.9\,\%$ of the dosed molecules (b). (c) A photo showing multilayers of D_2O adsorbed on the sample surface. Figure adapted from [153].

The **Arrhenius plot** $\ln r/\nu\Theta^n$ vs. $1/T$ analysis is used to determine the order of desorption n when it is not immediately clear from the shape and desorption rate maxima positions of the TPD spectra with differing initial coverages. The Polanyi-Wigner equation is rewritten under the assumption of constant E_d as

$$\ln \frac{r}{\nu\Theta^n} = -\frac{E_d}{k_B T}, \tag{3.10}$$

where r is the desorption rate. Then the spectra are plotted as $\ln r/\nu\Theta^n$ versus $1/T$ for different values of the desorption order n, and the plot closest to the straight line corresponds to the correct n.

The **Redhead analysis** provides the simplest method for extraction of the desorption energy E_d from even a single desorption spectrum. For a first-order desorption process and coverage-independent E_d, one can set the first derivative of equation 3.8 to zero and then express E_d approximately as

$$E_\mathrm{d} = k_\mathrm{B} T_\mathrm{max} \left[\ln\left(\frac{\nu T_{max}}{\beta} \right) - 3.46 \right], \tag{3.11}$$

where T_max is the maximum of the desorption peak. This allows a very quick calculation of E_d with the only parameter needed from experiment being T_max; the error due to approximations in deriving eq. 3.11 is less than $1.5\,\%$ provided the ν/β value falls between $10^8 - 10^{13}$. A similar formula is derived for second-order processes, where the coverage at T_max needs to be known [155, 157]. The main limitation of the Redhead analysis is that an educated guess has to be made about the desorption order and the prefactor.

The **inversion analysis**, developed by Tait et al. [156], is a powerful method for determination of both desorption energy E_d and prefactor ν from a set of TPD spectra with different initial coverages. Under the assumption of ν being independent of temperature and coverage, the desorption energy E_d is expressed from the Polanyi-Wigner equation

$$E_\mathrm{d}(\Theta) = -k_\mathrm{B} T \ln\left(-\frac{\mathrm{d}\Theta/\mathrm{d}t}{\nu\Theta^n}\right). \tag{3.12}$$

For a given n, the E_d is plotted as a function of fractional coverage Θ for several different values of ν. The combinations of E_d and ν are then used to simulate TPD spectra at different coverages, and the agreement is quantified by plotting the squared error between the experimental and simulated spectra. Typically, the squared error plot exhibits a clear minimum, and the correct combination of E_d and ν is found. The same approach can be applied to analyze TPD curves of second-order processes. Thus, given a sufficient experimental dataset, inversion analysis can be used to extract all the relevant quantities with minimum initial assumptions needed.

3.5 Low Energy Ion Scattering (LEIS)

Low-energy Ion Scattering (LEIS), also known as Ion Scattering Spectroscopy (ISS), is a highly surface-sensitive technique used to determine elemental composition of the sample. The sample is bombarded by light ions (typically of inert gases He^+ or Ne^+) of low energy (from 100 eV to a few keV) and the energy of the scattered ions is measured by a hemispherical analyzer. The energy depends on the masses of the incident ion and the target atom, the incident ion energy and the scattering angle. The main advantage of LEIS is its extreme surface sensitivity due to high neutralization probability of ions penetrating into deeper layers.

Although LEIS is regarded as a non-destructive technique, a special care must be taken to avoid excessive surface sputtering, especially on oxide samples. In practice this is done by minimizing ion beam current and the exposure time.

In this work, LEIS has been used mainly to distinguish between two oxygen isotopes on the surface, $^{16}\mathrm{O}$ and $^{18}\mathrm{O}$, in experiments aimed at reaction mechanism determination and oxygen exchange phenomena.

3.6 Low Energy Electron Diffraction (LEED)

Low energy electron diffraction is a technique used to determine the surface structure of single-crystalline or thin film materials. It can be used both qualitatively as a quick and straightforward method to check the surface symmetry or quantitatively (LEED IV) as a powerful tool to confirm proposed complex surface structure models.

In LEED experiments the sample is bombarded by an electron beam with energy of (10^1–10^2) eV. The electrons can be assigned a de Broglie wave with wavelength of

$$\lambda = \frac{h}{\sqrt{2mE}}, \tag{3.13}$$

which, for those energies, is units of Ångströms, commensurate with interatomic distances. When incident to an ordered lattice, the electron beam scatters and the reflected electrons interfere constructively and destructively, creating a diffraction pattern which is imaged on a fluorescent screen.

The surface sensitivity of LEED is determined by the inelastic mean free path, which is in the range of Ångströms (≈ several atomic layers) for low energy electrons. The information obtained from LEED pattern originates from an area with lateral diameter smaller than the coherence length of the electron beam, which for common LEED systems is in the range of 10^2 Å[151]. The LEED pattern of a crystal after preparation should ideally feature bright and sharp diffraction spots. The distances in a LEED pattern are dependent on the beam energy, but their ratio is constant. Using that information, a surface structure or a superstructure of the sample can be determined. Random surface impurities and defects affect the spot sharpness and background intensity.

3.7 Density Functional Theory

Many of the experiments described in this thesis were complemented by computational Density Funtional Theory (DFT) calculations using the VASP and Wien2k codes. The calculations were carried out by Matthias Meier from the University of Vienna and Magdalena Bichler from the Institute of Materials Chemistry, TU Wien. The simulations of ncAFM contrast were carried out by Igor Sokolović from the Institute of Applied Physics, TU Wien; utilizing the Probe Particle Model [150, 158]. Detailed information about the parameters and functionals used can be found in our jointly published papers [81, 108, 159–161].

3.8 Experimental setup

The work presented in this thesis was carried out in four different experimental apparatus, the following subsection gives their brief description.

3.8.1 Room temperature STM chamber

The room temperature STM data were acquired in a two-vessel UHV chamber referred to as the RT-STM, consisting of a preparation chamber and an analysis chamber connected by a gate valve and a magnetically-coupled manipulator rod. The preparation chamber is equipped with a VG Microtech EX05 scanning ion gun, e-beam sample heating stage on the manipulator, a single-pocket and a triple-pocket e-beam evaporators (FOCUS EFM 3 and EFM 3T), a quartz crystal microbalance (QCM) for monitoring the deposition rates, a quadrupole mass spectrometer and four high precision leak valves. One of the leak valves is equiped with a gas doser to achieve high local pressures at the sample surface. The chamber is pumped by a turbo pump and its base pressure is $<10^{-10}$ mbar, as measured by a cold-cathode Penning gauge.

The analysis chamber is equipped with an Omicron μ-STM, a VSI ErLEED, a VG Microtech XR3E2 dual-anode X-ray source, a SPECS Phoibos 100 hemispherical analyzer, a SPECS IQE 12/38 scanning ion gun, a SPECS EQ 22/35 electron gun, a Perkin Elmer Model 3017 Auger electron spectroscopy setup and high-precision leak valves. The base pressure in the analysis chamber is $<6\times10^{-11}$ mbar as measured by a Bayard-Alpert gauge, the chamber is pumped by an ion pump and is additionally equipped with a titanium sublimation pump. The tungsten tips used for STM measurements were electrochemically etched and then sputtered in the preparation chamber by 0.5 kV Ar^+ ions for 5 min. The STM images presented in this thesis were corrested for piezo creep and thermal drift as descirbed in reference [162].

3.8.2 The qPlus chamber

The nc-AFM and the low temperature STM data were measured in a commercial Omicron LT-STM setup equipped with a qPlus head and a custom preamplifier [163]. The setup consists of a preparation chamber (base pressure $<10^{-10}$ mbar) and an analysis chamber (base pressure $<10^{-11}$ mbar when the cryostat is cooled) connected by a gate valve and a servo motor actuated manipulator. The preparation chamber is equipped with a SPECS IQE 12/38 scanning ion source and the sample is heated resistively in the heating stage on the manipulator. The chamber further includes single pocket and triple pocket e-beam evaporators (FOCUS EFM 3 and EFM 3T), a residual gas analyzer and several high-precision leak valves, one of them with a directional doser. The chamber is pumped by a turbomolecular pump and an ion pump. Additionally it is equipped with a titanium sublimation pump.

The analysis chamber includes a qPlus STM/nc-AFM head inside a cryostat which can be cooled to LN_2 (78 K) or LHe (4.5 K) temperatures. The chamber is pumped by an ion pump and is equipped with a titanium sublimation pump. The tungsten tips used for nc-AFM meaurements were electrochemically etched and further treated by in-situ self-sputtering as described in reference [164] and scanning/bias pulsing on Cu(100) surface. Different tip treatments and functionalizations are described in relevant sections of this thesis.

3.8.3 The TPD chamber

The TPD and XPS results presented in this thesis were acquired in a chamber specifically designed for reactivity studies of oxide single crystal surfaces, schematic of the chamber is shown in Fig. 3.7. The setup was designed by Jiří Pavelec, and full details can be found in references [153, 165, 166]. The chamber (base pressure $<7\cdot 10^{-11}$ mbar, measured by a Bayard-Alpert gauge) is equipped with a liquid helium flow cryostat (Janis ST-400), which allows reaching temperatures below 50 K on the sample surface without the use of radiation shields. For TPD measurements, the gases are dosed by a home-built effusive molecular beam source. The beam is formed by expansion of 0.53 mbar of a given gas through two differentially pumped stages and precision-made orifices, resulting in a beam spot with diameter of $\approx$ 3.5 mm on the sample surface, which contains 99.9 % of the molecules dosed in the chamber (see Fig. 3.6 and ref. [153]). For each sample mount the beam dose is calibrated by adsorbing multilayers of D_2O and measuring the visible beam spot area. This allows precise calculation of the beam dose in terms of impinged molecules per unit area on the surface. For TPD measurements, the sample mount is then moved in front of the Hiden HAL 3F PIC quadruple mass spectrometer and is heated with a linear heating ramp controlled by a PID control loop. During the TPD measurement the sample is biased by -85 V to prevent electrons from the QMS from reaching the sample surface. The samples are mounted on a Ta sample plate using Ta clips, and a thin gold foil is put between the back of the sample and the sample plate to ensure a good thermal contact. Sample heating is provided by direct current, and temperatures are measured by a K-type thermocouple directly spot-welded to the sample plate.

The chamber is further equipped with a SPECS IQE 12/38 scanning ion source, a SPECS UVS 10/35 UV source, a SPECS XR50M X-ray source monochromated by a SPECS FOCUS 500 monochromator, a SPECS Phoibos 150 hemispherical analyzer, a SPECS ErLEED setup, a single pocket and a triple pocket e-beam evaporators (FOCUS EFM 3 and EFM 3T), quartz-crystal microbalance for monitoring the deposition rates and several high-precision leak valves, one of which is attached to a directional tube doser.

The sample is moved between positions needed for different techniques by a motorized and rotary manipulator (Thermionics RNN rotary platform), and a XYZ manipulator with a motorized vertical motion and manual XY positioning stage (Thermionics EMC). The QMS is mounted on the linear manipulator allowing movement close to the sample surface during TPD measurements.

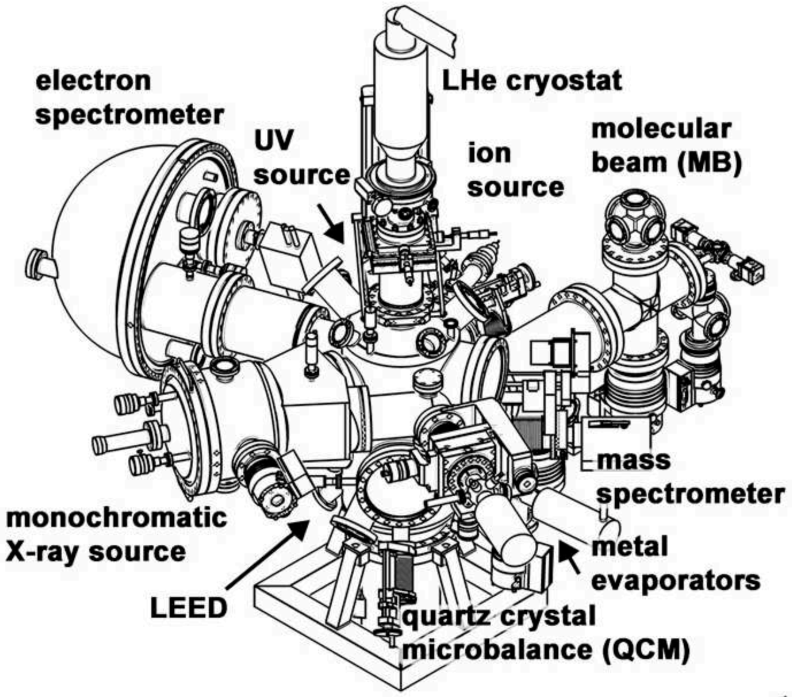

Figure 3.7: The schematic image of the TPD chamber. Figure reprinted from [153].

The chamber is primarily pumped by a turobomolecular pump with magnetic bearings, and four additional smaller turbomolecular pumps are used for differential pumping of various parts of the chamber (X-ray monochromator, first and second stage of the molecular beam, reservoir of the molecular beam, pumping of the ion gun and UV source, pumping of the rotational stage of the main manipulator).

3.8.4 The liquid-drop setup

The exposure of the surface to liquid water was conducted in a custom-designed side compartment designed by Jan Balajka and Jiří Pavelec. Details are described in references [11, 167, 168]. Briefly, the compartment features a sample stage, a cooled pointed rod (referred to as a “cold-finger”) above the sample stage, a container of liquid water separated by a valve and a zeolite cryo pump. For deposition of the liquid water drop on the sample *in vacuo*, water vapor is introduced in the compartment when the sample is not present (Fig. 3.8A), condenses on the cold-finger and forms an icicle (Fig. 3.8B). The valve to the liquid water container is closed and the water vapor is pumped by the cryo pump, effectively reinstalling UHV conditions. The sample is then moved from the load-lock of an UHV chamber to the sample stage in the compartment, and the valve to the load-lock is closed. Consequently, the cold-finger is heated, causing the icicle to melt (Fig.3.8C) and the liquid drop to fall on the sample surface (Fig. 3.8D). Then, the compartment is evacuated by the cryo pump again, and once in UHV, the sample can be transferred back to the main UHV chamber to be analyzed with surface science techniques.

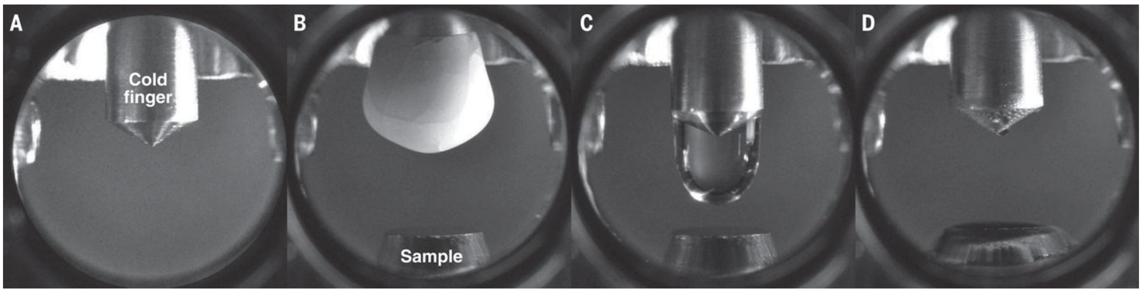

Figure 3.8: Dosing of liquid water in vacuum conditions by a custom-designed tool. A) Water vapor is introduced into the compartment when the sample is not present. B) Water condensates on the cold-finger and forms an icicle. The chamber is evacuated by a cryo pump. C) A sample is introduced under UHV conditions, the cold finger is heated causing the icicle to melt. D) The water drop falls onto the sample surface. The chamber is evacuated by cryo pump again, and the sample is transferred to the main chamber for analysis. Figure reprinted from [11].

This setup is currently installed on a UHV chamber equipped with an Omicron STM-1, an Omicron SPECTALEED, a VG XR3E2 X-ray source, a SPECS IQE 12/38 focused ion gun and a SPECS Phoibos 100 hemispherical analyzer. The base pressure of the chamber is $<10^{-10}$ mbar, as measured by a Bayard-Alpert gauge.

The liquid-drop results presented in this thesis were measured by this authors' colleagues Jan Balajka and Florian Kraushofer.

3.9 Sample preparation

The samples used in this thesis are natural single crystals of Fe_3O_4 and α-Fe_2O_3 cut and polished to expose the $Fe_3O_4(001)$, $Fe_3O_4(111)$, or the α-$Fe_2O_3(1\bar{1}02)$ facet. The polished crystals were purchased from SurfaceNet GmbH or Surface Preparation Lab. All the samples were mounted on Ta or Mo sample plates using Ta or Mo clips or wires; a thin foil of Au was put between the back of the sample and the sample plate to ensure a good thermal contact.

The surfaces were cleaned by sputtering (1 kV Ar^+ or Ne^+, 10 min) and annealing (930 K for the Fe_3O_4, 810 K for the Fe_2O_3) with every other annealing step done in background pressure of oxygen ($P_{O_2} = 5 \cdot 10^{-7}$ mbar) to avoid excessive reduction of the surface. This procedure was repeated until no foreign elements were observed in XPS spectra apart from Fe and O. In some cases, a small signal of Ta or Mo was observed, which we attribute to signal from the clips used for sample mounting. In new crystals, trace amounts of Mg, K, Na, Ca were commonly observed, but these disappeared with further cleaning cycles. The surfaces were also checked by

LEED and showed sharp spots with the desired symmetry (($\sqrt{2} \times \sqrt{2}$R45°) in the case of $Fe_3O_4(001)$ surface with subsurface cation vacancy reconstruction, (1×1) symmetry with no floretting pattern for the $Fe_3O_4(111)$ Fe_{tet} termination, and the (1×1) symmetry with no sign of the (2×1) spots in the case of a bulk-truncated α-$Fe_2O_3(1\bar{1}02)$). When possible, the quality of the surface was checked by STM or TPD with CO or H_2O as probe molecules. The details of specific surface preparations for different surface terminations are described and discussed in relevant sections of this thesis chapter.

4 Structure and reactivity of the α-Fe$_2$O$_3$(1$\bar{1}$02) surface

This chapter describes the α-Fe$_2$O$_3$(1$\bar{1}$02) surface as characterized by surface science methods in UHV, and deals with interaction of the stoichiometric (1×1) surface with water, both in UHV and after exposure to liquid water. The structure characterization and analysis of the pristine surfaces was summarized in a paper published jointly with this authors' colleagues (reference [108]), some data have also been shown in the Master theses of this author [169] and Florian Kraushofer [170]. The results concerning interaction of the stoichiometric α-Fe$_2$O$_3$(1$\bar{1}$02) with water were published in a paper (reference [160]), but this chapter provides additional data not shown previously. This chapter contains some data provided by this authors' colleagues, these contributions are clearly labeled in the text or in figure captions.

4.1 Introduction

One of the most exciting applications of hematite is in photoelectrochemical (PEC) cells for water splitting. The concept promises efficient harvesting of energy from sunlight and its direct conversion to chemical energy. In a photoanode of such a PEC cell the sunlight induces the generation of electron-hole pairs. The electrons are then transferred to the cathode, where they reduce water to H_2 and OH^-, while the holes are used for OH^- oxidation to O_2 at the anode (oxygen evolution reaction, OER). That way, spatially separated H_2 and O_2 gas is generated.

Hematite meets some of the important requirements for the PEC cell photoanodes: a small semiconductor bandgap (≈ 2 eV), durability in aqueous environments, environmental benignity and low cost. Theoretical solar-to-hydrogen efficiency of hematite photoanode lies around 15 %, but the real achievable values are much lower. The most notable reasons causing this discrepancy include very low hole diffusion length (2–4 nm) compared to relatively high light penetration depth ($\sim 10^2$ nm), short excited state lifetime ($\approx$ 1 ps) and poor electrical conductivity ($\sim$-10^{-2} cm^{2}V^{-1}s^{-1}). Perhaps the biggest issue is however the sluggish oxygen evolution reaction at the electrode/solution interface [54, 102, 171].

The systematic search for materials improving the OER kinetics is currently guided by computational screening. The OER is generally thought to proceed via a four-step pathway with *O, *OH, and *OOH as adsorbed intermediates (* indicates an adsorbed species) [172]. It was discovered relatively early on that the binding energies of isolated *OH and *OOH species always scale linearly and thus a single descriptor, such as the *OH binding energy or the orbital occupancy of the metal cation, can be used the predict the OER activity of a given material [172–174]. This approach has yielded significant success, but one its weak points is the initial assumption that on all materials the OER proceeds by the very same pathway. This neglects any water-water interactions on the surface, which can lead to formation of species different than just isolated, non-interacting *O, *OH, and *OOH. A hypothetical *OH group bound in a hydrogen-bonded network or water agglomerate will have a different binding energy from an isolated *OH species, and if this takes part in the OER reaction, then the isolated *OH is not a suitable descriptor.

In-situ identification of water structures formed on surfaces is an extremely challenging task, however, as it requires a detailed knowledge of the surface structure and a suitable technique to measure positions and interactions of the individual water molecules. The solid-liquid interface can be probed by various surface diffraction techniques, but none of those is sensitive to the positions of hydrogen atoms which are crucial to elucidating the water-water interacting structures. The task is typically also approached by molecular dynamics simulations, but these also often neglect the water-water interactions or work with non-dissociable water models.

In this chapter it will be shown that the water-water interactions do occur and play an important role on stoichiometric α-Fe$_2$O$_3$(1$\bar{1}$02), as the dominant species forming on the surface are highly stable partially-dissociated HO-H$_2$O dimers. The first part of this chapter provides a detailed characterization of the surface in UHV, the second part deals with identification of the HO-H$_2$O dimers formed after H$_2$O dosing in UHV and goes on to show that the same species are present even after the surface has been exposed to liquid water. Lastly, an unusual phenomenon of oxygen exchange between the surface and the adsorbed water will be described and discussed, and it will be shown that this only occurs upon desorption of the HO-H$_2$O dimers, but not during the actual exposure to liquid water. All of this shows that phenomena taking place on a solid-liquid interface can be much more complex than generally assumed, and that detailed case-by-case studies are the only way to identify those.

4.2 Atomic-scale structure of α-Fe$_2$O$_3$(1$\bar{1}$02)

Following the procedure described in previous works [118, 120], we treated a natural α-Fe$_2$O$_3$(1$\bar{1}$02) single crystal by sputtering (1 kV Ar$^+$, 10 min) and annealing (810 K, 10-20 min), with some annealing steps performed in partial pressure of O_2 to avoid excessive reduction of the surface. This was repeated until all contaminants detectable in normal emission XPS spectra were removed from the surface. Relatively sharp LEED patters were observed already after a few cleaning cycles. Initially, the LEED patterns exhibited strong charging effects with the incident electron energy above ≈ 90 eV, but with more cleaning cycles this threshold energy decreased to ≈ 20 eV. This increase of conductivity is most likely due to the bulk reduction of the crystal, as the oxygen atoms are sputtered preferentially during the cleaning cycles [175]. Interstitial Fe atoms are considered to be common defects donating charge to the hematite lattice, which leads to increased electrical conduction by small-polaron hopping [176].

4.2.1 Characterization of the (1 × 1) and (2 × 1) surfaces by XPS and LEED

Typical LEED patterns are shown in Fig. 4.1. The (2 × 1) surface was prepared by conducting the last annealing step in UHV, the (1 × 1) surface was prepared when the last annealing step was done in 10^{-6} mbar O_2 at a slightly lower temperature of 720 K. Contrary to previous observations [120], no difference was observed between preparing the (1 × 1) surface by oxidation of a freshly sputtered surface or the ordered (2 × 1) surface.

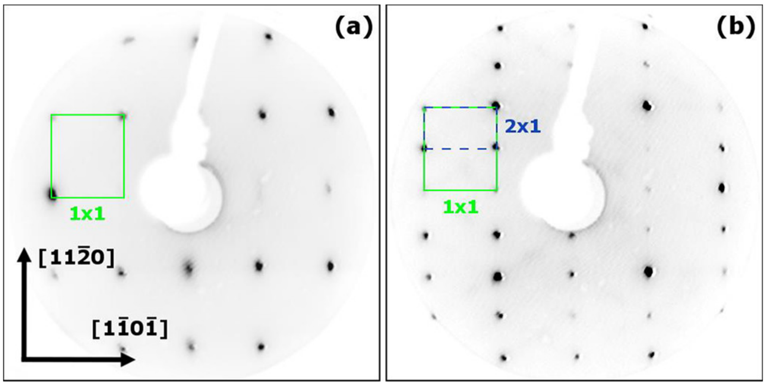

Figure 4.1: LEED patterns obtained from the clean (1 × 1) (a) and (2 × 1) (b) surfaces of α-$Fe_2O_3(1\bar{1}02)$ with an electron beam energy of 50 eV. Figure reprinted from [108].

Figure 4.2 shows the Fe $2p$ and O $1s$ regions of the XPS spectra acquired on the (1 × 1) and (2 × 1) surfaces in normal emission (a,b) and in 75° grazing emission geometry (c,d). The spectra were taken while the samples were heated to 423 K to prevent any water adsorption from the residual gas, as water is known to interact with both of these surface below this temperature [120, 121]. All the spectra were calibrated to the Fermi edge of the Ta sample plate. The positions and shapes of the Fe $2p$ and O $1s$ peaks of the (2×1) terminated surface are consistent across all the data and in agreement with previous measurements of α-Fe_2O_3 [51, 152]. On the (1×1) surface the whole XPS spectrum is shifted to lower binding energies by a varying degree in the range of $V_{BB} = 0.2$–0.5 eV, depending on sample history and preparation. This is most likely not due to sample charging effects, as both the surfaces were suitable for STM measurements, which indicates sufficient conductivity. Therefore we attribute this to upward band bending, which occurs because the Fermi level is closer to the conduction band minimum in the reduced, heavily n-type bulk than it is in the more stoichiometric (1×1) surface region.

The Fe $2p_{3/2}$ peak has a characteristic shape consisting of several features between 709 and 715 eV due to multiplet splitting [152]. The spectra of both the (1×1) and (2×1) surfaces are consistent with Fe^{3+}-containing compounds, as there is a pronounced shakeup sattelite peak located around 719 eV (highlighted by a blue arrow in Fig.4.2). The Fe $2p_{3/2}$ region measured on the (2×1) surface additionally exhibits a shoulder at ≈ 708.5 eV (highlighted by a red arrow, and illustratd in the insets in Fig.4.2a,c), indicating presence of Fe^{2+} cations. This shoulder is more pronounced in the spectra acquired in grazing emission geometry, which suggests the Fe^{2+} is located at or near the surface. In general, the XPS data from the (2×1) surface resemble those obtained from magnetite (Fe_3O_4), which contains both Fe^{2+} and Fe^{3+}.

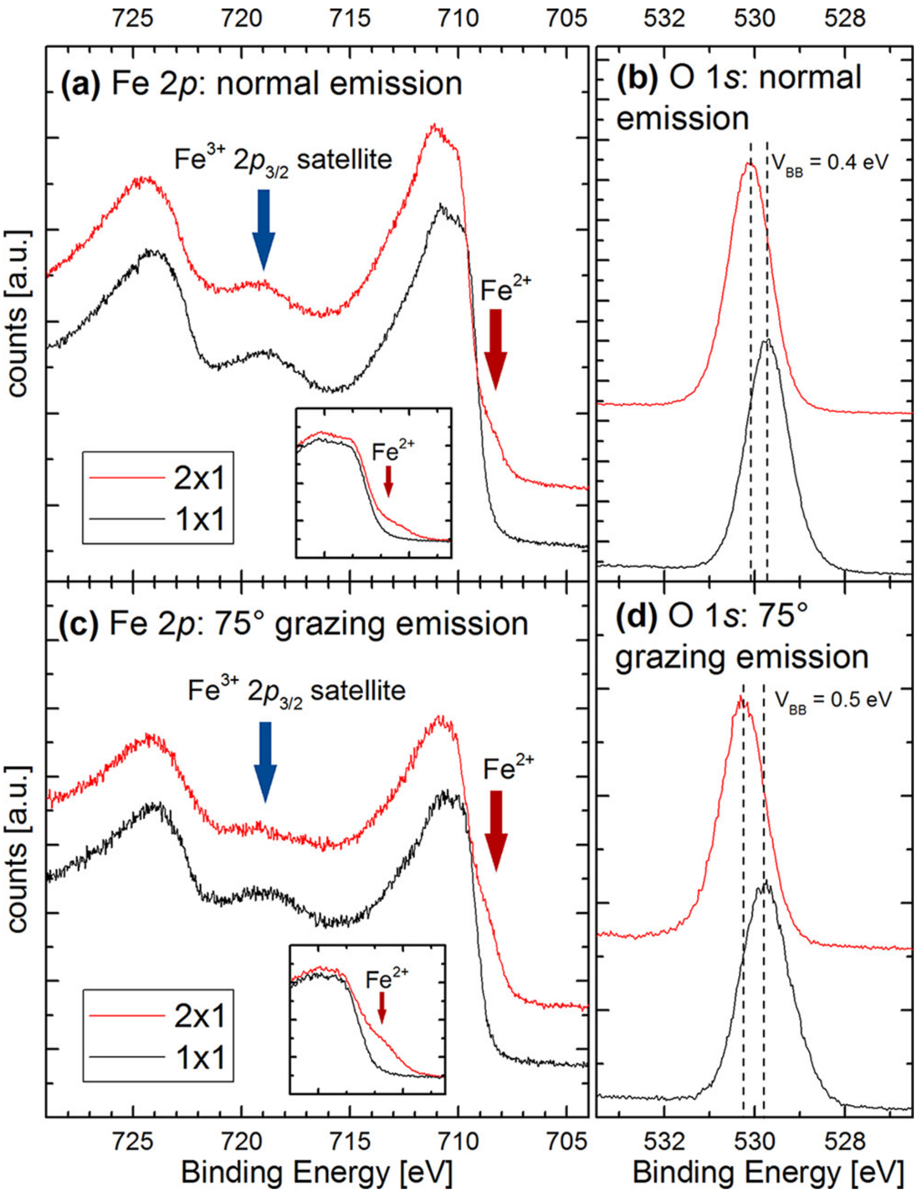

Figure 4.2: XPS spectra (monochromatized Al K) measured at 423 K of the Fe 2*p* (a,c) and the O 1*s* (b,d) peaks for the (1×1) and (2×1) terminated α-Fe$_2$O$_3$(1$\bar{1}$02) surface acquired at normal (a,b) and 75° grazing emission (c,d). The insets show direct comparisons of the low-binding-energy shoulder on the Fe $2p_{3/2}$ peak, aligned to remove the shift determined in (b) and (d) for clarity. The reduction in intensity of the Fe^{3+} shakeup satellite peak (blue arrows) coupled to the emergence of a low-binding-energy shoulder on the Fe $2p_{3/2}$ (red arrows) shows that Fe^{2+} cations are present on the (2×1) surface but not on the (1×1) surface. Data taken and analyzed by Florian Kraushofer, figure reprinted from [108].

4.2.2 SPM imaging of the (1×1) surface

STM images of the α-Fe$_2$O$_3$(1$\bar{1}$02)-(1×1) surface are shown in Fig.4.3. The images were acquired on the same sample area with (a) negative and (b) positive sample bias and thus represent filled and empty states, respectively. Both images are characterized by zigzag lines of bright protrusions running in the $[1\bar{1}0\bar{1}]$ direction, which are displaced by ≈ 5.0 Å in the $[11\bar{2}0]$ direction. This appearance is consistent with the bulk-truncated structure shown in Fig.4.3c, with one sublattice selectively imaged bright. Using point defects as markers (green and blue circles), we infer that the species imaged as bright zigzag lines differs between the filled and empty state images. STM simulations (inset), based on our theoretical calculations (carried out by M. Bichler, for details see [108]), suggest that the oxygen sublattice is imaged in filled states, whereas the empty state images reveal the surface iron sublattice. The nature of the defects is presently unknown, but it is likely that some are adsorbates from the residual gas.

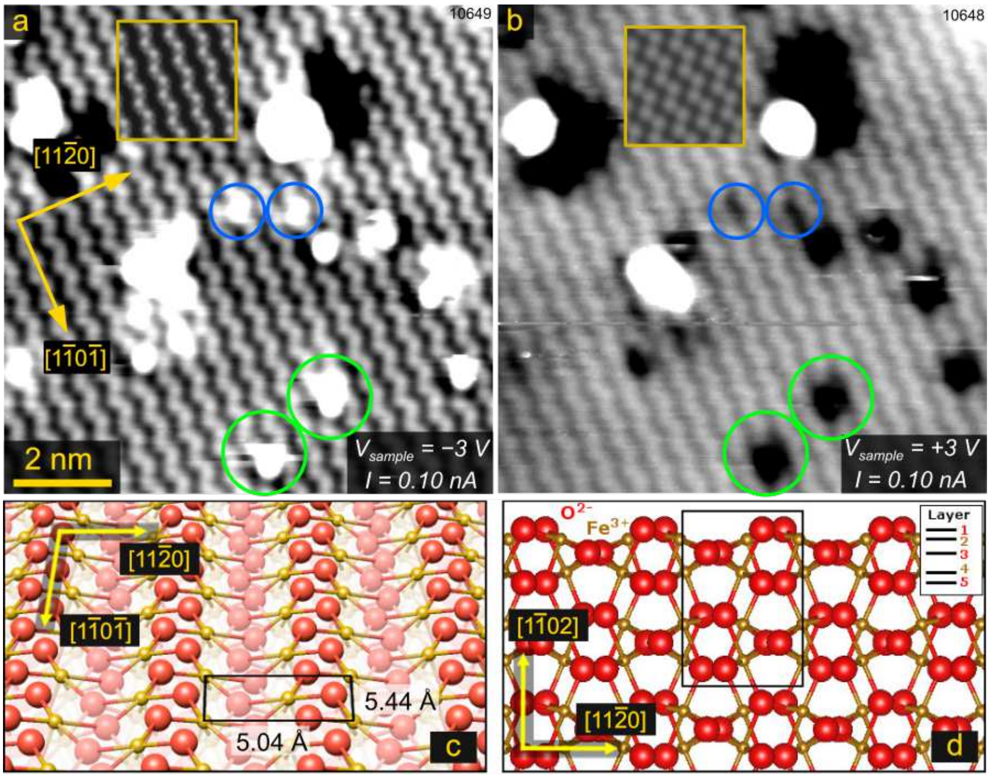

Figure 4.3: STM images of the α-$Fe_2O_3(1\bar{1}02)$-(1 × 1) surface imaging: (a) filled states ($V_{sample} = -3$ V) and (b) empty states ($V_{sample} = +3$ V). Both images were acquired on the same sample area and exhibit zigzag rows of bright protrusions running in the $[1\bar{1}0\bar{1}]$ direction. The relative positions of the defects marked in the green and blue circles suggest that a different sublattice is imaged for each bias polarity. The square insets in (a,b) show STM simulations based on the DFT+U calculations (carried out by M. Bichler, details in [108]), which perfectly agree with the measured data. Panels (c,d) shows the DFT+U optimized model of the bulk-truncated α-$Fe_2O_3(1\bar{1}02)$ surface.

Figure 4.4 shows α-$Fe_2O_3(1\bar{1}02)$-(1 × 1) surface imaged by ncAFM at 5 K. The images recorded at large tip–sample distance (panel (a)) resemble the contrast obtained in STM images, with zigzag rows of bright and dark features along the $[1\bar{1}0\bar{1}]$ direction. In this regime, the AFM contrast is dominated by electrostatic forces, and thus the images are sensitive to the distribution of charge at the surface. With a smaller tip–sample separation (Figure 4.4b,c), the image contrast becomes dominated by short-range interactions. This short-range tip–surface interaction on oxide surfaces is a mixture of ionic and covalent interactions and may be further influenced by effects such as Pauli repulsion or tip bending. On the (1×1) termination we observe only a weak interaction with the surface, as evidenced by small variations of the measured frequency shift (a few Hz). The observed zigzag rows in (b,c) are formed both by bright protrusions (corresponding to weaker attractive force or stronger localized repulsive force) and dark depressions (corresponding to stronger attractive force). The difference between images in panels (b) and (c) is that the one shown in (c) was acquired with higher oscillation amplitude (150 pm vs. 60 pm), and at a height closer the surface. Generally, in ncAFM imaging the contrast depends on tip termination and therefore it is not possible to a priori say which of the observed features correspond to surface cations and which to anions. Nevertheless, in this case, both possibilities fit to the bulk-truncated α-$Fe_2O_3(1\bar{1}02)$.

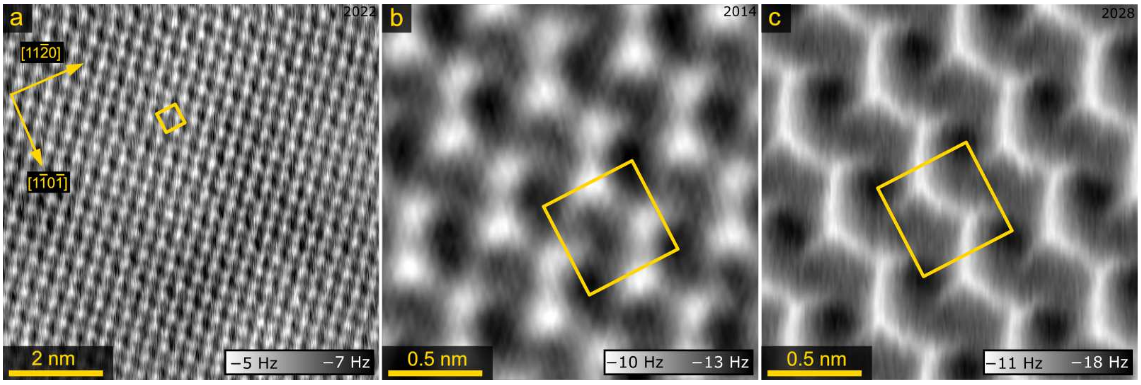

Figure 4.4: Constant-height ncAFM images of the α-$Fe_2O_3(1\bar{1}02)$-(1×1) acquired at 5 K showing zigzag rows running in the $[1\bar{1}0\bar{1}]$ direction. (a) $8{\times}8\,\mathrm{nm}^2$ image acquired with an oscillation amplitude of 150 pm and sample bias 0.05 V. (b,c) In the detailed data acquired at lower tip-sample distances, the zigzag rows are formed by both bright and dark features. The image in panel (b) was acquired a lower oscillation amplitude (60 pm). The image in panel (c) was acquired ≈ 20 pm closer to the surface relative to (b), the oscillation amplitude was 150 pm.

In panel (c) the bright features are resolved as sharp bright lines, which is typical for repulsive interaction at small tip-sample distances. Typically, these effect result from tip-bending. Without the knowledge of the tip termination, one can speculate that these bright features could correspond to the species which are physically higher on the surface, in this case the O^{2-} atoms. Following this assumption, the dark features would correspond to Fe^{3+} atoms. One notable phenomenon observed in the images shown in panels (b,c) is every second dark feature along the $[1\bar{1}0\bar{1}]$

direction is interacting significantly more strongly with the tip than its immediate neighbors. This pattern would in principle perfectly correspond to the antiferromagnetic ordering of Fe atoms in the hematite lattice, but it is not clear how this could be observed in images acquired with a nonmagnetic tip (tungsten tip treated by bias pulsing on Cu(110)). Moreover, antiferromagnetic contrasts measured by ncAFM typically have much lower corrugation and can only be observed after heavy signal processing [177]. For these reasons it is likely that there is another reason for this contrast modulation on the dark species, one which is currently unknown. No ncAFM contrast other than shown in Fig. 4.4 was observed on α-Fe_2O_3(1$\bar{1}$02)-(1 × 1).

4.2.3 SPM imaging of the (2 × 1) surface

Figure 4.5 shows STM images of the α-Fe_2O_3(1$\bar{1}$02)-(2 × 1) surface acquired with positive and negative sample bias on the same sample area. Both imaging conditions show paired zigzag rows of bright protrusions running in the [1$\bar{1}$0$\bar{1}$] direction. The paired rows have a repeat distance in the [11$\bar{2}$0] direction of 10.1 Å separated by a dark depression, consistent with the (2 × 1) periodicity observed in LEED. High-resolution images (panels (c,d)) of the surface show that the (2 × 1) unit cell contains a protrusion close to the center. A comparison of the point defects in the filled and empty state images (green circles panels (a,b)) suggests that the same surface species are imaged in each case. Over the course of many experiments, it was observed that the appearance of the (2 × 1) surface varies somewhat with the tip condition. Although a similar lattice of protrusions is always observed, the apparent depth of the dark depression between the rows varies, and in some conditions it is not resolved.

Noncontact AFM images of the α-Fe_2O_3(1$\bar{1}$02)-(2 × 1) surface aqcuired at 5 K are shown in Fig. 4.6. When measured at larger tip-sample distance (panel (a)), the images exhibits a clear (2 × 1) periodicity with bright, elongated features that rotate by 90° between neighboring rows. These features are too large to correspond to individual atoms. When scanning close to the surface with the standard tip prepared by pulsing on Cu(110) (panel(b)), we observe well-resolved features attractively interacting with the tip (dark species) which form a zig-zag pattern along the [1$\bar{1}$0$\bar{1}$] direction, and no species are resolved in the bright areas of the image. The (2 × 1) periodicity is not visible at the first glance, but upon closer inspection one can see that every second zig-zag line is slightly shifted in the [1$\bar{1}$0$\bar{1}$] direction, forming the (2 × 1) pattern. This is highlighted by the cyan rectangle in Fig. 4.6b,c. Panel (c) shows an image acquired with a differently prepared tip (scanned on $KTaO_3$ surface prior to approaching on hematite), which provides an inverted contrast compared to image shown in (b). Here, the same pattern previously observed in attractive interaction forces is measured in repulsive forces (bright species). The positions of the

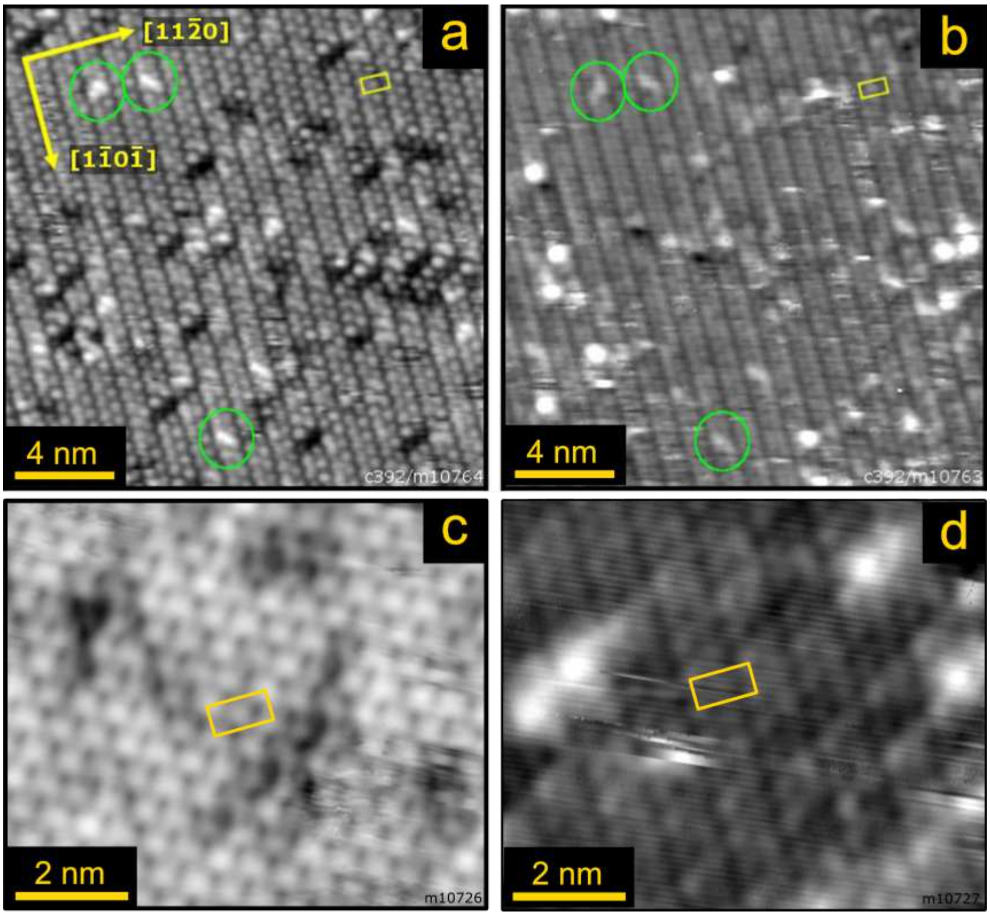

Figure 4.5: STM images of the α-$Fe_2O_3(1\bar{1}02)$-(2 × 1) surface imaging: (a) filled states ($V_{sample} = -2.5\,\mathrm{V}$) and (b) empty states ($V_{sample} = +2.5\,\mathrm{V}$). Both images were acquired on the same sample area and exhibit zigzag rows of bright protrusions running in the $[1\bar{1}0\bar{1}]$ direction. The relative positions of the defects marked in the green circles suggest that the same species are imaged in both images. (c,d) Slighly varying images can be acquired with different tip conditions. A higher resolution filled state image ($V_{sample} = -1.0\,\mathrm{V}$) is shown in panel (c), an empty state image ($V_{sample} = +2.0\,\mathrm{V}$, acquired on a different area) is shown in panel (d). Figure adapted from [108].

species is well reproduced in this image, including the slight phase shift of the neighboring zig-zag rows. A similar effect of contrast reversal was previously observed in the pioneering ncAFM works on TiO_2, and was attributed to tips terminated by atoms of opposite polarity [149].

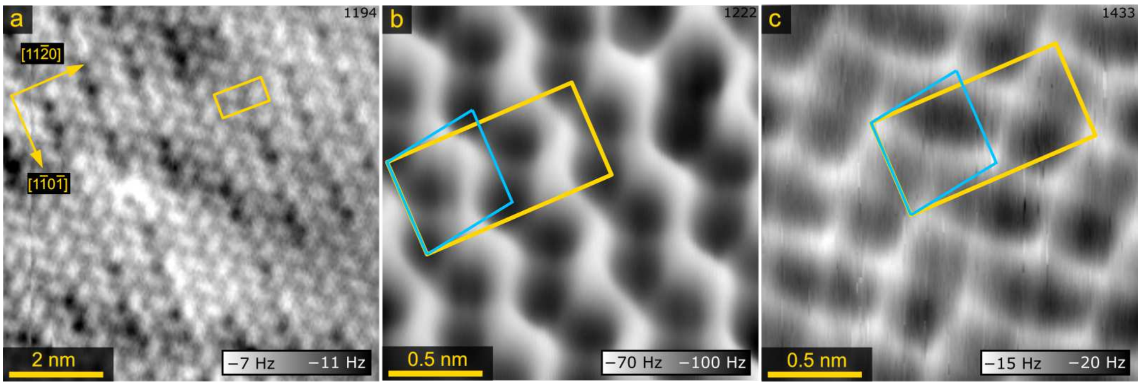

Figure 4.6: Constant-height noncontact AFM data acquired on (a) the α-$Fe_2O_3(1\bar{1}02)$-(2×1) surface (8×8 nm^2, 5 K, oscillation amplitude 500 pm). Panel (b) shows a detailed image of the same surface acquired at a smaller tip-sample distance and (2×2 nm^2, 5 K, oscillation amplitude 55 pm). Panel (c) shows an image measured with a different tip providing inverted contrast (2×2 nm^2, 78 K, 250 pm). The (2×1) unit cells are indicated by yellow boxes. A periodic lateral displacement of neighboring rows along the $[1\bar{1}0\bar{1}]$ direction is observed in (b), (c), as indicated by the cyan box.

4.2.4 Proposed models for the (1×1) and (2×1) surfaces

All the data acquired on the α-$Fe_2O_3(1\bar{1}02)$-(1×1) are consistent with the previously proposed bulk-truncated model (see Fig. 4.3 and 4.7). STM images reveal that two different sublattices are imaged in filled and empty states, and the STM simulations based on the bulk truncated model identify the species visible in filled states as O atoms, and the species visible in emtpy states as Fe atoms. Noncontact AFM images identify two distinct species on the surface, both of which form zig-zag rows in the $[1\bar{1}0\bar{1}]$ direction, consistent with the model. The XPS data show that the surface contains mostly Fe^{3+} cations and very little, if any, Fe^{2+}. Based on all these results we can safely say that our surface is bulk-truncated, and we do not see any signs of the first Fe-layer being partially depleted, as reported previously on surfaces prepared by chemical-mechanical polishing (referred to as the half-layer termination) [123, 126, 131].

For the α-$Fe_2O_3(1\bar{1}02)$-(2×1), none of the previously proposed models fit to the presented STM and ncAFM images. In our published paper we proposed a new model, named the "alternating trench" structure, which was based on an ordered array of surface oxygen vacancies. This provided very good agreement with the SPM and XPS data (see Fig. 4.7) and was the most energetically favorable out of all tested structures in DFT+U computations (for details, see [108]). Nevertheless, this model could not explain the adsorption behavior of simple molecules such as H_2O and O_2, and later surface X-ray diffraction (SXRD) and LEED-IV experiments conclusively disproved this model (not shown). The search for an alternative model is currently in progress.

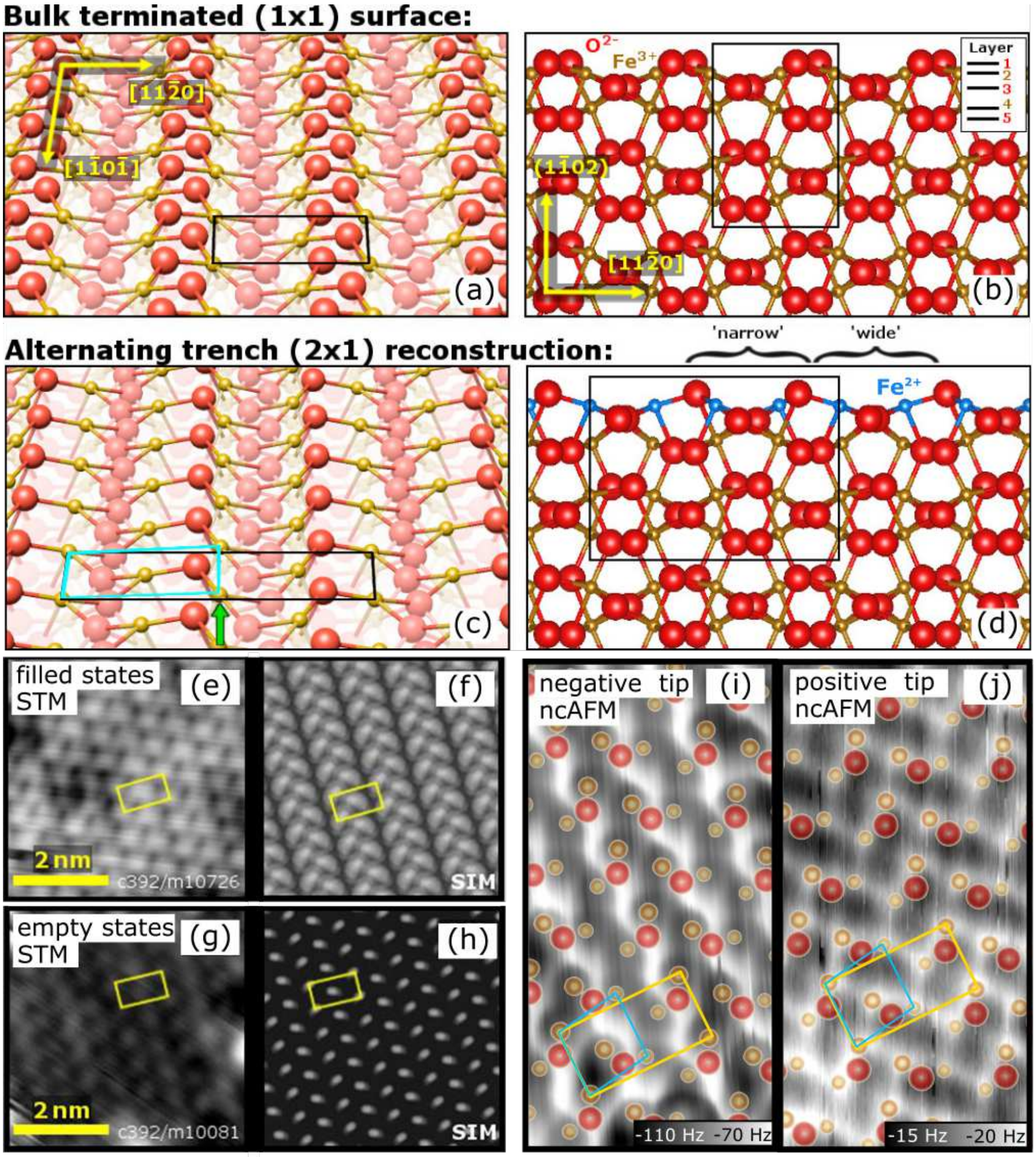

Figure 4.7: Proposed models for the (1 × 1) and (2 × 1) reconstructions of the α-Fe$_2$O$_3$(1$\bar{1}$02). (a,b) The previously proposed bulk-truncated model for the (1 × 1) surface is consistent with all the data acquired throughout this thesis. (b,c) The proposed “alternating trench” reconstruction is formed by an ordered array of oxygen vacancies on the surface. The model is consistent with all the data presented in this thesis, but has since been convincingly disproved by surface diffraction studies (not shown). (e,f,g,h) Comparison of the STM data imaging filled and empty states with the STM simulations based on the alternating trench model. (i,j) the ncAFM data acquired with different tips correspond very well to the cation lattice of the alternating trench model. Figure adapted from [108].

4.3 Water adsorption on α-$Fe_2O_3(1\bar{1}02)$-(1 × 1)

We studied the water adsorption on the bulk-truncated α-$Fe_2O_3(1\bar{1}02)$-(1 × 1) by surface science techniques in ultrahigh vacuum, and compared these results to the data acquired after exposure of the surface to liquid water. This section is divided into two parts: The first part provides evidence of the existence of HO-H_2O dimers on the hematite surface after exposure to liquid water, the second part focuses on the unusual observation of a rapid oxygen exchange phenomenon happening upon desorption of the adsorbed water.

4.3.1 Partially-dissociated water dimers at the water-hematite interface

Figure 4.8A shows TPD data acquired following exposure of the as-prepared surface to a calibrated molecular beam of D_2O at 100 K. The TPD data, acquired using a 1 K/s temperature ramp, resemble those previously shown by Henderson [120] with a major desorption peak at 345 K. This peak (highlighted by yellow color) saturates at a coverage of $1.27 \pm 0.07\,D_2O$ molecules per unit cell (uc), where $1\,D_2O/\mathrm{uc}$ corresponds to a coverage of $3.65 \times 10^{14}\,D_2O/\mathrm{cm}^2$. For higher initial coverages, a shoulder appears at the low-temperature side and develops into a second peak at $\approx 250\,\mathrm{K}$. At lower temperatures, water desorption continues up to a coverage of $1.90 \pm 0.10\,D_2O/\mathrm{uc}$ (highlighted by blue color), after which a peak corresponding to multilayer ice appears. Saturation of the first monolayer at a coverage of $\approx 2\,D_2O/\mathrm{uc}$ can be expected because the (1 × 1) unit cell contains two undercoordinated Fe^{3+} cations to which water molecules can bind.

The shape of the 345 K peak suggests a first-order desorption kinetics, as the desorption rate maximum stays constant with varying initial coverage (highlighted by the dashed vertical line in Fig. 4.8A). The peak shape was also analyzed by the Arrhenius $\ln r/\nu\Theta^n$ versus $1/T$ plot for two different initial coverages, shown in Fig. 4.8B,C. In both cases, the first-order desorption fits the data significantly better than zeroth- or second-order. At low $1/T$ values the plots deviate from the straight lines corresponding to ideal first-order desorption, which is most likely due to the high-temperature tail observed in the TPD spectra. Presumably, this tail is due to water adsorption on surface defects or step edges. Similar analysis for the low-temperature peak saturating at 250 K was not conclusive due to the irregular peak shape.

An inversion analysis of the 345 K peak, assuming first-order desorption kinetics, yields a best fit for an adsorption energy of $\approx 1.10\,\mathrm{eV}$, with a pre-exponential factor of $2{\cdot}10^{(15\pm1)}\,\mathrm{s}^{-1}$, see Fig. 4.9. Panel A shows the caluclated adsorption energies for three selected pre-factors between 10^{14} and $10^{16}\,\mathrm{s}^{-1}$. Panel B shows the data simu-

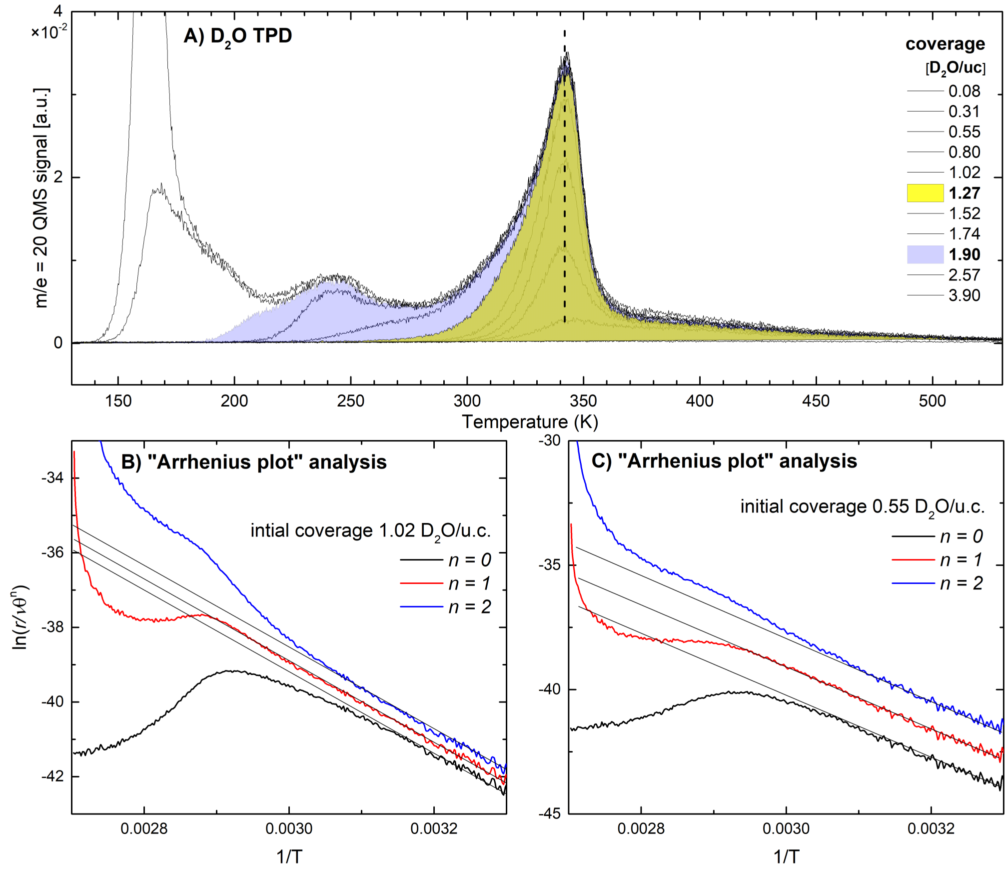

Figure 4.8: Characterization of water adsorbed on the bulk-truncated α-Fe$_2$O$_3$(1$\bar{1}$02) by temperature programmed desorption. (A) TPD spectra show two prominent peaks with desorption maxima at ≈ 345 K (highlighted by yellow) and ≈ 250 K (highlighted by blue). The ≈ 345 K peak maximum stays constant with varying initial coverage (highlighted by the dashed vertical line), suggesting first-order desorption kinetics. This was also checked by Arrhenius plot analysis for two different initial coverages, shown in panels B,C. In both cases, the straight line corresponding to first-order desorption fits the best to the plotted data. A similar analysis was inconclusive for the ≈ 250 K peak due to its irregular shape.

lated with pre-factor $2{\cdot}10^{15}\,\mathrm{s}^{-1}$ (green dotted line) superimposed on the measured data (blue solid line). Panel C shows the plot of the squared error between the simulated and measured data for a range of pre-factors between 10^{13} and $10^{19}\,\mathrm{s}^{-1}$, featuring a clear minimum at $\approx 2\cdot10^{15}\,\mathrm{s}^{-1}$. Finally, panel D shows curves simulated with pre-factors slightly lower and higher than the best-fit value determined in panel C. A similar analysis of the higher-coverage ≈ 250 K peak was unsuccessful due do the irregular peak shape.

XPS data (Figure 4.10) were acquired for various D$_2$O exposures up to 3.90 D$_2$O/uc, shown in panel A. The measurements were performed with grazing emission at 75°, at a sample temperature of 121 K. Already at low coverages, two extra peaks can be observed on the high binding energy side of the O 1s peak, which appear to grow

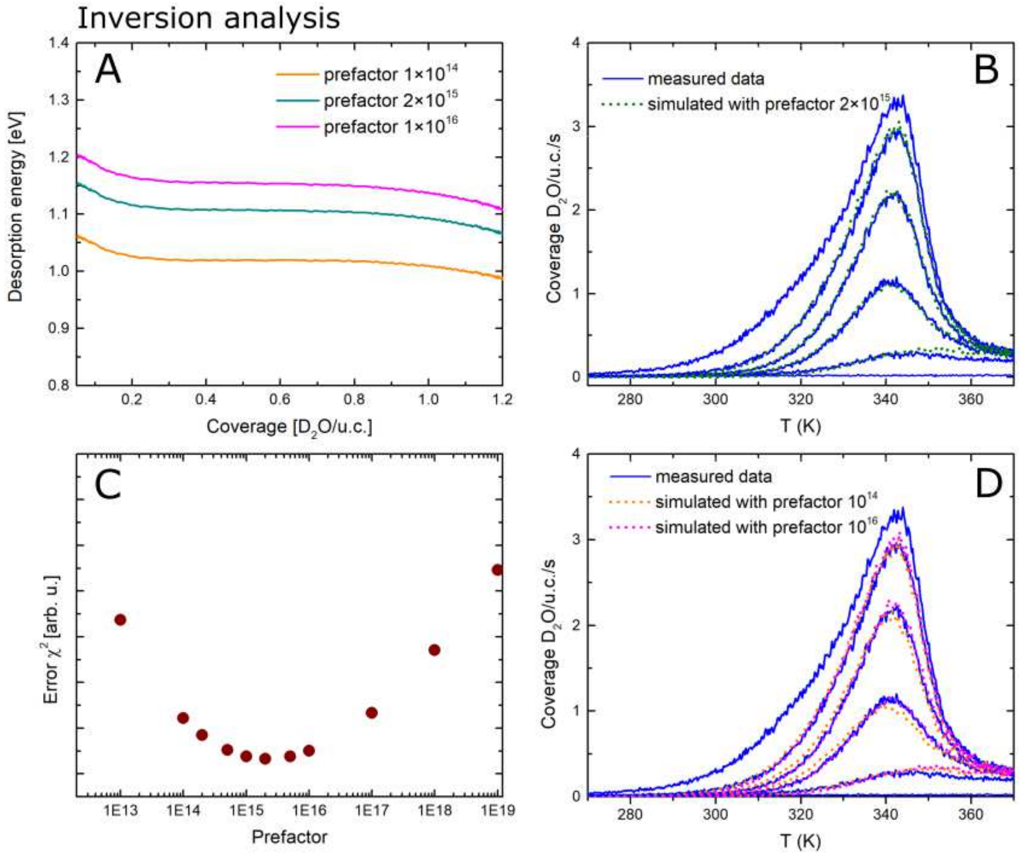

Figure 4.9: Inversion analysis of the D_2O TPD data acquired on stoichiometric α-$Fe_2O_3(1\bar{1}02)$. (A) Adsorption energy vs. coverage plot. (B) Measured desorption curves (blue) vs. curves simulated with desorption pre-factor of $2{\cdot}10^{15}\,s^{-1}$ (green dotted line). (C) Plot of squared error between the measured data and data simulated with various pre-factors. (D) Comparison of the measured desorption curves (blue) and curves simulated with pre-factors slightly lower (orange) and slightly higher (purple) than the best-fit value.

simultaneously with D_2O coverage. Two spectra corresponding to the saturation of the ≈ 345 K peak (panel B) and close to the saturation of the ≈ 250 K peak (panel C) were fitted and evaluated. The fitting was done by using a Shirley background and three pseudo-Voigt peaks, which in addition to the 530.4 eV component due to lattice O^{2-} anions identified peaks at 531.8eV and 533.4 eV; typical positions of OD and D_2O on metal oxide surfaces [159, 178, 179]. Integrating the peak areas, we find that the D_2O/OD ratio is 0.40 for both water coverages. Noting that dissociation results in two hydroxy groups (one so-called terminal $O_{water}D$ adsorbed at a cation site and an $O_{lattice}D$ group at an undercoordinated surface oxygen), this ratio suggests that approximately 45% of the water is molecularly adsorbed. Dissociation by the X-ray beam is ruled out because the same OD/D_2O ratio was obtained in the first and last O 1*s* scan. Above 1.74 D_2O/uc coverage, the OD component saturates and only the molecular D_2O component grows.

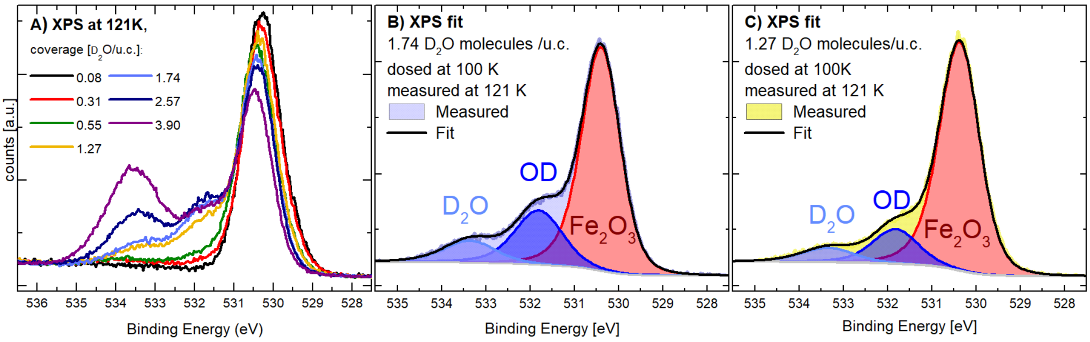

Figure 4.10: XPS characterization of the D_2O adsorbed on stoichiometric α-$Fe_2O_3(1\bar{1}02)$. (A) The O 1*s* region after varying dose of D_2O. In addition to the main peak corresponding to the lattice oxygen, two peaks at higher binding energy are observed. (B,C) Fitted spectra acquired on the surface with (B) 1.74 D_2O/uc (close to saturation of the ≈ 250 K TPD peak) and (C) 1.27 D_2O/uc (saturation of the ≈ 345 K TPD peak). The ratios of the 531.8eV and 533.4 eV suggest that in both (B) and (C) approximately 45% of the water is molecularly adsorbed. In all cases, D_2O was adsorbed at 100 K, the measurements (monochromatized Al Kα, 75° grazing emission) took place at 121 K.

Noncontact AFM was carried out to determine the structures of the two phases (desorption peaks) observed in TPD experiments. Figure 4.11A shows a contant-height ncAFM image acquired with a CO-terminated tip at 78 K following an exposure to 6 L (Langmuir, $1.33 \cdot 10^6$ mbar·s) of H_2O at 240 K. The functionalized tip was prepared on $Pt/Fe_3O_4(001)$, details of this approach are described in section 5.2.2 of this thesis. Judging from the TPD data, the sample preparation conditions correspond to a maximum coverage of 1.52 H_2O/uc, but there is likely a discrepancy in the temperature measurement in different setups. The resulting image exhibits zigzag rows of protrusions of similar frequency shift running in the $[1\bar{1}0\bar{1}]$ direction and has a (1 × 1) periodicity, consistent with one water molecule per surface cation. From the images alone, it is difficult to tell whether the protrusions show H_2O, OH, or both; therefore, this data is complemented by theoretical caluclations utilizing the WIEN2k code and the PBE+U approach (calculations carried out by M. Bichler) and simulations of the CO-tip ncAFM contrast using the Probe Particle Model [150, 158] (carried out by I. Sokolović). Further details of the computations and simulations are given in reference [160].

The lowest-energy (1 × 1) configuration (Figure 4.11C, $E_{ad} = 1.02\,\mathrm{eV}/H_2O$) based on partially dissociated water dimers is clearly favored over intact (0.84 eV/H_2O) or fully dissociated (0.92 eV/H_2O) water monomers. A water molecule and a terminal OH adsorb atop surface Fe cations (brown), completing their octahedral coordination environment. A hydrogen bond of 1.56 Å forms between the water and the terminal OH species on neighboring cations along the row. The H liberated by the dissociation forms an $O_{lattice}H$ with an undercoordinated surface O atom and forms a hydrogen bond (1.68 Å) back to the O of the dissociated water molecule. In Figure 2B, we show a simulation of the AFM contrast using the flexible CO tip model as implemented in the Probe Particle Model.

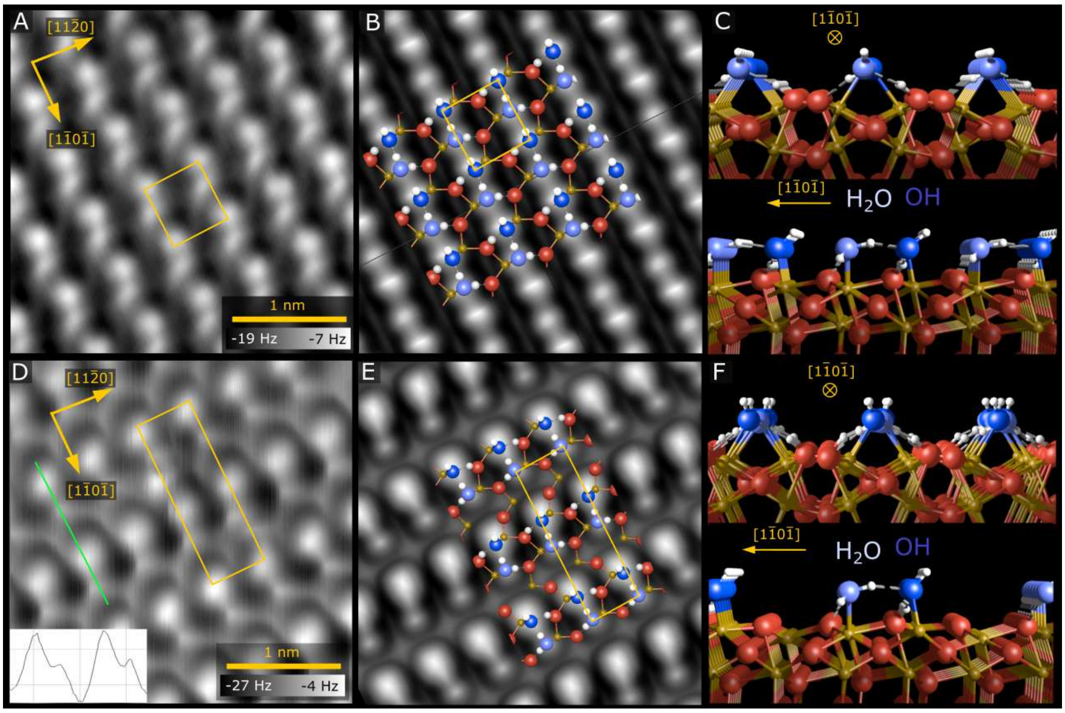

Figure 4.11: Noncontact atomic force microscopy and PBE+U results for H_2O on α-$Fe_2O_3(1\bar{1}02)$-(1 × 1). (A) Experimental ncAFM image of the (1 × 1) phase of adsorbed H_2O acquired at 78 K using a CO tip. (B) Simulated ncAFM image showing the force experienced by a flexible CO tip 7.13 Å above the (1 × 1) phase of adsorbed partially dissociated water dimers. The simulation is based on the minimum-energy PBE+U structure, which is shown as an overlay, and in DFT-derived models viewed along the [$1\bar{1}0\bar{1}$] and [$11\bar{2}0$] directions in panel (C). (D) Experimental nc-AFM image of the (1 × 3) phase of adsorbed H2O acquired at 4 K using a CO tip. The green line profile shows the four maxima corresponding to two dimer species. (E) Simulated ncAFM image showing the force experienced by a flexible CO tip 6.68 Å above the (1 × 3) phase of adsorbed partially dissociated water dimers. (F) Models of the minimum-energy DFT structure of the low-coverage phase. In both structures, OH and water are bound to undercoordinated Fe cations (brown), with one $O_{lattice}H$ formed at a surface oxygen (red). The O atoms of the intact and dissociated water molecules are shown in light and dark blue, respectively. Simulations of ncAFM images were carried out by I. Sokolović, DFT computations were carried out by M. Bichler. Figure reprinted from [160].

The TPD results suggest that a phase more favorable than the full-coverage (1 × 1) structure contains 1.27 D_2O/uc (peak at 345 K). The ncAFM image shown in Figure 4.11D was acquired at 4 K after the as-prepared α-$Fe_2O_3(1\bar{1}02)$-(1 × 1) surface was exposed to 10 L of H_2O at 300 K; again a CO-functionalized tip was used in constant-height mode. The image exhibits two types of protrusions, one slightly smaller than the other. These features form pairs along the $[1\bar{1}0\bar{1}]$ direction, with the axes of the pairs slightly rotated in alternating directions. This creates a (1×3) periodicity with four protrusions per (1×3) cell. If each of these protrusions is water or $O_{water}H$, a full (1×3) overlayer contains 1.33 D_2O/uc, which nicely corresponds to the 1.27 ± 0.07 D_22O/uc coverage determined from TPD.

DFT+U calculations based on four water molecules per (1×3) unit cell find the most stable structure (1.07 eV/H_2O) to be two partially dissociated water dimers. Between two dimers, one Fe cation site is left vacant. As before, the ncAFM simulation based on this structure (Figure 4.11E) agrees well with the experimental image (Figure 4.11D) and allows identifation of the larger bright feature as the terminal OH group and the smaller bright feature as the water molecule. There is also a very good agreement between the calculated adsorption energy of this phase and the desorption energy found from the inversion analysis of the TPD data (1.10 eV).

Both water phases have also been studied by ncAFM with non-functionalized tips, resulting in a relatively wide range of observed contrasts, summarized in Fig. 4.12. The varying contrast is most likely due to the tip being terminated either by a metal atom (from previous tip preparation on metal or metal oxide surfaces) or by a dissociated or molecular water (from scanning over water structures). Because the tip termination is unknown, the exact assignment of the observed species to H_2O or OH is not as straightforward as in the previous cases. Nevertheless, the data still contains valuable information not seen before in the detailed small-area images shown in Fig. 4.11. Figure 4.12A,B,C shows the α-$Fe_2O_3(1\bar{1}02)$-(1×1) surface with incomplete coverage of water adsorbed in the (1×3) phase. Panels A,B show the most common contrast achieved with non-functionalized tip, panel C shows an example of an alternative contrast. In all the images the water dimers are always oriented in the same way along the $[1\bar{1}0\bar{1}]$ direction, which is consistent with the fact that the surface does not have a mirror symmetry in this direction. The image in panel A shows that the (1×3) phase forms in patches, and a single isolated HO-H_2O dimer has not been observed after this preparation. Formation of a (1×3) structure on top of a bare (1×1) surface implies the existence of three equivalent domains shifted by (1/3) of the (1×3) cell. Such domains are indeed observed in wide-scan images, shown in Fig. 4.12A, where the (1/3) unit cell shift is highlighted by blue and red lines. Interestingly, in most cases the phase shifted domains are not seen in directly neighboring unit cells, which suggests that either lateral interactions of the neighboring HO-H_2O play a role, or that a formation of a HO-H_2O dimer induces distortion to the hematite lattice, which makes formation of a phase shifted dimer in the neighboring cell unfavourable. These effects seem likely from the experimental data, but they have not been studied computationally as that would require modelling of much larger supercells.

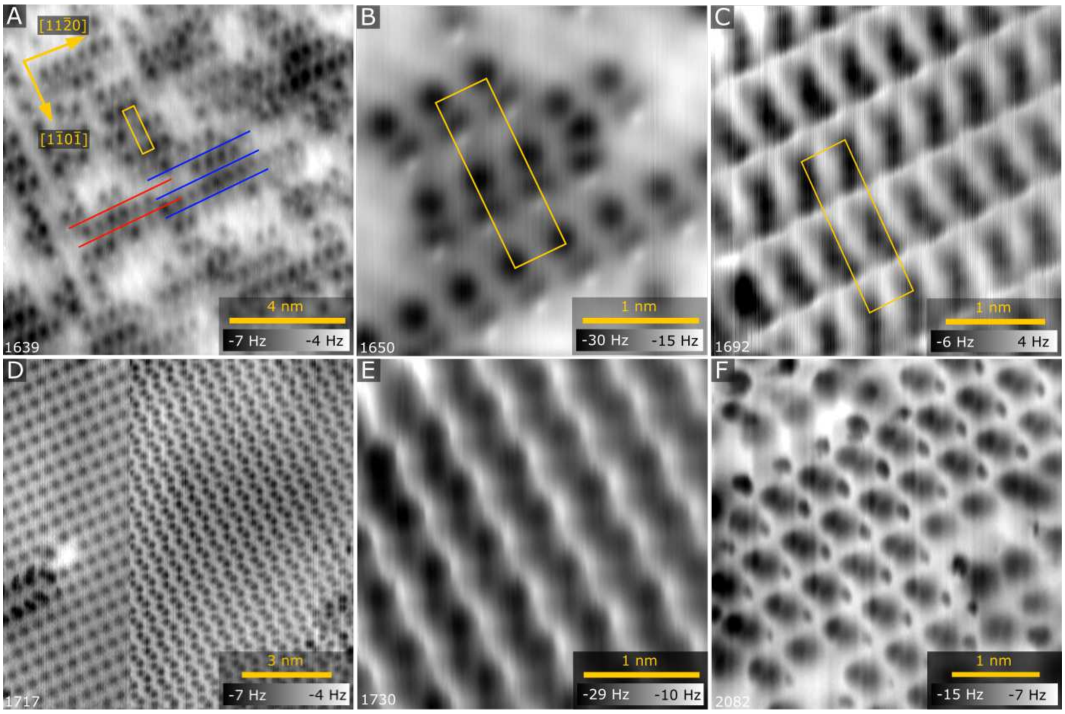

Figure 4.12: Noncontact atomic force microscopy (nc-AFM) images of the different (1 × 3) and (1 × 1) phases of water adsorbed on the α-Fe$_2$O$_3$(1$\bar{1}$02)-(1 × 1) surface. The images were taken with tips that were not purposely functionalized; spontaneous changes in tip termination resulted in different contrasts. Panels (A,B) show the most common contrast on the (1 × 3) phase. Red and blue lines highlight the existence of phase-shifted domains of the (1 × 3) structure. An alternative contrast showing the (1 × 3) structure is shown in panel (C). Different contrast types obtained on the (1 × 1) phase are shown in panels (D,E,F).

Figure 4.12D,E,F shows various contrasts achievable on the (1 × 1) phase of water dimers (full coverage). Here, tip changes are subjectively more common in comparison to imaging of the (1 × 3) phase; panel D shows such an event taking place during imaging. Regardless of the changing contrast, all the images show a (1 × 1) symmetry. Domains phase-shifted by half a unit cell are observed in the (1 × 1) phase, as shown in Fig. 4.13. In panel A, a domain boundary is imaged with a CO-terminated tip, panel B shows a domain boundary imaged with a non-functionalized showing similar contrast as in Fig. 4.12F.

According to the TPD experiments, the (1 × 3) structure is stable at room temperature, and thus attempts were made to detect it by RTSTM or LEED at room temperature. In RTSTM experiments it was found that the water overlayer is highly mobile, resulting in fuzzy images, see Fig. 4.14. Panel A shows a clean surface for reference, panels B and C show the same surface after exposure to water vapor. Only very small patches of features spaced with (1 × 3) symmetry were observed after H_2O dose at room temperature, highlighted by yellow circles in panel B. Panel C shows images of the surface exposed to H_2O at 282 K and measured at the same

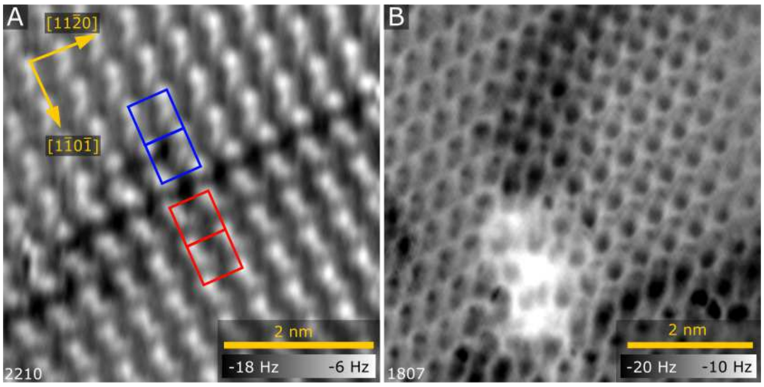

Figure 4.13: Domain boundaries observed in the full-coverage (1×1) phase imaged with (A) a CO-terminated tip and (B) a non-functionalized tip with unknown termination.

temperature (using a "poor man's LTSTM" - an RTSTM apparatus in a lab with windows open on a cold February night). In this image, one can see the rows in the $[1\bar{1}0\bar{1}]$ direction, but all the water adsorbed is highly mobile and dragged around by the tip. Likewise, no evidence of the (1×3) symmetry was found on LEED at room temperature. This suggests that the (1×3) is likely mobile or disordered at room temperature; this mobility could nevertheless be easily induced by the tip in STM imaging or the electron beam in LEED experiments.

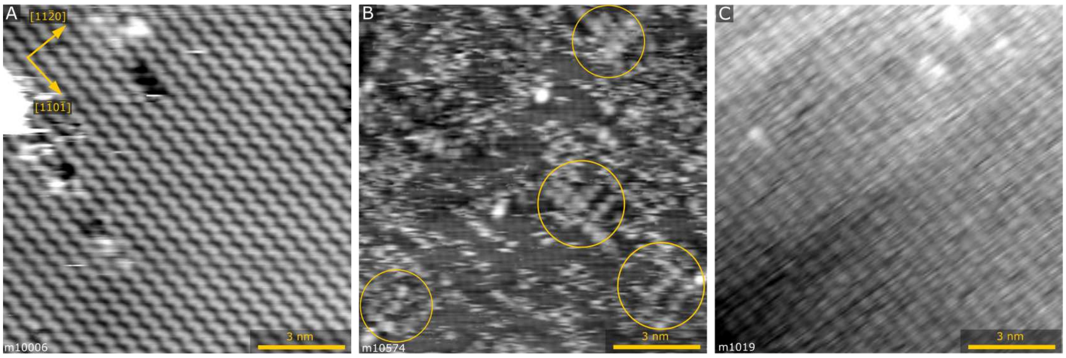

Figure 4.14: Scanning tunneling microscopy data of water adsorbed on the α-$Fe_2O_3(1\bar{1}02)$-(1×1) surface. (A)A clean surface, (B) room-temperature data after dosing 1 L water. The image features very small patches with a (1×3) symmetry, highlighted by the yellow circles. (C) Data acquired at ca. 282 K after dosing 60 L of water. The water molecules are dragged around by the tip (the fast scan direction is 38° off the horizontal direction) and the only resolvable features are the rows running along the $[1\bar{1}0\bar{1}]$ direction. Data taken by F. Kraushofer.

Exposure of the α-$Fe_2O_3(1\bar{1}02)$ to liquid water

While the UHV experiments are an ideal complement to theory, they do not tell whether the UHV-prepared surface would be relevant or even stable in liquid water and whether similar water species might form in that very different environment. As a first step toward answering this question, the UHV-prepared α-$Fe_2O_3(1\bar{1}02)$-(1×1) surface was exposed to a drop of ultrapure liquid water utilizing the custom-built water-dosing setup described in [11, 167] and in the methods chapter of this thesis. The liquid exposure experiments were carried out by Jan Balajka.

Figure 4.15 shows LEED patterns and XPS spectra obtained following UHV preparation and after exposure to liquid H_2O for $\approx 30\,s$ at room temperature. Both LEED images show a (1×1) periodicity, consistent with the bulk-truncated surface. O 1*s* and Fe 2*p* XPS spectra acquired at 320 K resemble those obtained at 121 K, with contributions from lattice O^{2-}, OH and H_2O. The intensity of the water-related features decreased over the course of the measurement because the measurement temperature ($\approx 320\,K$) is in the leading edge of the 345 K TPD peak. Interestingly, the H_2O/OH ratio also changed from 0.37 to 0.21, indicating a higher fraction of dissociated water with decreasing coverage. In view of the TPD tail above $\approx 370\,K$ (Fig. 4.8), we attribute the excess dissociated signal at least partly to steps or defect sites; at low coverage, these outweigh the partially dissociated dimers at regular lattice sites.

The cleanliness of the liquid-drop experiment was checked by measuring the O 1*s* and C 1*s* XPS regions after prolonged (5 min) exposure to liquid drop and subsequent flash annealing to 450 K to desorb the adsorbed water. The resulting spectra, shown in Fig. 4.16, feature only very small contributions corresponding to adventitious carbon and carboxylic species.

The similar appearance of LEED patterns and XPS spectra after exposure to liquid water does not, by itself, prove that the surface is the same as after dosing water vapor. It could in principle be morphologically different, terraces might be etched or a new phase might be grown on top. To test whether this might be the case, we measured the surface by ambient AFM before and after an hour long exposure to liquid water (measurements carried out by M. Müllner). The images are shown in Fig. 4.17, and save for mobile species, probably due to contamination, the images look very similar. Both images feature step bunches of 4–5 steps and meandering single steps (the measured step height 0.34 nm agrees well with the expected value of 0.37 nm). In both cases the terraces are $\approx 1\,\mu m$ wide. Thus, no significant morphological changes such as etch pits or islands are observed after the contact with liquid water.

Discussion

This section presented experimental and computational evidence for the existence of two distinct phases of adsorbed water on bulk-truncated α-$Fe_2O_3(1\bar{1}02)$ in UHV conditions, both of which consists of partially dissociated HO-H_2O dimers. Similar species have been previously reported on other metal oxide surfaces [89, 178, 180–

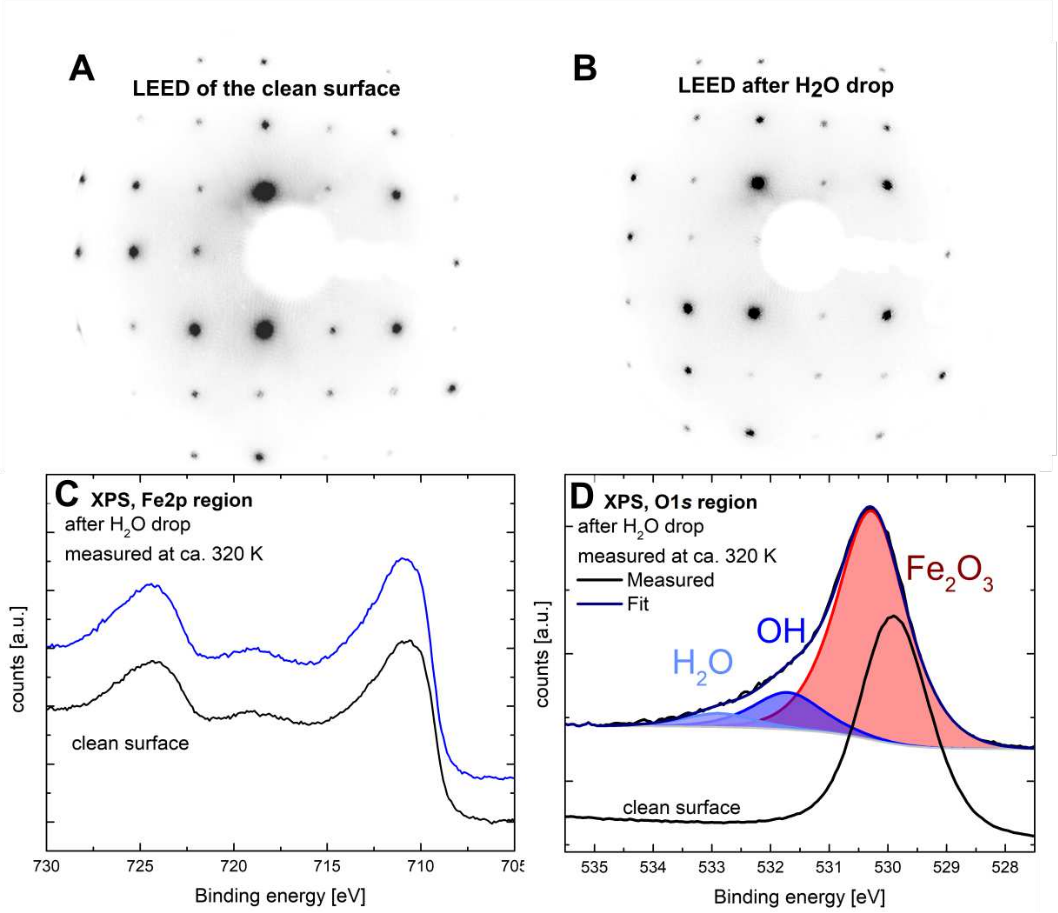

Figure 4.15: LEED patterns of the (A) clean α-$Fe_2O_3(1\bar{1}02)$-(1×1) surface and (B) after exposure to a liquid water drop, both acquired at 120 eV. (C,D) XPS spectra (Mg Kα) of the Fe 2p and O 1s regions before (black) and after (blue) exposure to liquid water. Experiments carried out by J. Balajka, figure reprinted from [160].

183] and thus appear to be common. The preference for the partial dissociation can be understood by the so-called cooperativity effect, which comes from the inherent directionality of the hydrogen bond [49]. The cooperativity effect is well-described in gas-phase water clusters, and it was shown recently that a similar phenomenon can be observed on water adsorbed on surfaces, where the bond of the water molecule to the surface has similar characteristics as an accepted hydrogen bond [184]. Therefore, on a surface where close proximity of undercoordinated cations allows formation of an intermolecular H-bond between the adsobed water molecules, this bond will be significantly strenghtened if the H-bond acceptor dissociates to form a negatively charges OH species. This in turn causes the H-bond donating water molecule to interact more strongly with the surface. For this to happen, undercoordinated oxygen atoms are required to receive the liberated proton and form a stable $O_{\text{lattice}}H$ group. Because these conditions are met on many oxide surfaces, partially disso-

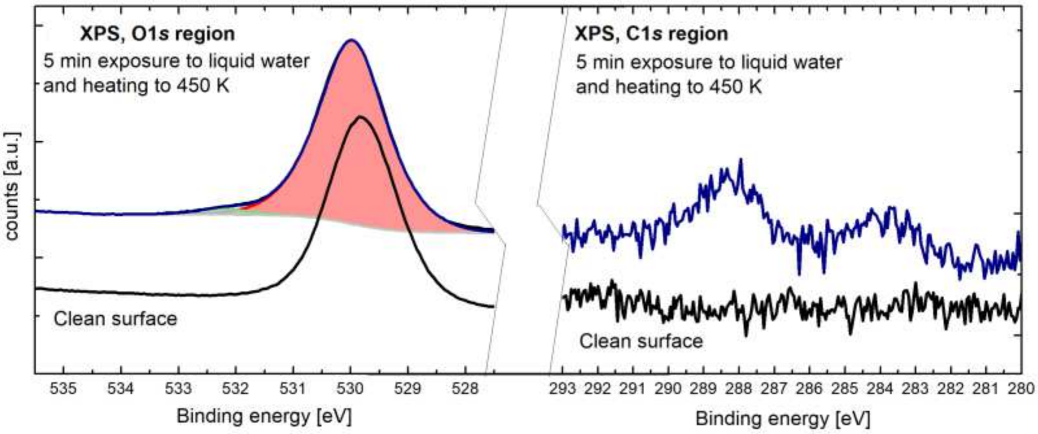

Figure 4.16: XPS (Mg Kα) acquired after exposure to liquid water for five minutes and subsequent heating to 450 K (blue) compared to spectra acquired on a clean surface (black). The O 1s and C 1s regions after the water exposure feature very small peaks corresponding to carbonaceous contamination (the vertical scale of the C 1s region has been magnified ca. 12× with respect to the O 1s region). Data taken by J. Balajka.

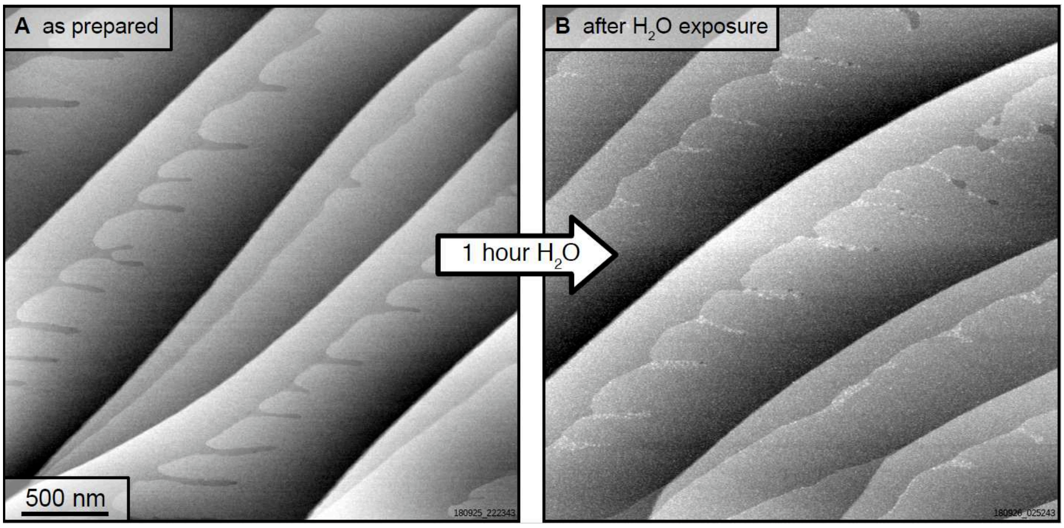

Figure 4.17: Ambient AFM images of α-$Fe_2O_3(1\bar{1}02)$-(1 × 1) before (A) and after (B) exposure to liquid water. Data taken by M. Müllner.

ciated water dimers are often reported as highly stable structures, even though at higher coverages often more complex structures prevail.

The liquid exposure experiments suggest that the UHV-prepared surface survives immersion in liquid water and that partially dissociated water remains when the sample is returned to UHV. It is useful to compare our results to surface X-ray diffraction experiments performed on α-$Fe_2O_3(1\bar{1}02)$ single crystals covered with a layer of liquid water [124, 130]. In these experiments, the sample was prepared by wet chemical etching followed by annealing in air, which produces a stoichiometric bulk termination. Structural refinements suggested that oxygen atoms complete the octahedral coordination shell of outermost Fe^{3+} cations, i.e., occupying the same positions as those shown for the oxygen atoms in the full-coverage water phase identified by ncAFM and DFT in this work. This surface was stable in water for (at least) 4 days [130], and in situ measurements of the immersed sample suggested that further water ordering continues at least 1 nm from the surface. Unfortunately, X-ray diffraction is not sensitive to the location of the H atoms; therefore, it is impossible to say whether these oxygen atoms result from partially dissociated water or not. Interestingly, though, there is evidence from ambient-pressure XPS experiments that OH can exist at the interface following the condensation of multilayer water on the UHV-prepared α-$Fe_2O_3(0001)$ surface [185], and a recent study of immersed hematite nanoparticles suggests that OH remains adsorbed at the interface in liquid water [186]. As such, it seems reasonable to suggest that partially dissociated dimers may form at the aqueous interface and thus that water–water interactions could be important in the OER.

4.3.2 Oxygen exchange at the water-hematite interface

Facile oxygen exchange between the lattice and adsorbed water layer is regarded as a first step of mineral dissolution, and thus the observation of such effect on a hematite surface in early surface science studies by Henderson [120] raised an interest in the geochemistry community [187–189]. In the cited study, Henderson observed significant $H_2^{18}O$ desorption signal after dosing $H_2^{16}O$ on an ^{18}O-enriched surface, which was initially interpreted as an evidence for dissociative water adsorption. Such oxygen scrambling is generally possible when two neigboring $O_{lattice}H$ recombine with the $O_{lattice}$ and desorb as H_2O, leaving an oxygen vacancy behind (which can be later repaired by an $O_{water}H$). Such a mechanism is however not consistent with the first-order behavior of the 345 K desorption peak observed on α-$Fe_2O_3(1\bar{1}02)$, as recombinative desorption typically results in second-order desorption peaks.

Now, with the knowledge that water adsorbs in the form of partially-dissociated dimers, the first order shape of the desorption peak can be rationalized if the HO-H_2O dimers do not spatially separate from the $O_{lattice}H$. Nevertheless, if this is the case then it is not clear why an extraction of an $O_{lattice}$ takes place given the availability of a simple recombination of species residing in close proximity.

To investigate the oxygen scrambling phenomenon, additional water TPD and liquid exposure experiments with isotopically-labelled ^{18}O (either in dosed water ($H_2^{18}O$) or in the ^{18}O-enriched hematite lattice) were carried out. While no specific reaction mechanism could be identified, we were able to show that the scrambling is intimately linked to the water desorption from the α-$Fe_2O_3(1\bar{1}02)$ surface at 345 K, and, importantly, it most likely does not take place during the actual liquid water exposure at the water-hematite interface.

Figure 4.18 shows a comparison of TPD spectra of D_2O (same as shown previously in Fig. 4.8) and a TPD spectrum of $H_2^{18}O$ taken with initial coverage of 1.90 $H_2^{18}O$/uc, corresponding to saturation of the full-coverage (1×1) phase. From the figure it is clear that ≈ 50 % of the water desorbing in the 345 K peak contains an oxygen extracted from the hematite lattice. Notably, such oxygen scrambling is not taking place during desorption of the full-coverage phase at ≈ 250 K, as the $H_2^{16}O$ signal is minimal below ≈ 310 K.

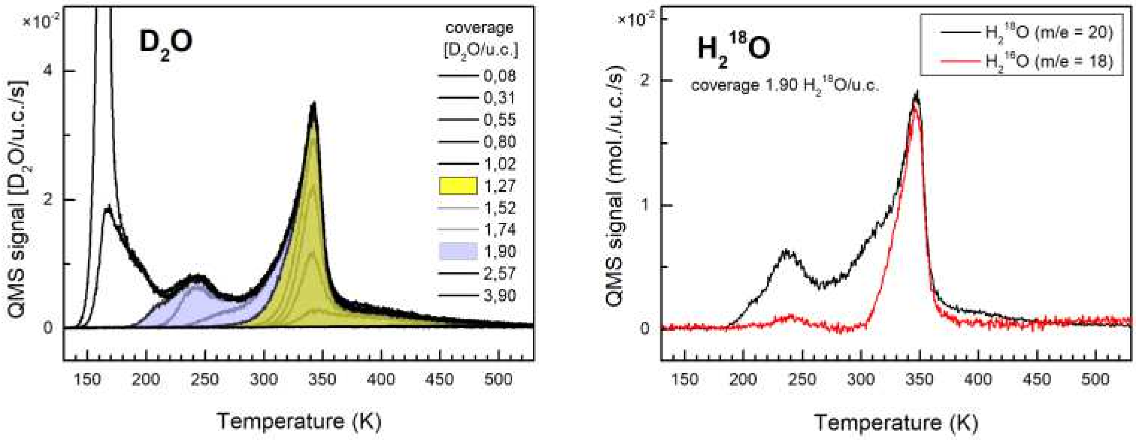

Figure 4.18: Temperature programmed desorption spectra of D_2O and $H_2^{18}O$ on bulk-truncated α-$Fe_2O_3(1\bar{1}02)$. In the case of $H_2^{18}O$, ≈ 50 % of the water desorbed in the 345 K peak contains oxygen atom scrambled from the lattice. Such effect is not observed in the water desorbing at lower temperature. The $H_2^{16}O$ line is plotted after subtraction of a spectrum taken in a blank experiment. The signal in a blank experiment is non-zero due to $H_2^{16}O$ adsorption from the background.

We further studied this phenomenon in the liquid drop setup (liquid drop experiments carried out by J. Balajka). Here, the surface was first isotopically enriched by ^{18}O by cleaning cycles with annealing steps done in ^{18}O at a temperature of 723 K. Such preparation consistently lead to a surface in which the top layer contains (61 ± 2) % ^{18}O, as measured by low energy ion scattering, shown in Fig. 4.19A. After exposing this surface to 6 mbar of $H_2^{16}O$ vapor and heating to 450 K, well above the highest water desorption peak, the LEIS spectra still feature signals from both ^{16}O and ^{18}O with the fraction of ^{18}O being (40 ± 3) %, which indicates decrease by ≈ 33 % in comparison to the freshly prepared surface (Fig. 4.19B). The same results were measured in two separate experiments with exposure times 10 and 60 min, and also after exposure to liquid water for several seconds. Importantly, no systematic change in subsequent scans was observed, which decisively rules out any damage to the surface by He^+ sputtering during LEIS measurements. Prolonged exposure (5 and 10 min) to liquid water results in higher exchanged oxygen ratio, the ^{18}O signal fraction drops to (32 ± 3) %, which is decrease of ≈ 50 % from the UHV prepared surface. Nevertheless, the prolonged exposure to liquid water also facilitates impurity transfer to the sample surface (as seen in the full LEIS spectrum shown in the right panel of Fig. 4.19 showing multiple small peaks between 600 and 1100 eV, consistent with presence of Na, Mg, K and Mo), therefore some of the ^{16}O signal might correspond to these oxidized species.

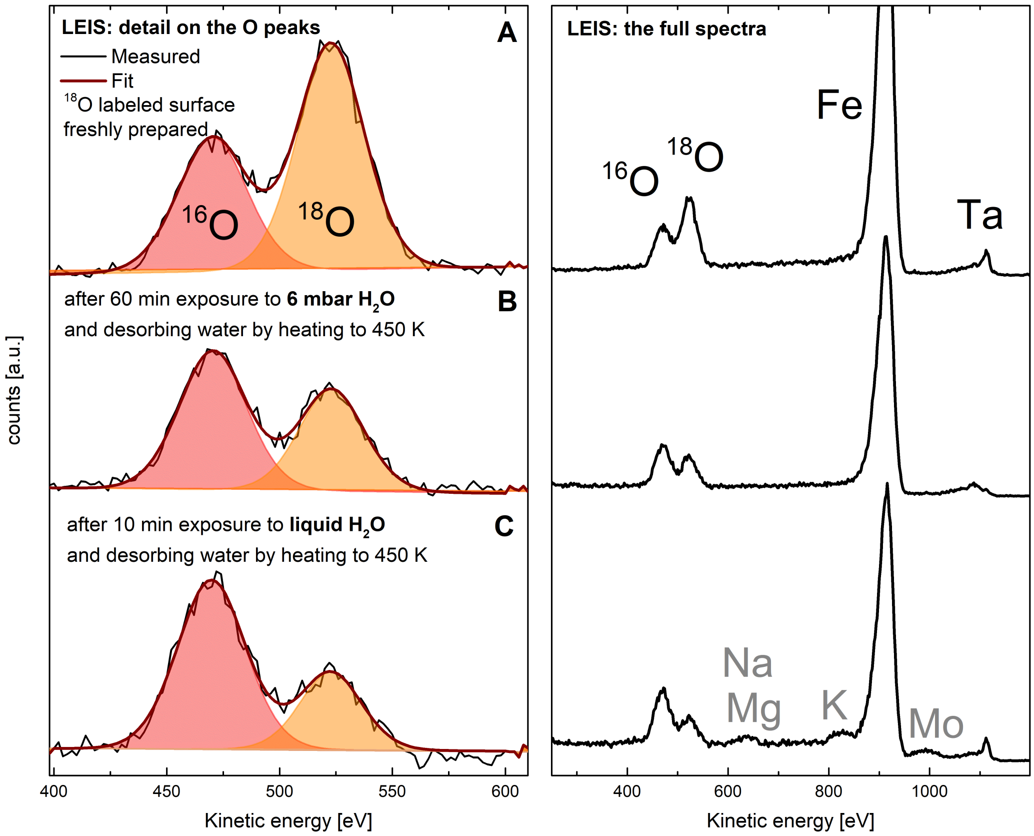

Figure 4.19: Low energy ion scattering measurements (1.225 keV He^+, 137°) taken (A) on the as-prepared ^{18}O-enriched α-$Fe_2O_3(1\bar{1}02)$ surface. Here, (61 ± 2) % of the oxygen signal corresponds to ^{18}O. (B) After exposure to 6 mbar H_2O for 1 hour, the fraction of ^{18}O decreases to (40 ± 3) %. The same result was observed after a 10 min exposure to 6 mbar water vapor and a few seconds long exposure to liquid water. (C) After 5 or 10 min long exposure to liquid H_2O the ^{18}O fraction decreases to (32 ± 3) %. These experiment are however significantly less clean than the previous ones, as evidenced by multiple small peaks in the LEIS spectrum between 600 and 1100 eV kinetic energy, which could correspond to Mg, Na, K and Mo. The peak at ≈ 1100 eV corresponds to tantalum clips holding the sample. Experiments carried out by J. Balajka.

4.3.3 Discussion

It was shown that significant amount of oxygen is exchanged between the hematite lattice and the desorbed water after water desorbs from the bulk-truncated α-$Fe_2O_3(1\bar{1}02)$ surface. This effect takes place regardless of whether the water was dosed as a vapor in UHV, or whether the surface was exposed to water in liquid phase.

The TPD data clearly show that the oxygen exchange does not take place when every surface cation site is occupied; only a very small $H_2^{16}O$ desorption peak is observed at $\approx 250\,K$. This is in stark contrast with the desorption of the lower coverage phase at $\approx 345\,K$, where close to 50 % of the desorbed water contains an oxygen atom from the lattice. This phase, saturating at 1.33 water molecules per unit cell, was previously identified as partially dissociated water dimers evenly spaced with an empty cation site in between, forming a (1×3) symmetry (see section 4.3.1). In this context the 50 % is an unexpected number, as it implies that on average, each water dimer exchanges one oxygen atom with the surface, suggesting a very specific mechanism. Previous STM and LEED experiment at room temperature imply that the dimers are likely mobile at temperature, therefore a question arises whether the oxygen exchange takes place during the diffusion of the water species (and/or their splitting and reforming on the surface), or during the actual desorption. If the diffusion process would be responsible, then the ratio of exchanged/unexchanged oxygen would correspond to the ratio of oxygen atoms in the top layer on the surface and in the adsorbed water layer, which is 3/2 for the (1×3) phase. Thus, we would expect to see 60 % of the desorbed water containing oxygen from the lattice. This is relatively close to the measured value, therefore it is difficult to resolve this question based on the current TPD dataset alone. Additional experiments could be carried out to provide a convincing answer: If the diffusion plays a role, then TPD spectra acquired with different heating rates should affect the ratio of exchanged/unexchanged oxygen. If the ratio stays constant, then it is likely that the exchange mechanism takes place during the desorption.

Experiments on the ^{18}O-enriched surface show that a similar phenomenon takes place when the surface is exposed to liquid water. Quantification of the $^{18}O/^{16}O$ ratio by LEIS shows that 33 % of the detected oxygen is exchanged after exposure to 6 mbar H_2O regardless of the exposure time between 10-60 min, and the same result is observed after liquid water exposure to several seconds. Assuming the top-layer sensitivity of LEIS (layer 1 in Fig. 4.3d), this result could be interpreted as an exchange of 33 % oxygen atoms in the top surface layer, which means two oxygen atoms per (1×3) unit cell. In the low-coverage phase of adsorbed water identified in UHV there are two water dimers per (1×3), so this result would agree perfectly with the results from the TPD, where ≈ 50 % of the desorbed water contains oxygen from the lattice. Nevertheless, looking at the model it is reasonable to assume that the LEIS also probes the O atoms between the top-layer rows as well (layer 3 in Fig. 4.3d). If the sensitivity for detection O atoms in layer 1 and layer 3 was the same, the observed 33% difference would correspond to exchange of four oxygen atoms per (1×3) unit cell, which is significantly more than observed in TPD. In any case, the amount of exchanged oxygen upon exposure to 6 mbar H_2O is independent of exposure time, which hints the exchange mechanism is not a continuous process happening during exposure, as was proposed on the half-layer terminated α-$Fe_2O_3(1\bar{1}02)$ [134]. When the liquid water exposure is prolonged to 5 or 10 min, the LEIS spectra show higher fraction of ^{16}O, but this is accompanied by impurity transport from the sample mount to the sample surface. LEIS spectra show additional small peaks corresponding to Mg, K, Na and Mo species, and thus the higher amount of ^{16}O could be due to these oxidised species.

The available data thus suggest that the oxygen exchange between the lattice and adsorbed water layer takes place only when the water layer is incomplete, that is in conditions corresponding to the existence of phase formed by partially-dissociated water dimers with neighboring vacant cation sites. Unfortunately, based on the current dataset the exact mechanism of the oxygen exchange can be only speculated about. At the moment, there is no simple or intuitive explanation, and the way to validate a highly unusual reaction pathway would require a detailed computational study.

The oxygen exchange could be potentially relevant for photoelectrochemistry, as oxygen extraction was identified as a rate-limiting step in first-principles study on some terminations of α-$Fe_2O_3(0001)$ [190]. The results presented in this section show that the oxygen extraction from a hematite surface can be surprisingly facile. It would be interesting to see whether such an effect takes place on other facets of hematite, or whether it is limited to the $(1\bar{1}02)$. Unfortunately, to the authors knowledge no experimental TPD results were published on the (0001) surface. Nevertheless, a similar effect was reported on isostructural alumina α-$Al_2O_3(0001)$ [191], but here the surface structure is unknown and the surface quality was only measured by LEED, thus the oxygen exchange might be due to other effects (such as a high number of surface defects).

The observed oxygen exchange phenomenon illustrates that even very simple model systems studied in highly idealized conditions can exhibit behavior which is very hard to explain. Potentially, this oxygen exchange phenomenon might be important for understanding photoelectrochemical performance of hematite or its dissolution properties, it is however difficult to assess this without the knowledge of the reaction mechanism.

5 Water Adsorption on Fe_3O_4 Surfaces

This chapter deals with studies of water adsorption on two dominant surfaces of Fe_3O_4, the (001) and the (111). Some data described here have been published in references [159, 192], but a substantial part of this chapter has not been presented before. This chapter contains some data provided by this authors' colleagues, these contributions are clearly labeled in the text or in figure captions.

Introduction

Elucidating the structures of water adsorption on solid surfaces is a notoriously difficult task which pushes both experimental and computational methods to their limits. Even on metal surfaces with small unit cells and homogeneous adsorption sites, the water adsorption behavior proved to be much more complex than the slightly distorted ice-like bilayer structures which were initially assumed [49, 193]. Instead, alternative structures have been observed and eventually rationalized by the so-called "2D ice rules" [49, 193, 194]. These state that water molecules adsorb atop the metal sites and form as many hydrogen bonds as possible; in a honeycomb lattice this means that each water molecule forms three hydrogen bonds: two donor and one acceptor. In a 2D network with flat-lying water molecules this can only go on for a few units; to continue further the imbalance between the available donor and acceptor sites requires existence of double-acceptor molecules [49, 193, 194].

On oxides, the situation is quite different. One reason is that sites on oxide surfaces are both cationic and anionic, and in many cases also highly inhomogeneous. The surface-water interaction is much stronger than in the case of metals, and the formation of the first monolayer is thus much more dependent on the surface structure. It has long been estabilished that water adsorbs by forming a bond between the oxygen atom and surface cations, and that water dissociation typically takes place on surface defects [121]. On reactive surfaces such as ZnO(0001) or $In_2O_3(111)$ water dissociation occurs [195, 196], leading to the adsorption of terminal ($O_{water}H$) and surface ($O_{surface}H$) hydroxyl groups on cations and anions, respectively. On the prototypical $TiO_2(110)$ suface, both dissociative and molecular adsorption has been observed on defect-free surface [197, 198], which was later rationalized by a very small barrier for dissociation, even though molecular adsorption is marginally preferred [178].

On several oxide surfaces, partially dissociated water dimers have been recently reported as highly stable structures [86, 160, 180, 182], and such species on α-$Fe_2O_3(1\bar{1}02)$ are thoroughly discussed in the previous chapter of this thesis. At higher water coverages, there is evidence of extended hydrogen bonded networks on some oxide surfaces [89, 199], similar to the behavior on metals. Nevertheless, the structures of such networks is typically determined by computational methods and the results are rarely compared to results from real space imaging techniques. STM images typically provide evidence that water is adsorbed on the surface, but the resolution if often insufficient to determine how many water molecules there is or how they bond together. The situation has changed with the emergence of ncAFM tools with functionalized tips, which have been shown to resolve individual water molecules and in some cases provide submolecular resolution, determine the direction of the hydrogen bond, and differentiate between molecular and dissociated species [139, 200]. However, so far this method has been mostly applied to water adsorbing on metals rather than oxide surfaces.

In this chapter, ncAFM with a CO tip is used as the main tool do image the structure of water agglomerates and extended hydrogen bonded networks on the (001) and (111) surfaces of Fe_3O_4. The results are combined with STM, XPS, TPD and computational results to provide an unified picture of phases formed by water on these surfaces.

5.1 Pristine $Fe_3O_4(001)$

Before going into the details of water adsorption behavior, it is useful to look at the pristine surface first and reiterate what is known about the structure of the SCV-reconstructed $Fe_3O_4(001)$ surface and the features commonly found on as-prepared surfaces. Figure 5.1 shows the top view on the model of the SCV reconstructed surface and two typical STM images. The undulating rows running in the [110] direction in the STM images correspond to 5-fold coordinated Fe_{oct} atoms on the surface (dark blue balls in panel (a)). The oxygen atoms (red balls in panel (a)) are not visible in STM images because they possess no density of states near the Fermi level. Their positions are however precisely known from surface diffraction studies and DFT calculations, and they can also be imaged by ncAFM (as will be shown later in this section). In a typical STM image, the individual Fe_{oct} cannot be resolved and the features forming the undulating rows correspond to pairs of Fe_{oct} atoms. The $(\sqrt{2} \times \sqrt{2})R45°$ surface unit cell, highlighted by the white square on panels (a,b) thus contains four surface Fe_{oct} atoms. The surface oxygen atoms without the Fe_{tet} neighbor (light blue balls) in the subsurface are labeled O* in panel (a); these form the typical adsorption site for metal adatoms on this surface (previously referred to as the “narrow” site) [69].

In STM images shown in panels (b,c), the typical surface defects are highlighted. The bright elongated species were previously identified as $O_{surface}H$; when measured at room temperature these exhibit characteristic hopping motion over the adsorption (“narrow”) site [73, 75, 201]. Even though these species are essentially a single H atom bound to the O* on a pristine surface, in STM data these are observed as increased LDOS of four neighboring Fe_{oct} atoms. Apart from $O_{surface}H$, other common defects include anti-phase domain boundaries (labeled APDB in 5.1c) and unreconstructed unit cells. Both of these are locally bulk-like, meaning they contain an additional Fe atom in the subsurface in comparison to the SCV surface [51, 202]. In further text these will be referred to as Fe-rich surface defects. On neighboring terraces the Fe_{oct} rows are rotated by 90° due to the spinel structure (shown in Fig. 5.1c)

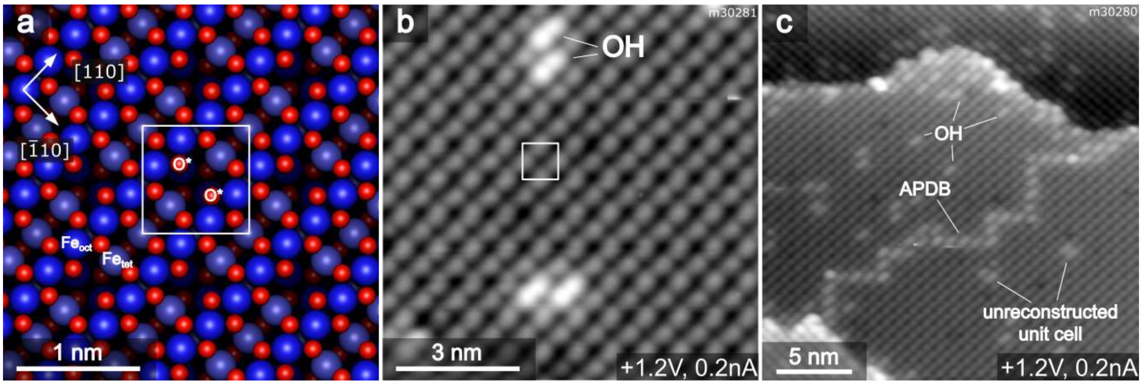

Figure 5.1: The $Fe_3O_4(001)$–$(\sqrt{2} \times \sqrt{2})R45°$ and its appearance in STM. (a) Top view on the SCV reconstructed Fe_3O_4(001) surface. The Fe_{oct}, Fe_{tet} and O atoms are drawn as dark blue, light blue and red balls, respectively. The $(\sqrt{2} \times \sqrt{2})R45°$ is highlighted by the white square. The O atoms without an Fe_{tet} neighbor are labeled as O*. (b) In STM images, only the surface Fe_{oct} atoms are visible. Individual atoms are typically not resolved, the visible features correspond to pairs of Fe_{oct}. The surface unit cell is highlighted by the white square. The elongated bright features correspond to $O_{surface}H$. (c) On neighboring terraces, the Fe_{oct} rows are rotated by 90°. Typical surface defects include anti-phase domain boundaries (APDB) and unreconstructed unit cells; both of these defects contain and extra Fe cation in the subsurface.

Figure 5.2 shows constant-height ncAFM and corresponding STM images with a “negative” tip (panels a-c) and “positive” tip (d-f). The assignment of the tip polarity was done by after the acquisition of the images by comparison of the measured data with the surface model. The negative tip ncAFM images (a,c) show surface Fe_{oct} as dark species (darker color corresponds to stronger attractive interaction) and surface O atoms as bright species. Individual surface O atoms are not visible in panel (a), but are well-resolved on panel (c). Images acquired with a positive tip (d,f) show the opposite contrast, here the dark species correspond to O atoms and bright species to Fe_{oct}. Individual surface O atoms are not visible in (d), but are well-resolved in (f). Panels (b,e) show constant-height STM images acquired simultaneously with images shown in (a,d); the comparison of STM and ncAFM images further validates the assignment of features observed in ncAFM data. Similarly to pioneering ncAFM works on TiO_2, the contrast reversal is common and sometimes takes place mid-scan (not shown).

The comparison of simultaneously acquired ncAFM and STM images further confirms the fact that the undulations of Fe_{oct} rows observed in STM are mainly due to an electronic effect [72]. The physical positions of the Fe_{oct} observed in ncAFM data (panel a) do not correspond to the strong undulations observed in STM (panel b). Also, the surface defects, which look quite prominent in STM images, are barely visible in the ncAFM data. This supports the claim that the origin of many defect seen in STM images lies in the subsurface, where extra cations affect the electronic structure of the surface Fe_{oct}. Lastly, in panel (f) missing dark depressions (O atoms) are observed (one of them labeled OH in the figure). These are most likely not oxygen vacancies, but surface $O_{surface}H$ species, as indicated by a comparison to corresponding STM image shown in Fig. 5.3.

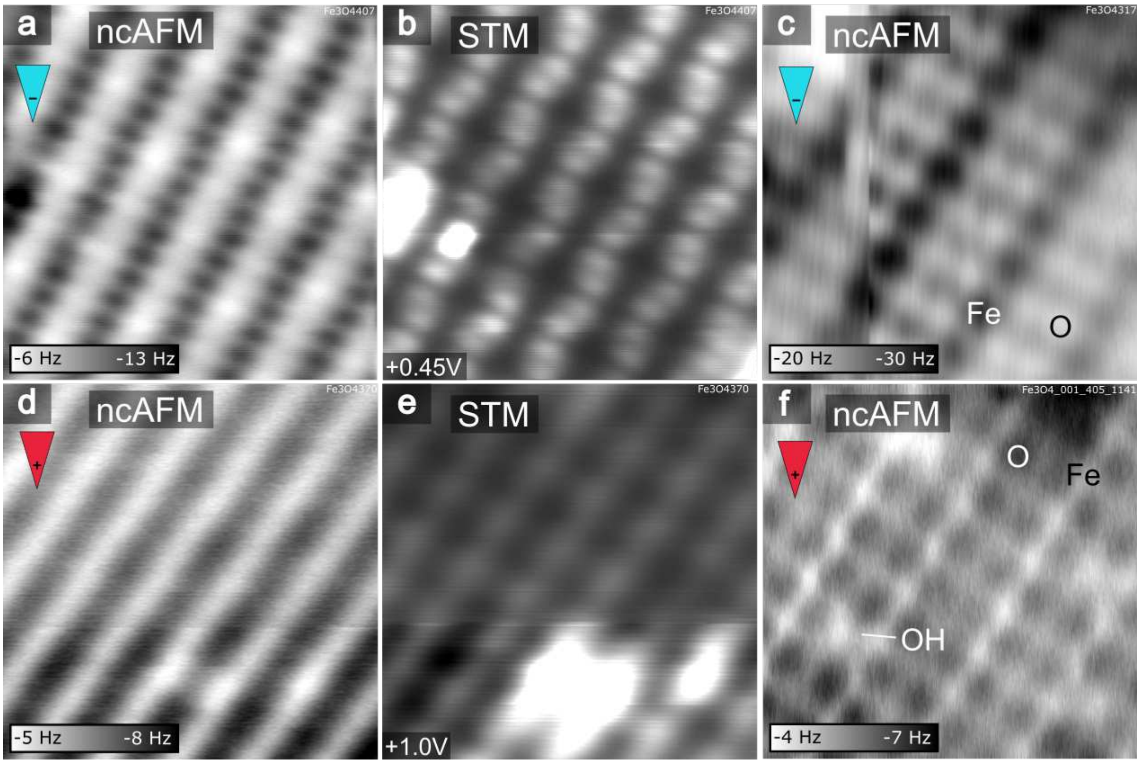

Figure 5.2: Constant-height ncAFM and STM images of the SCV reconstructed Fe_3O_4(001) surface acquired at 78 K. (a) ncAFM image acquired with a negative tip. This contrast shows surface cations as dark species, surface anions as bright species. ($U = 0.45\,\mathrm{V}$, $A = 100\,\mathrm{pm}$). (b) STM image acquired simultaneously to (a). (c) high-resolution ncAFM image, in which individual surface O atoms can be resolved. The fast-scan direction is vertical ($U = 0.15\,\mathrm{V}$, $A = 120\,\mathrm{pm}$). (d) ncAFM image acquired with a positive tip. This contrast shows surface cations as bright species, surface anions as dark species. ($U = 1.00\,\mathrm{V}$, $A = 150\,\mathrm{pm}$). (e) STM image acquired simultaneously to (d). (f) high-resolution ncAFM image, in which individual surface O atoms can be resolved. This image was acquired after desorbing the majority of previously dosed water by heating to 220 K for several minutes. The fast-scan direction is vertical ($U = 0.0\,\mathrm{V}$, $A = 250\,\mathrm{pm}$).

5.2 Water Agglomerates on Fe_3O_4(001)

The water TPD data acquired on Fe_3O_4(001) indicate very complex water monolayer formation on this surface. A detailed TPD study of water adsorption on this surface is presented in the PhD thesis of Jan Hulva [203]. The spectra feature five desorption peaks before the multilayer starts forming, labeled β, γ, δ, ε, φ in Fig. 5.4. The saturation coverage ε and φ is well below 1 D_2O molecule per surface unit cell and thus these peaks are assigned to adsorpion on surface defects; further confirmation of this assignment is provided below. The saturation coverages of peaks β, γ and δ are well reproducible and the phases saturate at close to 3, 6 and 8 molecules per

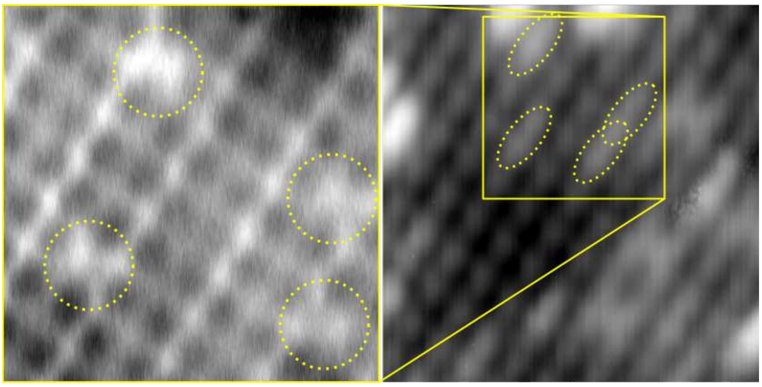

Figure 5.3: In ncAFM images acquired at 78 K, missing species corresponding to surface O atoms are observed. These are most likely not oxygen vacancies, but surface $O_{surface}H$ species; the right panel shows previously acquired STM image of a wider area. The positions of missing dark species in ncAFM image perfectly correspond to the positions of species looking identical to $O_{surface}H$ in the STM image (presence of H on the surface is observed as four brighter Fe_{oct} atoms, that is two "blobs"). Both images were acquired after desorbing the majority of previously dosed water by heating to 220 K for several minutes. Left panel: $U = 0.0\,V$, $A = 250\,pm$; right panel: $U = 1.2\,V$, $I = 0.025\,nA$.

surface unit cell. The absence of a phase saturating at 4 D_2O/uc already hints that a hydrogen-bonded network forms before all the surface cations are occupied (as there are 4 surface cations in a unit cell).

The assignment of the high-temperature peaks ε and φ is further confirmed by STM. On an as-prepared surface, a small number of $O_{surface}H$ is always present, and these species are known to recombine at elevated temperatures [75]. The resulting water desorbs in a broad peak labeled φ. Other species commonly present on as-prepared surfaces are Fe-rich defects (see Fig. 5.1). Figure 5.5B shows an STM image acquired at 78 K after a small amount of water vapor (≈ 0.05 L) was dosed at 78 K and the surface was subsequently annealed to 255 K. In this image, bright species appear on the domain boundary and on unreconstructed unit cells (highlighted by cyan arrow). Thus, the ε peak in the TPD spectra can be assigned to adsorption on Fe-rich surface defects.

Figure 5.5b shows an STM image of the $Fe_3O_4(001)$ surface after exposure to 0.1 L of H_2O at ≈ 120 K. At this temperature, far below the desorption threshold, surface mobility is low, and we observe a nonequilibrium state. The image, acquired at 78 K, exhibits isolated, bright protrusions on the Fe_{oct} rows due to adsorbed water (yellow arrow). It is not straightforward to determine whether the molecules are intact or dissociated from this image, but several water dimers are observed already at this coverage (red arrow). Interestingly, dimers have two apparent heights, so there may be two types of water dimers under these conditions. Finally, there are instances of multiple neighboring protrusions (green arrow), but it is difficult to know how much

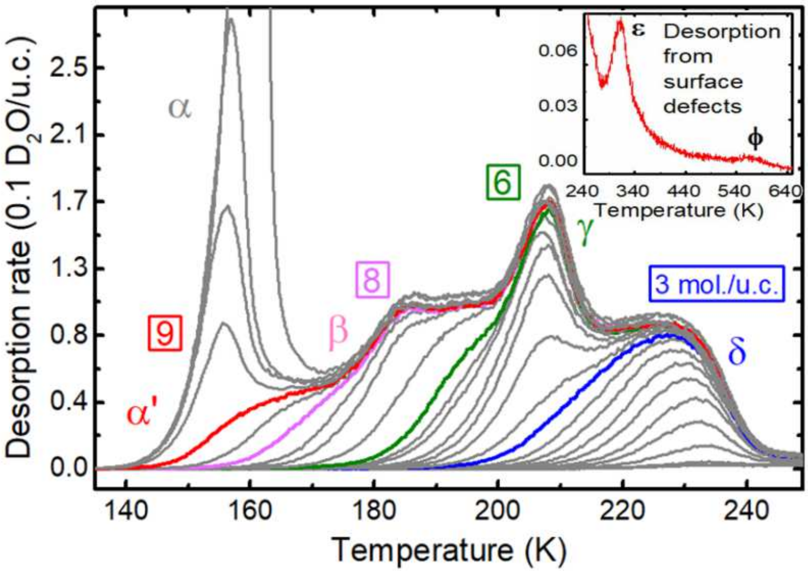

Figure 5.4: Experimental TPD spectra obtained for initial D_2O coverages ranging from 0 to 14 molecules per $Fe_3O_4(001)$–$(\sqrt{2} \times \sqrt{2})$R45° unit cell (Inset: higher temperature range showing desorption peaks ε and φ, which originate from surface defects). The colored curves indicate the coverages for which a particular desorption feature saturates. Data taken and analyzed by Jan Hulva, figure adapted from [159].

water is involved, and these could simply be two dimers. Nevertheless, this STM data suggests that water molecules can form larger agglomerates if adsorbed close to already adsorbed molecules.

Further STM and ncAFM study was conducted by two different approaches: Either a high amount of water vapor was dosed on the surface at temperatures ≤ 150 K and then the surface was gradually heated up to desorb the individual phases. Imaging at 78 K took place after each heating step. In the alternative approach, small doses of water were dosed on the clean surface at ≤ 120 K, followed by heating to ≈ 150 K to overcome any kinetic barriers needed for reaching the minimum energy structures; imaging took place at 78 K after each water dose. The first approach effectively follows the desorption behavior, the second approach probes the formation of the structures on a clean surface. In this case, the two approaches yielded qualitatively very similar results. The temperature readout on the manipulator of the LT-STM chamber is estimated to be ≈ 20 K lower than the actual temperature on the surface; in further text the quoted temperatures are corrected for this.

Figure 5.6 shows STM images acquired after dosing water vapor at ≤ 150 K and gradually heating to given temperatures. Image shown in panel (a) was taken directly after ≈ 3 L dose of H_2O at ≈ 140 K, and similar images were taken after dosing multilayers of H_2O and heating to 150 K. After this preparation, an overlayer with small patches of (2×2) or $(\sqrt{2} \times \sqrt{2})$R45° symmetry is observed (highlighted by

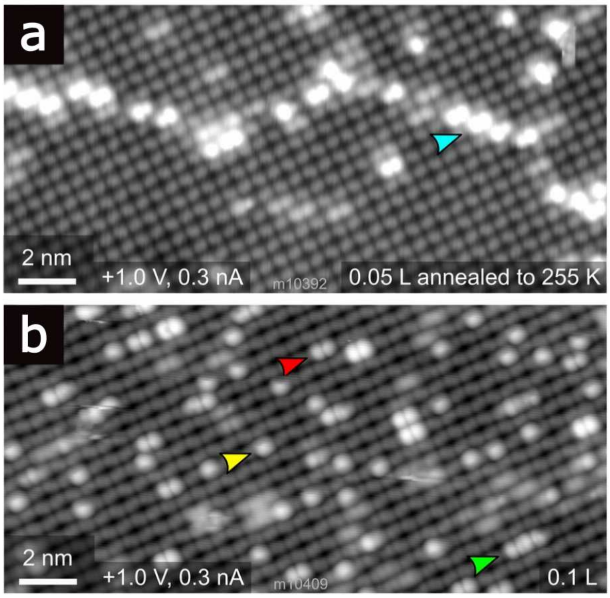

Figure 5.5: Water monomers, dimers, and multiple neighboring protrusions on the $Fe_3O_4(001)$ surface imaged by low-temperature (78 K) STM. (a) STM image acquired after 0.05 L of water was adsorbed and heated to 255 K. The surface is clean, except for protrusions located at surface defects including antiphase domain boundaries in the $(\sqrt{2} \times \sqrt{2})R45°$ reconstruction (cyan arrow). (b) STM image following adsorption of 0.1 L of water at 120 K. Isolated single protrusions (yellow arrow), double protrusions (red arrow), and multiple neighboring protrusions (green arrow) are due to water molecules adsorbed on the Fe_{oct} rows. Figure adapted from [159].

white squares in panel (a)). When the surface is heated between 160-180 K, only the Fe_{oct} rows can be resolved in the STM images; the fuzzines in the fast-scan direction indicates high tip-induced mobility of adsorbed species (panels (b,c)). After heating between 190-210 K the individual species on the Fe_{oct} can be resolved (panels (d-f)). The species are bright chains of varying length, often there is an unoccupied Fe_{oct} row between the chains. With increasing temperature the number of occupied Fe sites decreases and the majority of the chains are only two protrusions (up to four Fe_{oct} atoms) long. After heating to 220 K only a few very short chains remain, but the surface is densely packed with species looking identical to $O_{surface}H$ (panel (g)). Heating to 225 K leads to disappearance of these species, and majority of the adsorbed water is bound to defects (panel (h)).

The STM results can thus resolve the three different phases identified by TPD: The overlayer with (2×2) or $(\sqrt{2} \times \sqrt{2})R45°$ symmetry will likely correspond to the β desorption peak, the densely packed fuzzy phase would correspond to the phase desorbing in the γ peak, and the individual chains of varying length and apparent height desorb in the δ peak. What the STM cannot tell is the internal structure of these phases. Even the basic building blocks of the δ phase could be anywhere

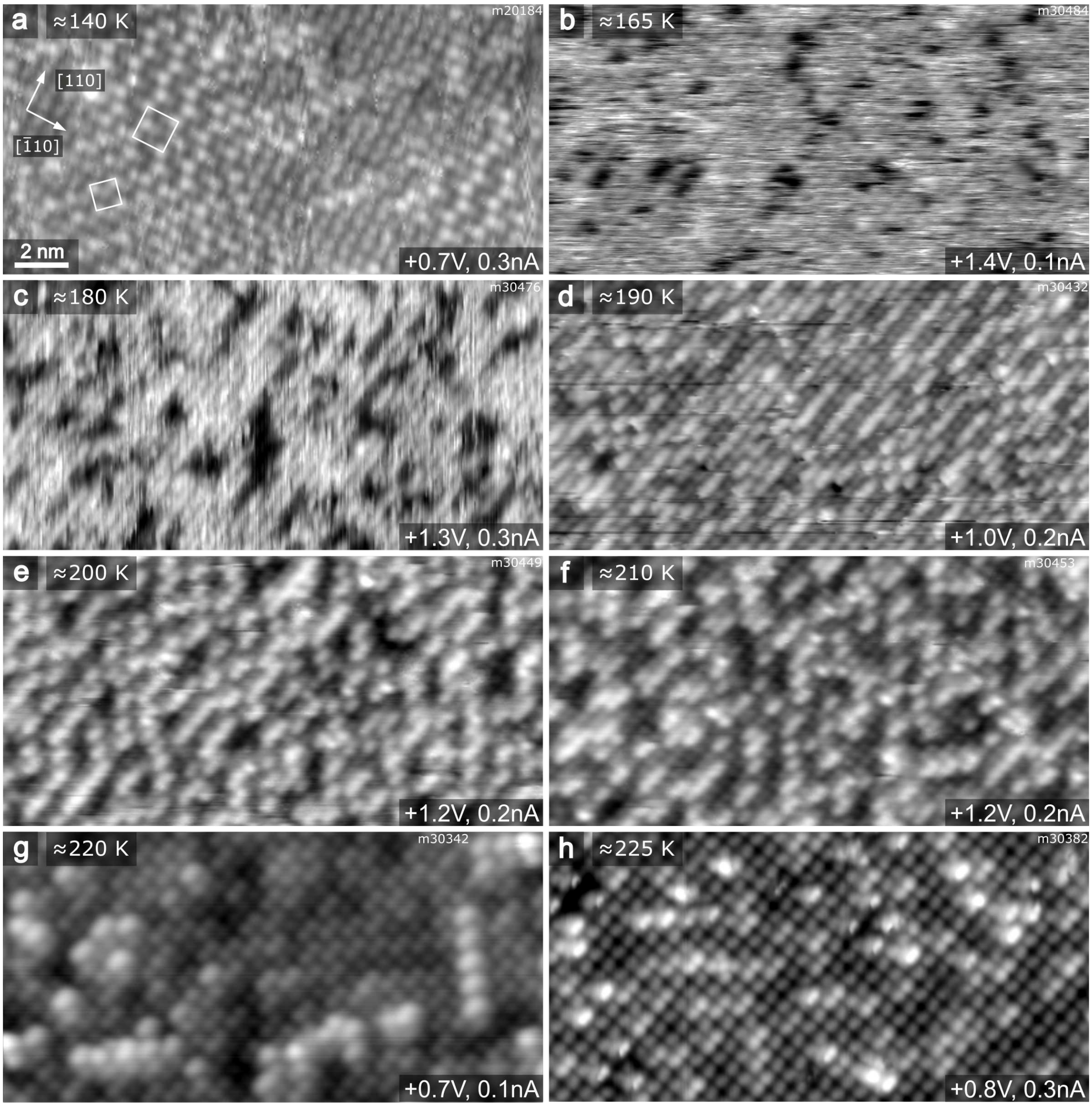

Figure 5.6: STM images of the $Fe_3O_4(001)$ after dosing H_2O vapor below 150 K and heating to given temperatures. In panels (a,c) the fast-scan direction is vertical.

between 2-4 H_2O molecules long, as the STM typically resolves the surface Fe_{oct} in pairs.

NcAFM imaging with a non-functionalized tip was attempted to resolve the internal structure of the smallest water agglomerates seen in Fig. 5.6e,f. The measured images are shown in Fig. 5.7a-c and constant-current STM images taken on the same area prior to ncAFM imaging are shown in panels (d-f). In this dataset it is clearly seen that water adsorbs on the surface and the individual water agglomerates protrude above the surface. Importantly, the interaction strength measured in ncAFM does not correlate with the apparent height observed in STM; yellow dotted circles in panels (a,d) highlight the examples of species looking alike an $O_{surface}H$ in STM, but AFM reveals these species are the same as the other agglomerates on the surface. Nevertheless, even in these ncAFM images it is very difficult to get any internal resolution of the individual species. The main reason for this is that the tip is very reactive towards the weakly bound water agglomerates, which results in frequent tip changes. No alternative ncAFM contrast was observed with non-functionalized tips on this system.

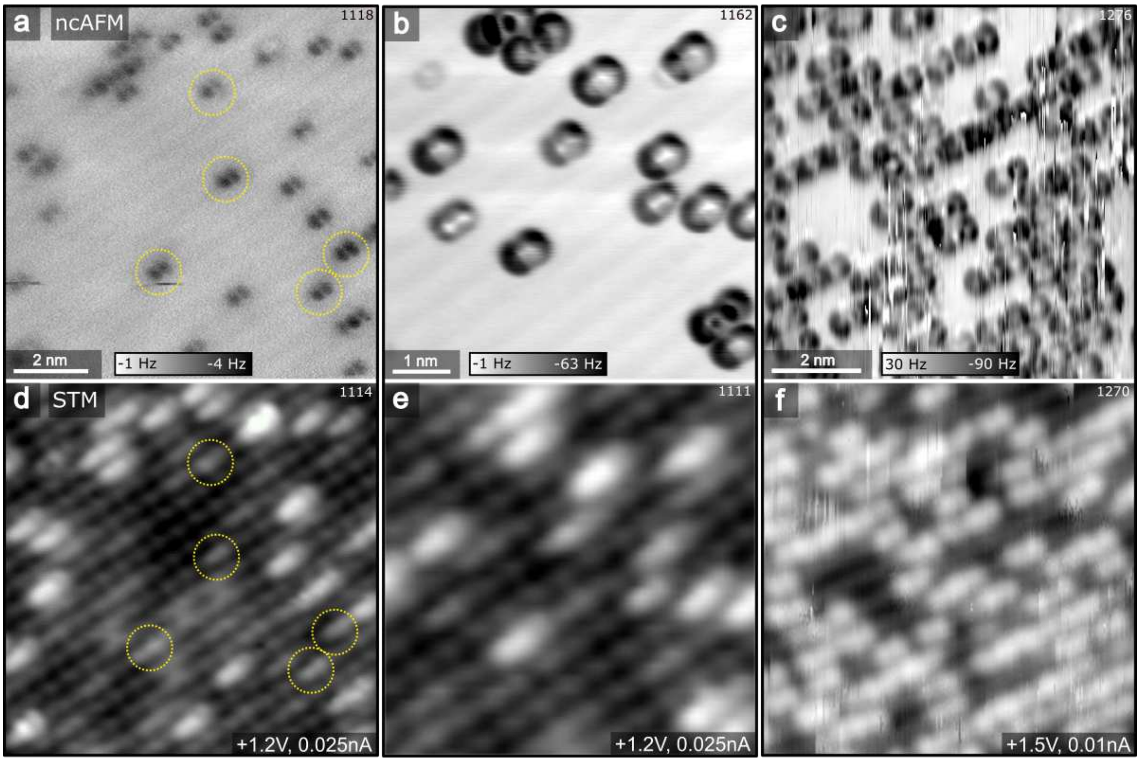

Figure 5.7: NcAFM and STM images of low-coverage H_2O on $Fe_3O_4(001)$. Panels (a-c) show constant-height ncAFM images, panels (d-f) show constant-current STM images acquired previously on the same areas. Comparison of the images acquired by the two techniques reveals that the same species in ncAFM can have greatly differing apparent height in STM imaging; dotted yellow circles in panels (a,d) highlight water agglomerates that look very similar to $O_{surface}H$ in STM images. Detailed ncAFM imaging of the water agglomerates is highly challenging because the tip interacts strongly with the adsorbed water, leading to frequent tip changes. Scanning parameters of the ncAFM images: (a) $A = 500\,\mathrm{pm}$, $U = 0.0\,\mathrm{V}$; (b) $A = 55\,\mathrm{pm}$, $U = = 0.0\,\mathrm{V}$; (c) $A = 40\,\mathrm{pm}$, $U = 0.0\,\mathrm{V}$;

NcAFM images acquired with a CO-terminated tip are shown in Fig. 5.8. In this dataset the sample was prepared by dosing given amount of water vapor at 120 K followed be heating to 150 K and imaging at 78 K. The CO tip preparation is described in section 5.2.2. Here, the contrast is greatly improved in comparison to the previously shown images, and individual water molecules can be resolved as highly localized repulsive signal (bright species). In panel (a), after $\approx 4\,\mathrm{L}$ H_2O dose, distinct species are observed on the surface, which are resolved as water dimers (red arrow) and trimers (blue arrow). Importantly, even when there is more of these species adsorbed directly next to each other on the same Fe_{oct} row, they remain separated in units of two or three water molecules with a wider gap in between. At slightly higher water coverage (panel (b), ≈6 L H_2O), the majority of the observed species are water trimers, and in areas where multiple neighboring Fe_{oct} are occupied additional molecules are bound in between the rows (yellow arrow). These additional molecules appear between the rows with $(\sqrt{2} \times \sqrt{2})$R45° periodicity, highlighted by yellow squares in panels (b-d). The water network still coexists with unoccupied Fe_{oct} sites on the surface. After a dose of ≈8 L H_2O (panels c,d) the surface is fully covered with the network occupying all the Fe_{oct} sites and additional molecules between the Fe_{oct} rows with $(\sqrt{2} \times \sqrt{2})$R45° symmetry. After a dose of ≈10 L H_2O new species appear on the surface, observed as bright species protruding above the surface (panels e,f). These species arrange in small patches with (2×2) symmetry (highlighted by green squares). At the borders of these patches these species were observed to be mobile (between subsequently acquired images), and they were also observed to be locally arranged in $(\sqrt{2} \times \sqrt{2})$R45° symmetry.

XPS spectra shown in Fig. 5.9 reveal that already at low coverages the adsorbed species are partially dissociated. In the O 1*s* region after water dosing, two additional components at 531.5 eV and 533.4 eV can be resolved apart from the main 530.1 eV component which is due to lattice O. These positions are consistent with dissociated and molecular water species found on on other oxide surfaces, respectively [160, 178]. At the coverage of 2.6 D_2O/u.c., corresponding to coexistence of dimer and trimer species observed in ncAFM data, the areas of the two fitted pseudo-Voigt components are quite comparable, which is consistent with one dissociated molecule per water dimer/trimer (as there are two O_sH species from a dissociated water molecule). When the water coverage is increased, the main signal increase is observed on the component corresponding to molecular water.

DFT computations (optPBE-DF, $U_{eff} = 3.61$ eV) were carried out by Matthias Meier to understand the water structures on the $Fe_3O_4(001)$; Figure 5.10 summarizes the most important results. Molecular adsorption of a water monomer ($E_{1,ad} = -0.64$ eV) is preferred over dissociation by 0.05 eV. However, when a dimer is formed, partial dissociation significantly stabilizes the structure ($E_{2,ad} = -0.92$ eV). This, similarly to the case of water adsorption on α-$Fe_2O_3(1\bar{1}02)$ described in the previous chapter of this thesis, is due to the so-called cooperativity effect, which seeks balance between the number of hydrogen bonds that each water molecule donates and accepts. In the case of $Fe_3O_4(001)$, however, the dissociation is also mediated by the surface reconstruction, and can only happen near the O* sites which accommodate the H^+ atom. Adding another water molecule to a dimer leads to formation of trimers which consist of two intact water molecules donating an H-bond to the dissociated molecule in between them (structure E_3 in Fig. 5.10). The DFT computations also identify an isomeric trimer with the same adsorption energy

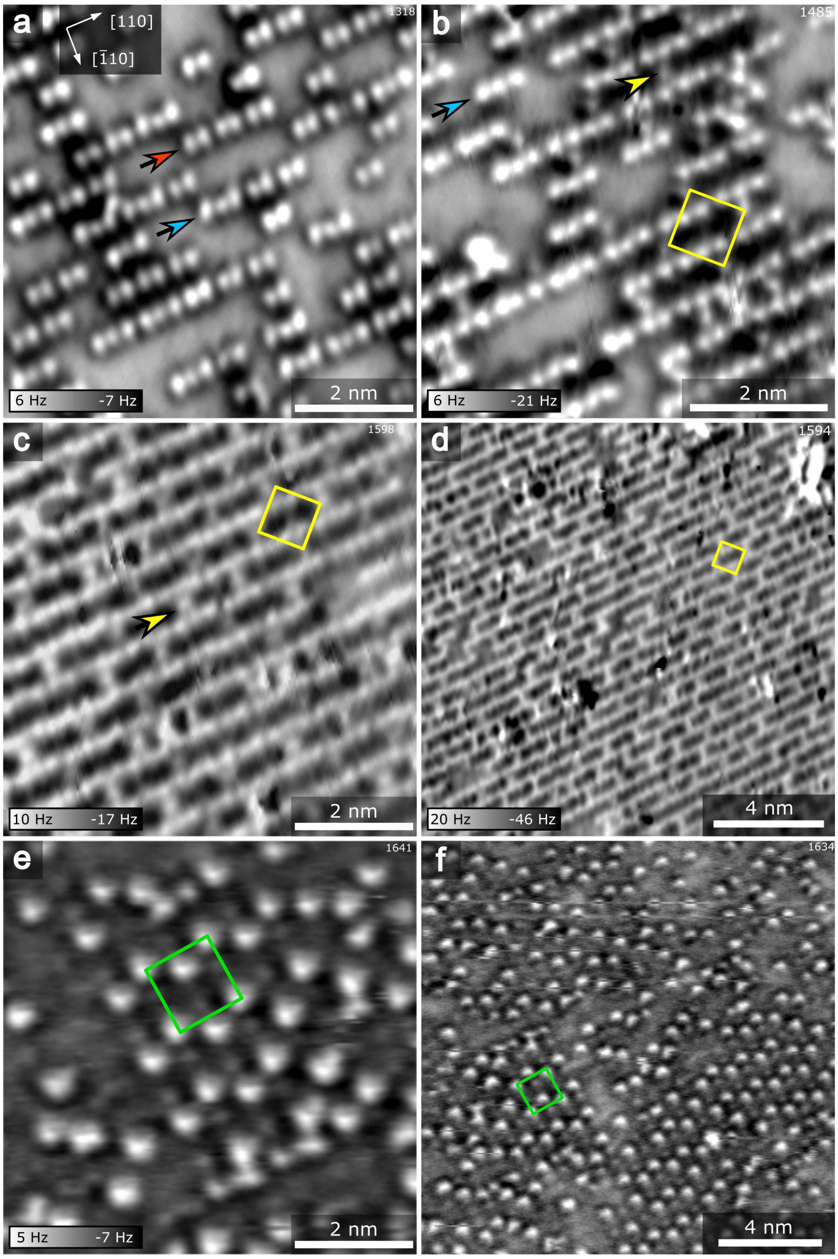

Figure 5.8: NcAFM images of H_2O on $Fe_3O_4(001)$, acquired with a CO-terminated tip. (a) After a water dose of ≈ 4 L, individual water dimers (red arrow) and trimers (blue arrow) are observed ($A = 45$ pm, $U = 0.0$ V). (b) After a water dose ≈ 6 L, additional water molecules are bound between the Fe_{oct} rows (yellow arrow), these species are arranged with $(\sqrt{2} \times \sqrt{2})$R45° symmetry (yellow squares). Some Fe_{oct} sites still remain unoccupied. ($A = 65$ pm, $U = 0.0$ V). (c,d) With increased water dose (≈ 8 L), the surface is fully covered with the $(\sqrt{2} \times \sqrt{2})$R45° water network ((c) $A = 110$ pm, $U = 0.0$ V; (d) $A = 115$ pm, $U = 0.0$ V;). (e,f) After a higher water dose (≈ 10 L) bright species appear, which protrude above the rest of the water overlayer, and are arranged in patches with (2×2) symmetry (green squares) ((e) $A = 65$ pm, $U = 0.0$ V; (f) $A = 200$ pm, $U = 0.0$ V;).

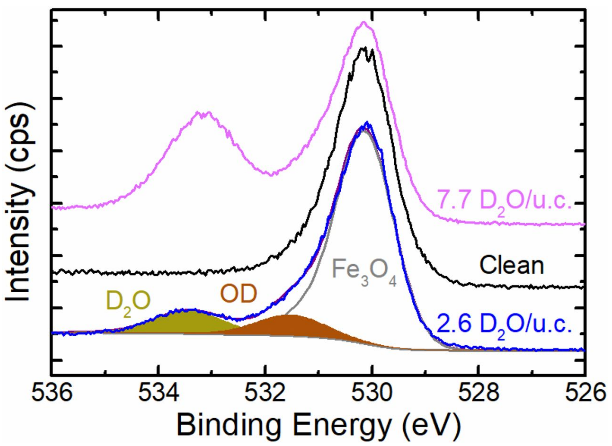

Figure 5.9: O 1*s* XPS data showing that the water agglomerates formed on Fe_3O_4(001) are partially dissociated. The as-prepared surface exhibits a single peak at 530.1 eV due to the lattice oxygen atoms. The 2.6 D_2O/u.c. corresponds to image shown in Figs. 5.6e,f and 5.8a; the XPS spectrum of this water coverage shows roughly equal contributions from OD and D_2O, consistent with one dissociated molecule per water dimer/trimer. Most of the additional water adsorbed at a coverage of 7.7 D_2O/u.c. is molecular. Data were measured at 95 K, with monochromatic Al K radiation and at a grazing exit of 80° for the emitted photoelectrons. Data taken and analyzed by Jan Hulva, figure reprinted from [159].

($E_{3,\mathrm{ad}} = -0.88\,\mathrm{eV}$), where an additional water molecules is bound via H atoms only; the molecule recieves an H-bond from the O*H and donates an H-bond to the other O* in the $(\sqrt{2} \times \sqrt{2})$R45° unit cell. This isomeric trimer species have however not been observed experimentally. In either case, electrostatic repulsion renders the adsorption of a lone H^+ at both O* sites energetically unfavorable at low coverage, and thus dissociation is limited to one molecule per $(\sqrt{2} \times \sqrt{2})$R45° unit cell. A full coverage of the trimer species identified here and observed in ncAFM imaging results in an area-averaged coverage of 3 H_2O/u.c, in a good agreement with the quantitative TPD results.

Finally, a stable structure was identified at a coverage of 6 H_2O/u.c., shown in Fig. 5.10. In this structure, all the adsorbed water molecules participate in a hydrogen-bonded network, and this network was found to be significantly more stable than other tested structures with 4 or 5 H_2O/u.c. All four Fe_{oct} sites in each $(\sqrt{2} \times \sqrt{2})$R45° unit cell are occupied by either H_2O or OH, and the rows are bridged by two additional water molecules attached solely through H bonds. In general, the structure is characterized by H_2O–OH–H_2O trimers and facilitates more ideal intermolecular bonding angles of 122–124° for intact water molecules. An attempt to computationally identify the structure formed by 8 H_2O/u.c. was made and the results were published in reference [159]. Nevertheless, this was done before the identification of the (2 × 2) symmetry observed in SPM studies and the computations were only done on a single unit cell, therefore the results likely do not present the global thermodynamic minimum.

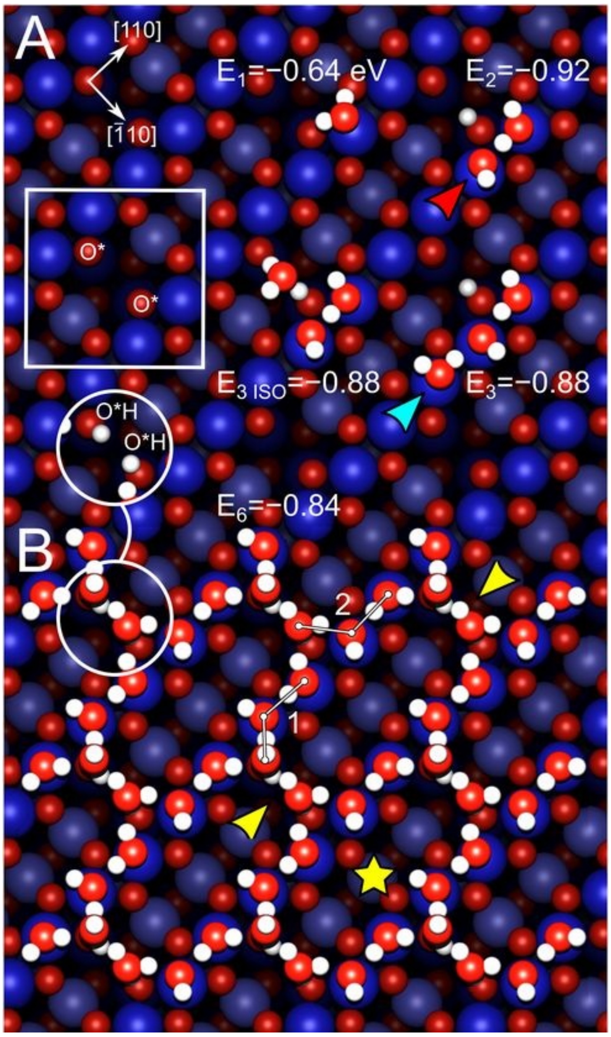

Figure 5.10: Top view of the minimum-energy structures determined by DFT for water coverages of 1, 2, 3 and 6 H_2O/u.c. Fe atoms are blue, O are red, and H are white. (A) An isolated molecule adsorbs intact, but partially dissociated water dimers and trimers are energetically preferred. Two partially dissociated trimer structures are calculated to be energetically degenerate. The $(\sqrt{2} \times \sqrt{2})R45°$ unit cell and both O* are highlighted. (B) DFT-based model at 6 H2O/u.c. showing a ring-like structure based on full occupation of the Fe_{oct} rows with OH or H_2O, and water molecules bridging the O* sites. These bridging molecules are adsorbed partly through H bonds to surface O*H groups. The O*H groups beneath the adsorbed molecules are shown in the topmost white circle. Alternatively, the structure can be viewed as based on a pair of H_2O–OH–H_2O trimers (labeled 1 and 2). Calculations carried out by M. Meier, figure adapted from [159].

5.2.1 Discussion

Water adsorption on $Fe_3O_4(001)$ was studied by STM, ncAFM, TPD, XPS and DFT computations. It was found that the most stable water species on the surface are partially dissociated dimers, which are anchored at the O* sites at the surface. Their energetic preference over a molecularly adsorbed water monomer was explained by the cooperativity effect between hydrogen and surface bonds. Partially dissociated water trimers formed by addition of an extra H_2O donating a H-bond to the dissociated OH were found to be marginally less stable (by 0.04 eV), and were commonly observed in ncAFM experiment. Longer hydrogen-bonded chains are not formed; one of the likely reasons is that the Fe-Fe distance (3 Å) is significantly longer than the O-O distances within the trimer, and so the molecular H_2O leans towards the dissociated OH in the centre of the trimer. Thus, for a longer chain to be formed, each additional water molecule would have to be tilted even more. For a water molecule adsorbed on an Fe_{oct} next to a trimer, it is much more energetically favourable to lean away from the trimer and form a separate dimer/trimer by binding to a water molecule near the next O* site along the Fe_{oct} row. DFT computations identified two isomeric partially dissociated trimer species, but only one of them has been observed experimentally. This suggests that the reliability of DFT computations on such complex systems might be limited. The computational results also indicate that it is unfavourable to adsorb an H^+ on both of the O* within the same unit cell, which limits the maximum coverage of the dimer/trimer species to one per SCV-reconstructed $(\sqrt{2} \times \sqrt{2})$R45° unit cell. The resulting maximum coverage of this phase is thus 3 H_2O molecules per unit cell, which agrees very well with the saturation coverage of the δ peak in TPD spectra.

The results presented here differ somehow from the previously published computational study of water adsorption on the same system [204, 205]. The cited work studied adsorption of 1, 2 and 4 H_2O molecules per unit cell and found that monomer adsorbs dissociatively, dimer adsorbs partially dissociated and the phase formed by 4 molecules per unit cell resembles a full coverage of the dimer species. The main reason for the differing results is the model used rather than different computational methods. The previous study assumed the distorted bulk-truncated model of the $Fe_3O_4(001)$ surface; the SCV model was unknown at the time. Since the publication of the data presented in this thesis [159], the found structures were independently confirmed by another computational approach showing very good agreement [206].

At coverages above 3 H_2O molecules/u.c., a stable hydrogen-bonded network structure was found with a coverage of 6 H_2O/u.c.. In this structure, all the surface Fe_{oct} are occupied and two additional water molecules bind via their H atoms to the surface O* sites. This results in a ring-like structure with a clear $(\sqrt{2} \times \sqrt{2})$R45° symmetry. Such a structure with molecules bridging the neighboring Fe_{oct} rows has been observed also in ncAFM images, although it was not possible to resolve that it is two water molecules forming each such bridge. The ring-like network is consistent with the "2D ice rules": Water forms closed-loop structures in which most of the molecules sit atop a cation site and both accept and donate a hydrogen bond; double-acceptor molecules are buckled up from the rest. The coverage of 6 H_2O/u.c. correlates perfectly with the saturation coverage of the γ peak identified by TPD.

At higher coverages, STM and ncAFM experiments identify additional species protruding above the existing water network. These species are relatively mobile during SPM scanning at 78 K, but tend to arrange in patches with (2×2) symmetry. The (2×2) pattern was later confirmed by temperature-programmed LEED study of water adsorption on $Fe_3O_4(001)$ thin films carried out in collaboration with group of H-J. Freund [192]. The (2×2) LEED spots appear after multilayer is desorbed and their disappearance correlates with desorption of the β TPD peak.

These results provide understanding of the initial stages of water adsorption on $Fe_3O_4(001)$. It was found that the surface structure governs water adsorption at all coverages before the multilayer adsorption. First the "special" O* sites anchor small partially dissociated water agglomerates, and then, before all the surface cation sites are occupied, a complex cooperatively-stabilized hydrogen bonded network forms. A question worth addressing is how these results relate to water adsorption at conditions relevant for applications. An ambient XPS study carried out by Kendelewicz et al. shows that almost no water adsorbs at room temperature at pressures lower than 10^{-4} Torr [179]. Above 10^{-2} Torr, signal corresponding to both dissociated and molecular water grows simultaneously, indicating that cooperative interactions take place. These results correspond very well to the presented findings in UHV. Recently, a combined STM, XPS and LEED study after exposure to liquid water was published, revealing that long-term exposure to liquid water induces structural changes to the $Fe_3O_4(001)$ surface. These changes are irreversible at room temperature, and were interpreted as a growth of an Fe-OH hydroxide phase, which is limited by the coverage of surface O*H species [12].

5.2.2 CO-tip preparation

The ncAFM tip was functionalized by picking up a CO molecule from Pt clusters deposited on the measured $Fe_3O_4(001)$ surface. The detailed procedure was the following: A submonolayer coverage of Pt was deposited on the surface, followed by heating to 550 K for 10 min to form large Pt clusters, which are far apart on the surface. This step must be done carefully, as increased temperature or prolonged annealing might lead to growth of a thin oxide film over the clusters, making them inert to CO [207]. Then, several Langmuir of CO was dosed on the surface at room temperature. This preparation leads to a surface with a few Pt clusters covered with CO and large areas of clean surface in between. It is known from previous TPD studies that CO on Pt clusters is stable up to 500 K [203].

The surface with well separated CO-covered Pt clusters can be studied in the same way as the clean surface. Water vapor can be dosed at low temperature in the same way as described before. This way, a reservoir of CO molecules is located just tens of nanometers from the measured surface and the tip can be re-functionalized at will.

The CO molecule can be picked up by scanning, bias pulsing or z-movement poking over the Pt cluster. A simple constant-current STM scan proved to be the easiest way to functionalize the tip with a high success rate. In ncAFM mode it is easy to see whether the tip if CO-terminated or not: when scanning over the Pt clusters, individual CO molecules should be seen as strong localized repulsive signal. Tips prepared this way can resolve individual water molecules as localized repulsive signal; this has been observed on all three iron oxide surfaces studied in this thesis. Similarly, when using non-functionalized tips, a similar contrast has not been observed on any of the three surfaces.

When the system is used to prepare CO-tips for measurements on a different sample, it is more convenient not to sinter the Pt by thermal annealing and leave it monodisperse prior to CO dosing. This is because the appearance of many CO-covered Pt clusters resembles images acquired with a double tip and since no two clusters look the same (see Fig. 5.11b), it is hard to assess the quality of the tip. It is also possible to use Rh or Ir instead of Pt, which bind CO very strongly as well. Images of characteristic Ir and Rh carbonyls are shown in Fig. 5.11c and discussed in section 6.2 of this thesis; images of characteristic Pt carbonyls are shown and discussed in references [80, 203].

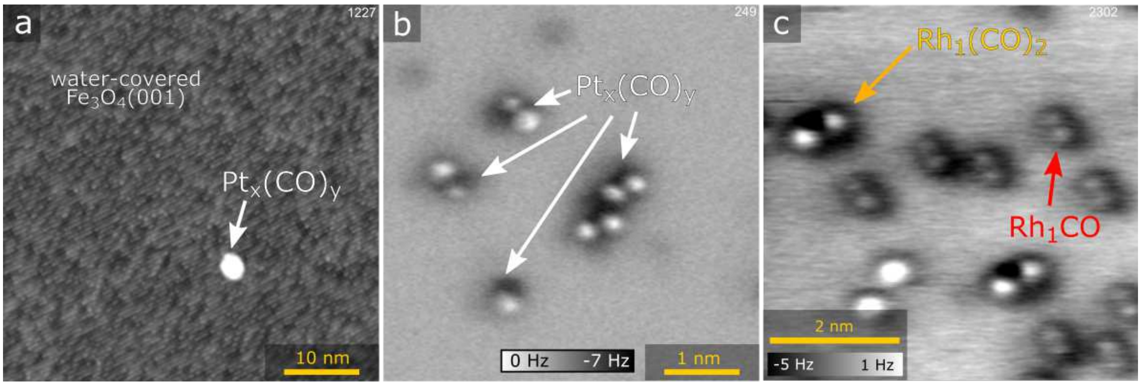

Figure 5.11: Preparation of a CO tip on $Fe_3O_4(001)$. (a,b) CO-covered Pt clusters with large areas of clean $Fe_3O_4(001)$ surface in between serve as a reservoir of CO for tip-functionalization. The areas of $Fe_3O_4(001)$ surface can then be easily studied with a CO-terminated tip. In panel (a), the surface is covered with 4 L H_2O; images shown in Fig.5.8 were acquired this way. (b,c) In ncAFM it is easy to recognize that to the CO-tip functionalization was succesful. When imaged with a CO-tip, localized circular protrusions are observed on the Pt clusters due to repulsive interaction between the CO on the cluster and CO on the tip. Nevertheless, it is difficult to recognize whether there is only one or more CO molecules on the tip. (c) When the $Fe_3O_4(001)$ is used only as a sample to prepare CO-tip on, it is easier to use single-atomic carbonyl species which are much better defined. Panel (c) shows well-defined RhCO and $Rh(CO)_2$ species; detailed discussion of their appearance is provided in section 6.3 of this thesis. (a) $U = 1\,V$, $I = 0.01\,nA$; (b) $A = 70\,pm$, $U = 0.55\,V$; (c) $A = 100\,pm$, $U = 0.0\,V$

5.3 Pristine $Fe_3O_4(111)$

The same experimental approach was used to study water adsorption on $Fe_3O_4(111)$. The experiments were carried out on an $Fe_3O_4(111)$ single crystal prepared by 1 kV Ar^+ sputtering and annealing to 930 K, with every second to tenth annealing step being done in a partial pressure of O_2. The last annealing step was done in O_2, followed by short (5 min) annealing in UHV. This recipe has led to Fe_{tet1}-terminated surfaces, although the quality of the surfaces varied somewhat, most likely depending on the history of the crystal. Figure 5.12 shows the model of the Fe_{tet1} termination and typical filled- and empty-states STM images. The 6 Åperiodicity observed in STM images corresponds to the spacing of the surface Fe_{tet} atoms. In all experiments, there is always a certain number of point defects whose appearance is strongly dependent on the bias voltage and condition of the tip. In empty-states images (panel b) the point defects often look quite homogeneous and it is tempting to interpret the missing protrusions as Fe_{tet} vacancies. Nevertheless, the empty-state image acquired on the very same surface (panel c) shows that there are multiple different point defect species which look alike in filled states images. In images acquired at 78 K (panel d) the concentration of point defects was lower, suggesting some of them might be due to adsorption from residual gas (which is almost non-existent when the sample is in the cryostat, as most of the molecules adsorb on the cryostat shields before they reach the sample). Lastly, panels (e,f) show simultaneously acquired constant-height STM and ncAFM images showing that even point defects looking the same in empty-states STM images can have different origins. The ncAFM image reveals that while one of the two alike-looking species could be due to a missing Fe_{tet} (yellow circle), the other one clearly origins from a different species adsorbed on top Fe_{tet} site or substituting an Fe_{tet} (magenta circle).

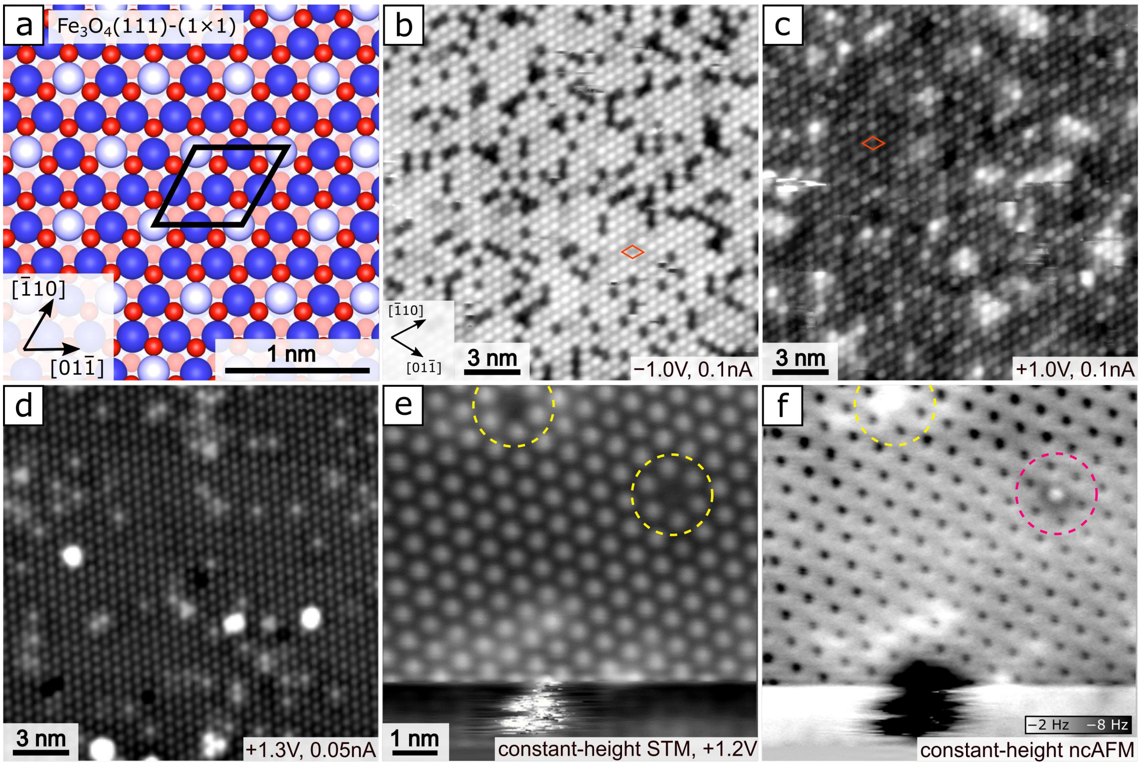

Figure 5.12: The “regular” Fe_{tet1} termination of the $Fe_3O_4(111)$ surface. (a) Top view on the surface model. The Fe_{tet}, Fe_{oct} and O atoms are drawn as light blue, dark blue and red balls, respectively. (b,c) Typical filled-states (b) and empty-states (c) STM image of the $Fe_3O_4(111)$ surface, both images acquired on the same surface. (d) An empty states image acquired at 78 K. (e,f) Constant-height STM and ncAFM images acquired simultaneously at 78 K. The highlighted point defects looking the same in STM are quite different in ncAFM. Room temperature STM images shown in (b,c) provided by F. Kraushofer.

Small variations in the sample preparation can result in formation of slightly reduced or oxidized phases on the Fe_{tet1} surface. When the surface is cooled down in a low partial pressure of O_2, this results in formation of small triangular terraces on the surface, presumably of an oxidized phase (Fig. 5.13a). The required O_2 partial pressures are very low, as such triangles have been observed even on surfaces cooled down pressures in the 10^{-9} mbar range. On reduced surfaces, patches of an alternative phase with honeycomb appearance are observed (Fig. 5.13b), which were previously interpreted as an Fe_{oct2} termination [90]. Alternatively, on reduced surface patches the so-called bi-phase can be observed coexisting with the Fe_{tet1} terminated surface (Fig. 5.13c) [92].

NcAFM imaging of the triangular species observed after oxidation was attempted, one of the images shown in Fig. 5.14a after simple contrast adjustment (top) and after high-pass filtering (bottom). The image shows that the triangular species are physically higher than the Fe_{tet1} terminated surface, and shows hints of their internal structure. However, more experiments need to be done to hypothesize about the exact atomic arrangement. NcAFM image of an Fe_{oct2} terminated area is shown in Fig. 5.14b.

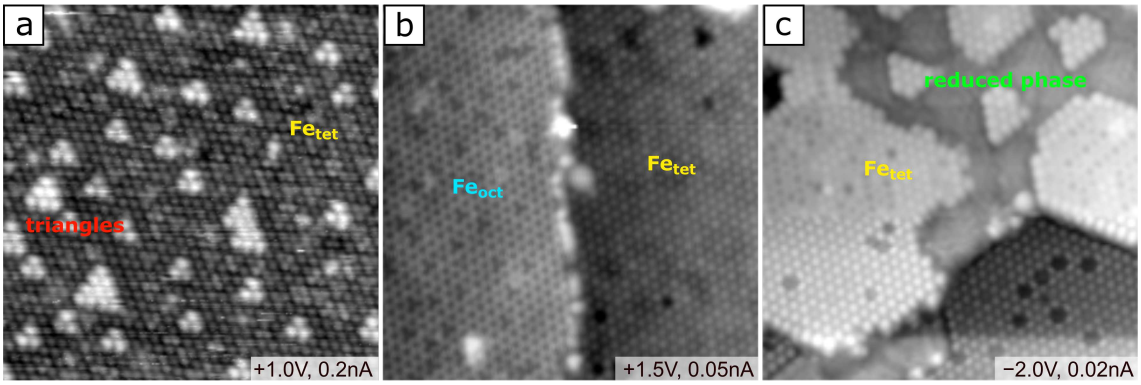

Figure 5.13: The alternative phases coexisting with the the Fe_{tet1} terminated $Fe_3O_4(111)$ surface with small variations of the surface preparation. (a) Small triangular species were observed when the surface was cooled down in a low (residual) partial pressure of O_2 (b) On slightly reduced surfaces, patches with honeycomb structure can be observed. These were previously interpreted as an Fe_{oct2} termination [90]. (c) On more reduced surfaces, phases resembling the so-called bi-phase are observed [92]. Image in panel (a) was measured by F. Kraushofer.

Grazing emission XPS spectra acquired after oxidizing the surface for 2 h and then cooling to 550 K before evacuating the O_2 show prevalence of Fe^{3+} near the surface (Fig. 5.15). Flashing to 930 K in UHV changes the situation and a low binding-energy shoulder appears in the Fe $2p$ region, indicating presence of Fe^{2+}. The Fe $2p$ region then stays the same even after 10 cleaning cycles without oxidation, even though in STM experiments such preparation typically leads to patches of Fe_{oct2} or bi-phase. No significant changes are observed in the O $1s$ region.

NcAFM images reveal that there are additional species commonly present on top of the clean Fe_{tet1} surface at 78 K. These species are highly mobile with applied bias, which makes them invisible in STM; figure 5.16a-e shows ncAFM and simultaneously acquired STM images acquired with varying bias voltage. With no applied bias (panel a) the species are immobile and well-resolved in ncAFM. When a −0.5 V bias is applied (probing filled states) the species become mobile, but still visible

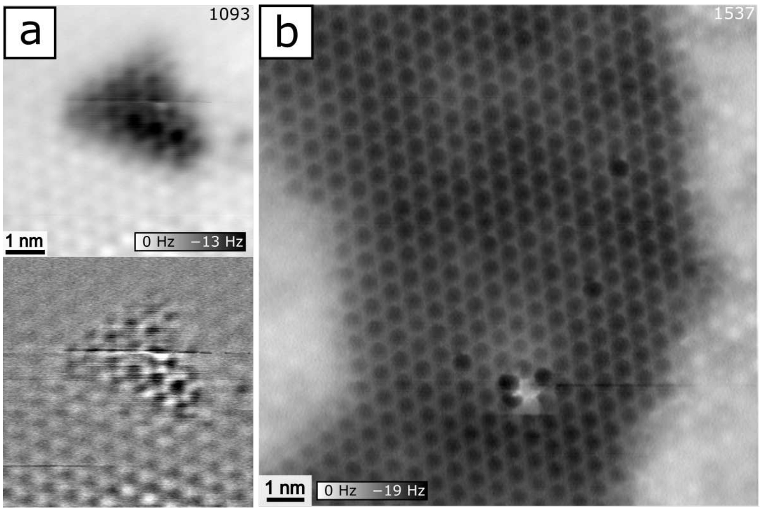

Figure 5.14: NcAFM images of structures appearing on the Fe_{tet1} after oxidation and reduction. (a) An ncAFM image of the tringular species appearing after oxidation. The top panel shows the image after simple contrast adjustment, the bottom panel shows the high-pass filtered image. Hints of internal structure are observed, but the atomic arrangement is unclear. (b) An ncAFM image of an Fe_{oct2} surface.

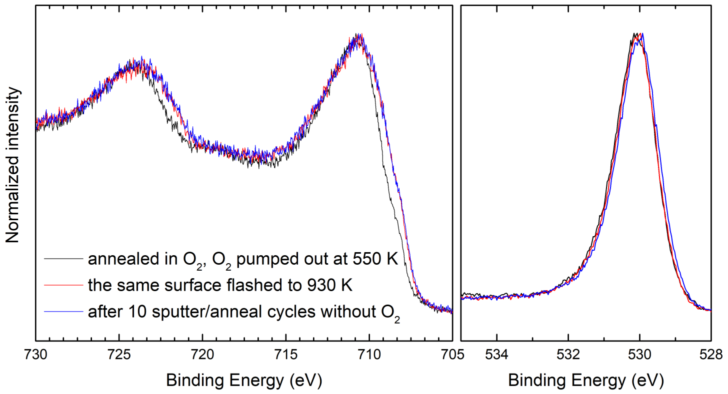

Figure 5.15: Grazing emision XPS spectra (70° from surface normal) taken after different surface preparations. When the surface is cooled down in O_2 background, the Fe $2p$ region indicates majority of Fe^{3+}. Simple flashing to 930 K in UHV induces increase of Fe^{2+} signal. Spectra taken after 10 cycles without oxidation look almost identical to the ones after flashing, even though this preparation typically leads to reduced surface in STM experiments.

in ncAFM. The corresponding STM image resolves the cation lattice with varying contrast; areas occupied by the unknown species are resolved best (panel b). Upon increasing the bias voltage to -0.8 V (panel c) the species are highly mobile, which results in fuzzy image in both ncAFM and STM. STM only resolves individual features on the borders of previously unoccupied areas. At -1.5 V (panel d), ncAFM resolves the cation lattice; in STM the contrast is inverted to previous cases and areas previously unoccupied by the unknown species are resolved best. When the polarity of the bias voltage changes, both the ncAFM and STM images perfectly resolve the cation lattice (images taken with +1.5 V sample bias, panel e). An ncAFM image taken subsequently without any bias voltage show the same immobile species as panel (a), although at different positions (not shown). Panels (f-j) show the same ncAFM images as panels (a-e), but with superimposed (1×1) grid. This shows that the new species sit atop the cation sites and rarely occupy two directly neighboring sites. The commonly observed nearest-neighbor distance is 10.4 Å, a full coverage of an overlayer with this spacing would result in a $(\sqrt{3} \times \sqrt{3})$R30° pattern. Small patches of such pattern are indeed observed in image shown in panel (g) (overlayer unit cell highlighted in red), and weak extra spots corresponding to $(\sqrt{3} \times \sqrt{3})$R30° are also seen in the FFT of this image (not shown).

The additional species were observed after various surface preparations. Figure 5.17 shows representative STM images of slightly reduced and slightly oxidized surfaces, on both of which these species were observed, albeit on the oxidized surface the number of these species was lower. Flashing of the surface to ≈ 700 K didn't seem to have significant effect on the species concentration.

Summary and discussion

The surfaces prepared by the given recipe are predominantly terminated by an Fe_{tet1} layer. The STM images, especially the ones taken at 78 K indicate that the prepared surfaces can be locally of very high quality. STM and ncAFM imaging reveals that there is at minimum three types of common defects, one of them is likely Fe_{tet1} vacancies. By analogy to Fe_3O_4(001), one of the other defect types could presumably be surface hydroxyls, as a small amount of water adsorbs on the surface above room temperature [89]. Such assignment would be also consistent with the fact that much less species were observed when the surface was measured in the Q+ chamber where water vapor is efficiently pumped by the cryostat. The exact assignment of individual points defect on the surface is nevertheless very difficult by STM, as the appearance is strongly dependent on bias voltage and tip condition.

NcAFM identifies additional species, which are highly mobile with applied bias, and thus are invisible in STM imaging. It is currently unclear whether these are adsorbates from the residual gas or intrinsic surface defects. The species were observed both on slightly reduced and slightly oxidized surfaces, thus it is unlikely that they would present initial stages of surface oxidation/reduction. Flashing the surface to ≈ 700 K did not lead to lowering the surface concentration of these species, which might indicate that these are not adsorbates. Nevertheless it is possible that these species adsorb on the surface when the still warm sample is inserted into the cryostat, causing desorption from the sample stage. If these species are adsorbates, a good candidate molecule would be CO, which is known to adsorb atop cation sites and the observed $(\sqrt{3} \times \sqrt{3})$R30° pattern might easily origin from repulsive interactions

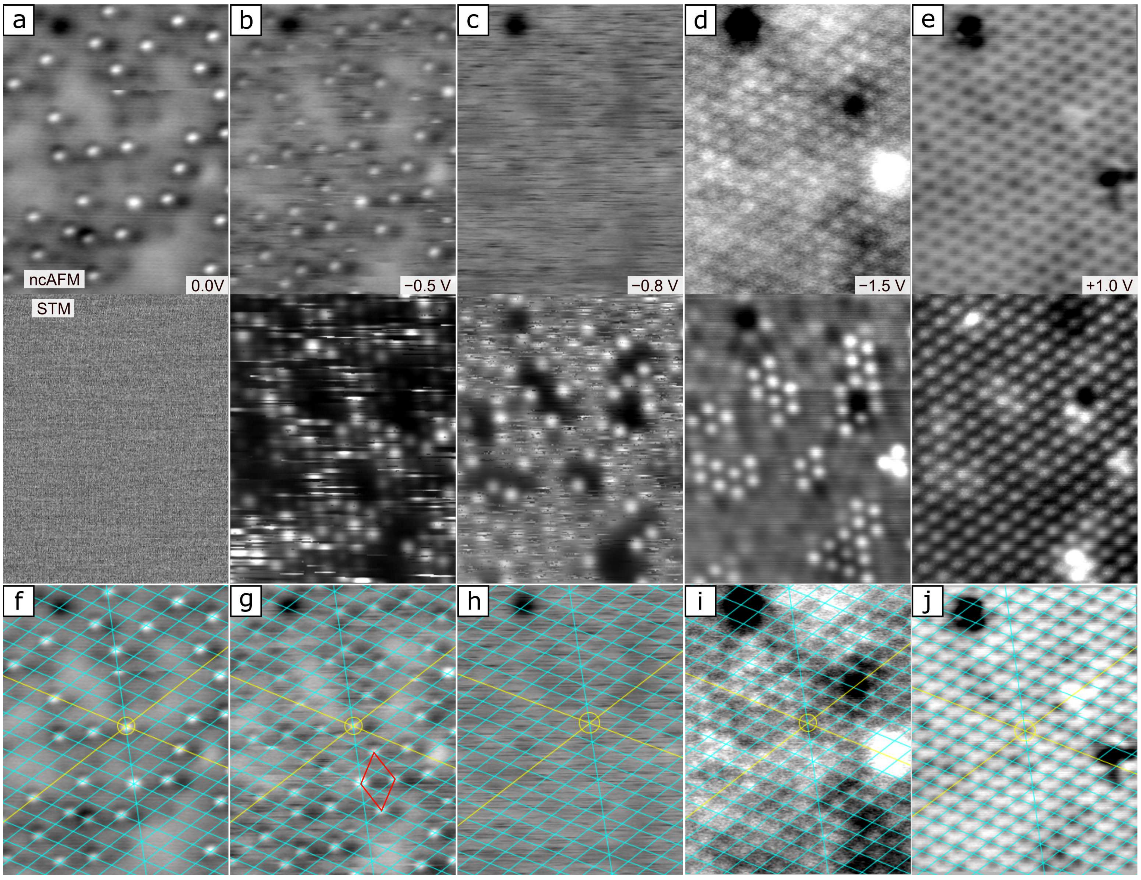

Figure 5.16: NcAFM imaging of the mobile species observed on the Fe_{tet1} surface. (a-e) ncAFM (top) and STM (bottom) images of the same spot on the surface with varying bias voltage between $-1.5\,V$ and $+1.0\,V$. Only at bias voltage close to $0\,V$ the additional species are visible. With increasing bias voltage, the species become mobile and both ncAFM and STM images resolve the Fe_{tet1}. (f-g) The same ncAFM images with superimposed (1×1) grid. The local $(\sqrt{3} \times \sqrt{3})R30°$ ordering is highlighted by the red unit cell in panel (g).

between neighboring molecules, similarly to what was observed on $Fe_3O_4(001)$ [208]. Further experiments to confirm or disprove this hypothesis should be done by dosing CO stepwise directly into the cryostat.

When the surface is cooled down in low O_2 background pressure (below 10^{-8} mbar), characteristic triangular species are observed on the surface. When the O_2 background pressure is higher ($5 \cdot 10^{-7}$ mbar) during cooling to 550 K, then XPS indicates majority of Fe near the surface is in 3+ oxidation state. Simple flashing to 930 K in UHV changes the Fe $2p$ region and leads to an increase of Fe^{2+} near the surface. Previous STM work has shown than even prolonged annealing does not lead to disappearance of the triangular species, but rather to their coalescence [209], therefore it is likely that the surface prepared by cooling in $5 \cdot 10^{-7}$ mbar O_2 presents an oxidized phase other than the small triangles.

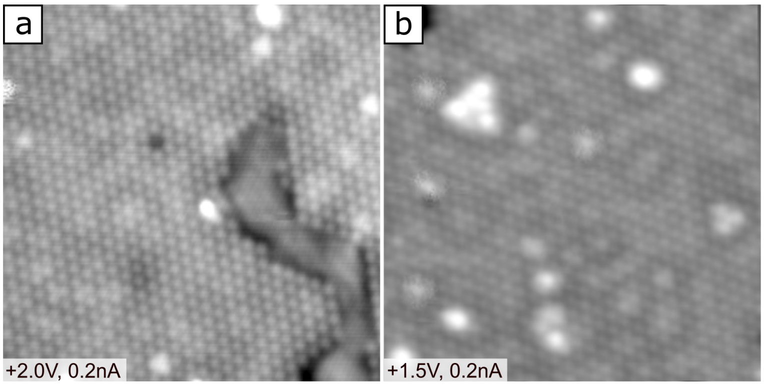

Figure 5.17: Representative STM images of surfaces on which the additional species shown in Fig. 5.16 were observed. Image shown in pane (a) shows patches of reduced surface, image in panel (b) was prepared by annealing the surface shown in (a) in $5 \cdot 10^{-7}$ mbar O_2 for an hour. This surface features triangular species characteristic of surface oxidation.

When the surface is prepared by a few cleaning cycles without oxidation, patches of reduced surfaces are observed. The structure previously identified as Fe_{oct2} termination was imaged ny ncAFM, and the appearance in ncAFM is similar to STM. NcAFM imaging of the more reduced phases with bi-phase ordering was not attempted.

5.4 Water Agglomerates on $Fe_3O_4(111)$

Water adsorption on an Fe_{tet1} terminated $Fe_3O_4(111)$ surface was studied by TPD, XPS, STM, and ncAFM with a CO terminated tip. Figure 5.18 shows D_2O TPD spectra acquired on the $Fe_3O_4(111)$ after surface preparation corresponding to Fe_{tet1} surfaces. Similarly to the case of $Fe_3O_4(001)$, there are multiple desorption peaks saturating before the multilayer growth. The individual desorption peaks, labeled β, γ and δ, are highlighted by blue, green and pink colors in Fig. 5.18 and saturate at $\approx$1.5, 2 and 3 D_2O/uc. Between $\approx$260-400 K, the trailing edge of the highest desorption peak shows multiple small shoulders, labeled δ', δ'' and ε. The last desorption peak, φ, has its maximum at $\approx$ 550 K, as shown in the inset of Fig. 5.18. It is likely that this peak corresponds to dissociative water adsorption on surface defects; it also has very similar characteristics to the peak observed on $Fe_3O_4(001)$ at the same position.

STM and ncAFM measurements were carried out to image the species desorbing in the ε peak. Figure 5.19 shows characteristic triangular species that appear on the surface after dosing water at room temperature. Panel (a) shows large-scale STM image acquired at room temperature after dosing $\approx$3 L H_2O; the image features an intermediate coverage of new monodisperse species not observed on the surface prior

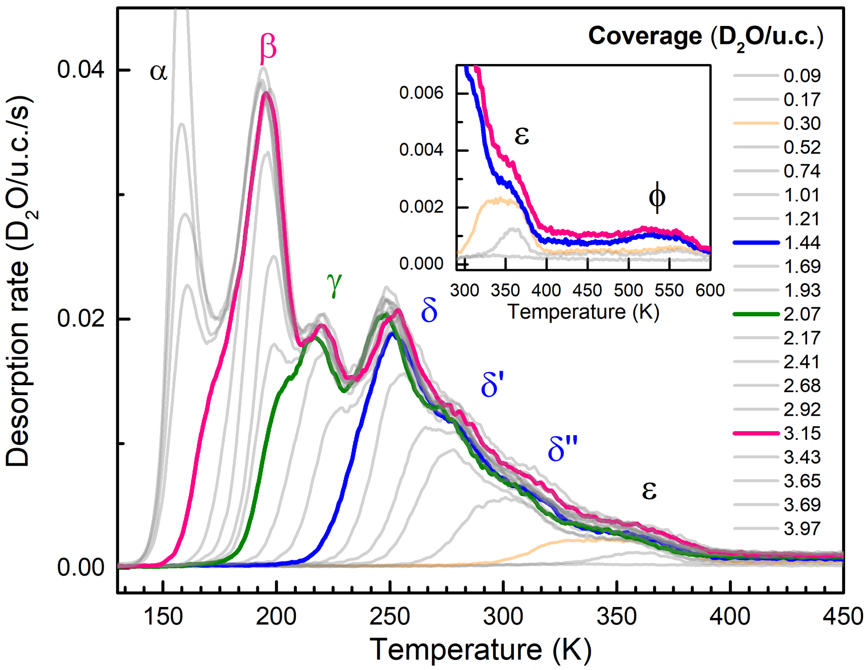

Figure 5.18: Experimental TPD spectra obtained for initial D_2O coverages ranging from 0 to 4 molecules per $Fe_3O_4(111)$–(1×1) Fe_{tet1} unit cell (Inset: higher temperature range showing desorption peaks ε and φ). The colored curves indicate the coverages for which a particular desorption feature saturates.

to water dosing. A detailed STM image acquired at 78 K after H_2O dose at 150 K and subsequent heating to 300 K is shown in panel (b). Panel (c) shows a ncAFM image acquired with a CO-terminated tip on the highlighted area in (b). In both STM and ncAFM the new species are clearly resolved as triangular species. While the triangular appearance in STM image might be due to a single species which affect the electronic structure of three neighboring Fe_{tet} cations, the ncAFM shows that each triangle actually consists of three species. Panel (d) shows two ncAFM images acquired on the same spot with tip-sample distance different by ≈ 40 pm; the comparison shows that in both cases the triangles look very symmetric. The dark point in the middle of the triangles observed at lower tip-sample distances is most likely due to attractive tip interacion with the three species forming the triangle rather than attractive interaction with an extra species in the middle. Lastly, panel (e) shows the same image as panel (d), but with a superimposed grid aligned with the single bright spots on the surface, which most likely correspond to positions of Fe_{tet} cations. The grid points are well aligned also with the bright spots forming the triangular species indicating that the triangles are likely formed by three species sitting atop Fe_{tet} and possibly leaning towards the center of the triangle.

In most experiments the coverage of the triangular features was between 0.03 and 0.05 triangles per surface unit cell. This was observed in both RT-STM and

Q+ chambers, regardless of whether the 3 L water was dosed at room temperature in RT-STM setup or at low temperature before heating to room temperature in the Q+ chamber (although the coverage the measured in the Q+ experiments might be less representative, as the larger-scale images also featured a small number of $Pt_x(CO)_y$ clusters for CO-tip preparation). If every triangle consisted of three water molecules, this would result in coverages between 0.09 and 0.15 H_2O/uc. These values correspond reasonably to coverages measured in TPD experiments, which show that at 300 K the surface can stabilize ≈ 0.30 D_2O/uc (curve highlighted by orange in Fig. 5.4). This number however also contains the broad φ peak which is likely due to adsorption on surface defects. When the orange TPD curve is integrated between 300-400 K, a coverage of 0.16 D_2O/uc is found, which agrees well with the coverage observed in STM.

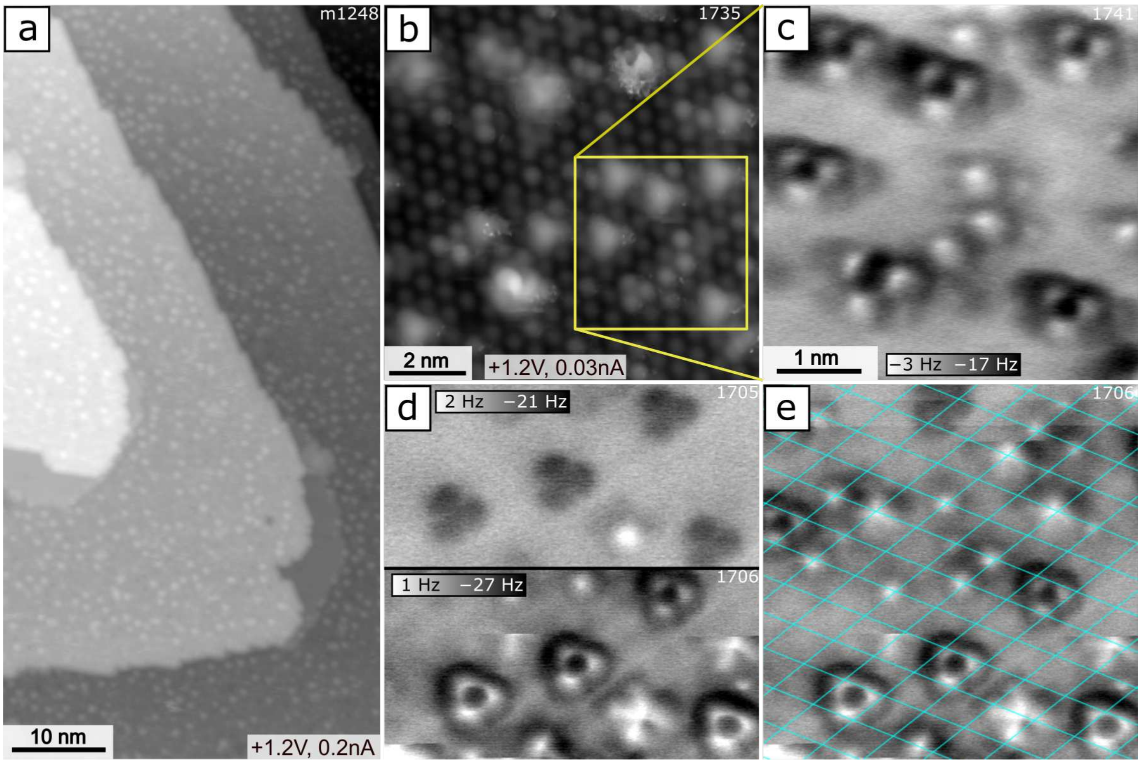

Figure 5.19: STM and ncAFM characterization of water species, which are stable on $Fe_3O_4(111)$ at 300 K. (a) A room temperature STM image acquired after dosing 3 L H_2O. This image was acquired by F. Kraushofer. (b,c) Low-temperature (78 K) STM and ncAFM images acquired with a CO-terminated tip. In both STM and ncAFM the species are clearly triangular. (The brightest species seen in panel (b) is likely a $Pt_x(CO)_y$ cluster.) (d) Comparison of two ncAFM images acquired on the same spot at different tip-sample distance (≈ 40 pm lower in the bottom panel). (e) An ncAFM image overlaid with a hexagonal grid aligned with isolated bright species on the surface, which presumably correspond to positions of Fe_{tet}. The grid points are well-aligned with the bright points of the triangles. All ncAFM images were taken with $U = 0$ V, $A = 100$ pm.

Phases formed by higher coverage of water on $Fe_3O_4(111)$ were studied by STM and ncAFM at 78 K. Figure 5.20a shows an STM image acquired at 78 K after dosing 3 L H_2O at 200 K and heating to 250 K. While the image clearly indicates the presence of adsorbates, it is impossible to say anything about their structure and STM scanning induces mobility. Figure 5.20b shows an STM image acquired after dosing another 7 L H_2O at 180 K. Here, the mobility of adsorbed species is lower and it can be seen that the species arrange in a (2 × 2) pattern (the (2 × 2) unit cell highlighted in red).

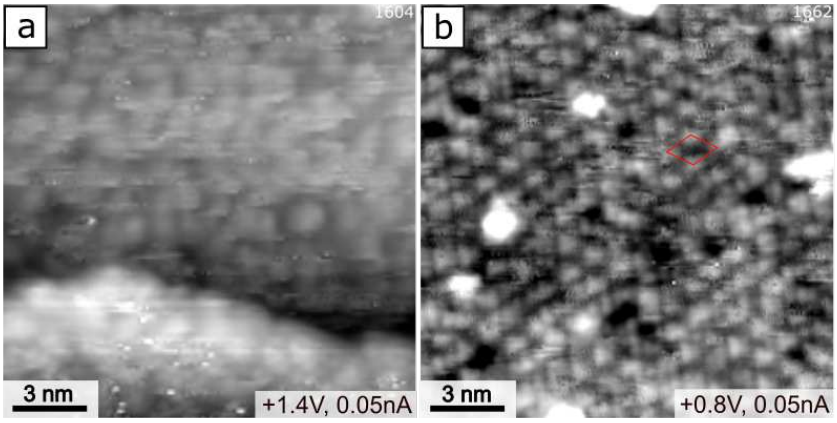

Figure 5.20: STM imaging of phases formed by water on $Fe_3O_4(111)$. (a) Image acquired at 78 K after dosing 3 L H_2O at 200 K and heating to 250 K. (b) After dosing another 7 L H_2O at 180 K. Here the adsorbed species arrange in (2 × 2) pattern; the (2 × 2) unit is highlighted in red.

Figure 5.21 shows ncAFM images of water structures on $Fe_3O_4(111)$ acquired with a CO tip at 78 K. In panel (a), the sample was prepared by dosing 3 L H_2O and subsequent heating to 160 K, and the ncAFM imagle clearly resolves specific well-defined agglomerates, highlighted by yellow and green ovals. Assuming each circular bright species corresponds to a water molecule, the agglomerates highlighted by yellow consist of six species and are observed in three different orientations due to the symmetry of the surface. The agglomerates highlighted by green consist of four species and have a three-fold symmetry. At slightly higher coverage, shown in panel (b) the individual agglomerates are observed linked together, as highlighted by cyan color. This image was acquired in a separate experiment after dosing 3 L H_2O at $\approx$ 200 K. Panel (c) shows the same surface as panel (a), but the image was acquired on an area previously scanned by STM. The STM imaging induces water mobility on the surface and the subsequent ncAFM images thus shows disrupted structures that are metastable at this coverage. Here, a clear trend is observed where the individual water hexamers link to other water species by formation of structures resembling incomplete hexagonal rings (highlighted by white arrows). The image also features small clover-shaped dark species, highlighted by a red circle. Panel (d) shows the same image as panel (c), but with an overlaid (1 × 1) grid and brightness/contrast adjustment, so that faint dark points corresponding to surface Fe_{tet} are visible on the clean surface areas. The grid position is aligned with the Fe_{tet} and the image shows that the outer molecules of the hexamers sit atop Fe_{tet}. Additionally, it shows that the clover-shaped features are centered around an Fe_{tet}, therefore these are different species from the triangles observed at room temperature.

This data thus shows that the dominant species at lower coverage are isolated water agglomerates consisting of six water molecules arranged in a specific shape, in which the outer molecules sit atop four neighboring Fe_{tet} cations and the two inner molecules sit in between. These species are most commonly observed isolated, and the highest possible coverage of such isolated species is one hexamer per a (2 × 2) cell. This translates to 1.5 H_2O/uc, which is in excellent agreement with the 1.44 D_2O/uc found in TPD as a saturation coverage of the δ peak. In reality, the ordering of the water hexamers is not ideal, and comparison of panels (a) and (b) in Fig. 5.21 suggests that water tetramers form in areas where it is sterically not possible to fit an isolated hexamer. In areas with locally higher water coverage the species were found to be linked together. In image shown in panel (b) of Fig. 5.21 the water coverage was analyzed by counting of individual water molecules, resulting in a coverage of ≈ 1.4 H_2O/uc; this data thus likely show a representative image of a surface prior to desorption of a δ TPD peak.

Figure 5.22 shows two CO-tip ncAFM images of a higher-coverage water phase. The surface was prepared in conditions which should lead to saturation of the γ TPD peak (7 L H_2O at 180 K (panel a) or 6 L H_2O at 160 K (panel b,c)). The ncAFM can clearly resolve individual agglomerates which are arranged in a superstructure with a (2 × 2) symmetry. The long-range ordering is clearly seen in panel (a), a detailed image with a grid overlay is shown in panel (b). The images shown in Fig. 5.22b,c show multiple different water agglomerates: Some of them clearly originate from the species previously observed at lower coverage, as they feature structures resembling the linked hexamers (highlighted by cyan), others look like complete or incomplete hexagonal rings (green circle). The dominant species, however, are the species highligted by yellow circle which are formed by water molecules arranged in a shape resembling paired angle brackets (⟩⟩). Similarly to the previously observed hexamers (Fig 5.21a), these contain six water molecules, are observed in three orientations due to the symmetry of the surface, and arrange in a (2 × 2) pattern. However, as discussed previously, isolated hexamers arranged in a (2 × 2) pattern can only add up to a maximum coverage of 1.5 H_2O/uc and indeed, by counting the individual bright points in Fig. 5.22c, a coverage of ≈ 1.6 H_2O/uc is found. Thus, it is not clear why the observed structure should be significantly different from the ones observed previously (Fig. 5.21b), notwithstanding the fact that the preparation conditions should lead to a significantly higher coverage (γ TPD peak saturates at 2.07 D_2O/uc). However, upon closer inspection of a detailed image shown in 5.22c,

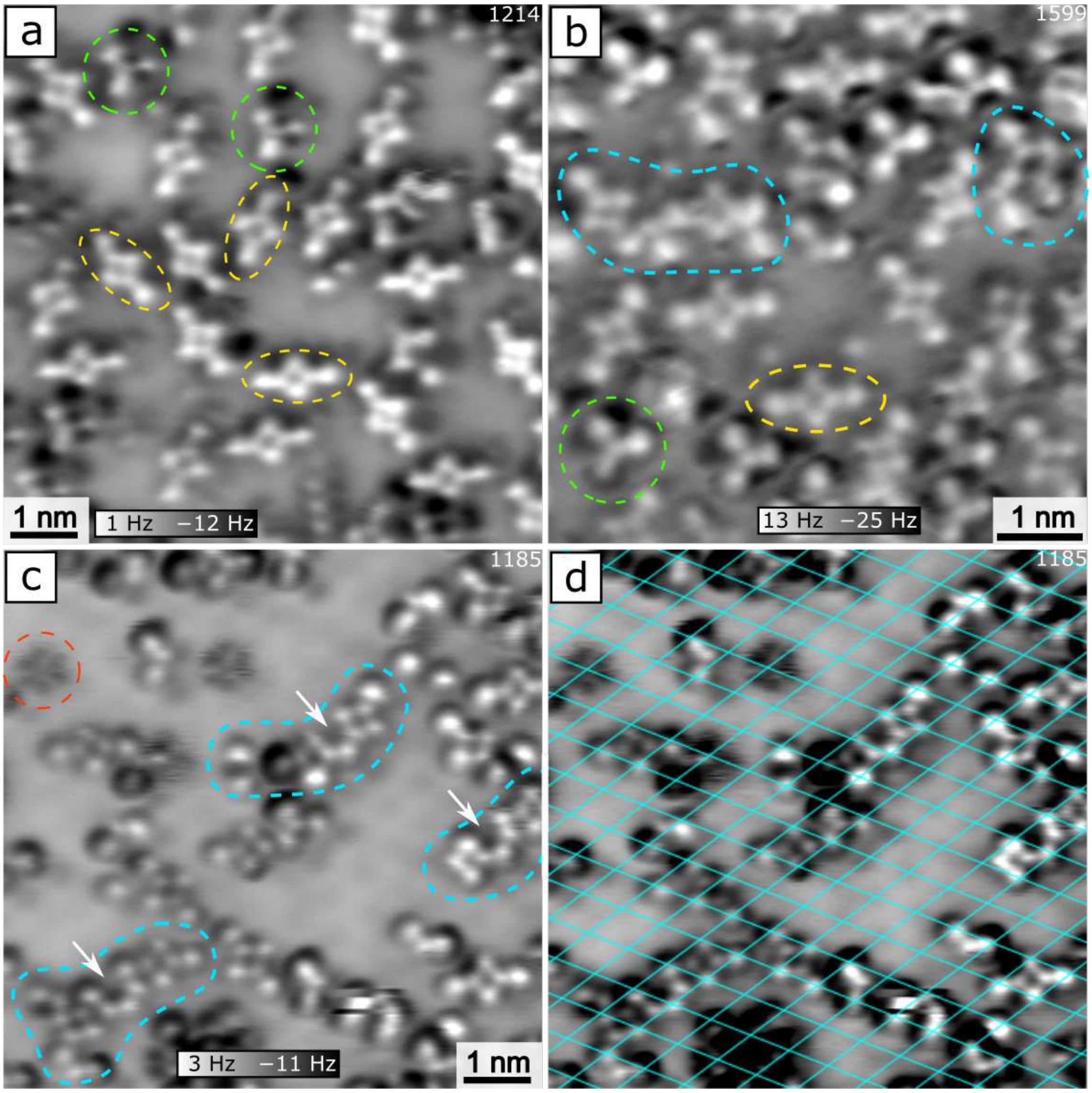

Figure 5.21: NcAFM images (CO tip, 78 K) of a phase formed by $\approx 1.5\,H_2O$/uc. on an Fe_{tet} terminated $Fe_3O_4(111)$. (a) At lower coverage, the dominant species are well-defined water hexamers (yellow). Additionally, a small number of water tetramers is observed (green). (b) When the coverage is slightly increased, the species link together (cyan). (c,d) A ncAFM image acquired on an area prevously scanned with STM, which induces water mobility on the surface. The image thus shows metastable configurations with locally increased coverage coexisting with areas of clean surface. The water hexamers are found to link together by formation of incomplete hexagonal rings (white arrows). Additionally, a low number of small clover-shaped species is observed (red). (d) The same image with a grid ovelay. The grid is aligned to the surface Fe_{tet}, showing that the outer molecules of the hexamers reside atop the Fe_{tet}.

one can resolve additional faint features in between the individual agglomerates, the right side of panel (c) shows the relevant areas highlighted by red circles with adjusted brightness/contrast so that the fainter features are better visible (original image is shown on the left). In each of the highlighted areas, three additional spots are found between the individual agglomerates. Notably, in all cases where the additional spots are observed, at least two of the surrounding brighter agglomerates are of the bracket-shaped type. Thus it seems likely that formation of the bracket-shaped agglomerates allows accomodation of three additional water molecules in spaces between the agglomerates. Assuming a full coverage of such network, this would lead to a maximum coverage of 2.25 D_2O/uc, which is in reasonable agreement with the 2.07 D_2O/uc found in TPD. Counting all the spots including the fainter ones in 5.22c leads to a coverage of ≈ 2 D_2O/uc.

XPS was used to find whether the water phases are formed by intact, dissociated or partially dissociated water. Figure 5.23a shows the O 1s region of grazing emission XPS spectra acquired at 140 K after dosing varying amounts of water on the Fe_3O_4(111) between 90-120 K. The spectrum corresponding to water coverage of ≈ 2.9 D_2O/uc was taken in a separate experimental run with slightly different sample position and the surface possibly being slightly reduced (as discussed at the end of this section). The XPS spectra show that above 0.3 D_2O/uc water adsorbs in a mixed mode; the components corresponding to both molecular ($\approx$ 533.4 eV) and dissociated ($\approx$ 531.4 eV) water are clearly resolved in spectra corresponding to doses of 0.7 D_2O/uc and above. At the lowest coverage (0.3 D_2O/uc), the situation is not that clear, as the water-related signal is very low. The presence of low coverage water phase is clearly indicated by the change of the O 1s peak shape and maximum position which is shifted by ≈ 0.1 eV in comparison to the clean surface (panel (b)), and this change is reversible with water desorption. Nevetheless, based on this data it is very difficult to say whether the adsorbed water is dissociated or molecular. At higher coverages, fitting of the spectra corresponding to water coverages of 0.7, 1.4 and 1.9 D_2O/uc with three pseudo-Voigt peaks indicates that in all cases there is a majority of molecular D_2O ($\approx 55\,\%$ molecular D_2O at 0.7 and 1.4 D_2O/uc; $\approx 66\,\%$ molecular D_2O at 1.9 D_2O/uc).

The experimentally observed structures were modelled by DFT computations done by Matthias Meier; some of the tested models are shown in Fig. 5.24. The computations are still an ongoing project; this paragraph thus provides more of a progress report rather than finished work. Before describing the individual water structures it is instructive to look again at the clean surface, shown in panel (a). The unit cell highlighted in yellow; the dotted yellow circles highlight two different sites inside the unit cell. One of these sites is atop a surface O atom, the other one is in between three surface O atoms. The lowest experimentally observed phase was small triangles formed by three species sitting atop neighboring Fe_{tet} cations; the triangles are thus centered around one of these two highlighted sites. The DFT results however show that any sort of triangular arrangement of three molecules is less stable than the previously reported partially-dissociated water trimer shown

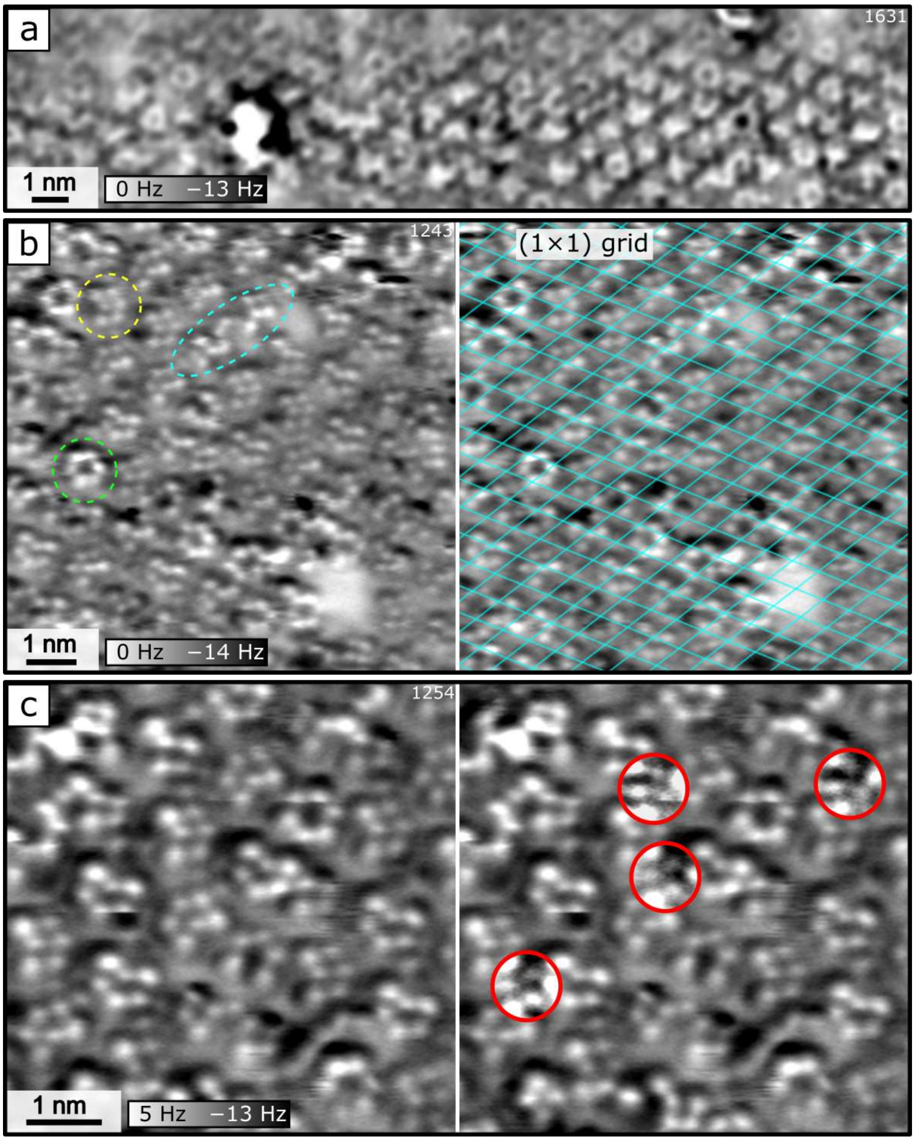

Figure 5.22: NcAFM images (CO tip, 78 K) of a phase formed by $\approx 2\,H_2O$/uc. on an Fe_{tet} terminated $Fe_3O_4(111)$. (a) The images clearly show long-range ordering which is seemingly formed by equidistantly spaced individual water agglomerates. (b) High-resolution images reveal that the individual agglomerates are of various types. Many agglomerates feature complete or incomplete hexagonal rings (green), but the dominant species are formed by six water molecules arranged in a shape resembling paired angle brackets (⟩⟩); highlighted by yellow. Similarly to previous observations at lower coverage, some species were clearly formed by linking of individual water hexamers (cyan). The same image with a (1 × 1) grid shown on the right, indicating the agglomerates arrange in a (2 × 2) pattern. (c) Detailed images reveal that there are additional water molecules stabilized in between the bracket-shaped hexamers. The left panel shows the original image, the right panel highlights the areas in which three additional species are observed.

in panel (b) [89, 210]. As the experimental evidence for triangular agglomerates is very convincing, alternative structures involving modification of the Fe_{tet} surface

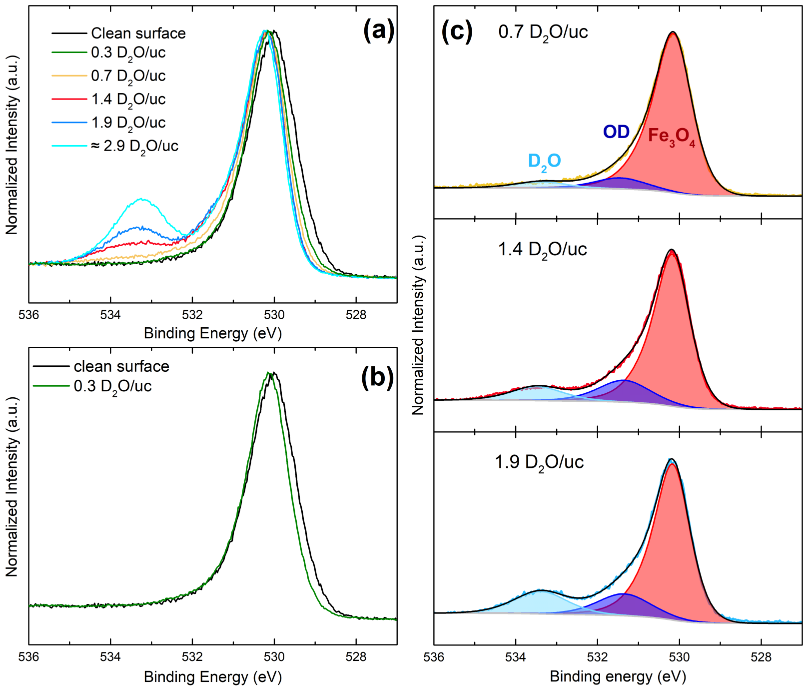

Figure 5.23: Grazing emission XPS spectra (monochromated Al Kα; 67° from surface normal) acquired on $Fe_3O_4(111)$ after dosing various amounts of D_2O. All the spectra are normalized on maximum, the data was taken at 140 K after water dose between 90-120 K. (a) At coverages above $\approx$0.3 D_2O/uc, components corresponding to both molecular ($\approx$ 533.4 eV) and dissociated ($\approx$ 531.4 eV) water are resolved. (b) A clean surface spectrum compared to a dose of $\approx$0.3 D_2O/uc. The O 1s peak shape changes, but the higher binding energy components are not resolved. The change is reversible with water desorption. (c) Fitting of the O 1s region with three components indicates that at 0.7 and 1.4 D_2O/uc there is $\approx$ 55 % molecular D_2O; at 1.9 D_2O/uc there is $\approx$ 66 % molecular D_2O.

were considered. One of such structures is shown in panel (c), where an additional Fe_{oct} resides on top of the surface, centering a water triangle. On a surface with an extra Fe cation, this structure is favourable in comparison to a partially-dissociated trimer, but it can be easily argued that this is mainly due to the instability of an extra Fe cation on a pristine Fe_{tet} surface. Alternative models were considered for the water triangles which keep the stoichiometry of the clean surface; one of the concepts was cation migration ($Fe_{tet} \rightarrow Fe_{oct} + Fe_{tet,vacancy}$). But even in these preliminary calculations, the energy gained by forming a triangular agglomerate around an Fe_{oct} barely compensated the energy loss caused by the formation of an $Fe_{tet,vacancy}$; the previously reported water trimer still remains the most stable structure found by DFT at this water coverage. Panel (d) shows one of the considered models for experimentally identified water hexamers. This structure utilizes concepts from both structures (b,c); it essentially consists of two partially-dissociated water trimers, one of which is of the same kind as shown in (b). The other trimer, however, lacks the surface O atom to which the molecular water can bind via a H-bond, and thus an extra Fe_{oct} was considered as a site for the molecular water adsorption. Again, multiple ways to create the extra Fe_{oct} were considered and the preliminary energy trends are very similar to the case of a trimer. On a stiochiometric Fe_{tet} surface, this hexamer structure is less stable than the previously reported water network. The situation changes when an extra Fe_{oct} is introduced to the surface, but it is not clear where the Fe_{oct} might come from.

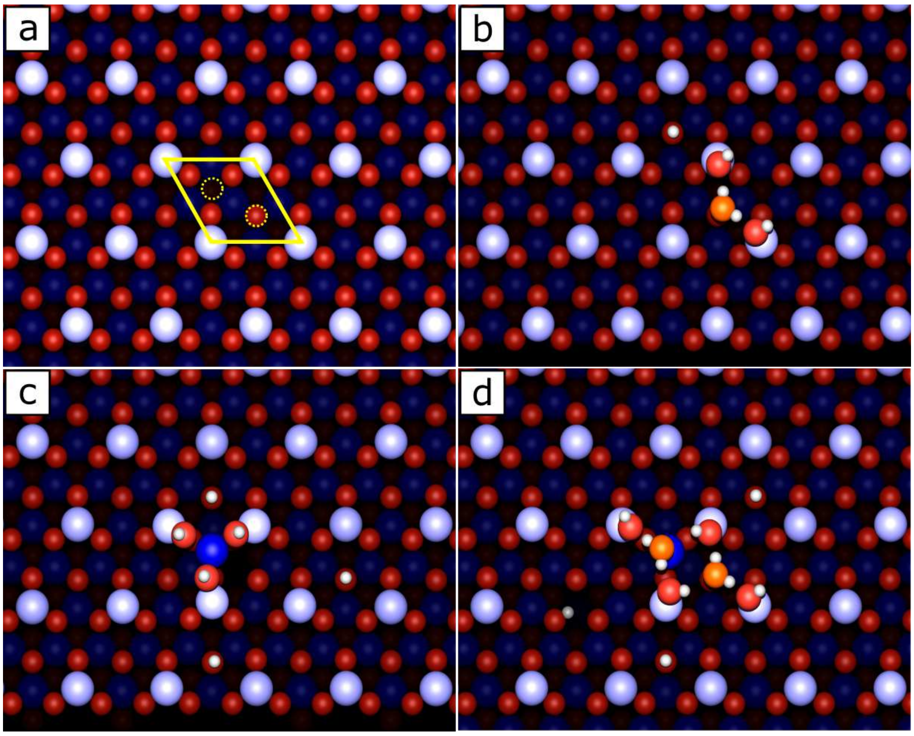

Figure 5.24: Structures considered for modelling water adsorption on $Fe_3O_4(111)$. (a) The clean Fe_{tet} terminated surface. The unit cell is highlighted by yellow, the dotted circles highlight two inequivalent sites within the unit cell. (b) The most stable trimer structure as identified by DFT. This structure was first reported in [89] (c) The experimentally identified trimer structure formed by three species sitting atop neighboring Fe_{tet} cations. The DFT computations suggest such structure can only be stable with the presence of an extra Fe_{oct} cation. (d) Model considered for the water hexamer. The hexamer consists of two partially-dissociated trimers. One of these trimers is the same as shown in (b), the other one is stabilized by an additional Fe_{oct} cation. In this model, the Fe_{oct} was taken from a surface Fe_{tet} site to keep the stoichimetry. Preliminary calculations were carried out by M. Meier.

Effects of different surface preparation

Figure 5.25 shows comparison of D_2O TPD spectra taken after different surface preparations. In the left panel, the shown spectra correspond to surfaces prepared by ten cleaning cycles without oxidation (orange) and after 20 min long oxidation (purple). The comparison shows that these two prepatations lead to very similar water TPD spectra. The middle panel shows a TPD spectrum of a surface prepared by cooling down to 550 K in an O_2 background before evacuating (blue). This spectrum looks vastly different from the other spectra, as it features only one major desorption peak with a shoulder and a long high-temperature tail. The yellow spectrum was taken after flashing the same surface to 930 K directly after acquisition of the blue spectrum. Lastly, the spectra in the right panel were taken after nominally the same preparation, but in a different experimental run. The green spectrum seems to feature desorption peaks at the same positions as the yellow spectrum, but these desorption peaks are present in different ratios to each other. This spectrum did not significantly change upon prolonged reduction or oxidation. The reason for the different appearance currently remains unclear; one possible reason is that the surface was reduced due to the high number of cleaning cycles over the sample history. Nevertheless, the sample reduction was not evidenced by XPS and LEED pattern also did not feature any floretting spots which would indicate presence of extended bi-phase terminated areas.

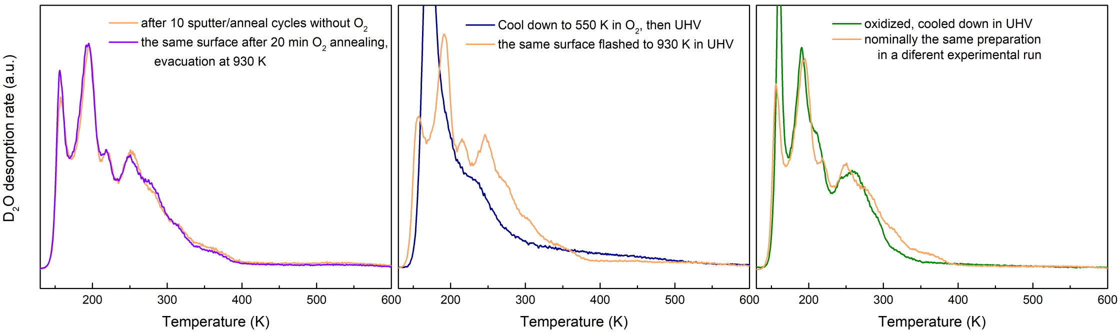

Figure 5.25: Water TPD spectra taken after different surface preparations.

5.4.1 Summary and Discussion

Water adsorption on $Fe_3O_4(111)$ was studied using TPD, STM, ncAFM and XPS, the experimental data were complemented by preliminary DFT calculations. The TPD and ncAFM data show that water adsorbs in the form of isolated water agglomerates up to the coverage of 1.5 D_2O/uc, and the individual agglomerates arrange in a (2×2) pattern. Above the coverage of 1.5 D_2O/uc the individual agglomerates restructure, which allows them to link together and accomodate additional water molecules. XPS data clearly show that the agglomerates as well as the submonolayer network are partially disociated. The saturation coverages of the lower-coverage phases agree very well in quantitative TPD and ncAFM analysis.

The ncAFM provides compelling evidence of the individual water agglomerate structures, but such structures were not confirmed to be the most stable in DFT computations as long as pristine, defect-free Fe_{tet} terminated surface is assumed. Starting at the phase stable at room temperature (ε peak in TPD), STM and ncAFM images clearly show that this phase is formed by three species sitting atop neighboring Fe_{tet} cations. At room temperature this phase saturates between 0.09 and 0.15 D_2O/uc, which agrees well with the TPD results indicating saturation coverage of 0.16-0.30 D_2O/uc. Nevertheless, in DFT calculations a triangular arrangement of three water molecules is unstable against formation of partially dissociated water trimers identified in a previous study [89, 210]; such species were however not observed experimentally. One way to make the triangular species more stable in DFT calculations is by introducing an extra Fe_{oct} cation on the surface, but it is not clear where such surface modification would come from in experiment.

Moving on to the higher coverage phase, the ncAFM reveal agglomerates formed by a very specific arrangement of six water molecules. The maximum coverage of these hexamers adds up to 1.5 D_2O/uc, which is in agreement with the saturation coverage of the δ peak found in TPD (1.44 D_2O/uc). DFT modelling of such structure suggests that such structure can only be stable with an additional cation, otherwise the previously reported water network is energetically favourable [89, 210]. When the water coverage increases, the individual water hexamers link together and eventually restructure to a different shape, which seems to allow accomodation of additional molecules in the empty spaces between the hexamers. A full coverage of such network would result in water coverage of 2.25 D_2O/uc which is in reasonable agreement with the saturation coverage of the γ peak found in TPD (2.07 D_2O/uc).

While the disagreement between the experiment and theory is displeasing, the experimental datasets presented in this thesis are remarkably consistent both with each other and with the works previously published in the group of H.-J. Freund [89, 210]. In the cited literature, water adsorption on $Fe_3O_4(111)$ thin films was studied using TPD, temperature-programmed LEED (TP-LEED), IRAS and DFT computations. The reported TPD spectra look very similar to the ones showed here, and the TP-LEED data show that the (2 × 2) ordering appears after desorption of the multilayer and is still weakly visible at the δ peak maximum at 255 K, above which a (1 × 1) pattern is observed. This agrees very well with the findings of this work showing that the hexamers desorbing in the δ peak are the first species to arrange in a (2 × 2) pattern and the symmetry remains at higher water coverages. The previously published IRAS spectra identify two adsorption bands when measured at 300 K, and by isotopic labelling experiments it was found that a 2720 cm^{-1} band corresponds to terminal O_wD hydroxyls, while a 2680 cm^{-1} band is due to surface O_sD. The latter band (2680 cm^{-1}) was still present when measuring at 350 K, which suggests it corresponds mostly to water adsorbed on defects. The band corresponding to terminal O_wD hydroxyls, was only observed at 320 K and below, thus it likely corresponds to the phase formed by small triangles identified in this thesis. The small triangular species were also observed in previous STM studies of $Fe_3O_4(111)$ thin films, and were as well attributed to initial stages of water adsorption [192], although they were never a subject of more detailed investigations. At temperatures below 300 K (corresponding to higher water coverages) the IRAS spectra show complex changes indicating hydrogen bonding of the species.

The preliminary computational data presented here are also perfectly consistent with the previous studies: On a perfect, stoichiometric, defect-free Fe_{tet1} terminated surface, the previously published structures present the thermodynamic minima; the structures observed in ncAFM should thus be unstable against formation of these. The situation changes when the surface is modified with additional Fe cations, but the number of extra cations needed for stabilizating saturation coverage of hexamers is quite high (0.25 extra Fe per unit cell). In any way, it is clear that either the Fe_{tet} surface is modified by water adsorption and thus the DFT provides an accurate description of the wrong system, or the DFT approach does not describe this system accurately enough. Given the fact that two groups arrived to the same results independently, the first scenario seems more likely. There are several possible ways to modify the Fe_{tet} surface: One possibility is that the Fe_{tet} terminated surface intrinsically contains additional Fe cations. A bare surface with additional cations was however shown to be less stable in DFT computations, and the ncAFM data also do not show any evidence of isolated Fe_{oct} on the surface. Another possibility is that surface diffusion might take place and a surface Fe_{tet} might migrate to a neighboring Fe_{oct} site which would center the water agglomerates. Such a scenario was tested for the case of water trimers and hexamers, but still wasn't shown to be energetically favourable in comparison to the previously identified species and networks; the resulting Fe vacancy on the surface is too energetically expensive. This leads to the idea that the extra Fe cations might diffuse from step edges or patches of Fe_{oct} termination, both of which are commonly present on as-prepared Fe_{tet} surfaces. Out of the mentioned scenarios this seems more plausible, but a direct experimental evidence is currently missing. A problematic aspect of this hypothesis is that the diffusion would have to be remarkably facile, as the water agglomerates were observed after the systems were not annealed higher than 150 K. Clearly, more work needs to be done to fully understand the reasons for stability of the experimentally identified water agglomerates on $Fe_3O_4(111)$.

An interesting question is whether it is possible draw any general trends from comparing water adsorption on $Fe_3O_4(111)$ and $Fe_3O_4(111)$. The answer is positive, as on both surfaces water first adsorbs in the form of isolated partially-dissociated water agglomerates with very specific molecular arrangements. Similarly, on both surface a complex hydrogen-bonded networks forms before all the surface cations are occupied. The desorption temperatures of the dominant phases are roughly in the same range, although on $Fe_3O_4(111)$ the smallest agglomerates are significantly more stable than the water dimers on $Fe_3O_4(001)$. Generally, the formation of the smallest agglomerates seems to be quite different on the two surfaces: While on $Fe_3O_4(001)$ the process of the dimer formation involves meeting of two molecularly adsorbed H_2O and the dissociation only takes place later due to the cooperativity effect which greatly stabilizes the structure, on $Fe_3O_4(111)$ a similar process was not found. While previous DFT studies found partially dissociated water dimers to be the most stable agglomerate species on $Fe_3O_4(111)$, they were only marginally more favourable in comparison to the same coverage of isolated, dissociated water monomers [89, 210]. A lower coverage of isolated monomers was then shown to be significantly more stable than the dimer structure. As shown in this chapter, no dimer species were observed in experiment, although more ncAFM measurements should be done to disprove their existence at intermediate coverages. Instead, triangular trimer species were found to be very stable, but the reasons for their stability or the process of their formation currently remains unknown. The available data suggest that the $Fe_3O_4(111)$ surface might be surprisingly dynamic even at low temperatures, and the probable process of Fe diffusion to the surface is qualitatively similar to the observed behavior of the $Fe_3O_4(001)$ system after exposure to liquid water [12]. In summary, this chapter shows that water adsorption on magnetite surfaces can be well-described at ideal conditions and many similarities can be drawn between the two dominant surfaces. Nevertheless, previously non-envisioned effects most likely take place and Fe diffusion to the surface will most likely happen on both surfaces upon exposure to realistic conditions; in the case of $Fe_3O_4(111)$ it possibly happens already in UHV at 150 K.

6 Single Metal Adatoms on Fe_3O_4 surfaces

This chapter deals with stability and reactivity od metal adatoms and small clusters and on the (001) and (111) surfaces of Fe_3O_4. The first three sections of this chapter deal with Ni, Ir and Rh adatoms on $Fe_3O_4(001)$ and the presented data have been published in papers [161, 211, 212]. The last section of this chapter contains preliminary results on Pt and Rh adatom stability on $Fe_3O_4(111)$; these data have not been presented before. This chapter contains data provided by this authors' colleagues, these contributions are clearly labeled in the text or in figure captions.

6.1 Nickel Doping Enhances the Reactivity of $Fe_3O_4(001)$ to Water

This section describes the effects of Ni doping on water adsorption at the $Fe_3O_4(001)$ surface, with a view towards understanding the enhanced performance of spinel ferrites for the water-gas shift and oxygen-evolution reactions. Water adsorption on two different Ni-doped surfaces was studied: a surface with twofold coordinated Ni adatoms on top, and a surface with Ni atoms incorporated into its octahedral sites. This section was published as a paper [211].

Introduction

Hydrogen is proposed as a convenient and environmentally friendly alternative to fossil fuels, but its industrial production remains economically unviable. Typically, H_2 is produced by steam reforming of methane, followed by the water-gas shift reaction (WGS; $CO + H_2O \rightarrow CO_2 + H_2$). The high-temperature stage of the latter reaction is performed by iron oxide catalysts stabilized by chromium, and magnetite (Fe_3O_4) is believed to be the active phase [213]. Alternative doping materials are being studied to (a) replace potentially harmful Cr as a stabilizing agent of the active phase and (b) improve the activity and/or selectivity of the catalyst [213–217]. Mixed oxides of iron and transition metals are also relevant for other catalytic applications, most notably the oxygen evolution reaction (OER), whose sluggish kinetics present a major bottleneck in H_2 production by sunlight-driven water splitting [27, 171, 218–220]. Nickel-iron oxides and (oxy)hydroxides exhibit high catalytic activity for OER, and in some cases even surpass more expensive state-of-the-art OER catalyst such as IrO_2 and RuO_2 [218, 220, 221]. The exact mechanisms of WGS and OER on oxide surfaces are still debated [213, 222], but in both the H_2O adsorption and dissociation belong to important reaction steps.

In this work, the effect of nickel doping on the reactivity of Fe_3O_4(001) to water is studied. Two different Ni geometries can be formed by choosing appropriate preparation conditions: metastable Ni_1 adatoms with twofold coordination to surface oxygen, and Ni atoms incorporated into the octahedral sites of the support. Using TPD, XPS and STM it is shown that both configurations change how water adsorbs on the surface. The Ni_1 adatoms dissociate water, leading to Ni-OH species and surface hydroxyl groups, both of which are stable above room temperature. The incorporated Ni is not directly accessible to adsorb water, but modifies the electronic properties of surface iron atoms creating sites where water binds more strongly than on the undoped Fe_3O_4(001) surface. Both the adatom and the incorporated species affect the formation of the partially-dissociated dimers and trimers previously observed on the clean surface (described in chapter 5).

Results

Figure 6.1A shows a typical STM image of the Fe_3O_4(001) surface with labeled common defects and corresponding model of the SCV-reconstructed surface. The appearance of the STM images, the structure and the common surface defects are described in the previous chapters of this thesis. When Ni is evaporated onto this surface at room temperature, isolated protrusions appear between the rows (blue circles in Fig. 6.1B). It was previously shown that these are due to isolated Ni adatoms that bind to the two surface oxygen atoms in a unit cell which lack a subsurface tetrahedral neighbor (labeled O* in the inset of Fig. 6.1A). Locally, this site resembles a bulk-continuation site, and is essentially where the next (tetrahedrally coordinated) Fe cation would reside if the spinel structure were continued outward. Metals such as Au, Ag, Pt are stable in the twofold coordinated site to temperatures as high as 650 K, but ferrite-forming metals such as Ni, Co, Ti, Mn or Zr prefer octahedral sites in the spinel lattice (Fig. 6.1C), consistent with the structure of the respective spinel ferrites [51, 69, 70, 78]. When the vacant subsurface octahedral site is filled by a foreign atom, the interstitial Fe_{tet} moves back into the other subsurface octahedral site of the unit cell, and this cation arrangement closely resembles a bulk-truncated Fe_3O_4(001) surface [70, 82]. For Ni, the transition from adatom to octahedral coordination occurs at ≈ 465 K, and the occupation of subsurface sites has been confirmed by quantitative normal incidence x-ray standing waves measurements [70, 71]. The subsurface Ni atoms are not observed directly in STM, but their presence modifies the electronic structure of nearby surface Fe cations causing them to appear brighter in empty states (red circles in Fig. 6.1C). The appearance is similar to an additional Fe cation in the subsurface (see the defect labelled “unreconstructed cell” in Fig. 6.1A). In addition to subsurface Ni, we also observe bright protrusions within the surface Fe row in Fig. 6.1C (yellow circles), which we attribute to Ni substituting fivefold coordinated Fe atoms in the surface layer. This site has been shown to be a metastable site for Co, Rh and Ir, with the substituted Fe_{oct} and the interstitial Fe_{tet} moved into the octahedral vacancies of the surface reconstruction [82, 161, 212]. Upon annealing to higher temperatures the Ni atoms diffuse further into the bulk and the clean $(\sqrt{2} \times \sqrt{2})R45°$ reconstructed surface is recovered.

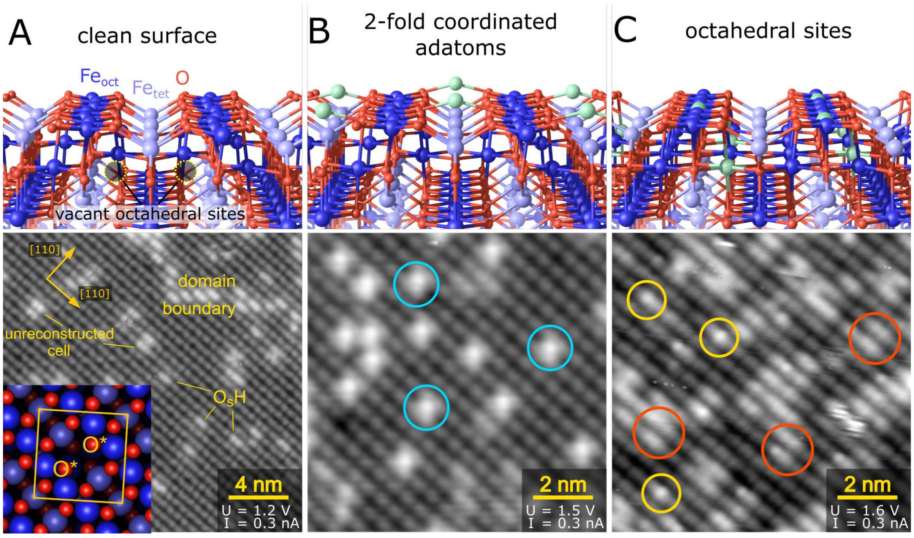

Figure 6.1: Characterization of Ni adsorption at the $Fe_3O_4(001)$ surface by STM. A) The clean $Fe_3O_4(001)$ surface features subsurface cation vacancies that give rise to the $(\sqrt{2} \times \sqrt{2})R45°$ symmetry (Fe_{oct}, Fe_{tet}, O, and Ni atoms are dark blue, light blue, red, and light green, respectively). Each surface unit cell has two O* atoms that do not have a tetrahedral Fe neighbor (inset in panel A). The STM image shows the clean surface and common defects: surface OH groups, anti-phase domain boundaries and unreconstructed unit cells. B) Metal adatoms adsorb in the 2-fold coordinated site formed by the O* atoms, circled in blue in the STM image are some Ni atoms in this configuration. The Ni adatom coverage is 0.15 ML in this image. C) Like other spinel-ferrite forming metals, Ni can incorporate into the vacant octahedral sites in the subsurface or replace a surface Fe_{oct} atom in a metastable configuration. These two types of incorporated Ni are highlighted by red and yellow circles in the STM image, respectively. In panel C the Ni coverage was 0.40 ML before the incorporation. Figure reprinted from [211].

A water TPD spectrum acquired on a perfect $Fe_3O_4(001)$–$(\sqrt{2} \times \sqrt{2})R45°$ surface features three distinct desorption peaks below 260 K (black curve in Fig. 6.2). A detailed description of the individual features present in this TPD spectrum was provided in the previous chapter of this thesis. Comparing the water desorption spectra of the $Fe_3O_4(001)$ surface enriched with Ni adatoms and incorporated Ni species allows us to identify the desorption states linked to the presence of Ni. Figure 6.2A shows D_2O TPD spectra taken after three different preparations, each with an initial D_2O dose of 9.75 molecules per unit cell. On the surface enriched with 0.4 monolayer (ML) Ni adatoms we observe three desorption peaks above 250 K, labeled ζ, η and ϑ in Fig. 6.2A. When the same amount of Ni is incorporated into the surface by annealing to 450 K prior to the water adsorption, the η and ϑ peaks disappear, and the ε peak is the most prominent desorption feature above 250 K. This feature was already present on the clean surface, albeit to a much lesser extent. The ζ peak is significantly lower compared to the adatom case. To estimate the amount of water desorbing above 250 K, the area under the TPD curves was integrated. The high-temperature D_2O signal scales linearly with the adatom coverage, and the number of desorbed D_2O molecules is roughly three times the number of adatoms (inset in Fig. 6.2B). This suggests multiple water molecules bind either directly to, or in the vicinity of, one single adatom site. A similar plot for the surface with incorporated Ni is shown in the inset of Fig. 6.2C. The amount of water desorbing from the incorporated Ni-related states is significantly lower. The interpretation is however not as straightforward as in the adatom case, because some of Ni might have diffused into deeper layers during the 450 K pre-annealing. TPD spectra taken after pre-annealing to 680 K were comparable to clean surface measurements, which shows Ni atoms diffuse into the bulk at elevated temperatures, in accord with previously published results [70].

One interesting consequence of the Ni doping is that the δ peak, located at ≈ 240 K, is significantly decreased compared to the clean surface. This suggests that the addition of Ni affects the formation of the partially-dissociated water agglomerates studied previously. The presence of the β and γ peaks suggests the hydrogen-bonded network can still be formed, although its characteristics are slightly changed. In the adatom case the γ peak increases in intensity and shifts to lower temperature relative to the data from the clean surface. The β peak is no longer resolved, and appears more as a low temperature tail of the γ peak. In the incorporated Ni case, these effects on the β and γ are not observed, and the most significant change relative to the clean surface is the slight decrease of the β peak.

Figure 6.3 shows detail of the D_2O TPD spectra acquired after different loadings of Ni adatoms and incorporated Ni atoms. The complex effects of varying the Ni adatom coverage are shown in panel A. The δ peak sharply decreases at low adatom coverage, but stays roughly constant above 0.2 ML. The γ peak first significantly increases with increasing Ni adatom coverage, but above 0.2 ML decreases again. The β peak is poorly resolved at higher Ni adatom coverage. Importantly, the

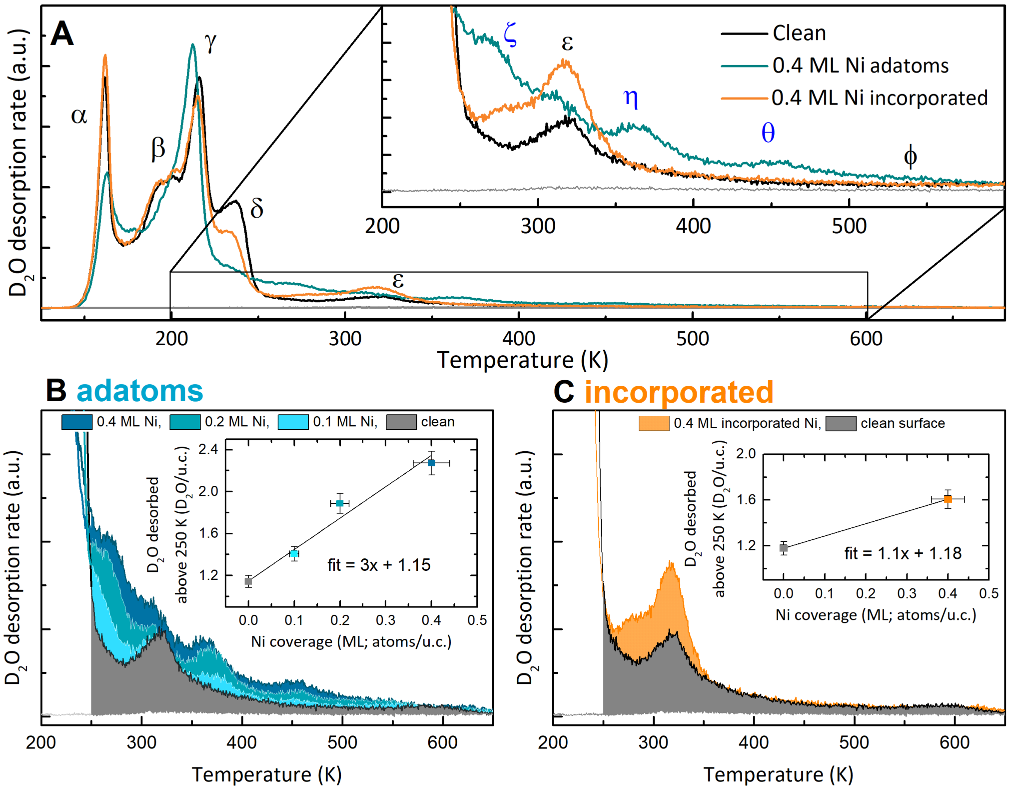

Figure 6.2: Temperature programmed desorption (TPD) studies of water on Ni/Fe$_3$O$_4$(001) surfaces. A) Water TPD spectra of 0.4 ML Ni adatoms and 0.4 ML incorporated Ni species on the Fe$_3$O$_4$(001) surface. The D$_2$O dose is 9.75 molecules per unit cell in both cases. Compared to the clean surface (black curve), the Ni adatoms give rise to three desorption peaks labeled ζ, η and ϑ. The incorporated Ni species enhances the ε peak, which is associated with Fe-rich surface defects. B, C) Integrating the areas under the TPD curves for different initial Ni coverages allows quantification of the amount of water desorbing above 250 K. In the adatom case (B), the amount of desorbing D$_2$O molecules scales linearly with the initial adatom coverage and the number of D$_2$O related to Ni is approximately three times the number of adatoms. C) Incorporating Ni leads to a significantly lower amount of water desorbing above 250 K, closer to one molecule per Ni atom. Data taken by Jan Hulva, figure reprinted from [211].

capacity of the first monolayer increases with increasing Ni adatom loading, as judged by the decreasing size of the multilayer peak (α). In the case of incorporated Ni (panel B), increasing the Ni coverage leads to decrease of the δ and γ peaks. The β peak stays roughly constant, and the overall capacity of the first monolayer slightly decreases.

XPS was used to discern whether the surface bound water is dissociated or molecular. Figure 6.4 shows the effect of adsorbed water on the Ni 2p and O 1s regions of the XPS spectra taken on surface with Ni adatoms (Fig. 6.4A,B) and surface with incorporated Ni (Fig. 6.4C,D). In the adatom case, after dosing D$_2$O

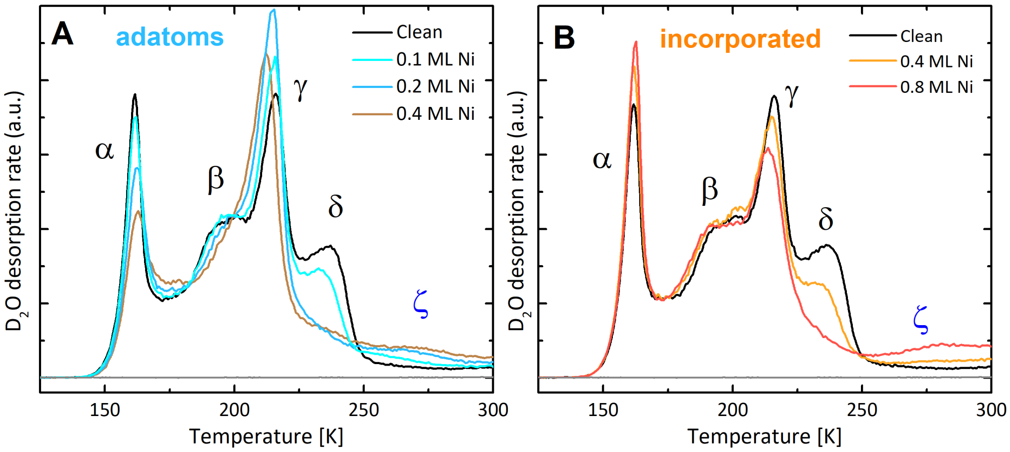

Figure 6.3: D_2O TPD spectra aquired on $Fe_3O_4(001)$ surface with different coverages of Ni adatoms (A) and incorporated Ni (B). The D_2O dose is 9.75 molecules per surface unit cell in all spectra. Data taken by Jan Hulva, figure reprinted from [211].

at 100 K and heating to 236 K for several minutes, we observe contributions from both dissociated and molecular water. After increasing the temperature to 300 K, only dissociated water is present. This shows that water desorbing in peaks ε, η and ϑ comes from recombination of dissociated water, but water desorbing in the ζ peak is at least partially intact. The situation is similar for incorporated Ni atoms (Fig. 6.4D), here the ε desorption peak is also formed by recombinative desorption, and ζ is at least partially molecular. Inspecting the Ni $2p$ region, we find that adsorbing water on the Ni adatoms changes the shape and position of the Ni $2p$ peak (Fig. 6.4A, all spectra taken at 300 K). Before water exposure, the peak is slightly asymmetric due to a small fraction of Ni being incorporated during deposition. The peak shape after water exposure suggests a convolution of several components with contributions from bare adatoms (854.0 eV), and at least one additional peak centered at ca. 856.0 eV corresponding to a more oxidized species. No changes are observed on the peak corresponding to incorporated Ni; both the shape and the position stay constant with water dosing and heating up to 450 K (Fig. 6.4C).

In addition to spectroscopic identification of the water adsorbed on different Ni species, STM measurements were carried out to image the surface after exposure to water. Figure 6.5A shows the surface with 0.13 ML Ni adatoms after deposition at room temperature. Here almost all the adatoms occupy the same site within the surface unit cell and have the same apparent height. After room temperature exposure to approximately 15 L H_2O using a directional doser, several types of different bright protrusions are present (Fig. 6.5B). A small number of adatoms (0.010 ML, representative species highlighted by cyan circles in Fig. 6.5B) occupy the same adsorption geometry as in Fig. 6.5A. The majority of the species (0.059 ML, red circles in Fig. 6.5B), however, have a different appearance and appear slightly offset from

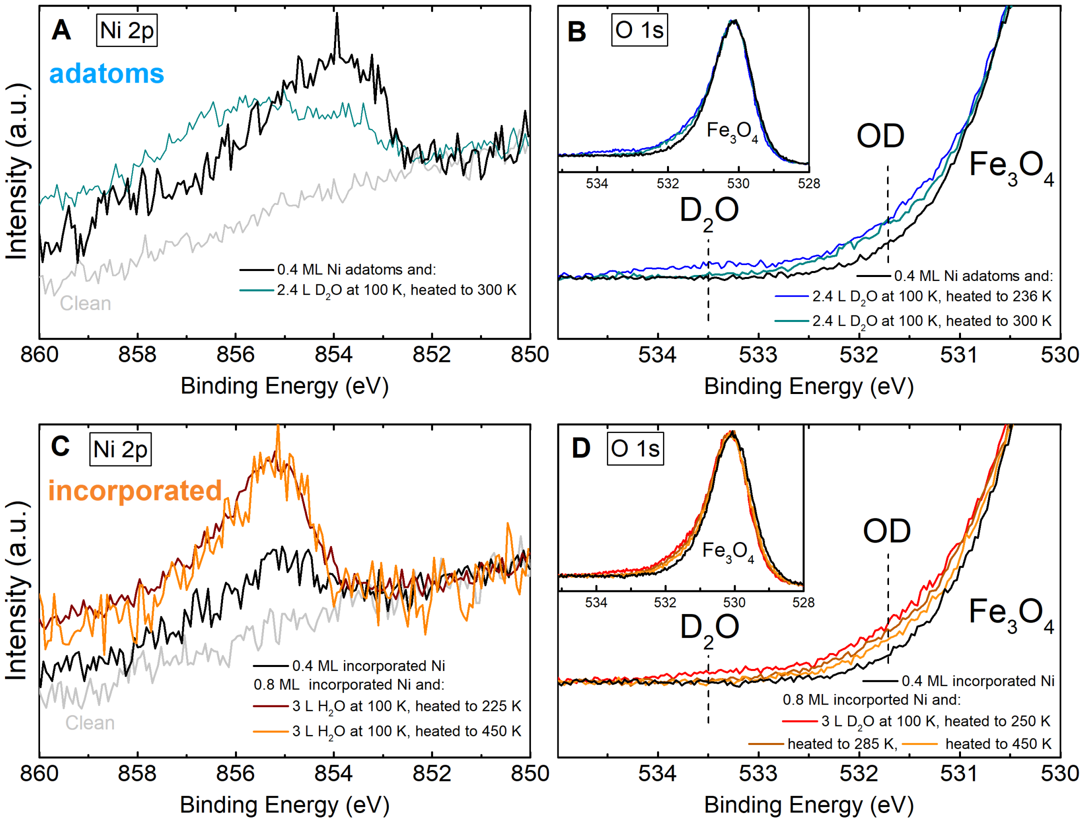

Figure 6.4: X-ray photoemission spectra (XPS) of the Ni adatoms (A, B) and incorporated Ni atoms (C, D) on Fe_3O_4(001) before and after water dosing. A) The Ni 2*p* peak of 0.4 ML Ni adatoms changes both shape and position after D_2O dosing at 100 K and heating to 300 K. B) Dosing D_2O at 100 K and heating to 236 K results in a mixed-mode water adsorption with contributions of both molecular and dissociated D_2O. After heating to 300 K only dissociated water remains on the surface. C) The shape and position of the Ni 2*p* peak of the incorporated Ni atoms does not change with water dosing and heating to various temperatures below 450 K. D) On the incorporated Ni atoms below 285 K there is a significant contribution of molecular D_2O; above this temperature all the adsorbed water is dissociated. The reference spectra of the surfaces before D_2O exposure (black) were taken at 300 K. Data in panels A, C are normalized to the background, in panels B, D normalized to the maximum. Data taken by Jan Hulva, figure reprinted from [211].

the regular twofold-coordinated adsorption site. Moreover, these species exhibit a characteristic hopping motion in STM movies, oscillating from side to side over the regular twofold-coordinated adsorption site; Fig. 6.5C highlights this motion showing three frames from an STM movie acquired in the highlighted area of Fig. 6.5B. In addition, we observe some larger, poorly-defined features (0.037 ML, green circles in Fig. 6.5B), which we tentatively assign to Ni clusters. Summing up the number of Ni-related species observed after water dosing (assuming the bigger species contain two Ni atoms), the coverage of 0.14 ML correlates well with the initial adatom coverage of 0.13 ML. In addition to the changes to the Ni adatoms, the surrounding surface also changes, and the coverage of surface O_sH groups increases by roughly a factor of five (0.006 ML in Fig. 6.5A, 0.032 ML in Fig. 6.5B). These species also undergo a characteristic hopping motion described previously [73], and are thus easily distinguished from features with a similar appearance such as incorporated Ni. A room-temperature STM study of water adsorption on incorporated Ni was not conducted, because TPD indicates that these species readily desorb very close to 300 K.

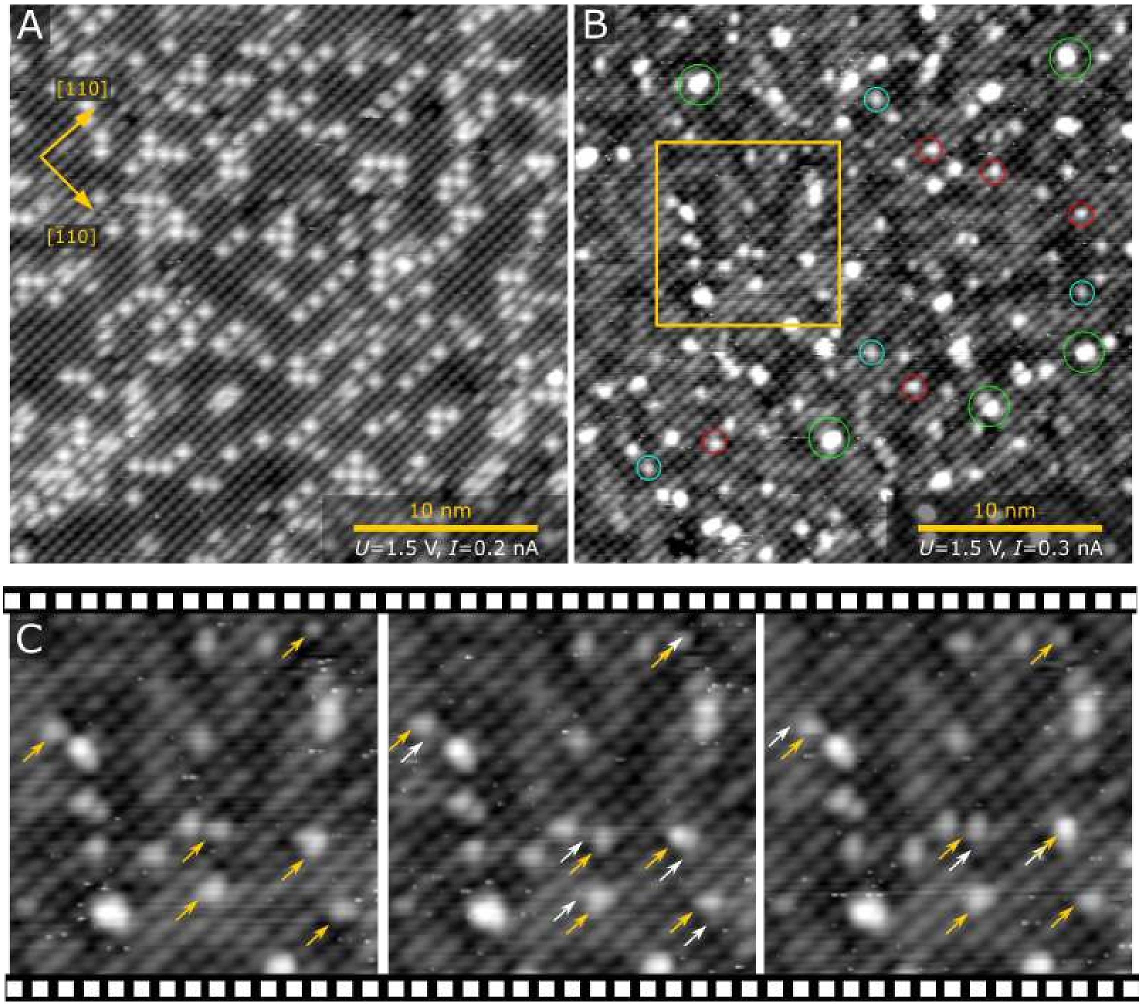

Figure 6.5: STM images acquired on the $Fe_3O_4(001)$ surface after deposition of 0.13 ML Ni adatoms (A) and after dosing 15 L H_2O on the surface with Ni adatoms at room temperature (B, C). After the water dosing, almost all the adatoms change their shape and the surface is more hydroxylated compared to (A). Some of the nickel-related species show a distinctive hopping motion highlighted in (C). The positions of these species are marked by yellow arrows in each frame, the white arrows point to their previous positions. The well-documented movement of surface O_sH groups [73] is not highlighted. Figure reprinted from [211].

It should be noted that while the same effects have been observed in repeated STM experiments, the extent of the resulting hydroxylation varied independently on the amount of dosed water (between 10–200 L). In some cases, only a minority of the adatoms transformed into the newly observed species and the observed surface hydroxylation was significantly weaker than in Fig. 6.5B. This is most likely due to variations in dosing temperature. To test this hypothesis, additional XPS experiments were carried out comparing 50 L D_2O on the surface at 300 K and 270 K (Fig. 6.6). After dosing at 300 K the Ni 2*p* region shows an almost negligible increase in the higher binding energy shoulder compared to the as-prepared surface (the spectra are offset for clarity), while the O 1*s* region reveals minimal, but clearly detectable hydroxylation. Importantly, no detectable hydroxylation is observed after water dosing on the pristine surface, even when the dose is increased to 1000 L at a pressure of 10^{-6} mbar (data shown and discussed in the PhD thesis of Jan Hulva [203]). After dosing another 50 L at 270 K and heating to 300 K, the Ni 2*p* peak shape changes; the component at 854 eV decreases, and the higher binding energy shoulder increases. This correlates with more hydroxyls in the O 1*s* region. It is thus concluded that variations of dosing temperature around room temperature have an effect on the amount of water that is adsorbed.

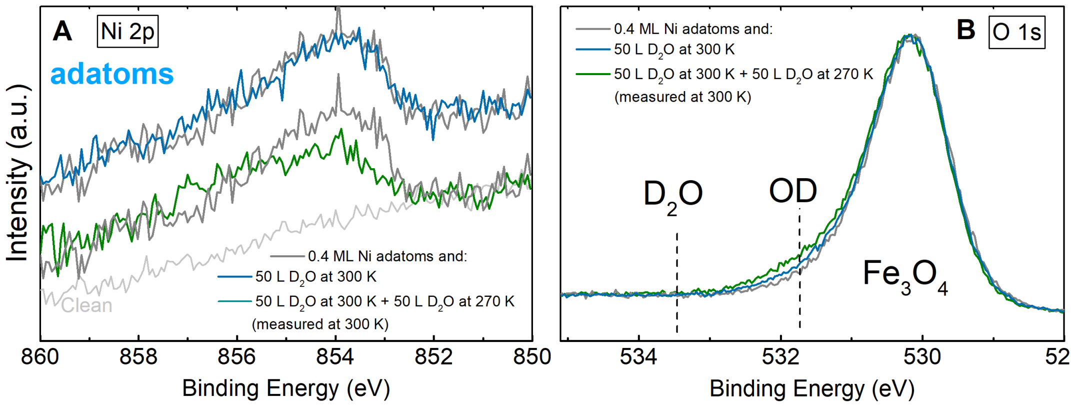

Figure 6.6: XPS spectra acquired after dosing D_2O at 270 K and 300 K. Dosing water at 300 K has little effect on the shape of the Ni 2*p* peak corresponding to Ni adatoms (spectra offset for clarity), and the O 1*s* region shows slight hydroxylation. Lowering the dosing temperature to 270 K induces changes in the shape of the Ni 2*p*, where the main component at 854 eV is lowered and a small contribution appears at higher binding energy. The O 1*s* region shows stronger hydroxylation compared to dosing at 300 K. Data taken by Jan Hulva, figure reprinted from [211].

Discussion

The experimental data acquired on Ni-doped $Fe_3O_4(001)$ surfaces show that both Ni adatoms and incorporated Ni atoms enhance the reactivity of the surface towards water. Combined, the data for the adatom surfaces suggest that water dissociates at 2-fold coordinated Ni adatoms, resulting in Ni-OH species and H atoms adsorbed at the O* sites on the surrounding Fe_3O_4 surface. Since the oscillating features observed in STM images (cyan circles, Fig. 6.5) are the majority species, it is reasonable to assign them to Ni-$(OH)_x$. Thus, the η and ϑ peaks in TPD (Fig. 6.2A) result from recombinative water desorption occurring at these sites. Quantification of the TPD spectra suggests that each Ni atom is associated with multiple OH groups, but it is not clear if the η and ϑ peaks are due to sequential desorption of Ni-bound OH, or if one peak is perhaps due to an OH group bound to Fe in vicinity of the Ni adatom. Possibly, one of the peaks could correspond to desorption from the minority species observed in STM, tentatively assigned to small Ni clusters.

The water TPD spectra acquired on the $Fe_3O_4(001)$ surface with incorporated Ni atoms do not show any new desorption states above room temperature. This is not surprising, since the majority of incorporated Ni atoms are buried in the subsurface and not available for direct interaction with water. Instead, the primary effect of Ni incorporation is an increase in the intensity of the ε and ζ peaks that were already present on the clean surface. This can be understood given the previous assignment of the ε peak to water adsorption on Fe-rich defects [159], as incorporation of the Ni atom clearly affects the electronic structure of the surface Fe atoms as judged by STM (Fig. 6.1C) [70]. The effect is very similar to that observed at the domain boundaries and unreconstructed unit cells, where a local reparation of the bulk-like spinel lattice results in defect sites that have been reported to dissociatively adsorb methanol [202]. Consistent with this interpretation, XPS shows water dosing has no effect on the incorporated Ni atoms, and water bound in the ε peak is purely dissociated. The origin of the ζ peak is unclear, but similar to the adatom case, water bound in this state is at least partially molecular. Most likely this peak is linked to molecular water that is hydrogen-bonded to water dissociated at point defects (or Ni adatoms) on the surface. Alternatively, this peak could correspond to desorption from the minority surface Ni atoms (yellow circles in Fig. 6.1C).

It is interesting that both the Ni adatoms and the incorporated Ni atoms reduce the intensity of the δ TPD peak compared to the clean surface. As shown in the previous chapter, the δ peak is attributed to partially-dissociated water agglomerates. In the case of the Ni adatoms, it seems likely that the Ni adatoms prevent the formation of these partially-dissociated species because they occupy the same O* sites which are required for the accomodation of the surface hydroxyl groups. The concomitant increase in the γ peak suggests that a long-range hydrogen bonded network can still be formed at higher coverage. In that light, the incorporated Ni should not prevent the formation of dimers/trimers, since the recovery of the bulk-like spinel structure should increase the amount of surface O sites without subsurface tetrahedral neighbors, similar to the O* on the clean surface. While the assumption that these sites with Ni in the subsurface have the same properties as the O* sites is only tentative, such a surface is conceptually similar to the bulk-truncated $Fe_3O_4(001)$ surface calculated by Mulakaluri et al. [204, 205], where partial dissociation was indeed found to be favored. One possible explanation is that the ζ peak at $\approx$270 K is due to partially-dissociated species bound to defect sites induced by the presence of the Ni dopants. Since most metals become cationic at this surface and donate electrons to the Fe sublattice, similar effects can be expected for water adsorption on different metal adatoms on the $Fe_3O_4(001)$ surface.

Relating these results to water-gas shift (WGS) reaction, the activation of the surface for water adsorption and dissociation is a desirable effect. Water dissociation can be one of the rate-limiting steps in WGS and having OH groups bound with different strengths on the surface (which the TPD spectra on the Ni_1 adatoms suggest) might prevent dissociated water being bound too strongly to take part in further reaction steps. Therefore, it is assumed the presence of 2-fold coordinated adatoms on the surface could improve the WGS activity of Fe_3O_4, although the instability of these species towards incorporation at elevated temperatures is problematic.

In the case of oxygen evolution reaction (OER), potential catalyst materials are commonly identified by computational screening with the binding energy of an OH group used as a descriptor of OER activity [173, 174]. Our results show the OH groups bind with different strengths at the Ni-related sites, which will likely affect the OER performance. The closest comparable system to Ni_1/Fe_3O_4 would be $NiFe_2O_4$, which has been suggested to be one of the active phases in OER [222] and has also been successfully utilized in efficient OER catalysts [223, 224]. On the $NiFe_2O_4(001)$ surface, the first proton release upon water adsorption has been identified as the rate-limiting step [222]. Our STM results show the OH and H are spatially separated on $Ni_1/Fe_3O_4(001)$, which could in principle lead to lowering of this rate limiting step. Nevertheless, the major difference between the two systems is the coordination of the Ni atoms (5-fold on $NiFe_2O_4(001)$, 2-fold as an adatom on $Fe_3O_4(001)$), which will most likely affect the reaction mechanism, and without further computational study it is not trivial to guess in what way. An equally interesting question related to OER is how stable the Ni species would be in electrochemical environment, and how the growth of any (oxy)hydroxide phase would affect the system. Such phases are highly stable and suspected to be the active phase on many Ni/Fe catalysts [27, 218, 220]. In this regard, the results presented in this work provide an initial test of stability upon exposure to water vapor, and we propose the $Fe_3O_4(001)$ surface to be a good model system for well-defined studies of adatom reactivity in more realistic conditions.

6.2 Coordination Defines Adsorption in a Model Single-Atom Catalyst: Ir_1/Fe_3O_4

This section deals with interaction of single Ir_1 adatoms with CO. It will be shown that the CO adsorption geometry crucially depends on the initial coordination of the Ir_1 adatom, and such behavior can be rationalized by analogy to coordination chemistry. In general, the presented results show that even adatoms of the same metal on the same surface can exhibit very different adsorption properties; a characterization of a single-atom catalyst is thus only complete when the local environment of the adatoms is described. The results presented here were published in a paper [161], but this section contains some additional details.

Introduction

The field of single-atom catalysis (SAC) came about as an attempt to increase the per-atom reactivity of heterogeneous catalysts by downsizing the active nanoparticles to the ultimate limit. Nevertheless, it soon became clear that single metal atoms on surfaces will have different properties from the nanoparticles of the same metal supported on the same surface. One of the reasons for this is that nanoparticles are typically metallic, but the electronic structure of single atoms is strongly modified by their interaction with the surface. Given that a strong adatom-surface interaction is a stability-defining parameter in many SAC systems, it is clear that the reactivity of the single adatoms must be affected by the choice of the support and very likely also by the exact site they bind to. Reaction mechanisms can also differ in the single-atom limit due to the lack of nearest neighbour metal sites, making it difficult to predict which metal/support combination might be the best choice for a particular reaction. Theoretical screening studies suggest several Me_1/FeO_x systems will outperform Pt for CO oxidation [225, 226], but exactly which depends on the reaction mechanism that is assumed. Moreover, it is not clear whether the assumed adsorption site exists in real SAC systems, which are complex, often inhomogeneous, and difficult to characterize.

Aside from the promise of ultimate per-atom reactivity, SACs are also exciting for their potential to deliver excellent selectivity, which could be achieved if all the single atom sites are the same (see also Fig. 1.1). From this point of view, an ideal SAC resembles coordination complexes used in homogeneous catalysis, where all the single metal atoms are stabilized by chemical bonds to the ligands, and all are in the same local environment. The analogy to homogeneous catalysis suggests that the catalytic properties of SACs should depend strongly not only on the adatom-support interaction strength, but mainly on the local coordination of the metal. There is some evidence of this effect [37, 38], but most fundamental work has focused on Pt-based SACs rather than metals such as Rh and Ir.

This work focuses on precise description of sites which single Ir_1 atoms can occupy on a well-defined $Fe_3O_4(001)$ support. It will be shown that the initial Ir_1 coordination can be well correlated with the ability of the model catalyst to adsorb CO, and the structures of the individual $Ir(CO)_x$ carbonyls can be rationalized by analogies to coordination chemistry. The $Ir_1/Fe_3O_4(001)$ system was selected because Ir_1/FeO_x catalysts have already been shown to be active for both CO oxidation [225, 226] and the water-gas shift reaction [227], where CO is a reactant, and because Ir-based coordination complexes are common in homogeneous catalysis. Moreover, IrO_2 is an important catalyst for water oxidation [228, 229], and an efficient Ir-based SAC might present a way to reduce the amount of Ir required for this important reaction. Finally, the interaction of CO with metallic Ir is well characterized [230–232], allowing direct comparisons to be made. This work shows that Ir atoms can take three different geometries with 2-, 5- and 6-fold coordination to the lattice oxygen. The 2 and 5-fold sites bind CO more strongly than metallic Ir, and form structures consistent with Ir(I) and Ir(III) coordination complexes. The 6-fold site is energetically preferred, but is subsurface and unable to adsorb CO. In contrast to most of SACs, this system is deactivated by Ir_1 incorporation rather than thermal sintering.

Results

Figure 6.7A shows an STM image of the UHV-prepared $Fe_3O_4(001)$-$(\sqrt{2} \times \sqrt{2})R45°$ surface after 0.13 ML Ir was thermally evaporated onto the sample at room temperature. Isolated Ir_1 adatoms appear as bright protrusions between the rows, as has been observed previously for a variety of other metals on this surface [51]. The adsorption site is essentially where the next tetrahedrally-coordinated Fe cation would reside in the spinel structure, suggesting a 2-fold coordination to the substrate. This is in line with our DFT calculations (optB88-DF, $U_{eff} = 3.61\,eV$, calculations carried out by Matthias Meier), which find a strong binding energy ($-5.2\,eV$ with respect to a single Ir atom in the gas phase) and small positive charge of 0.5 e for an Ir adatom in this position. An STM simulation of the structure shown in Fig. 6.7B (inset in Fig. 6.7A) is consistent with the measured data. Some double protrusions are also observed (red arrow), which are attributed to Ir_2 dimers; these disappear already upon mild annealing in experiment. This suggests that Ir dimers are unstable with respect to Ir adatoms, similarly to previous observations of Ag, Pt and Rh on this surface [78, 80, 212]. Further details about the Ir dimers are provided in section 6.4.

When the model SAC is heated to 623 K (Fig. 6.7C), the 2-fold Ir_1 adatoms disappear, and protrusions located within the surface Fe rows are observed instead. The most common species are isolated bright features (green circle), which are identified as Ir atoms substituting 5-fold Fe atoms in the surface layer. Our DFT calculations (Fig. 6.7D) show that this site is 1 eV more stable than the 2-fold site, and that the Ir is more oxidized in this configuration (Bader charge 1.4 e). In the model shown, the Fe atom displaced by Ir occupies one of the octahedral vacancies in the third layer. This change in the subsurface cation ordering would manifest as an elongated, less bright feature close to the Ir-related protrusion (see accompanying STM simulation (inset in Fig. 6.7C)). While this is observed in some cases, the Fe exchange with the bulk is already facile at this temperature [51], thus it is also possible that the excess Fe diffuses into deeper layers. In this case, a single bright protrusion in the row would be observed. When the sample is heated to 723 K (Fig. 6.7E), the number of 5-fold Ir atoms decreases, and an increased number of the bright protrusions elongated in the [110] direction (yellow circle) is observed. Our DFT calculations suggest that these features are due to Ir adatoms in 6-fold coordinated sites in the third layer, which is a further 1 eV more stable than the 5-fold site in the surface layer. The Ir has a similar Bader charge of 1.4 e. In the corresponding STM simulations, the defect appears as either a single or double protrusion, depending on whether the displaced Fe disappears to the bulk or remains in the 3rd layer. In the final step of the experiments, the sample was heated to 973 K. This results in large Ir clusters spread widely over the surface.

XPS measurements of the room-temperature-prepared $Ir_1/Fe_3O_4(001)$ surface (Fig. 6.8A) reveal a single Ir 4*f* 5/2 peak with binding energy of 61.1 eV for the 2-fold coordinated Ir species. Heating the sample to 450 K for 7 minutes leads to a broad Ir 4*f* spectrum with a maximum at 62.0 eV, although a shoulder remains at 61.1 eV suggesting the transition to the more oxidized 5- and 6-fold coordinated states occurs slowly at this temperature. At 500 K, the spectrum exhibits a single peak at 62.1 eV, close to the 61.8 eV reported for octahedrally coordinated Ir^{4+} in $IrO_2(110)$ [233]. When the sample is annealed at 960 K, the Ir 4*f* signal shifts to 60.8 eV, consistent with the formation of metallic Ir nanoparticles. It should be noted that the sample temperatures in the XPS/TPD setup were measured by a thermocouple spot-welded directly on the sample mount, and thus are more reliable than those measured in the STM chamber, where the thermocouple is placed further away from the sample plate on the annealing stage. Additionally, the sample mount was getting loose during STM experiments, therefore we estimate the annealing temperatures to be up to 100 K lower than indicated by the thermocouple readout in the STM chamber.

To study how the different coordination environments affect the reactivity of the model catalyst we performed TPD experiments using isotopically labelled ^{13}CO as a probe molecule (Fig. 6.8B). First, 0.3 ML Ir was deposited on the freshly prepared $Fe_3O_4(001)$ surface, and the model catalyst with 2-fold Ir exposed to 1 ML

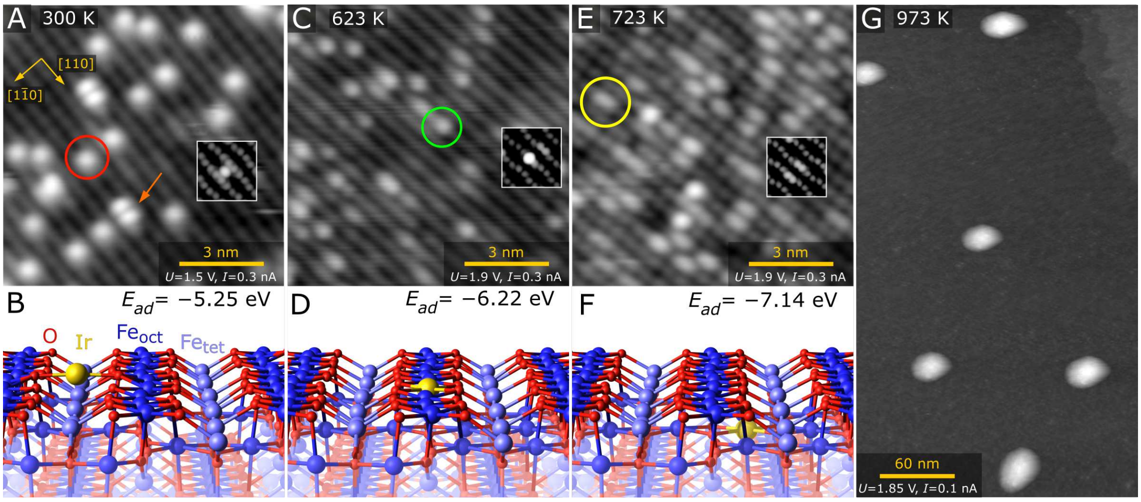

Figure 6.7: Determining the local structure of the $Ir_1/Fe_3O_4(001)$ model catalyst using room-temperature STM and DFT. (A) Ir_1 atoms evaporated directly onto the $Fe_3O_4(001)$ surface at 300 K are imaged as bright protrusions between the Fe rows of the support (red circle in STM image). Double protrusions are metastable Ir_2 dimers (orange arrow). (B) DFT-derived minimum-energy structure of the 2-fold coordinated Ir adatom on $Fe_3O_4(001)$. An STM simulation based on this structure is shown as an inset in panel A. (C) After annealing to 623 K, Ir atoms appear as bright protrusions within the Fe row in STM images (green circle). (D) DFT-derived minimum energy structure of the 5-fold coordinated Ir atom incorporated within the $Fe_3O_4(001)$ surface, with the corresponding STM simulation shown as an inset in panel C. (E) At 723 K, some of the bright protrusions within the row are replaced by extended bright protrusions in STM (yellow circle). Some small irregular clusters are also observed. (F) DFT-derived minimum energy structure of the 6-fold coordinated Ir adatom incorporated in the subsurface layer of $Fe_3O_4(001)$. An STM simulation based on this structure is shown as an inset in panel E. (G) Annealing at 973 K leads to formation of metallic Ir clusters with an apparent height of ≈ 3 nm. Computations carried out by M. Meier, figure reprinted from [161].

^{13}CO using a calibrated molecular beam source at 100 K. The sample was then heated with a temperature ramp of 1 K/s and the desorbing species monitored by a mass spectrometer. We have previously shown that CO interacts weakly with the as-prepared $Fe_3O_4(001)$ surface [208], desorbing in two peaks below 120 K. The addition of the 2-fold coordinated Ir adatoms leads to a new desorption feature at ≈ 610 K, well above the temperature where CO desorbs from metallic Ir surfaces (500-560 K) [230–232]. In addition to significant ^{13}CO desorption signal we observe a small, broad $^{13}CO_2$ peak at ≈600 K (see inset in Fig. 6.8B). Above 600 K, no adsorbed CO is detectable by XPS, and the Ir 4*f* signal appears at 62.1, as in Fig. 6.8A.

In previous work by Jan Hulva [203], the desorption energy of the Ir_1-related ^{13}CO TPD peak was estimated using the Redhead equation to be ≈ 2.4±0.1 eV. This was calculated under the assumption of no entropic contribution due to translational

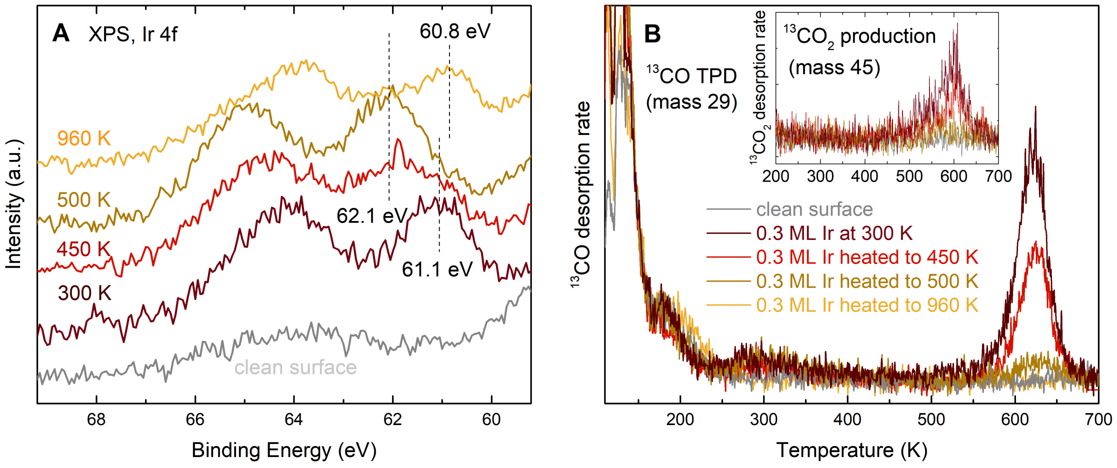

Figure 6.8: Experimental characterization of the $Ir_1/Fe_3O_4(001)$ model catalyst by X-ray photoelectron spectroscopy (XPS) and temperature programmed desorption (TPD). (A) In XPS, the Ir 4*f* peaks shift to higher binding energy as the sample is heated, consistent with the occupation of more stable, higher coordination sites predicted by DFT. At 960 K, the peak shifts back to the position of metallic Ir due to the formation of metallic Ir nanoparticles. (B) ^{13}CO-TPD shows a single peak at 610 K due to desorption from Ir. This peak reduces in intensity when the sample is heated prior to CO adsorption (peaks below 300 K are due to the $Fe_3O_4(001)$ support [208]). No CO desorption is observed from the Ir nanoparticles formed when the sample is heated to 960 K. Figure reprinted from [161].

or rotational degrees of freedom on the surface, leading to a maximum prefactor value of $3\times10^{18}\ s^{-1}$ at 620 K. In the same work, experiments on $Fe_3O_4(001)$ surface labelled with ^{18}O proved that the CO_2 originates via a Mars-van-Krevelen mechanism by extraction of O from the lattice. By comparison of the desorption peak areas after correcting the mass spectrometer sensitivity, it was estimated that 12-15 % of the Ir-adsorbed CO is oxidized during the TPD experiment [203].

When the samples were pre-annealed at 450 K prior to CO adsorption (to convert the 2-fold Ir to 5- and 6-fold Ir), the TPD peak position remained at the same temperature, but lower in intensity. There are three possible explanations for this effect: (1) Either the CO binding energy is identical at the 2- and 5-fold sites, (2) the 2-fold Ir diffuses to the 5-fold site with the CO molecule still attached during the TPD experiment, or (3) the 5-fold coordinated Ir does not adsorb CO at all. With increasing pre-annealing temperature, the peak gets smaller and eventually disappears. This is because Ir atoms incorporated in subsurface 6-fold coordinated sites are inaccessible to CO. The continued lack of a CO desorption peak after annealing the sample to 960 K suggests that the Ir nanoparticles observed in STM are encapsulated by iron oxide. This is attributable to the so-called strong metal-support interaction (SMSI), a well-known phenomenon previously observed for Pt nanoparticles on both $Fe_3O_4(001)$ and $Fe_3O_4(111)$ [207].

To investigate how the CO adsorbs on Ir_1 and how the system evolves during the TPD ramp we performed further imaging experiments and DFT calculations. Figure 6.9 shows STM images taken after depositing 0.2 ML Ir and dosing ≈ 58 L CO. The majority species observed in this experiment look similarly to bare Ir_1 adatoms, but are slightly elongated in the direction parallel to the Fe_{oct} rows (orange arrows in Fig. 6.9A,B). Additionally, there is a small number of brighter double-lobed features oriented perpendicularly to the Fe_{oct} rows, highlighted by cyan arrows in Fig. 6.9A,B. Further ncAFM experiments combined with DFT calculations clearly identify the elongated species as IrCO monocarbonyls and the double-lobed features as $Ir(CO)_2$ dicarbonyls (shown in Fig. 6.11). In all room temperature experiments, ca. 80-90 % of the carbonyl species was IrCO monocarbonyls and only 10-20 % $Ir(CO)_2$ dicarbonyls, regardless of the varying CO dose between 10 and 60 L. To test whether the mono- and dicarbonyls form on the same Ir_1 adatoms, the system shown in Fig. 6.9B was scanned with a 3.5 V bias do desorb the CO molecules, and the subsequently acquired image shown in panel (C) reveals no detectable difference between the Ir_1 species which previously accomodated one or two CO molecules (white arrows).

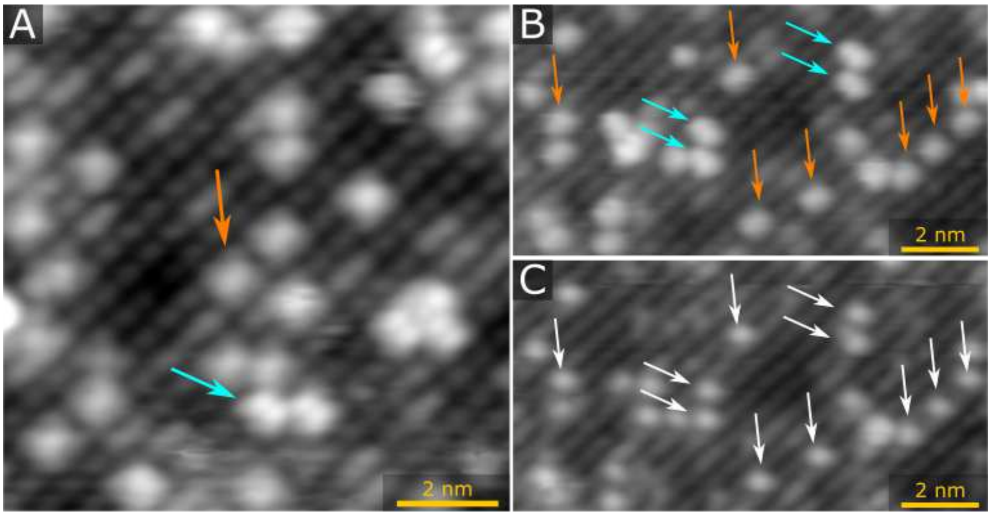

Figure 6.9: STM images acquired on the $Ir_1/Fe_3O_4(001)$ system after dosing 10 L CO at room temperature. (A,B) The majority species protrusions look similarly to bare Ir_1 adatoms, but are slightly elongated in the direction parallel to the Fe_{oct} rows (orange arrows). A small number of double-lobed species oriented perpendicular to the Fe_{oct} rows is observed. Further ncAFM experiments and DFT calculations clearly identify the elongated species as IrCO and the double-lobed species as $Ir(CO)_2$ (C) When the CO is desorbed by scanning with 3.5 V bias, the subsequently acquired image shows that the IrCO and $Ir(CO)_2$ form on the Ir_1 adatoms that appear the same in STM.

When the CO-saturated $Ir_1/Fe_3O_4(001)$ is annealed to 700 K and imaged again at 300 K (Fig. 6.10A), the majority species are circular protrusions located in the Fe_{oct}

rows, consistent with the appearance of 5-fold coordinated Ir_1 described previously. Given the mentioned inaccuracy of the temperature readouts in the STM chamber, it is not clear whether the CO is still adsorbed on the 5-fold coordinated Ir_1 or not. To find this out, a small area in the middle of the STM image was scanned with a 3.5 V and the image was taken again with the same scanning parameters (panel (B), the area scanned with high bias is highlighted by the yellow square). The 3.5 V scan should result in desorption of any adsorbed CO. Indeed, in the area scanned with high bias, all 5-fold Ir_1 have significantly higher apparent height ($\approx$ 110 pm, compared to $\approx$ 70 pm in panel (A)), indicating desorption of CO. Such difference in apparent height is consistent with the STM simulations of a 5-fold coordinated Ir_1 with and without CO; the models and corresponding STM simulations are shown in bottom right of each panel in Fig. 6.10. Outside of the area scanned with high bias, the apparent height of the on-the-row species the same as in panel (A), which decisively rules out any significant tip change. This dataset thus answers the question how the system evolves during the temperature ramp in TPD experiments: Although the CO is adsorbed on Ir_1 in the regular adsorption site which is 2-fold coordinated to the substrate, during the temperature ramp it migrates to the site 5-fold coordinated to the substrate, and the CO desorption takes place predominantly from here.

The details of the invidiual Ir carbonyl structures are best resolved in ncAFM images acquired with a CO-terminated tip. Figure 6.11A shows STM and ncAFM measurements of the same area on of a 0.08 ML $Ir_1/Fe_3O_4(001)$ surface; the surface was prepared as in Fig. 6.7A and then exposed to 3 L CO at room temperature. The images were acquired using a CO-functionalized tip at 78 K. While in STM the majority species on this surface are protrusions between the surface Fe rows that are slightly elongated in the Fe_{oct} row direction (orange arrow), in ncAFM the same species are resolved as two distinct protrusions. The bright contrast results from a repulsive interaction between the CO on the tip and the CO adsorbed on the Ir adatom. The supporting DFT calculations (panel (B)) show that adsorption of a single CO on the 2-fold Ir causes it to move towards the surface and form a weak bond to a subsurface O atom (Ir-O bondlength = 2.3 Å), which is offset from the Ir adatom along the Fe_{oct} row direction. The molecule thus tilts away from the surface normal to form an almost linear CO-Ir-subsurface O atom axis. The Ir has 3 bonds to lattice oxygen, and one to the CO molecule, in a pseudo-square-planar configuration. Two distinct protrusions are observed in ncAFM because the system switches rapidly between the two equivalent O atoms in the subsurface. This reorients the CO molecule to maintain the plane of the square, and a superposition of the two states is measured. The barrier for the switching process is calculated to be less than 0.1 eV. The distance between the protrusions observed in ncAFM appears larger than that calculated by DFT because the CO molecules adsorbed

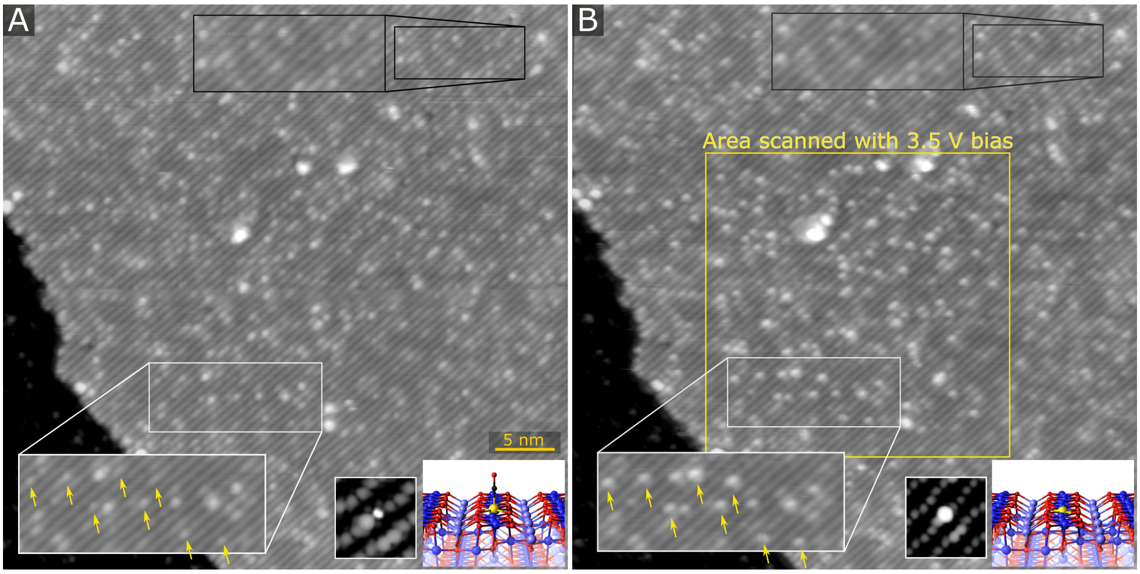

Figure 6.10: Evidence that CO remains adsorbed on the Ir_1 after it changes site to the incorporated 5-fold geometry. Panels A and B show room-temperature STM images acquired on the same area of a sample prepared by dosing 58 L CO on the surface with 0.2 ML 2-fold Ir_1. The sample was annealed to ca. 700 K to incorporate the resulting species into the 5-fold sites. Both images are scanned with the same parameters (U = 1.5 V, I = 0.3 nA), but before taking the image shown in B, a small area in the center (yellow square) was scanned with high bias (3.5 V). The in-the-row species in this square are significantly brighter than on the same area of panel A (the apparent height of the species marked with arrows is ca. 70 pm in panel A and ca. 110 pm in panel B). This is consistent with CO desorbing from the 5-fold Ir_1. The insets in bottom right of each panel show the DFT models and corresponding STM simulations (provided by M. Meier). The insets in the top right of each panel show that this effect is not observed outside of the area scanned with high bias, which decisively rules out any significant tip change taking place between acquisition of the two images.

on the surface and tip repel, and are then able to relax away from one another. In the configuration shown in Fig. 6.11B, the CO has a binding energy of -2.69 eV, while the Ir has a Bader charge of 0.83 (increased by 0.33 relative to the bare 2-fold adatom). An alternative explanation for the features seen in Fig. 6.11A is that two CO molecules are adsorbed on each Ir atom, and oriented parallel to the Fe_{oct} row direction (creating a tetrahedral environment for the Ir). Such a configuration was calculated, and the adsorption energy was calculated to be -1.6 eV per molecule. However, the structure is unstable against the dicarbonyl configuration shown in Fig. 3B (-2.4 eV per CO molecule), in which the CO adsorption create a square planar environment for the Ir atom. Such species are imaged as bright double-lobed protrusions with their axis perpendicular to the Fe_{oct} direction (Fig. 6.11C, cyan arrows). Our DFT calculations suggest that the Ir atom in the dicarbonyl is twofold coordinated to the support and has a Bader charge of 0.77, which is close to that of the monocarbonyl. The average binding energy of -2.4 eV suggests that binding a second CO molecule is strongly favoured thermodynamically, and thus should occur in the absence of kinetic limitations. We attribute the prevalence of IrCO species in our data to a combination of the low CO pressures used ($p_{CO} = 1 \cdot 10^{-8}$ mbar), and the repulsion between the IrCO and approaching CO molecules, which reduces the probability that $Ir(CO)_2$ can be formed. At catalytically relevant CO pressures, this limitation will be quickly overcome and the $Ir(CO)_2$ should dominate at room temperature for 2-fold coordinated Ir adatoms.

When the CO-exposed $Ir_1/Fe_3O_4(001)$ sample shown in Fig. 6.11A,C is annealed to 600 K and re-imaged at 78 K, some $Ir(CO)_2$ species remain, but the majority of protrusions are located within the surface Fe rows (see blue arrows in Fig. 6.11E). These species are very bright in ncAFM, consistent with strong repulsion between the CO on the tip and at the surface. This further confirms that the Ir species migrate to the 5-fold coordinated site in the surface prior to the desorption of the CO molecules.

Summary and Discussion

The presented results clearly show that Ir adatoms can occupy multiple cation-like sites on $Fe_3O_4(001)$, and that the barriers between them are low enough that switching can occur at reaction temperatures relevant to single-atom catalysis. Increasing the coordination from 2-, to 5- and eventually 6-fold is energetically downhill, so once Ir is incorporated into the subsurface it will be difficult to recover. Such an incorporation phenomenon has been observed before on this surface and was rationalized by the analogy to spinel ferrites ($M_xFe_{2\text{-}x}O_4$), which are stable for many 3d transition metals (M = Ti, Mn, Co and Ni) [70, 71, 82]. However, the same cannot be said about Ir, which does not typically form spinel ferrites and no $Ir_xFe_{2\text{-}x}O_4$ synthesis has been reported. There indeed is a significant difference between behavior of Ir and the ferrite forming metals on $Fe_3O_4(001)$: Upon prolonged thermal annealing the ferrite-forming metals diffuse deep into the bulk, but the Ir stays in the first subsurface layer and agglomerate here instead. The initial incorporation of Ir into the first subsurface layer however still remains a bit surprising, although compounds with Ir octahedrally coordinated to O^{2-} exist (rutile IrO_2, for example). Our results thus show that incorporation into the oxide might deactivate an Ir-based SAC well before thermal sintering into nanoparticles. Distinguishing between the 5- and 6-fold species would be difficult by transmission electron microscopy because their position is identical with respect to the surrounding cation lattice viewed from above, and it is likely that incorporation occurs under reaction conditions.

A very important result of this work is the finding that CO induces stronger interaction of the Ir_1 species with the $Fe_3O_4(001)$ substrate and leads to Ir_1 stabilization on the surface. This is evident on the IrCO monocarbonyl in the regular

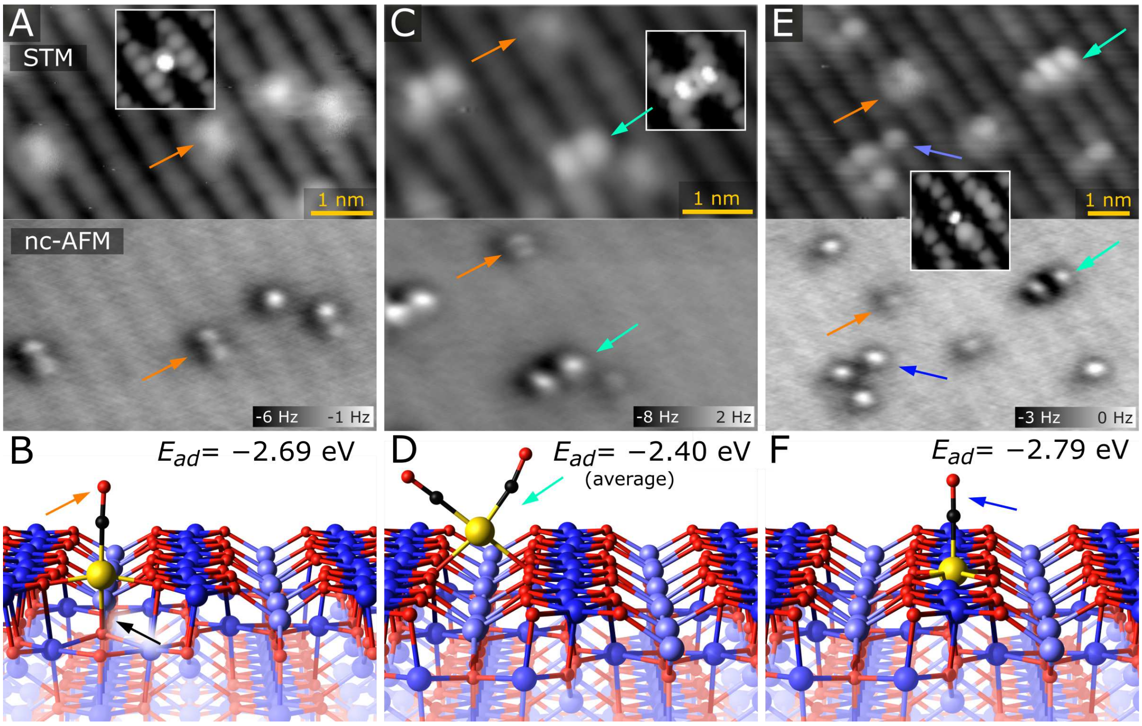

Figure 6.11: STM/ncAFM images of the $Ir_1/Fe_3O_4(001)$ model catalyst following exposure to CO at room temperature. All images were acquired at 78 K using a CO-functionalized tip. (A) IrCO species (orange arrow) dominate when CO adsorbs on 2-fold coordinated Ir adatoms, and are imaged either as elongated protrusions between the surface Fe rows in STM (resolved into two distinct protrusions in ncAFM) and, in a minority of cases, as single bright protrusions. Note that the Fe rows of the support are imaged dark in the ncAFM images as these atoms weakly attract the CO tip. (B) DFT-derived minimum-energy structure of an IrCO monocarbonyl. Note the additional bond (black arrow) that forms between the Ir adatom and an O atom in the subsurface layer, leading to a pseudo-square-planar environment. (C) $Ir_1(CO)_2$ dicarbonyls appear with a significantly lower density, and are imaged as bright double protrusions perpendicular to the Fe rows (cyan arrow) in both STM and ncAFM. (D) DFT-derived minimum-energy structure of an Ir_1 dicarbonyl. Note the square planar environment of the Ir adatom. (E) Heating the sample to 600 K leads to bright protrusions within the surface Fe rows (blue arrow). (F) Minimum-energy structures for the IrCO species formed at the 5-fold Ir atom calculated using DFT. Adsorbing the CO molecule completes an octahedral environment for the Ir atom. The insets shown in panels A, C and E are STM simulations based on the structures shown in B, D, and F, respectively. All images were taken with 1.5 V sample bias. DFT computations carried out by M. Meier, figure reprinted from [161].

adatom adsorption site, where an extra bond to the subsurface O is formed upon CO adsorption, and the double-lobed appearance in ncAFM serves as a direct experimental proof of this effect. The stabilizing effect of CO is however present in all the studied structures: with the adsorbed CO, the Ir stays in the 5-fold site up till

$\approx 600\,K$ (seen in the TPD results), but without the CO it would incorporate to subsurface already at $\approx 500\,K$ (evidenced by the XPS results taken in the same setup). Such a CO-induced stabilization is not common, and many previously published works have reported exactly the opposite effect with the CO being an accelerator of adatom sintering [26, 77, 80, 234, 235]. Even on this very same $Fe_3O_4(001)$ substrate, Pt and Pd adatoms were previously shown to rapidly diffuse and agglomerate upon CO adsorption [77, 80], which at the time was rationalized by the preference of the adatom to keep its bond order. Now it is clear that such interpretation is too simplistic and there must be a different explanation for the effects of CO adsorption. A plausible rationalization is found by analogy to coordination complexes: The Ir clearly prefers square-planar configuration which it forms upon formation of both mono- or dicarbonyls, and which would indeed be expected for a low spin d8 configuration of Ir(I). The stabilization effect then comes mainly from the fact that such an arrangement is possible to form on this $Fe_3O_4(001)$ surface due to the favourable spacing of the lattice O, which allows filling of the so-called coordination vacancies of the square-planar geomtery with CO (in the case of dicarbonyl) or CO and lattice O (in the case of monocarbonyl). Similarly, the 5-fold Ir can be understood as an octahedral complex with one coordination vacancy, and filling this with CO stabilizes the system. Comparison to the cases of Pt and Pd on the same surface reveals that the Pt and Pd prefers linear PtCO geometry, which leads to breaking of one of the bonds to the surface and allowing diffusion.

The analogy to coordination complexes is also borne out by the local magnetic moments and Bader charges obtained in our DFT calculations. The stable Ir dicarbonyl has a magnetic moment of 0, as expected for an ideal square planar Ir(I) complex in a low spin d8 configuration. The monocarbonyl is unable to reach the ideal square-planar geometry due to the constraints of the surface lattice, and its magnetic moment is an imperfect 0.3. Completion of the octahedral environment at the 5-fold Ir_1 again leads to a magnetic moment of 0 in DFT, consistent with the low-spin Ir(III) state. In contrast, the bare 2-fold and 5-fold Ir adatoms have non-zero magnetic moments of 1.11 and 0.28, respectively. It is thus difficult to assign a formal oxidation state to these and a similar behavior is expected for any adatoms which are not coordinatively saturated. Comparison of Bader charges of a bare 2-fold coordinated Ir_1 (0.50) with Ir cabonyls in the same site (0.77 for IrCO and 0.83 for $Ir(CO)_2$) further confirms that CO changes the electronic structure of the Ir. This effect is important because the CO stretch frequency is typically used to measure the charge state of metal atoms in SAC, but is clearly not an innocent probe of the system, similarly to previous reports on Au_1/MgO [236].

All of this shows that SAC systems share many properties of both heterogeneous and homogeneous catalysts. In the single-atom limit, the bonding environment of the adatom will play a significant role in the strength with which reactants are bound, and in the number of reactants that can be bound at the single site. Therefore, synthesizing single-atom variants of established nanoparticle catalysts is not an optimal approach, and experimental and theoretical screening is required to determine the metal/support combinations representing the best bet for a particular reaction. This, of course, requires the catalytic mechanisms at work to be firmly established. We show here that CO_2 can be formed by extraction of O from the lattice, but that this process requires significant energy. Additionally, from our results it is not entirely clear which species catalyze the CO oxidation, as it is clearly not all of the Ir_1 adatoms. It is tempting to assign the CO_2 production to the $Ir(CO)_2$ dicarbonyls, and such a hypothesis is supported by the comparison of the number of dicarbonyls found in STM experiments (10-20 %) with the amount of produced CO_2 in TPD data (12-15 % of the CO is converted). Nevertheless, preliminary DFT computations do not support such scenario, and suggest another mechanism might take place at Ir_1 sites close to defects or incorporated Ir_1 sites (experimental evidence of such species is shown in section 6.4). Li et al. [225] recently proposed that CO oxidation can occur with extremely low barriers through an OCOO intermediate adsorbed at the single site. In our view, such a process could be promoted by an adatom geometry possessing two coordination vacancies such as the 2-fold Ir demonstrated here. The 5-fold Ir, more stable at reaction temperatures, could not perform this function. Similar considerations hold for more complex reactions such as hydroformylation [43, 44], which is typically performed by Rh complexes in solution and is a target for heterogenization by SAC. To mimic the mechanism of the complex requires that CO and an alkene are simultaneously coordinated at the metal centre, which is something that only the 2-fold Ir could facilitate. While parallels to homogeneous catalysis clearly exist, O^{2-} is not a common ligand in such systems, and much needs to be learned about how the rigidity of the crystal lattice will affect the catalytic properties. Recent literature reports that a so-called adaptive coordination, i.e. the ability to break and re-make multiple bonds between the single atom and the substrate during the catalytic reaction, is required for succesful heterogenization of selected reactions [237]. It will thus be interesting to see whether this can be done on oxide surfaces.

6.3 Adsorbate-induced Structural Evolution Changes the Mechanism of CO Oxidation: Rh/Fe_3O_4(001)

The structure of a catalyst often changes in reactive environments, and following the structural evolution is crucial for the identification of the catalyst's active phase and reaction mechanism. This section presents an atomic-scale study of CO oxidation on a model Rh/Fe_3O_4(001) "single-atom" catalyst, which has evolves very differently depending on which of the two reactants, O_2 or CO, is adsorbed first. It will be shown that O_2 destabilizes Rh atoms, leading to the formation of Rh_xO_y clusters; these catalyze CO oxidation via a Langmuir–Hinshelwood mechanism at temperatures as low as 200 K. However, if CO adsorbs first, the system is poisoned for direct interaction with O_2, and CO oxidation is dominated by a Mars-van-Krevelen pathway at 480 K. This section is based on a published paper [212].

Introduction

Supported rhodium catalysts show high activity for a number of reactions, including CO oxidation [238–241]. It is generally accepted that Rh nanoparticles supported on rigid, irreducible substrates catalyze CO oxidation via the Langmuir–Hinshelwood (L–H) or Eley–Rideal (E–R) mechanisms, where the CO and O_2 molecules either coadsorb on the surface (L–H), or one of the molecules reacts directly from the gas phase with the other molecule adsorbed on the surface (E–R) [32, 242–247]. However, the reactivity of the system is often affected by the choice of support, and reducible supports enable an alternative pathway, the so-called Mars-van-Krevelen (MvK) mechanism. Here, oxygen is extracted from the metal oxide lattice to oxidise CO, and the lattice is repaired by O_2 from the gas phase [38, 79, 161, 248, 249]. Metal–support interactions are not always beneficial, however, and encapsulation by the support can completely deactivate the catalyst [70, 71, 161, 207]. Improving a catalyst's activity, selectivity, and stability requires the optimization of atomic-scale processes that are very difficult to ascertain on working catalysts. This motivates the use of well-defined model systems studied by the surface science approach, which can provide atomic-scale insights.

In this section it is studied how CO oxidation proceeds on a Rh/Fe_3O_4(001) model "single-atom" catalyst. Using a combination of temperature-programmed desorption (TPD), scanning tunneling microscopy (STM), and X-ray photoelectron spectroscopy (XPS), we show the system is active for CO oxidation by both L–H and MvK mechanisms, depending on which of the reactants the surface is exposed to first. Oxygen adsorption leads to formation of superoxo (O_2) species bound to Rh_1 adatoms, which rapidly agglomerate to small Rh_xO_y clusters. The clusters contain weakly bound oxygen, which reacts with CO below room temperature. In contrast, CO adsorption on the bare Rh_1 species poisons the system for O_2 adsorption, but CO oxidation nevertheless takes place via a MvK mechanism at ca. 480 K. Two different deactivation mechanisms are observed: the oxidised clusters become inactive after the first desorption of the weakly bound oxygen, while the Rh_1 adatoms incorporate into the support lattice as the CO desorbs.

Results

Rh species on Fe_3O_4(001)

Figure 6.12a,b shows STM images of the Fe_3O_4(001) surface before and after deposition of Rh. Panel (a) shows an STM image of the clean surface and a corresponding model of the SCV reconstructed surface. After deposition of Rh at room temperature, isolated Rh_1 adatoms appear as bright protrusions (red circles in Fig. 6.12) sitting between the Fe_{oct} rows. In addition to the single Rh_1 adatoms, larger elongated species (cyan circle in Fig. 1b) are observed, which in subsequent STM scans exhibit a distinctive hopping motion over the adsorption site (Fig. 6.12c,d). These species are identified as metastable Rh_2 dimers, and can be split into two Rh_1 adatoms by bias pulsing or high-bias scanning. Fig. 6.12e,f shows this process on two STM images acquired on the same spot: in Fig. 6.12e two Rh_2 dimers are observed (cyan arrows), Fig. 6.12f shows pairs of isolated Rh_1 adatoms (smaller paired arrows) appearing instead of the Rh_2 after the surface was scanned with a +3 V bias. The observed hopping of the Rh_2 is restricted to the given adsorption site, and thus it does not lead to destabilization of the system by diffusion or agglomeration. Further details about the Rh_2 dimers are shown in section 6.4. Apart from the dimer hopping, no mobility of Rh species is observed in subsequently acquired STM images at room temperature under UHV conditions. The Fe_3O_4(001) surface supports the Rh_1 adatoms even at significantly higher coverages; Fig. 6.13 shows an STM image of 0.5 ML Rh/Fe_3O_4(001) featuring a high density of Rh_1 adatoms, and XPS spectra acquired on an Fe_3O_4(001) surface with varying Rh coverage between 0.1 and 0.8 ML Rh showing virtually no difference in Rh 3d peak shape or position.

At elevated temperatures, the Rh_1 adatoms are unstable against incorporation into the Fe_3O_4(001) support. As was shown in the previous sections of this thesis, such a phenomenon has been observed for several different metal adatoms on Fe_3O_4(001) before and the foreign adatom can either substitute a 5-fold coordinated surface Fe_{oct} or incorporate in the vacant octahedral site of the SCV reconstruction [70, 71, 82, 161]. Schematic representations of the three possible sites of Rh_1 near the surface are shown in insets in Fig. 6.14. The incorporation of Rh takes place at temperatures above ≈ 450 K and can be followed both in STM and XPS, as shown in Fig. 6.14a,b. STM images taken after annealing to 500 K show predominantly elongated (orange circle) and circular (purple circle) features on the Fe_{oct} rows, which is consistent with Rh_1 incorporated into the subsurface 6-fold site or surface 5-fold site, respectively. Such a behavior was previously observed for a number of other metals on this surface and STM simulations of such species are shown in the previous section of this thesis and references [70, 161]. Additionally, an increased number of bigger brighter features, presumably Rh clusters, and a very small number of remaining 2-fold Rh_1 adatoms (red circle) is observed. Fig. 6.14b shows the Rh 3d region of

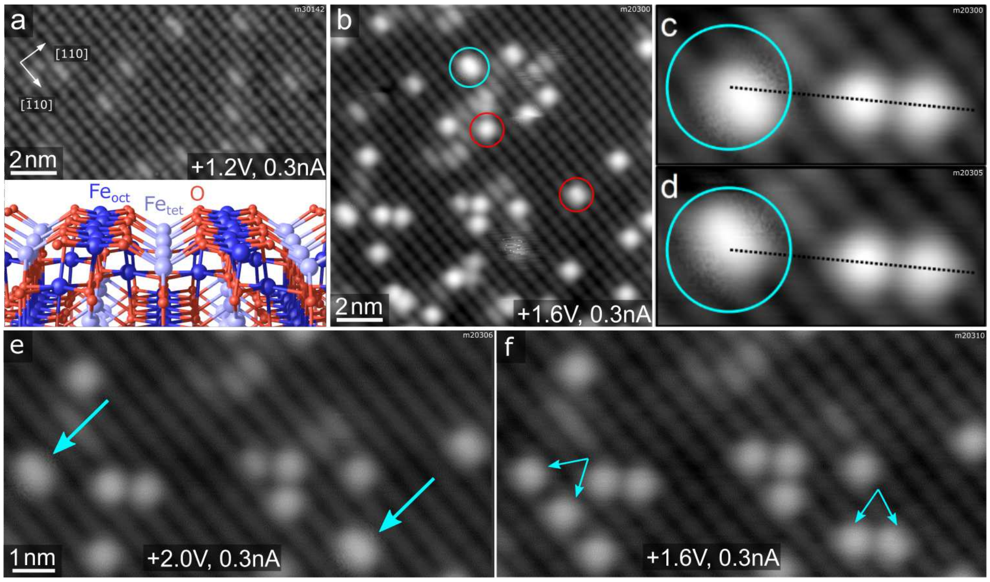

Figure 6.12: Characterization of the Rh/Fe_3O_4(001) system by STM. (a) STM images of pristine Fe_3O_4(001) surface. The inset shows a model of the Fe_3O_4(001) surface with the octahedral Fe_{oct}, tetrahedral Fe_{tet} and O atoms being represented by dark blue, light blue and red spheres, respectively. (b) After deposition of 0.2 ML Rh at room temperature, the majority species are Rh_1 adatoms (red circles), but the image also shows slightly elongated species which we identify as Rh_2 dimers (cyan circles). (c,d) The Rh_2 dimers exhibit characteristic hopping motion in subsequent STM images (broken lines for guidance). (e,f) Scanning with a +3 V bias results in dissociation of the Rh_2 dimers (cyan arrows in panel e) into pairs of single Rh_1 adatoms (paired cyan arrows in panel f). The +3, V scan was performed between acquisition of images shown in (e) and (f). Data taken by R. Bliem, figure reprinted from [212].

XPS spectra taken after depositing 0.6 ML Rh and heating to different temperatures. After deposition at 300 K, the Rh 3*d* peak maximum is located at ≈ 307.7 eV, but its broad shape suggests convolution of several components. Apart from the main signal corresponding to 2-fold Rh_1, the additional XPS components might come from the Rh_2 dimers or Rh_1 adatoms residing in the vicinity of surface defects or step edges. On different samples, small variations of the peak maximum between 307.7 and 308.1 eV were observed, most likely depending on the relative number of these species. After heating to 400 K, the low-binding-energy side of the peak decreases (around ≈ 307.2 eV) and the peak maximum shifts to 308.0 eV. Heating above 450 K leads to an increase of a higher-binding-energy component at 309.5 eV and a decrease of the signal at 308.0 eV. After heating to 650 K, the 308.0 eV peak is no longer observed, and the 309.5 eV component is dominant. Prolonged heating above this temperature leads to a decrease and eventual disappearance of the Rh signal in XPS, consistent with diffusion of Rh into the Fe_3O_4 bulk (Fig. 6.15).

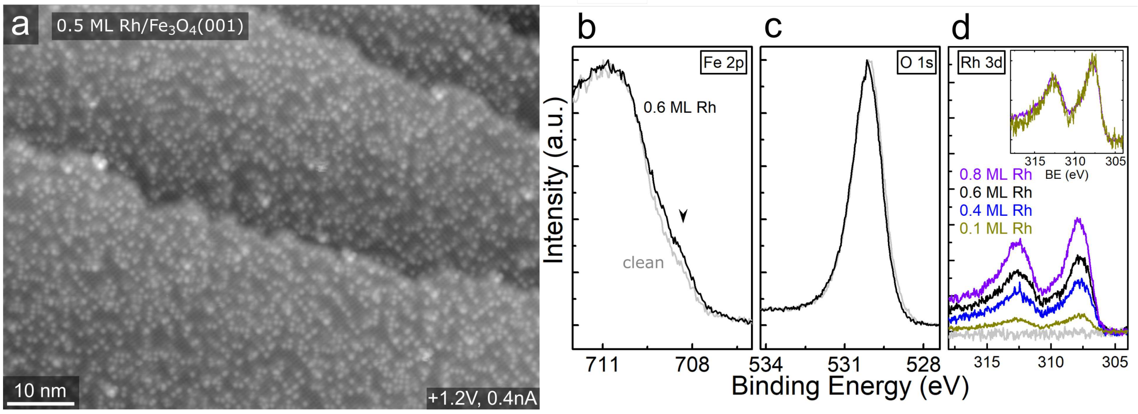

Figure 6.13: The Fe_3O_4(001) surface can support single Rh adatoms up to high coverages. (a) STM image of 0.5 ML Rh/Fe_3O_4(001) showing that the majority of Rh stays as single Rh_1 adatoms. (b-d) The Fe 2*p*, O 1*s* and Rh 3*d* regions of XPS spectra acquired on Rh/Fe_3O_4(001) with varying Rh coverages. Notably, the normalized spectra shown in the inset of panel (d) show that the shape and position of the Rh 3*d* peak is virtually the same for 0.1 ML and 0.8 ML coverage of Rh. XPS data taken and analyzed by J. Hulva, figure reprinted from [212].

Thus, we attribute the 309.5 eV component to Rh incorporated into the Fe_3O_4(001) substrate.

The Fe 2*p* and O 1*s* regions only show small differences with Rh deposition and heating (Fig. 2c,d). Upon Rh deposition, an Fe 2*p* shoulder at ≈ 708.5 eV slightly increases in comparison to the clean surface, indicating an increased amount of Fe^{2+} near the surface. This shoulder decreases again upon heating, presumably because the Rh incorporates and thus the number of near-surface cations decreases.

Exposing Rh/Fe_3O_4(001) to O_2

When the Rh_1/Fe_3O_4(001) system is exposed to O_2 at room temperature, the Rh_1 adatoms become mobile and begin to agglomerate. Figure 6.16a–c shows three frames of an STM movie acquired while keeping a constant background pressure of $2 \cdot 10^{10}$ mbar O_2 in the analysis chamber. Single adatoms (highlighted by red circles) form well-resolved oxidised Rh_2O_x dimers (yellow rectangles) and subsequently bigger Rh_xO_y clusters (purple rectangle). Over the course of the STM movie, no O_2 adsorption was observed on the Rh_2 dimers (cyan circle). After dosing a higher amount of O_2 in the preparation chamber (50 L), the majority species observed in STM are small Rh_xO_y clusters, although some adatoms remain (Fig. 6.16). Scanning of the oxidised Rh_xO_y species is difficult because the tip is very unstable, with frequent tip changes suggesting the presence of weakly bound species that interact with the STM tip. A comparison of the cluster density following saturation exposure with the initial adatom coverage suggests that the majority contain at most 2–3 Rh atoms. The fact that similar Rh agglomeration was observed after O_2 exposure in

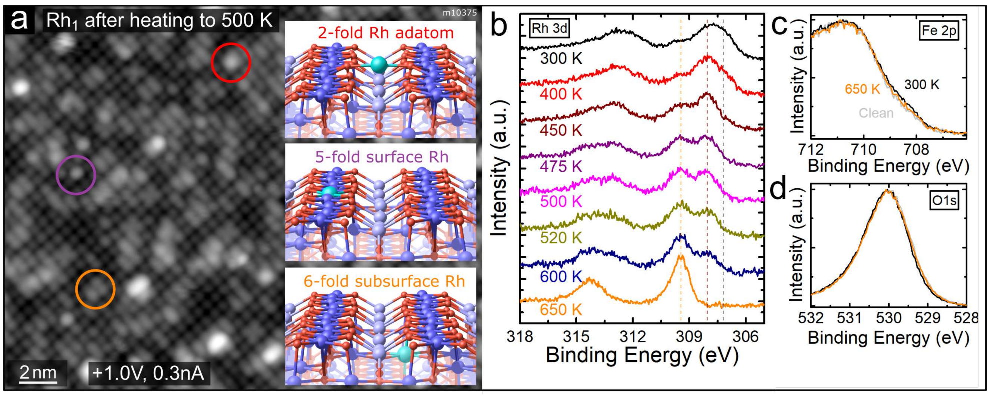

Figure 6.14: Rh_1 adatoms incorporate into the $Fe_3O_4(001)$ support upon annealing above 450 K. (a) STM images after deposition of 0.4 ML Rh and heating to 500 K show predominantly circular protrusions (highlighted by purple colour) and elongated protrusions (orange colour) on the Fe_{oct} rows. Only a very small number of Rh_1 remain in the 2-fold coordinated site between the Fe_{oct} rows (red colour). We identify the new species as Rh_1 incorporated in the octahedral cation sites near the surface, consistent with previously reported studies of various metal adatoms on $Fe_3O_4(001)$ [70, 161]. Schematic representations of these sites are shown in the insets and labelled with the color of the corresponding circle. (b) Rh $3d$ region of the XPS spectra (monochromatized Al Kα, grazing emission) taken after heating to different temperatures (measured after cooling back to 300 K). Upon heating to 400 K the Rh $3d$ peak maximum shifts to 308.0 eV, as the low binding-energy shoulder at 307.2 eV decreases. Heating above 450 K leads to an increase of the 309.5 eV component, which becomes dominant above 600 K. We attribute this component to Rh incorporated into the octahedral sites of the $Fe_3O_4(001)$ surface. (c,d) The Fe $2p$ and O $1s$ peaks corresponding to the first and last spectra shown in (b). Notably, in the Fe $2p$ region the shoulder at ≈ 708.5 eV slightly increases upon Rh deposition, indicating an increased amount of Fe^{2+} near the surface. This shoulder decreases again upon heating as the Rh cations diffuse into deeper layers. XPS data taken and analyzed by J. Hulva, figure reprinted from [212].

the preparation chamber suggests that the mobility observed in STM movies is not solely tip-induced. After heating the surface with oxidised Rh_xO_y clusters to 400 K, no structural differences are observed, but the imaging becomes much more stable, suggesting desorption of the weakly bound species or restructuring of the clusters.

Fig. 6.17 shows O_2 TPD measurements from the clean $Fe_3O_4(001)$ surface (grey curve) and from the surface with 0.6 ML Rh (orange and brown curves). On the pristine $Fe_3O_4(001)$ surface, O_2 physisorbs below 70 K (desorption peak labelled α in Fig. 6.17a), but in our work this phase could not be saturated due to the O_2 dosing temperature (60 K) being within this desorption peak. Thus, desorption already takes place before the start of the heating ramp and the magnitude and shape of the α peak varies in repeated measurements due to slightly varying time between dosing and heating. Above 100 K, the O_2 TPD acquired on the pristine surface exhibits

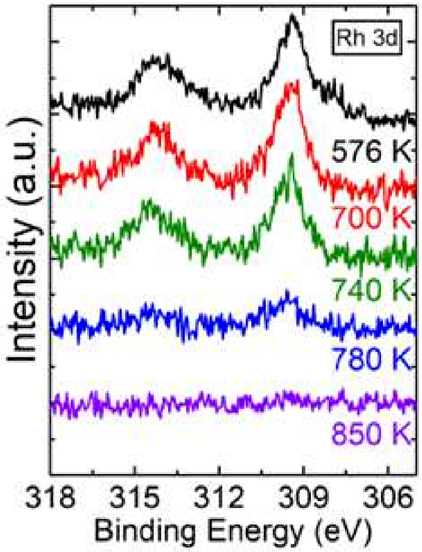

Figure 6.15: Annealing to elevated temperatures causes diffusion of Rh into the bulk, eventually recovering the pristine Fe$_3$O$_4$(001) surface. Each of the shown spectra (Al Kα, grazing emission) was taken after annealing to the given temperature for 5–15 minutes. After the last annealing to 850 K, a Rh signal is no longer discernible. Data taken by J. Hulva, figure reprinted from [212].

two distinct peaks, labelled β and γ in Fig. 6.17a, which presumably correspond to desorption from defects, domain boundaries, and/or step edges. The presence of Rh$_1$ adatoms on the surface prior to O$_2$ dosing leads to an increase of these two desorption peaks and induces a sharp new desorption peak, δ, at $\approx$330 K. When the TPD measurement was repeated on the same sample (following termination of the previous heating ramp at 570 K), the δ peak was no longer present (brown curve in Fig. 6.17a), and a similar result was observed in a separate experiment when the first heating ramp ended already at 380 K, before any Rh incorporation took place (evidenced by XPS spectra).

XPS characterization of O$_2$ adsorption on Rh/Fe$_3$O$_4$(001) is shown in Fig. 6.17b,c. Spectra taken directly after Rh deposition at 200 K and dosing 1.5 L O$_2$ at 60 K reveal two new components in the O 1s region at 533.7 and 536.9 eV (red curve in Fig. 4b). The 536.9 eV signal quickly decreases over time and completely disappears within several minutes. This is consistent with O$_2$ physisorbed on Fe$_3$O$_4$(001) readily desorbing at 60 K. The 533.7 eV component remains unchanged upon heating to 105 K, but disappears upon heating above 250 K (blue and orange curves in Fig. 6.17b). After heating to 300 K (orange curve), the spectrum in the O 1s region closely resembles the spectrum acquired on a pristine Fe$_3$O$_4$(001) surface (grey curve), save for a very small and broad shoulder between 530–535 eV, which can be attributed to a small amount of water adsorbed on surface defects. Upon heating

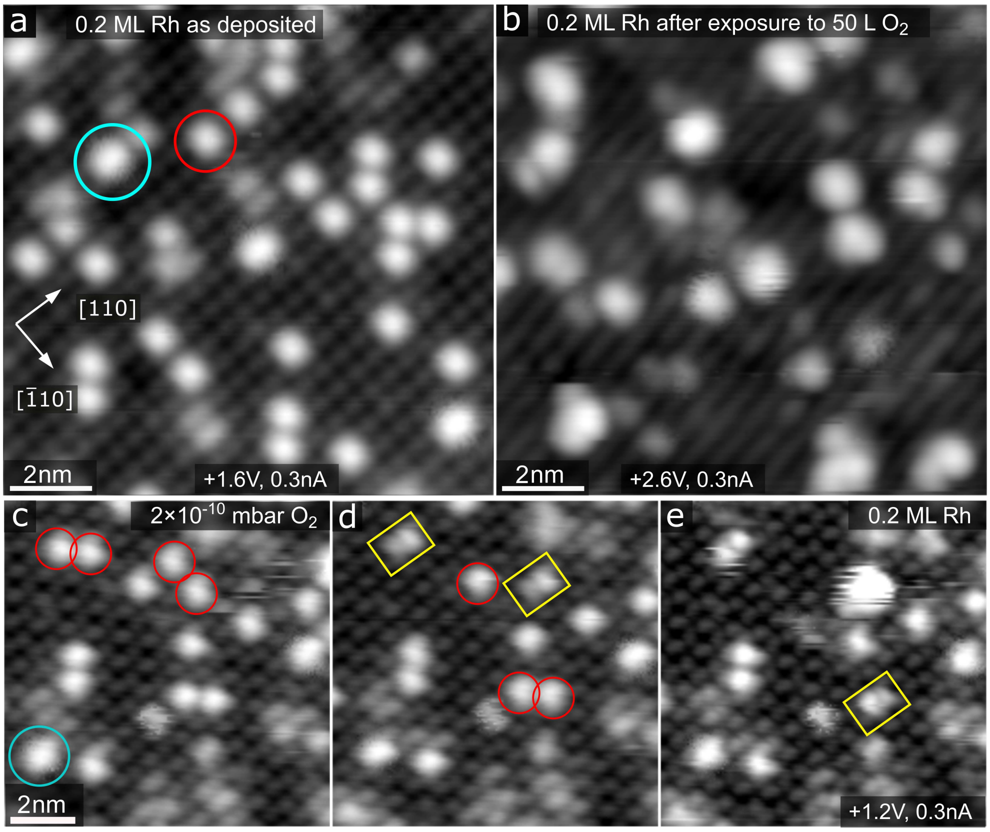

Figure 6.16: STM of $Rh_1/Fe_3O_4(001)$ and its interaction with oxygen. (a–c) Three frames from an STM movie acquired while keeping a constant O_2 background pressure of $2{\cdot}10^{10}$ mbar. Panel (a) shows a majority of single Rh_1 adatoms (red circles). During the O_2 exposure these species first form well-resolved Rh_2O_x clusters (yellow rectangles in panels (b) and (c)) and subsequently bigger nanoparticles (purple rectangle in panel (c)). (d) After a high dose (50 L) of O_2 at room temperature the imaging becomes unstable, and the majority species are larger bright clusters of varying size and shape. A few Rh_1 adatoms remain; one of them is highlighted by the red circle. Panels (c-e) originally shown in a PhD thesis of R. Bliem, figure reprinted from [212].

to higher temperatures up to 730 K, no significant change is observed in the O 1*s* region.

The adsorption of O_2 can also be followed in the Rh 3*d* region. Fig. 6.17c shows spectra taken after Rh deposition (0.6 ML), dosing O_2 at 60 K, and heating to different temperatures. Directly after Rh deposition at room temperature the shape of the Rh $3d_{5/2}$ peak has a maximum at ≈ 307.7 eV, but as mentioned previously, its shape suggests convolution of several components. A small shoulder at ≈ 309.5 eV corresponds to Rh incorporated in the octahedral sites of the support. After dosing O_2 at 60 K, the maximum of the Rh $3d_{5/2}$ peak shifts by ≈ 0.9 eV to 308.6 eV. Heating to 300 K induces a further shift to ≈ 309.0 eV, and this position remains the same with heating to 400 K. At this temperature, a small shoulder at 308.2 eV appears.

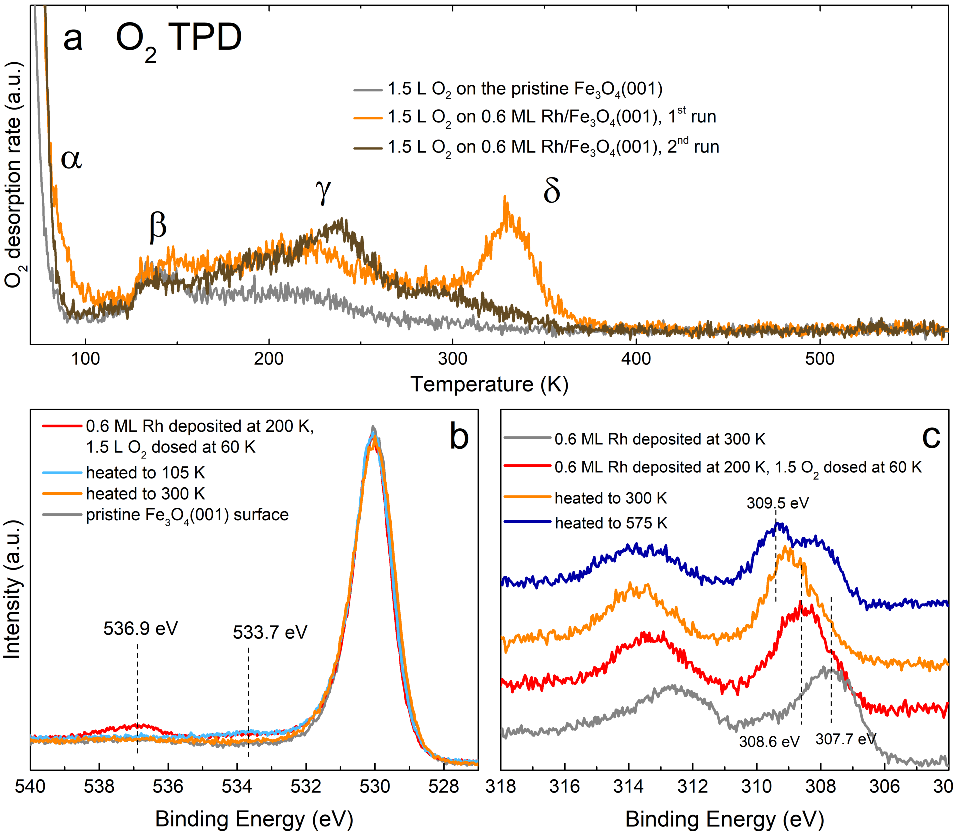

Figure 6.17: Spectroscopic characterization of O_2 adsorption on Rh/Fe$_3$O$_4$(001) by TPD and XPS. In all spectra, 1.5 L O_2 was dosed at 60 K. (a) O_2 TPD spectra acquired in the first (orange curve) and second (brown curve) dosing on 0.6 ML Rh/Fe$_3$O$_4$(001). Notably, the δ peak at $\approx$330 K appears only in the first dosing experiment. Reference spectra of the clean surface are plotted in grey. (b,c) Details of the O 1*s* and Rh 3*d* XPS regions (monochromatized Al Kα, grazing emission) of 0.6 ML Rh/Fe$_3$O$_4$(001) after O_2 dosing and heating to different temperatures. Compared to the pristine Fe$_3$O$_4$(001), two new components in the O 1*s* region are identified, having their maxima at 533.7 and 536.9 eV. The spectra taken after heating above room temperature look identical to the orange curve taken at 300 K. The whole O 1*s* region is shown in the inset in (b). (c) Adsorption of O_2 at 60 K causes a $\approx$0.9 eV shift of the Rh 3*d* peak, and a further shift is observed upon heating to 300 K. Heating above $\approx$500 K leads to growth of the 309.5 eV component corresponding to Rh incorporated into the substrate. Up to 300 K, the spectra were taken at the temperatures given; for higher temperatures, the spectra were taken after cooling the sample back to 300 K.

Heating above 460 K causes growth of the 309.5 eV component corresponding to incorporated Rh and slight increase of the signal at 308.2 eV. Above 700 K only the signal from the incorporated Rh remains. The Fe 2*p* region does not show any significant changes with O_2 adsorption and heating (not shown). The question of how the changes in XPS spectra correlate to the O_2-induced Rh_1 agglomeration observed by STM is covered in the discussion section.

Exposing Rh/Fe_3O_4(001) to CO

The same experimental approach as utilized above for O_2 was used to study CO adsorption on the Rh_1 adatoms. Figure 6.18 shows five frames of an STM movie recorded while keeping a background pressure of $5\cdot10^{-9}$ mbar CO in the analysis chamber. In panel (a), the vast majority of the Rh_1 species have an apparent height of ≈ 180 pm (red circle). Over the course of the movie, the apparent height of the individual Rh_1 species abruptly decreases to 95–125 pm (panels b–d) and eventually almost all of the Rh_1 appear darker (panel (e)). We attribute this change to the formation of monocarbonyl RhCO, and the reduction of the apparent height to the modification of empty Rh states near the Fermi level through the interaction with CO. With higher doses of CO, we also observe double-lobed species oriented perpendicular to the surface Fe rows, which we assign as $Rh(CO)_2$ (orange arrow in Fig. 6.18e and Fig. 6.19). NcAFM measurements of the Rh carbonyls acquired with a CO-terminated tip at 78 K are shown in Fig. 6.19. These reveal that both the Rh mono- and dicarbonyls appear strikingly similar to the Ir carbonyls described in the previous section, and one would indeed expect similar behavior for these two metals. As in the Ir case, the concentration of the dicarbonyl species never exceeded 25 % of the total, which we attribute to the low pressures used in our experiments. Additional details about the formation mechanism of the $Rh(CO)_2$ species are provided in section 6.4. Neither the monocarbonyls nor dicarbonyls appear to interact with molecular O_2, as no changes were observed upon subsequent O_2 exposure in room-temperature STM measurements.

In ^{13}CO TPD experiments on 0.5 ML Rh/Fe_3O_4(001), we observe a ^{13}CO desorption peak with a maximum at ≈ 530 K, which has an additional shoulder at ≈ 450 K (Fig. 6.20a). Comparison to the spectrum acquired on the pristine Fe_3O_4(001) reveals that all the desorption signal above 250 K is related to Rh, and that the presence of Rh leads to disappearance of a defect-related ^{13}CO desorption peak at ≈ 190 K. On Rh/Fe_3O_4(001), a small ^{13}CO signal is observed at ≈ 480 K, which we attribute to CO oxidation via a Mars-van-Krevelen mechanism. This phenomenon has been previously observed for Ir single atoms and Pt clusters on Fe_3O_4(001) [79, 161]. No CO desorption is observed above 580 K and in XPS spectra the C 1*s* region is featureless after heating to these temperatures (Fig. 6.20c). The CO desorption features below 200 K in the TPD spectra correspond to CO adsorption on the clean Fe_3O_4(001) surface [208]. Focusing on the Rh 3*d* and C 1*s* regions of the XPS spectra, CO adsorption at 60 K induced a shift of the Rh 3*d* peak maximum to 308.5 eV accompanied by the emergence of C 1s peak components at 290.6 eV and 287.3 eV. The 290.6 eV peak corresponds to adsorption of CO on the bare Fe_3O_4(001) surface

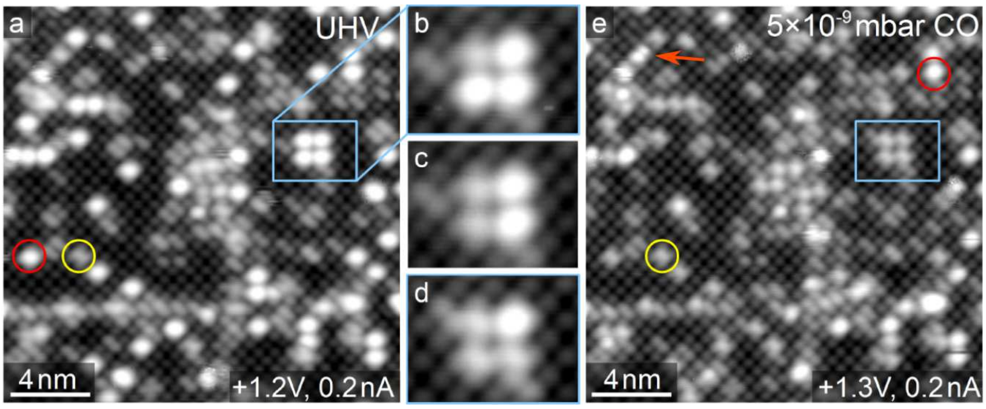

Figure 6.18: Adsorption of CO on the Rh1/Fe_3O_4(001) followed by STM. In panel (a), acquired in UHV, the vast majority of the Rh_1 adatoms (red circle) have an apparent height of $\approx$ 180 pm. (b–d) During exposure in $5{\cdot}10^{-9}$ mbar CO, the individual Rh_1 change their apparent height one by one to $\approx$ 95–125 pm. We identify these as Rh(CO) species. (e) After a CO dose of $\approx$ 10 L, the majority of Rh_1 are darker. The images also show a few double-lobed features (orange arrow), which we attribute to $Rh(CO)_2$ dicarbonyls. Detailed images of these species are shown in Fig. 6.19. Data taken by R. Bliem, figure reprinted from [212].

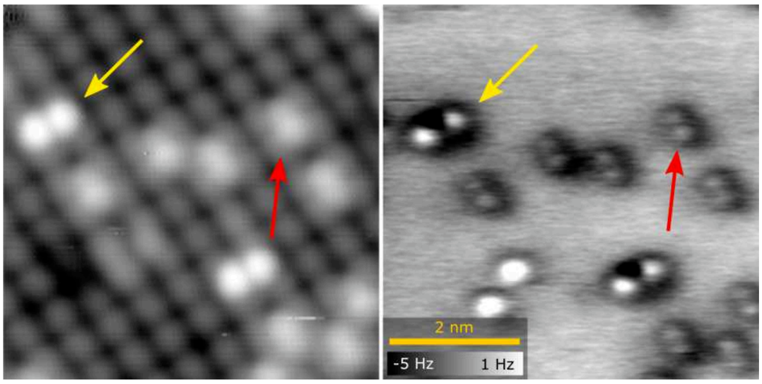

Figure 6.19: STM (a) and ncAFM (b) images acquired at 78 K with a CO-terminated tip on the same spot of the Rh_1/Fe_3O_4(001) surface after exposure to CO. The red arrow marks the RhCO monocarbonyl species, which is resolved as a faint double protrusion in the ncAFM images. By analogy to Ir_1/Fe_3O_4(001) described in the prevous chapter, this is because an additional bond to the subsurface O is formed to complete a pseudo-square-planar geometry, and the system rapidly switches between being bonded to one of the two equivalent subsurface O atoms. Yellow arrows mark the dicarbonyl $Rh(CO)_2$ species. These adopt the ideal square-planar geometry without formation of any additional bonds. Figure reprinted from [212].

[208]. Heating to 300 K leads to desorption of CO from Fe_3O_4(001), so that only CO bound to the Rh species remains (287.3 eV component in the C 1s region). The Rh 3d peak maximum shifts to lower binding energy (308.2 eV), and this position stays constant upon heating to higher temperatures. After the CO desorption from

the Rh species above ≈ 500 K, the majority of the Rh incorporates into the surface, clearly evidenced by the increase in intensity of the component at 309.5 eV.

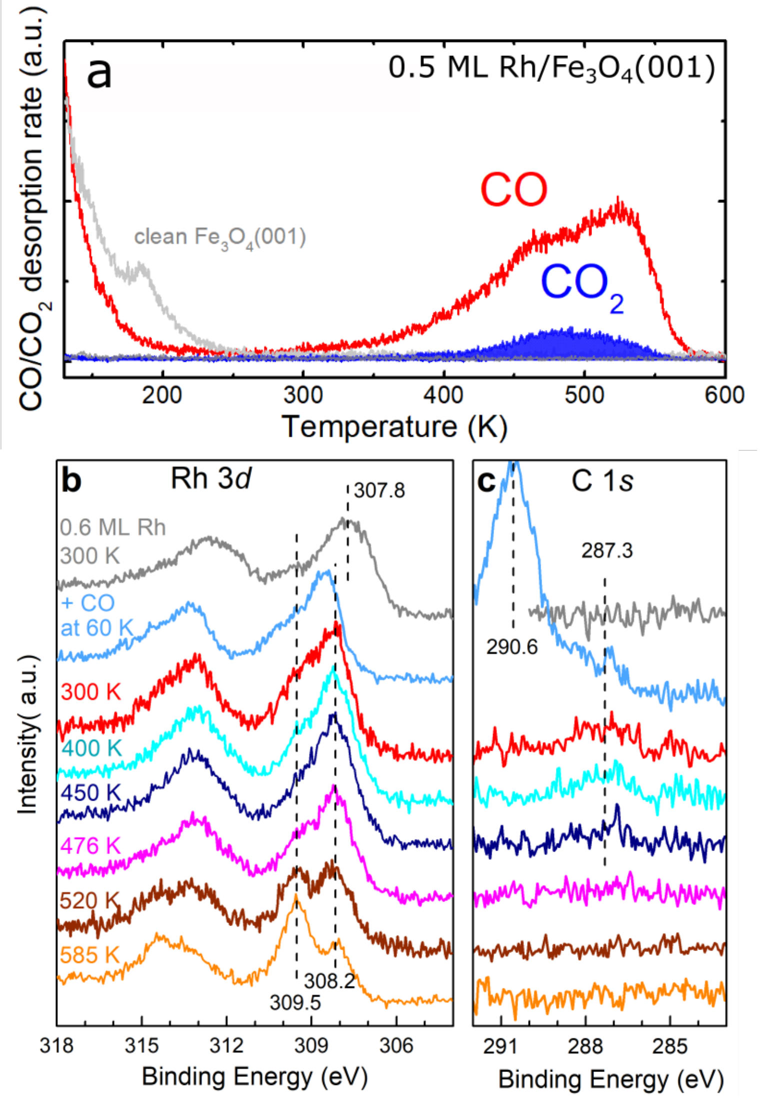

Figure 6.20: TPD and XPS characterization of CO adsorbed on Rh/Fe_3O_4(001). (a) CO desorbs from 0.5 ML Rh/Fe_3O_4(001) in a peak with a maximum around 530 K. A smaller signal of CO_2 is observed peaking around 480 K. (b) Adsorption of CO at 60 K on 0.6 ML Rh/Fe_3O_4(001) shifts the Rh 3*d* photoemission peak maximum to 308.5 eV, but heating to 300 K shifts the maximum to 308.2 eV. With annealing to temperatures above 500 K, a new component develops at 309.5 eV, due to Rh incorporated into the Fe_3O_4(001) support. (c) In the C 1*s* region of the XPS spectra, adsorption of CO at 60 K results in a dominant feature at 290.6 eV, corresponding to CO adsorbed at the Fe_3O_4(001) surface [208], and a smaller peak at 287.3 eV, corresponding to CO adsorbed on the Rh species. The 287.3 eV component is still observed after heating to 450 K. Above this temperature, no C 1*s* signal is observed in XPS. Data taken by J. Hulva, figure reprinted from [212].

Sequential dosing experiments

Sequential ^{13}CO and $^{18}O_2$ dosing experiments were performed to find out whether the Rh adatoms or Rh_xO_y clusters can co-adsorb CO and O_2. Fig. 6.21a–d shows the CO (red) and CO_2 (blue and orange) signals desorbing from a 0.5 ML $Rh/Fe_3O_4(001)$ sample exposed to CO and O_2 at different temperatures and in a different order. The blue area corresponds to CO_2 formed via a MvK mechanism ($^{13}C^{16}O_2$, mass 45), while the orange area indicates CO_2 formed by a L–H mechanism ($^{13}C^{16}O^{18}O$, mass 47). Fig. 6.21a provides a reference in which the sample was saturated by ^{13}CO at 300 K. Dosing O_2 on the sample predosed with ^{13}CO at 130 K (panel b) leads to a lower CO desorption signal, and the overall amount of CO_2 produced is increased. The CO_2 signal produced via a MvK mechanism is comparable to the previous case, but we observe an additional low, broad $^{13}C^{16}O^{18}O$ signal between 200–500 K corresponding to CO_2 formed by a L–H mechanism. Overall, roughly 35 % of the CO_2 produced is formed by the L–H channel.

The situation changes dramatically when the same gases are dosed with the order reversed (panel c). Dosing the $^{18}O_2$ before the ^{13}CO at 130 K leads to a significantly enhanced mass 47 signal, which now exhibits a clear maximum at ≈ 340 K. The sum of masses 29, 45 and 47 is however significantly reduced compared to the previous CO-first experiments, which suggests that, overall, less CO can adsorb on the system once it is saturated with O_2 at 130 K, but a significantly higher proportion of adsorbed CO is converted to CO_2. The overall amount of CO_2 produced is comparable to the case shown in Fig. 6.21b, but now the majority (≈ 60 %) forms via the L–H channel. If the system is predosed with O_2 at 300 K prior to CO adsorption, the observed CO_2 TPD signal shown in Fig. 6.21d is significantly enhanced between 400 and 500 K in both reaction channels. In this experiment, the amount of CO_2 formed is the highest (≈ 35 % higher than in the previous two cases), and approximately 50 % is formed by the L–H channel. These experiments, with O_2 predosing at 130 and 300 K, likely differ in that the oxygen-induced Rh_1 diffusion should be suppressed at low temperature, and additional oxygen is bound at sites linked to Rh species (see Fig. 6.5a). No CO_2 formation by any mechanism is observed in the absence of Rh species (panel e).

Discussion

The experimental data acquired on the $Rh/Fe_3O_4(001)$ model catalyst clearly show that Rh_1 adatoms sinter rapidly when exposed to O_2 at room temperature, forming small Rh_xO_y clusters that are active for CO oxidation. Given the extremely low O_2 pressure used in the STM movies, it seems likely that just one O_2 molecule is sufficient to create a mobile oxidised Rh species, probably Rh_1O_2. This suggests that oxygen adsorption significantly weakens the interaction of the Rh adatom with

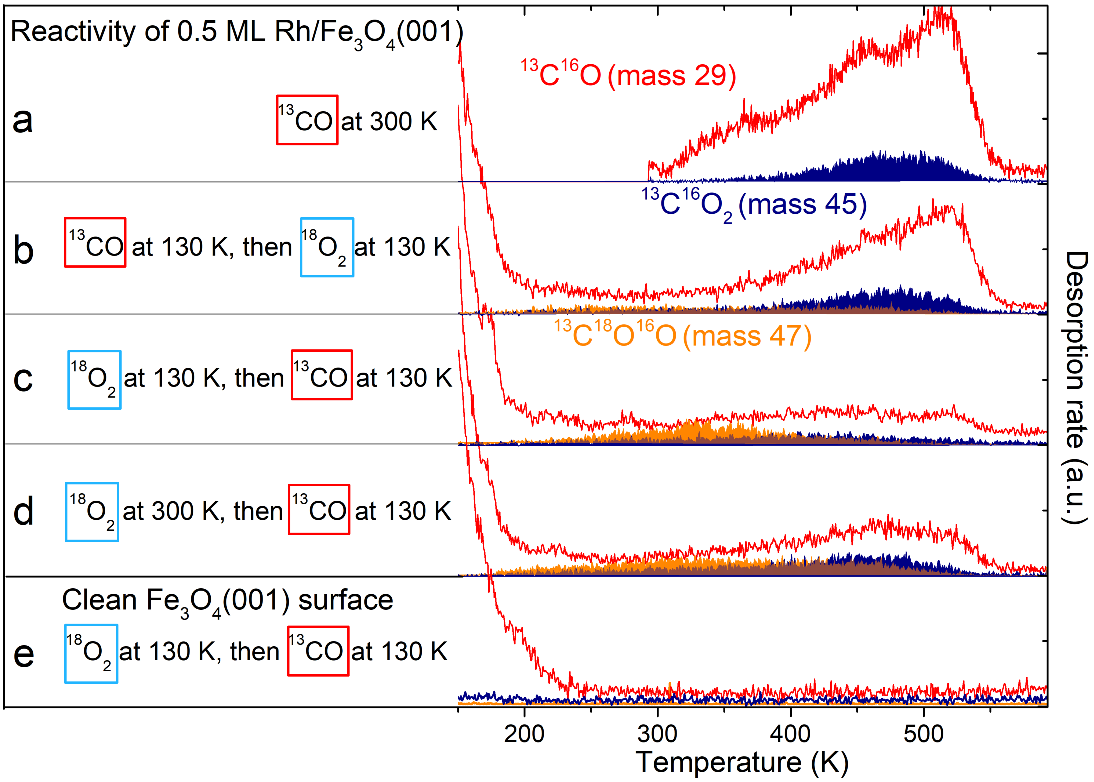

Figure 6.21: Probing the reactivity of 0.5 ML $Rh/Fe_3O_4(001)$ by TPD after sequential dosing of ^{13}CO and $^{18}O_2$. Red traces correspond to ^{13}CO, blue areas to $^{13}C^{16}O_2$ produced via a MvK mechanism and orange areas correspond to $^{13}C^{16}O^{18}O$ produced via a L–H mechanism. (a) Dosing ^{13}CO at 300 K results in spectra comparable to Fig. 6.20a. (b) Dosing ^{13}CO at 130y,K, then $^{18}O_2$ at 130 K leads to a lower ^{13}CO desorption signal, but overall higher $^{13}CO_2$ production below 400 K. (c) Dosing $^{18}O_2$ first at 130 K, then ^{13}CO at 130 K leads to significant CO_2 signal produced by the L–H mechanism, the MvK channel is suppressed. (d) Dosing $^{18}O_2$ at 300 K, then ^{13}CO at 130 K leads to similar results as (c), but with more CO_2 produced above 400 K in both reaction channels. (e) No CO_2 formation by any mechanism is observed in the absence of Rh species. Figure adapted from [212].

the support. DFT calculations for oxygen adsorption on the Rh_1/Al_2O_3 system predict significant electron transfer from Rh to O_2, and the formation of superoxo $(O_2)^-$ species [240]. In the O 1s XPS data taken after O_2 adsorption below 100 K (Fig. 6.17b) we do observe a peak at 533. eV, which is close to the position expected for superoxo species [250]. However, this peak disappears after heating above 250 K, suggesting a further reaction with Rh takes place. We also observe a strong positive binding energy shift in the Rh 3d XPS peak maximum (Fig. 6.17c) after O_2 dosing at 60 K (308.6 eV), which shifts further to $\approx$ 309.0 eV upon heating above 250 K. The position observed at 60 K is already close to that expected for RhO_2 (308.6 eV) [251] or Rh_2O_3 (308.3 eV) [251, 252], and thus could be already interpreted as a signal corresponding to the oxidised Rh clusters. Nevertheless, the further shift above

250 K accompanied with the disappearance of the superoxo component in the O 1s region suggests that the agglomeration takes place between 100 K and 250 K, and the O 1s signal of the resulting Rh_xO_y nanoparticles is indistinguishable from that of the O_2 in the Fe_3O_4 support.

Our room-temperature STM movies of O_2 exposure (Fig. 6.16a–c) suggest that the mobile Rh_1O_2 species interact strongly with bare Rh adatoms to form a well-defined double protrusion (presumably with Rh_2O_2 stoichiometry). The addition of yet another mobile Rh_1O_2 seems common, and would in principle yield clusters of nominal Rh_3O_4 stoichiometry. These clusters appear larger, and have a scratchy appearance due to the interaction with the STM tip. The cluster density observed following 50 L O_2 exposure suggests that the clusters rarely grow larger than 2–3 Rh atoms, but it cannot be concluded how many O_2 molecules can ultimately be adsorbed on each cluster, nor whether the formation of these clusters results in the abstraction of one or more O atoms. Nevertheless, the O_2 TPD measurements clearly show that some of the O atoms are weakly bound, and desorb as molecular O_2 just above room temperature in the absence of CO (Fig. 6.17a). The Rh 3d spectrum is barely changed by this desorption; only a very small shoulder appears at $\approx$ 308.2 eV (green curve in Fig. 6.17c), which suggests the clusters remain oxidised. This shoulder gets significantly more pronounced after heating to 460 and 575 K (purple and cyan curves in Fig. 6.17c), and at the same time the component corresponding to incorporated Rh appears (309.5 eV). In the TPD spectra there is no O_2 desorption signal observed above 380 K (up to 660 K, where the acquisition was stopped), therefore it seems likely that the oxygen from Rh_xO_y clusters gets accommodated in the Fe_3O_4 lattice as the Rh incorporates, and the 308.2 eV component in this case indicates an intermediate step between Rh_xO_y on the surface and Rh incorporated in the lattice. Repeating the oxygen exposure (after its desorption at $\approx$ 350 K, but before the Rh incorporation at higher temperatures) does not replenish the weakly bound O_2, suggesting that the clusters restructure to a stable configuration, and that the weakly bound oxygen was a consequence of the agglomeration process.

When the O_2-sintered sample is exposed to CO at low temperature and TPD is performed, CO_2 is found to evolve from the sample in a broad signal between 200–500 K (Fig. 6.21d). Isotopic labelling of the reactants shows that the majority of the CO_2 formed below $\approx$ 400 K is produced by the L–H channel, with the molecular O_2 being the oxidising agent. The observation of a similar result when the initial O_2 exposure was performed at 130 K instead of 300 K hints that O_2-induced sintering happens already at low temperatures. Interestingly, the CO_2 signal at higher temperature is reduced in intensity when the O_2 exposure is performed at 130 K. The comparison of these two datasets suggests that the oxygen bound above 300 K (δ peak in Fig. 6.17a) is facilitating the CO_2 formation by the L–H channel, and the oxygen adsorbed below 300 K likely blocks a small number of sites for CO adsorption. An alternative explanation is that at 300 K the $^{18}O_2$ spills over to the Fe_3O_4 surface, which leads to the increased CO_2 production above 400 K. In this case the process would be MvK, but due to the previous spillover from Rh it would be measured in both $^{13}C^{16}O_2$ and $^{13}C^{16}O^{18}O$ signals. Reexposing the surface to O_2 following CO_2 desorption is not expected to facilitate further CO_2 production via a L–H mechanism, because the remaining Rh_xO_y clusters seem to be inert for further interaction with O_2.

When the $Rh_1/Fe_3O_4(001)$ sample is exposed to CO first, the Rh adatoms do not become mobile at room temperature. It was shown in the previous secton that CO adsorption allows Ir_1 adatoms to achieve highly-stable square-planar environments, and the STM/ncAFM images for Rh_1 appear very similar. In the case of Ir_1 the enhanced stability was rationalized by analogy to Ir(I) complexes, and it seems reasonable to expect similar behavior for Rh(I), which can also adopt the preferred square planar d8 configuration. The XPS spectra acquired on the CO-saturated $Rh/Fe_3O_4(001)$ system show almost no change in the Rh 3*d* region when heated to temperatures between 300 K and 450 K, suggesting most of the Rh carbonyls still exist at 450 K, and are still present before the CO_2 production takes place via a MvK mechanism at $\approx$ 480 K. Exposing the CO-saturated sample to O_2 does not lead to visible changes in STM or XPS, nor does it lead to significant low-temperature CO_2 production. We conclude that CO poisons the Rh adatoms for O_2 adsorption, at least under the low-pressure conditions. We thus do not form OCOO species, which have been proposed as possible intermediates in prior studies of CO oxidation by Rh-based single-atom catalysts [225, 253]. This could be because the Rh atom is inaccessible to the O_2 molecule once the CO is present, or because adsorbing both molecules on the same Rh adatom is energetically unfavourable. The situation could be different at higher pressures where the kinetic limitations are more easily overcome. A more likely scenario, however, is that stable $Rh(CO)_2$ dicarbonyls would be formed and the catalyst would remain poisoned for CO oxidation via a L–H mechanism. Our TPD experiments show that a small amount of CO is oxidised to CO_2 at high temperature via a MvK mechanism, but this is followed by immediate incorporation of Rh into the support, which ultimately deactivates the catalyst.

6.4 The role of local environment in the structural evolution of $M_2(CO)_x$ species

In previous sections of this thesis the $M_1/Fe_3O_4(001)$ model "single-atom" catalysts were thoroughly described, with the focus on the single M_1 adatoms and the local coordination of the adsorption sites (M=Rh,Ir). In both of these systems, the single adatoms sitting on a pristine SCV-reconstructed surface were clearly identified as the majority species. A small number of M_2 dimers was observed upon deposition and some single M_1 adatoms were likely sitting in unit cells modified by additional cations incorporated in the Fe_{oct} sites. The latter is also suggested by the CO TPD spectra which show a decrease of some defect-related TPD peaks when selected metals are deposited (see previous sections or reference [203]). The low concentration of these "minority" species, combined with the clearly demonstrated instability of the dimers lead to a comfortable assumption that their contribution to the overall system reactivity is likely negligible. However, later findings motivate a closer inspection whether such an assumption is warranted: (1) On both Rh and Ir/Fe_3O_4 systems, the highest achievable $M_1(CO)_2$ dicarbonyl concentration is limited to $\approx$10-25 % of the total, and this number seems to be independent on the CO dose. In both cases, DFT computations clearly show that a formation of $M_1(CO)_2$ dicarbonyls is thermodynamically preferred over M_1CO monocarbonyls with additional CO in the gas phase. The prevalence of monocarbonyls can be rationalized by kinetic barriers hindering the dicarbonyl formation, but this does not explain why the dicarbonyl concentration is independent on the CO dose. (2) On both Rh and Ir/$Fe_3O_4(001)$ systems, a small fraction of the CO is converted into CO_2 via a Mars-van-Krevelen mechanism (a detailed coverage-dependent TPD and XPS study of both Rh and Ir is presented in a PhD thesis of Jan Hulva [203]). The small converted fraction (between 8-15 % in both Rh and Ir cases) suggests that this process is not catalyzed by the majority species, but rather by other species in a specific local environment, e.g. "magic-sized" clusters, adatoms close to defects or adatoms close to other adatoms. For these reasons, a detailed analysis of the STM datasets is repeated with the focus on the "minority" species, which could potentially be responsible for the observed behavior.

Results

Figure 6.22 shows an STM image of nominally 0.3 ML Ir after deposition at 300 K. The coverage of individual Ir atoms on the surface (in the regular 2-fold site or in Ir_2 dimers) is 0.26 ML, as determined by counting of the individual species in the STM image. Out of the total Ir coverage, 0.06 ML ($\approx$25 %) is bound in the Ir_2 dimers. These numbers vary somehow on images acquired in different datasets, but in the analyzed images at total coverages above 0.15 ML Ir, there was at minimum $\approx$10-15 % of Ir bound in dimers. Table 6.1 summarizes analysis of three STM images with varying Ir coverage acquired in three different experiments. In this small sample size, the fraction of Ir bound in Ir dimers seems to increase with the total Ir coverage. A closer inspection of the individual Ir_2 dimers reveals that many of them (between 50-65 % on the analyzed images) are located slightly offset from the regular adsorption site, with one of the Ir atoms sitting in the regular site and the other being bound next to it; examples of these offset Ir_2 dimers are highlighted in yellow in Fig. 6.22B. Nevertheless, there is always a significant fraction of Ir_2 dimers which looks symmetric or their relative position is hard to resolve; examples of these are highlighted by red ovals. A very small number then resides in the "wide" site, highlighted in green. The grid alignment also reveals that there is a small number of Ir_1 adatoms occupying a "wide" site, examples highlighted in purple. In subsequent STM images, all the Ir_2 dimers are immobile. It is possible that the Ir_2 dimer splitting could be achieved by scanning with increased bias as was observed on Rh_2; such an experiment was however not carried out.

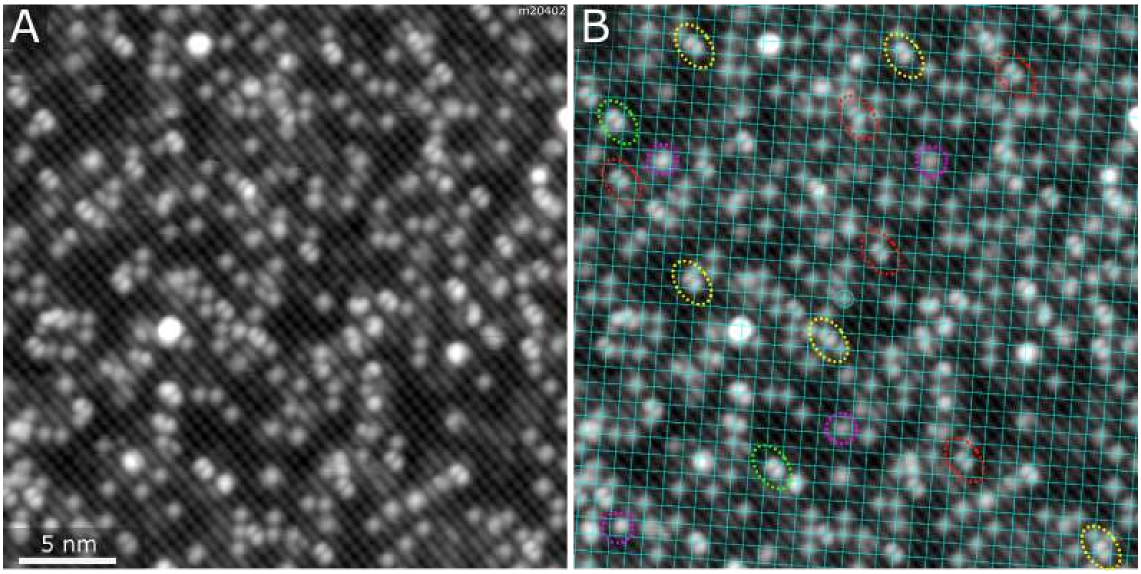

Figure 6.22: A typical STM image taken after deposition of 0.26 ML Ir on Fe_3O_4 at 300 K features predominantly single Ir_1 adatoms. The most common "minority" species are Ir_2 dimers. This particular image features 0.032 ML Ir_2, meaning that 0.064 ML Ir is bound in Ir_2, which corresponds to 25 % of the total Ir coverage. Panel (B) shows the same image as panel (A), but with a $(\sqrt{2} \times \sqrt{2})R45°$ grid overlay. Examples of dimers located slightly offset the regular adatom adsorption site are highlighted by yellow, examples of dimers located symmetrically at the adsorption site are highlighted by red, dimers located on top the "wide" site are highlighted in green.

Table 6.1: Analysis of the Ir_2 dimer concentration on three STM images in different experiments.

image no.	total Ir coverage	Ir_2 coverage	fraction of Ir in Ir_2
m20163	0.157 ML	0.010 ML	13 %
m20558	0.200 ML	0.020 ML	20 %
m20402	0.258 ML	0.032 ML	25 %

A similar analysis was carried out on the Rh/Fe_3O_4(001) system. Figure 6.23 shows an STM image of with 0.15 ML Rh after deposition at 300 K (coverage found by analysis of the image). In this image, 0.02 ML (≈16 %) is bound in Rh_2 dimers. The Rh_2 dimers are located slightly asymmetric with respect to the regular adatom adsorption site, and in subsequent STM images many of them exhibit distinctive hopping motion over the "narrow" site, as discussed in the previous section. The individual Rh_2 dimers can be broken into pairs of Rh_1 adatoms by high-bias scanning, as shown in Fig. 6.12. In contrast to Ir_1, Rh_1 adatoms were not observed to occupy a "wide" site, and also the Rh_2 were not found centered around a "wide" site. Analysis of four STM images acquired in different datasets is summarized in table 6.2. Here, the fraction of Rh bound in Rh_2 seems lower than in the case of Ir_2, but this is most likely due to the overall lower coverage of Rh. When compared to the Ir data of similar coverage (0.157 ML, see table 6.1), the fraction of adatoms bound in dimers is fully comparable. In either case, a bigger sample size would be highly desirable to draw firm conclusions about the relative concentrations of Ir and Rh dimers and their possible coverage dependence.

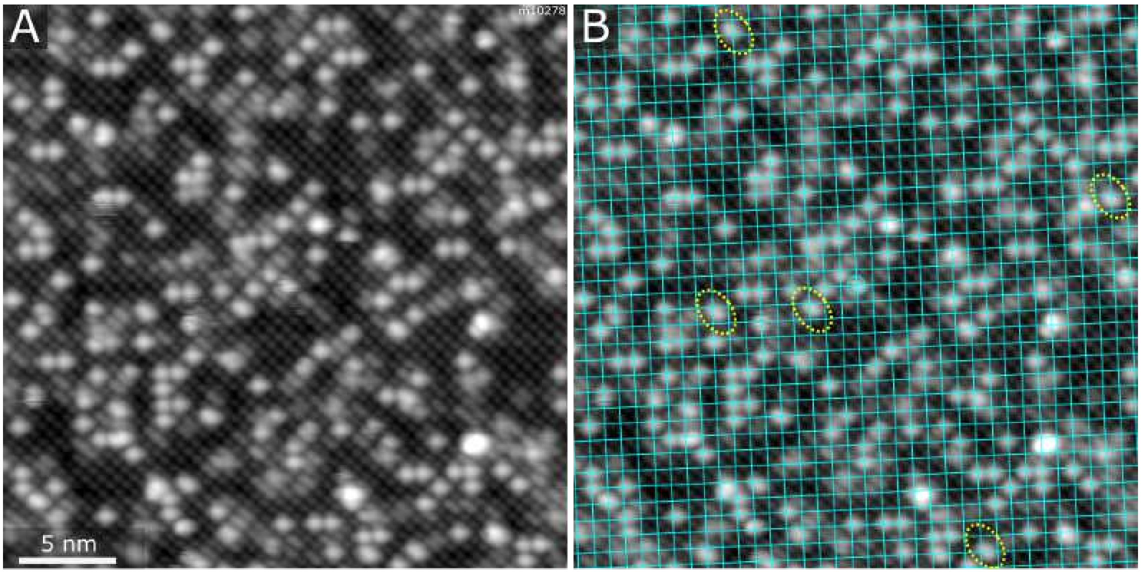

Figure 6.23: A typical STM image taken after deposition of 0.15 ML Rh on Fe_3O_4 at 300 K features predominantly single Ir_1 adatoms. The most common "minority" species are Rh_2 dimers. This particular image features 0.012 ML Rh_2, meaning that 0.024 ML Rh is bound in Rh_2, which corresponds to 16 % of the total Ir coverage. Panel (B) shows the same image as panel (A), but with a $(\sqrt{2} \times \sqrt{2})R45°$ grid overlay. Several Rh_2 dimers are highlighted in yellow.

The interaction of Rh_2 dimers with CO is illustrated in Figure 6.24 which shows frames from an STM movie acquired on nominally 0.2 ML Rh/Fe_3O_4(001) scanned in a $5 \cdot 10^{-9}$ mbar background pressure of CO. In the scanned area, there were six clearly resolved Rh_2 dimers prior to CO dosing (labeled by numbers 1-6) and three

Table 6.2: Analysis of the Rh_2 dimer concentration on three STM images in different experiments.

image no.	total Rh coverage	Rh_2 coverage	fraction of Rh in Rh_2
m21805	0.139 ML	0.005 ML	7 %
m20195	0.142 ML	0.008 ML	11 %
m10278	0.146 ML	0.012 ML	16 %
m10359	0.179 ML	0.015 ML	17 %

species which looked similar, but had slightly different shapes (7-9). While this is clearly a very small sample size, highly specific structural changes were observed for all of these during the CO exposure, providing evidence that (a) all of these species are Rh_2 dimers and (b) upon CO adsorption, a significant portion of the Rh_2 dimers splits into two Rh_1, and in some cases this leads to formation of $Rh(CO)_2$ dicarbonyls. The right side of the figure shows the individual steps of the $Rh_2(CO)_x$ structural evolution upon CO adsorption: dimers labeled 1 and 2 first become very bright and scratchy, then the scratchiness disappears and the apparent height switches between two states several times. Eventually the dimer splits into a well-resolved $Rh(CO)_2$ dicarbonyl and a RhCO monocarbonyl. In case of dimer labeled 2, the resulting dicarbonyl appears on a perfectly clean surface, where no defects or incorporated cations were observed before, which further proves that surface modification is not required to stabilize a dicarbonyl. The dimers labeled 3,4 split into two Rh_1 species, out of which at least one is incorporated. The dimers labeled 5,6 formed a well-resolved double-lobed feature, which stayed stable for the rest of the STM movie (15 frames, ≈ 50 min). The non-standard looking dimers (7,8,9) behaved similarly to the standard ones: dimers 7,9 split up into an incorporated Rh and a surface RhCO, dimer 8 split into a well-resolved $Rh(CO)_2$ dicarbonyl and a very bright feature (not shown).

At the end of the shown STM movie, there are 18 species which have a dicarbonyl appearance, highlighted in Fig. 6.25. Many of these species are slightly rotated or have additional species right next to it (discussed further below). Out of these 18, not a single one was formed by a simple adsorption of a second CO on a standard-looking monocarbonyl. Three of the well-defined dicarbonyls clearly originated from Rh_2 dimers, the others were formed on Rh adatoms which differed from the rest by their apparent height, shape or position within the surface unit cell before the CO exposure. Most likely, these slightly different Rh_1 adatoms occupy sites modified by defects or incorporated adatoms.

The commonly observed "minority" species were analyzed to find species potentially responsible for the observed CO oxidation reactivity. On $Rh/Fe_3O_4(001)$ saturated with CO, the most common species other than mono-and dicarbonyls is a dicarbonyl with an additional bright spot on an Fe_{oct} row right next to it, these

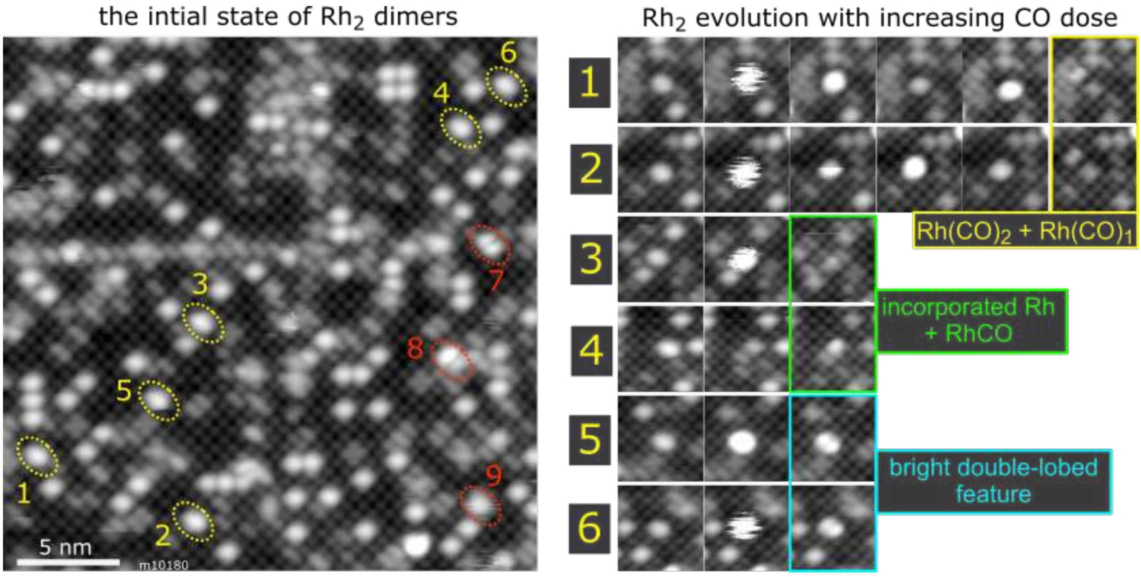
the intial state of Rh_2 dimers

Rh_2 evolution with increasing CO dose

Figure 6.24: Analysis of the CO reactivity of Rh_2 dimers. The left panel shows a frame from the start of an STM movie taken in a $5{\cdot}10^{-9}$ mbar background pressure of CO. In this image there are six clearly identified Rh_2 dimers, labeled 1-6. Additionally, there are three Rh_2 dimers which have slightly different appearance, labeled 7-9. The left panel shows details of the frames from the STM movie, which highlight the structural evolution of the Rh_2 dimers. After several changes, dimers labeled 1,2 evolve into a $Rh(CO)_2$ dicarbonyl and a RhCO monocarbonyl. Dimers labeled 3,4 end up as incorporated Rh and a RhCO monocarbonyl. Dimers labeled 5,6 evolve into bright double-lobed features which stayed stable throughout the STM movie. Dimers 7-9 behaved similarly (not shown, described in the text). STM movie acquired by R. Bliem.

species are highlighted by yellow in Fig. 6.26A. Especially on images acquired at 78 K, such species are well resolved and are observed in four different positions rotated by 90° due to the symmetry of the surface. On Ir/Fe_3O_4(001), similar species were found (highlighted in cyan in Fig. 6.26B), although the position of the three bright protrusions is slightly different from the Rh case. Here, two bright spots are located between the Fe_{oct} rows with an additional bright spot on the Fe_{oct}, placed equidistantly from the other two. This results in two possible arrangements rotated by 180°, both of which are observed in STM images. In both Rh and Ir cases, the same species were observed when measuring at room temperature. The relative coverages were not quantified, as that would require much bigger datasets given the very low concentrations.

Based on their STM appearance it can be speculated that both of these observed Rh and Ir-based species are formed by two M_1 adatoms occupying the same unit cell that stabilize three CO molecules between them. In the case of Rh, the plausible structural model would be a 2-fold coordinated adatom in the centre of a $Rh(CO)_2$ dicarbonyl, with an incorporated 5-fold coordinated adatom in the same unit cell

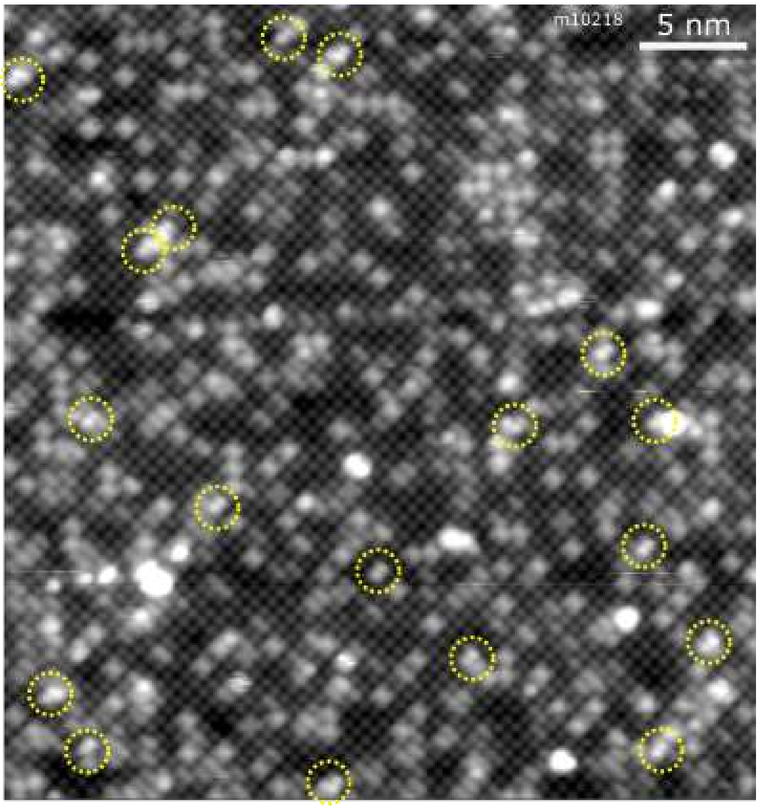

Figure 6.25: The last frame from the STM movie shown in the previous figure. The species with dicarbonyl appearance are highlighted by yellow. Many of these have an additional bright spot next to it. Importantly, the dicarbonyls are not formed by a simple adsorption of an additional CO on a monocarbonyl.

forming an additional RhCO monocarbonyl. Overall, this would lead to a local $Rh_2(CO)_3$ arrangement in the $Fe_3O_4(001)$ unit cell. In the case of Ir, the common triple-lobed species look more like a Ir_2 dimer with an extra spot on the the Fe_{oct} row, possibly corresponding to an additional adsorbed CO molecule.

Discussion

In this short section, the role of local environment on the CO adsorption properties of Ir and Rh species on $Fe_3O_4(001)$ was studied by STM. It was found that even though the single Ir_1 and Rh_1 adatoms on the pristine surface can coordinate two CO molecules to form very stable dicarbonyls, such species rarely form by simply adsorbing the two molecules in UHV. By analysis of STM movies, it was found that the vast majority of dicarbonyl species observed after CO dosing originate on adatoms with a modified local environment - either M_2 dimers or M_1 adatoms occupying a unit cell with extra cations. These results explain why the coverage of dicarbonyls was previously observed to be independent on the CO dose: on the pristine surface, the kinetic barrier for the dicarbonyl formation is likely too high, but

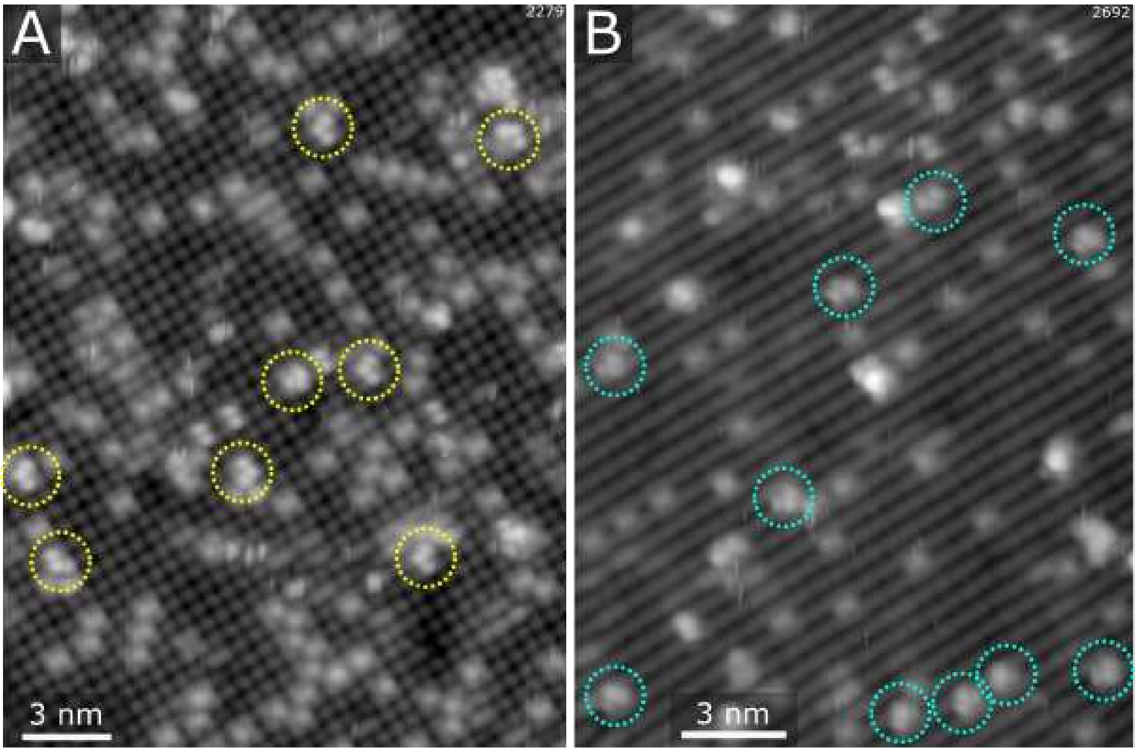

Figure 6.26: Species commonly observed on CO-saturated $Rh/Fe_3O_4(001)$ (A) and $Ir/Fe_3O_4(001)$ (B). In both cases, the species consist of three bright protrustions. The STM images were taken at 78 K, but similar species were observed at room temperature.

the presence of extra cations in the immediate proximity lowers it. The maximum coverage of the observed dicarbonyls thus dependes mainly on the number of the M_2 species or M_1 adatoms on modified unit cells, not on the CO dose.

One possible reason for the high kinetic barrier on isolated adatoms is the repulsive interaction between the adsorbed CO and the CO in the gas phase. Thus, a potential mechanism of the formation of the dicarbonyl on the M_2 species or M_1 adatoms on modified unit cells lowers the barrier by adsorbing a CO molecule on the site next to the already existing monocarbonyl. This leads to existence of two monocarbonyls in immediate proximity, and from this state it might be easier to diffuse one of the CO to form a dicarbonyl and an empty cation site next to it. If this hypothetical mechanism is correct, then the commonly observed dicarbonyl species with a bright dot on a Fe_{oct} row right next to it would form when the empty adsorption site is refilled by CO from the gas phase.

Overall, this section focused on description of $M_x(CO)_y$ species which could potentially be responsible for the previously observed CO oxidation reactivity via a Mars-van-Krevelen mechanism. While the presented STM data cannot firmly identify the active species, they can provide plausibility arguments for a detailed computational study. The preliminary computational data already ruled out both monocarbonyls and dicarbonyls on the pristine surface as the active species. In STM, the next most commonly observed species were triple-lobed features with the three bright spots arranged in specific shapes, and it is hypothesized that these might correspond to two adatoms in the same unit cell coordinating three CO molecules. Given the fact that the local environment was shown to play a crucial role in the formation of the dicarbonyls, it can be speculated that a similar effect can be present on the reactivity of the dicarbonyls, and the presumed $M_2(CO)_3$ species might be active for CO oxidation. One experimental way to further support this hypothesis would involve a CO TPD study on surfaces prepared by depositing M_1 adatoms on top of the surface which already features adatoms incorporated in the 5-fold sites. This will lead to increased number or adatoms residing in sites modified by additional cations and if this hypothesis is correct, this should greatly increase the CO oxidation reactivity. Ultimately, the exact reaction mechanism will have to be identified by a computational study, one which is being carried out by Matthias Meier.

6.5 Stability and reactivity of Pt and Rh species on $Fe_3O_4(111)$

This short section describes very preliminary results acquired on the Pt/$Fe_3O_4(111)$ and Rh/$Fe_3O_4(111)$ systems. The main motivation for these studies is the question whether single adatoms can be stabilized on the $Fe_3O_4(111)$ surface and how their local coordination affects reactivity. It would be especially interesting to compare the results with the same reactivity experiments on $Fe_3O_4(001)$, as the coordination and local environment of any stable adatoms on $Fe_3O_4(111)$ will surely be different from the 2-fold site observed on the (001) surface of the same oxide. The work shown here is not completely finished at the moment and should be taken mainly as a progress report.

Figure 6.27A shows Pt $4f$ regions of XPS spetra taken after depositing 0.1 ML Pt on the Fe_{tet1} terminated $Fe_3O_4(111)$ surface and heating to different temperatures. Here, 1 ML corresponds to 1 adatom per the Fe_{tet1} unit cell, that is $3.21{\cdot}10^{14}$ adatoms/cm^2. After deposition at 150 K, the Pt $4f_{7/2}$ peak maximum is located at ≈ 72.4 eV. The peaks get slightly broader after heating to 200 and 250 K, but the maximum position remains unchanged. The peak position starts to slightly shift to lower binding energy starts with heating to 300 and 350 K. After heating to 500 K, the whole peak is shifted to ≈ 71.4 eV.

Similar experimental data for Rh/$Fe_3O_4(111)$ are shown in Fig. 6.27B. Here, the Rh $3d_{5/2}$ peak maximum is located at 308.5 eV upon deposition at 150 K, and the peak shape and position remains the same upon heating to 250 K. At 300 K, the peak start shifting to lower binding energy and at 450 K and 500 K the peak maximum is found at ≈ 307.7 eV. Interestingly, upon heating to 700 K a new component develops at higher binding energy of ≈ 309.3 eV, and this component seems to appear at the expense of the 307.7 eV component.

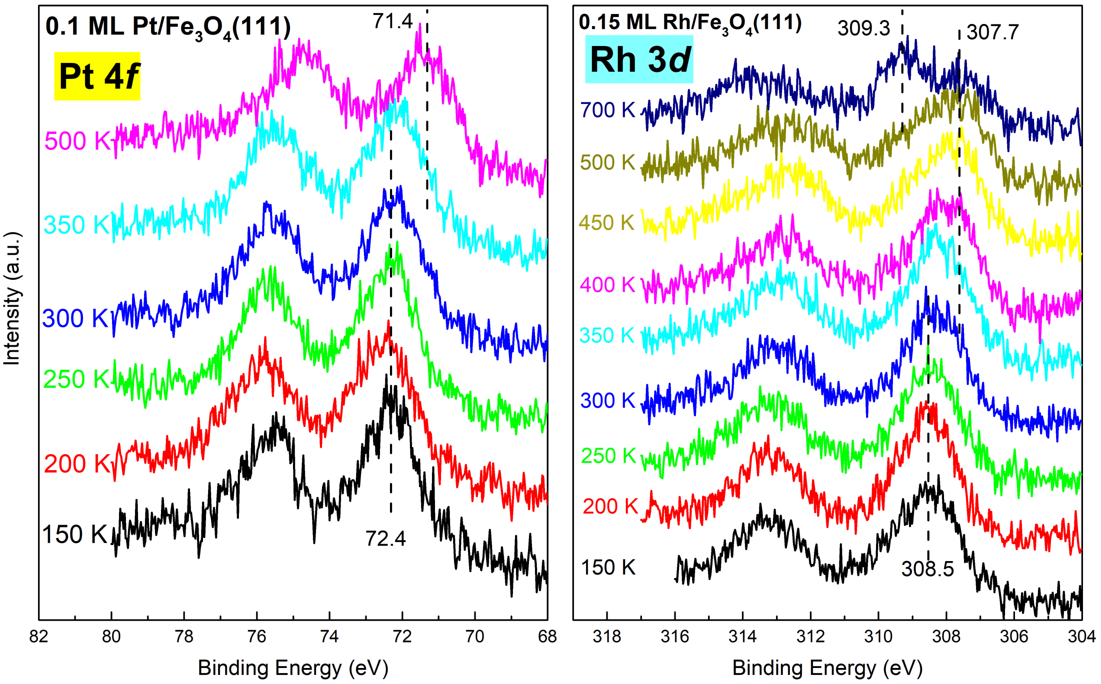

Figure 6.27: $Pt/Fe_3O_4(111)$ (A) and $Rh/Fe_3O_4(111)$ (B) systems characterized by XPS. In both cases, the metals were deposited at 150 K. The XPS spectra were taken after heating to given temperatures.

Preliminary TPD data focusing on ^{13}CO reactivity of $Fe_3O_4(111)$ surfaces modified by Pt are shown in Fig. 6.28. The surface modified by 0.1 ML Pt deposited at 150 K exhibits several ^{13}CO desorption states above 250 K, and a small $^{13}CO_2$ signal between ≈ 450-600 K (signal multiplied by a factor of 5 in Fig. 6.28B). In the repeated TPD run (after the end of the first TPD ramp at 630 K), the amount of ^{13}CO desorbing above 250 K significantly decreases and a broad TPD peak with a maximum at ≈ 450 K is resolved in the spectrum. The corresponding $^{13}CO_2$ signal is also decreased and shifted to lower temperatures in comparison to the previous TPD run. Looking at the region below 250 K, the presence of Pt in the first TPD run seems to increase a ^{13}CO TPD peak at ≈ 130 K, but in the second run it is again significantly lower. In the second TPD run there is also a very pronounced ^{13}CO TPD peak at ≈ 220 K, but as will be discussed below, this effect is most likely not due to the surface modification by Pt, but rather due to background water adsorption above ≈ 400 K, which is desorbed in the first TPD run to 630 K.

Figure 6.29 shows similar dataset for the $Rh/Fe_3O_4(111)$. Here 0.15 ML Rh was deposited at ≈ 150 K. In the first TPD run, there are two well-resolved TPD

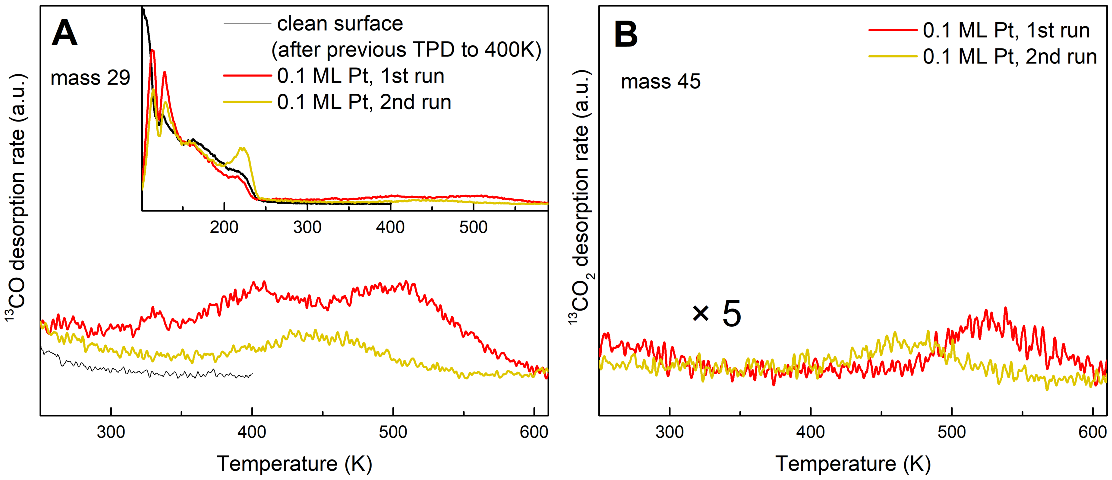

Figure 6.28: Pt/Fe_3O_4(111) studied by ^{13}CO temperature programmed desorption. Panel (A) shows the ^{13}CO spectra acquired in the first and second TPD run on the same system. Inset in top right shows the whole spectrum starting at 110 K. The black lines correspond to the "blank" experiment on the Fe_3O_4(111) without any Pt. Panel (B) shows the corresponding $^{13}CO_2$ traces (signal multiplied 5× in comparison to panel (A)).

peaks above 250 K with their maxima at ≈ 400 K and 490 K. A small $^{13}CO_2$ signal is observed between ≈ 450-600 K. In the second run, however, both the TPD spectra are almost featureless between 300-600 K, only a barely-resolved ^{13}CO TPD feature is seen at ≈ 430 K. Below 250 K, similar effects are observed as in the Pt case: In the first run, a desorption peak at ≈ 130 K is significantly increased, but decreases again in the second run. In the second run, another TPD peak at ≈ 220 K is significantly more pronounced.

6.5.1 Discussion

This short section shows preliminary results acquired on the Pt/Fe_3O_4(111) and Rh/Fe_3O_4(111) systems. In the case of Pt, the XPS dataset shows that the Pt species do not change much when deposited and measured at 150 K or when heated to 300 K. The Pt $4f_{7/2}$ peak maximum is located at 72.4 eV, which is significantly higher than the 71.5 eV position found for single adatoms on Fe_3O_4(001) [203], indicating more oxidized species. Upon heating to 350 K, the peak maximum slightly shifts to lower binding energy, and after heating to 500 K it is located at 71.4 K, already close to the position of metallic Pt (71.2 eV [254]). This dataset thus shows that the Pt species likely agglomerate above 300 K to form bigger clusters, the nature of the species formed upon deposition at low temperature is not clear. While it could be assumed that a deposition of very low metal coverage at cryogenic temperatures might result in isolated adatoms, such an interpretation is not consistent

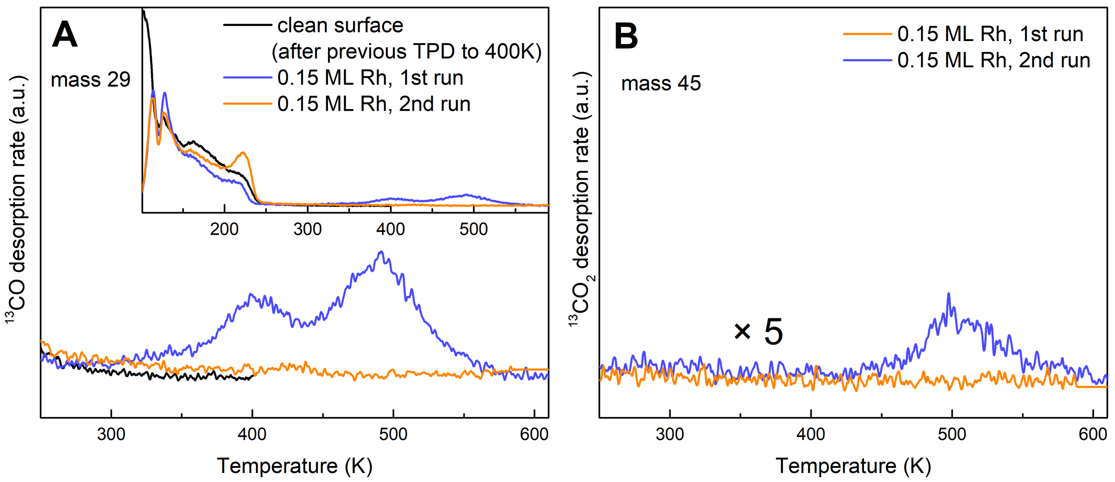

Figure 6.29: Rh/Fe_3O_4(111) studied by ^{13}CO temperature programmed desorption. Panel (A) shows the ^{13}CO spectra acquired in the first and second TPD run on the same system. Inset in top right shows the whole spectrum starting at 110 K. The black lines correspond to the "blank" experiment on the Fe_3O_4(111) without any Rh. Panel (B) shows the corresponding $^{13}CO_2$ traces (signal multiplied 5× in comparison to panel (A)).

with the available literature which studied the same system by room temperature STM after deposition of 0.08 ML Pt at ≈ 110 K, and identified the Pt species as small single-layer clusters [100]. In the cited literature, the Pt species deposited on Fe_3O_4(111) thin film showed relatively broad lateral size distribution and were found to be randomly dispersed on the surface. Interestingly, at 0.08 ML Pt coverage the STM appearance did not significantly change after heating to 600 K. Such a result is hard to reconcile with the XPS data presented here, where the Pt $4f_{7/2}$ maximum position shifts by ≈ 1 eV after heating the sample to 500 K. Possibly, this inconsistency could be due to different surface preparation or different adatom adsorption properties of Fe_3O_4(111) thin films and single crystals. In any case, it is clear that more experiments need to be done to address the questions Pt species stability on Fe_3O_4(111).

The XPS data acquired on the Rh/Fe_3O_4(111) system intially show a similar development as the Pt species. The Rh 3d peak maximum is located at ≈ 308.5 eV when measured directly after 0.15 ML Rh deposition at 150 K, and the position doesn't significantly change after heating to 200 or 250 K. This peak maximum position is higher than the 307.8-308.1 eV observed on the Rh/Fe_3O_4(001) system (see Fig. 6.14), indicating more oxidized species. After heating to 300 K, on the Rh/Fe_3O_4(111) system a low-binding-energy shoulder appears at ≈ 307.7 eV, which gets more pronounced with heating to 350 and 400 K, until it becomes dominant after heating to 450 and 500 K. Such a behavior likely corresponds to agglomeration to small Rh clusters; the peak position at 307.7 eV is still oxidized with respect to the position of metallic Rh (307.2 eV [254]). Importantly, after heating to 700 K, the 307.7 eV component significantly reduces in intensity, and a new component with a maximum at 309.3 eV becomes dominant. This can be explained by the Rh incorporating into the $Fe_3O_4(111)$ substrate, similarly to the behavior observed on $Fe_3O_4(001)$. The position of the incorporated Rh $3d_{5/2}$ peak maximum is quite close to the 309.5 eV observed on $Fe_3O_4(001)$. An interesting question is whether the small Rh species incorporate as whole clusters, or whether the individual Rh atoms separate from the clusters and migrate into the bulk. Both scenarios are possible, as on $Fe_3O_4(001)$ the incorporation was clearly preferred to agglomeration, and diffusion further into the bulk was clearly preferred over agglomeration in the immediate subsurface [212]. Nevertheless, as in the case of Pt/$Fe_3O_4(111)$, while the development of the system with heating can be well explained, the data do not provide a clear answer to the question whether the initial state at 150 K corresponds to single Rh adatoms, small Rh clusters or both.

The TPD experiments were carried out to provide initial tests of reactivity of Pt/$Fe_3O_4(111)$ and Rh/$Fe_3O_4(111)$ systems for ^{13}CO oxidation. The presence of both Pt and Rh induces new desorption states above 250 K, and a small $^{13}CO_2$ signal was observed accompanying the ^{13}CO desorption in both cases. In the case of Pt, several desorption features were observed in this region, and in the second TPD run (after the termination of the first TPD ramp at 630 K) the ^{13}CO desorption signal is significantly reduced. This suggests it is likely related to small Pt species whose number is reduced after agglometarion at elevated temperatures. In the second TPD run, the ^{13}CO desoption peak maximum is located at ≈ 450 K, and the small amount $^{13}CO_2$ evolves at a high-temperature tail of this peak at ≈ 470 K.

A notable feature appearing in the second TPD run is the significantly increased "defect" peak at ≈ 220 K. However, this is most likely not due to the evolution of Pt species, but rather to the reduced amount of water adsorbed from the background. Such an effect was reported in the supplemental information of a paper studying CO adsorption on this surface [88], and was later reproduced in our lab as well, although on a slightly reduced surface (not shown). The absence of this peak in the "blank" spectra shown in Figs. 6.28 and 6.29 is due to the fact, that the shown spectrum was taken in a series of TPD runs which were terminated already at 400 K. On a pristine surface, the ^{13}CO desorption spectrum is featureless above 250 K, but a small amount of water is stable even at 550 K (see Fig. 5.18), and likely blocks some sites for ^{13}CO adsorption.

The desorption peak at ≈ 130 K seems to roughly correlate with the presumed surface coverage of Pt: In the first run it is significantly increased in comparison to the pristine surface, but in the second run, as the Pt agglomerates, its maximum lies between the pristine surface and the first run on Pt/$Fe_3O_4(111)$. Comparing the data to previous studies, a TPD spectrum acquired after dosing CO at 300 K on 0.08 ML

Pt/Fe_3O_4(111) showed a broad desorption feature at ≈ 495 K [100]. This is relatively consistent with the data shown in this thesis, although there are multiple desorption features resolved in the dataset presented here. This could be either due to the CO dosing taking place already at ≈ 110 K, or due to the higher resolution achieved by using isotopically-labelled ^{13}CO and dosing by a focused molecular beam.

The first ^{13}CO TPD run acquired on 0.15 ML Rh/Fe_3O_4(111) resembles the data on Pt/Fe_3O_4(111): It also features two dominant ^{13}CO desorption peaks above 250 K and a small $^{13}CO_2$ signal appearing at the trailing edge of the higher ^{13}CO desorption peak. In the second run, however, both the ^{13}CO and $^{13}CO_2$ spectra are almost featureless. Such a behavior is consistent with the Rh incorporation that was observed in the XPS dataset.

It is interesting to compare the CO TPD data from the Fe_3O_4(111) to the similar datasets acquired on the Fe_3O_4(001) [203]. At first sight, the datasets show remarkable similarities: Pt and Rh data acquired on both surfaces show multiple desorption features with the temperatures of the highest ones being quite comparable between the two surfaces (Pt/Fe_3O_4(001) at ≈ 520 K, Pt/Fe_3O_4(111) at ≈ 510 K; Rh/Fe_3O_4(001) at ≈ 530 K, Rh/Fe_3O_4(111) at ≈ 490 K). However, on metal/Fe_3O_4(001) systems the highest desorption peak is clearly dominant, especially at low metal coverages. In contrast, on the Fe_3O_4(111), multiple desorption features of similar intensities are observed already at very low metal loadings. Another clear difference is seen in the CO_2 signal, which in most metal/Fe_3O_4(001) systems is observed at temperatures corresponding to the leading edges of the CO desorption peaks, but on the two metal/Fe_3O_4(111) described here the CO_2 desorption is found at temperatures corresponding to the trailing edges of the CO desorption peaks. This hints that despite the obvious similarities of the TPD experiments on the two surfaces, the CO oxidation mechanism might be a little different. In any case, much more work needs to be done to understand the stability and reactivity of metal adatoms or small metal clusters on Fe_3O_4(111). Without any doubt, the metal species will structurally evolve both with heating and with accomodating adsorbates and these effects will presumably be even stronger on the (111) surface than on the (001), as the (111) likely lacks a universally preferred adatom site [98]. All these processes need to be described before speculating about exact reaction mechanisms. A thorough understanding of these phenomena might offer fascinating insights into iron oxide surface reactivity, although the experimental work will likely be complicated by the Fe_3O_4(111) surface dynamics, the commonly observed coexistence of multiple surface phases on this surface and the difficulty of describing individual surface features whose appearance significantly varies with scanning conditions in SPM imaging.

Summary

In this thesis I have studied three dominant iron oxide surfaces, focusing on their structure, reactivity to water and reactivity to CO when modified by metal adatoms and clusters. The main motivation for these studies is in catalysis, where nanoparticles of both hematite α-Fe_2O_3 and magnetite Fe_3O_4 are commonly utilized as catalyst supports.

The first studied surface was α-$Fe_2O_3(1\bar{1}02)$. This surface can be prepared to show two distinct surface reconstructions in UHV, one of which was shown to be bulk-terminated. Water vapor was found to adsorb on this surface in the form of partially-dissociated water dimers at all coverages up to multilayer formation. Importantly, the data acquired following exposure of the surface to liquid water indicate that the surface survives the immersion and similar partially-dissociated species are most likely present after the contact with liquid water. It was also found that upon desorption of these partially-dissociated water dimers in UHV, roughly half of the O atoms is exchanged between the water and the α-$Fe_2O_3(1\bar{1}02)$ and a similar result was observed after the exposure to liquid water. This result is puzzling at the moment and indicates a counter-intuitive desorption mechanism. While this phenomenon was not fully explained, the evidence for the existence of partially-dissociated water dimers on this surface is compelling, and the observed structures are consistent with the previously published in-situ spectroscopic data. Since hematite is regarded as a very promising photoanode material for photoelectrochmical water splitting, it is argued that it should be computationally tested whether the observed strong water-water interactions can play a role in the catalytic activity of the material for this application.

Utilizing the same approach, the (001) and (111) surfaces of magnetite Fe_3O_4 were studied in UHV. Non-contact AFM with a CO terminated tip was used as the main tool to image the water structures with molecular resolution. On both of the studied surfaces, small partially dissociated water agglomerates were identified as very stable structures which dominate the water adsorption until a more complex partially-dissociated hydrogen-bonded network forms at higher (but still submonolayer) coverages. Even though the TPD spectra look relatively similar and individual water phases desorb at comparable temperatures on the two surfaces, the surface structure was found to play a very important role in water adsorption on

both facets. On the (001) surface, the small partially-dissociated water dimers and trimers are only stabilized at specific sites at the surface, and these small agglomerates anchor the complex water network which forms later. On the (111) surface, highly specific shapes of water agglomerates were observed. These could not be fully rationalized by DFT calculations carried out on a perfectly stoichiometric surface, but one of the plausible models assumes aditional Fe cations on the surface stabilizing the observed structures. This hypothesis will be followed on further and it will be very interesting to see whether the additional Fe cations can originate via a diffusion path from the bulk. If that indeed is the case, it would provide strong evidence of the surface being surprisingly dynamic even at cryogenic temperatures.

The last chapter of this thesis studied the $Fe_3O_4(001)$ and $Fe_3O_4(111)$ surfaces modified by Ni, Rh, Ir and Pt. On the $Fe_3O_4(001)$, all the studied metals are stable in the form of isolated adatoms, but the group 9 metals (Ni, Rh, Ir) could also be incorporated into the octahedral sites of the $Fe_3O_4(001)$ surface by thermal annealing. The main research focus of this chapter was the effect of the local environment of the adatom site on adsorption properties and reactivity of the adatom. In the case of Ni it was found that presence of this metal on the surface activates the system for dissociative water adsorption above room temperature. The Ni adatoms were found to accomodate multiple OH which were bound with different strengths. The water adsorbed on the incorporated Ni then had the same characteristics as water adsorbed on intrinsic cation-rich defects of the $Fe_3O_4(001)$ surface.

A significant part of this thesis deals with the interaction of metal adatoms with CO. By STM, ncAFM, TPD and XPS, it was found that Rh and Ir adatoms are significantly stabilized by CO adsorption, which is in stark contrast to previous studies of Pt and Pd on the same surface, where CO was shown to mobilize the adatoms. In this thesis, the effect of CO was rationalized by analogy to coordination chemistry. Both Rh and Ir are group 9 metals, which are commonly observed in square-planar d8 complexes. On the $Fe_3O_4(001)$, such a coordination environment is sterically possible, and formation of the preferred geometry leads to stabilization of the system. In contrast, the previously studied Pt and Pd prefer a linear geometry, and formation of such geometry weakens the interaction with the substrate and leads to increased mobility.

On both Rh and Ir it was found that the adatoms can coordinate two CO molecules. This is highly intriguing, as previous computational studies have proposed high activity of single atoms on FeO_x by a pathway which includes coadsorption of two molecules, CO and O_2, on a single adatom. Experiments targeting this mechanism were carried out in this thesis, but it was found that O_2 adsorption mobilizes single Rh adatoms, which leads to formation of small oxidized Rh_xO_y clusters with weakly bound oxygen. It was shown that these species are active for CO oxidation via a Langmuir-Hinshelwood mechanism at temperatures as low as 200 K, but are deactivated by the desorption of the weakly bound oxygen, which cannot be replenished. When the Rh adatoms were exposed to CO prior to O_2, the adatoms were inactive for O_2 adsorption, but the system was found to catalyze CO oxidation via a Mars-van-Krevelen mechanism at $\approx 480\,K$. The deactivation mechanism of both the Rh and Ir/Fe_3O_4(001) systems was found to be incoporation of single atoms into the substrate rather than sintering into bigger nanoparticles.

The last chapter of this thesis also provided analysis of the minority species which were commonly observed on the Rh and Ir/Fe_3O_4(001) systems. STM movies taken in a small background pressure of CO reveal that CO adsorption on such species often leads to formation of dicarbonyls. Importantly, such dicarbonyl formation was not observed on single adatoms sitting on a pristine surface, most likely due to kinetic limitations. It could not be concluded which of the observed species are active for the observed CO oxidation by a Mars-van-Krevelen mechanism, but it seems likely that it is the minority "dimer-like" species rather than single adatoms on the pristine surface. The last section of this chapter also provided perliminary results on Pt and Rh stability and CO oxidation reactivity on when deposited on the Fe_3O_4(111) surface.

In summary, this thesis provides significant fundamental insights into iron oxide surfaces structure, stability and reactivity. A coherent picture of phenomena governing water adsorption on iron oxide surfaces in UHV was presented, and a detailed study of the interaction of CO adsorption on various metal adatoms on Fe_3O_4(001) was carried out. On all three studied systems, previously unforeseen phenomena were observed, which highlights the importance of detailed surface science studies carried out on a case-by-case basis.

References

1. Ertl, G. Reactions at Surfaces: From Atoms to Complexity (Nobel Lecture). *Angewandte Chemie International Edition* **47,** 3524–3535 (2008).
2. Woodruff, D. P. Adsorption and reaction at stepped surfaces: a historical viewpoint. *Journal of Physics: Condensed Matter* **28,** 491001 (2016).
3. Van Lent, R., Auras, S. V., Cao, K., Walsh, A. J., Gleeson, M. A. & Juurlink, L. B. F. Site-specific reactivity of molecules with surface defects—the case of H_2 dissociation on Pt. *Science* **363,** 155–157 (2019).
4. Nowotny, J., Alim, M. A., Bak, T., Idris, M. A., Ionescu, M., Prince, K., Sahdan, M. Z., Sopian, K., Mat Teridi, M. A. & Sigmund, W. Defect chemistry and defect engineering of TiO_2-based semiconductors for solar energy conversion. *Chemical Society Reviews* **44,** 8424–8442 (2015).
5. Reece, C., Redekop, E. A., Karakalos, S., Friend, C. M. & Madix, R. J. Crossing the great divide between single-crystal reactivity and actual catalyst selectivity with pressure transients. *Nature Catalysis* **1,** 852–859 (2018).
6. Salmeron, M. & Schlogl, R. Ambient pressure photoelectron spectroscopy: A new tool for surface science and nanotechnology. *Surface Science Reports* **63,** 169–199 (2008).
7. Kolmakov, A., Gregoratti, L., Kiskinova, M. & Günther, S. Recent Approaches for Bridging the Pressure Gap in Photoelectron Microspectroscopy. *Topics in Catalysis* **59,** 448–468 (2016).
8. Tao, F., Nguyen, L. & Zhang, S. Design of a new reactor-like high temperature near ambient pressure scanning tunneling microscope for catalysis studies. *Review of Scientific Instruments* **84,** 034101 (2013).
9. Söngen, H., Reischl, B., Miyata, K., Bechstein, R., Raiteri, P., Rohl, A. L., Gale, J. D., Fukuma, T. & Kühnle, A. Resolving Point Defects in the Hydration Structure of Calcite (10.4) with Three-Dimensional Atomic Force Microscopy. *Physical Review Letters* **120,** 116101 (2018).

10. Faisal, F., Stumm, C., Bertram, M., Waidhas, F., Lykhach, Y., Cherevko, S., Xiang, F., Ammon, M., Vorokhta, M., Šmíd, B., *et al.* Electrifying model catalysts for understanding electrocatalytic reactions in liquid electrolytes. *Nature Materials* **17,** 592–598 (2018).
11. Balajka, J., Hines, M. A., DeBenedetti, W. J. I., Komora, M., Pavelec, J., Schmid, M. & Diebold, U. High-affinity adsorption leads to molecularly ordered interfaces on TiO_2 in air and solution. *Science* **361,** 786–789 (2018).
12. Kraushofer, F., Mirabella, F., Xu, J., Pavelec, J., Balajka, J., Müllner, M., Resch, N., Jakub, Z., Hulva, J., Meier, M., *et al.* Self-limited growth of an oxyhydroxide phase at the Fe_3O_4(001) surface in liquid and ambient pressure water. *The Journal of Chemical Physics* **151,** 154702 (2019).
13. Campbell, C. T. The Energetics of Supported Metal Nanoparticles: Relationships to Sintering Rates and Catalytic Activity. *Accounts of Chemical Research* **46,** 1712–1719 (2013).
14. Bell, A. T. The Impact of Nanoscience on Heterogeneous Catalysis. *Science* **299,** 1688–1691 (2003).
15. Hansen, T. W., DeLaRiva, A. T., Challa, S. R. & Datye, A. K. Sintering of Catalytic Nanoparticles: Particle Migration or Ostwald Ripening? *Accounts of Chemical Research* **46,** 1720–1730 (2013).
16. Bartholomew, C. H. Mechanisms of catalyst deactivation. *Applied Catalysis A: General* **212,** 17–60 (2001).
17. Haruta, M., Kobayashi, T., Sano, H. & Yamada, N. Novel Gold Catalysts for the Oxidation of Carbon Monoxide at a Temperature far Below 0 °C. *Chemistry Letters* **16,** 405–408 (1987).
18. Haruta, M. Size- and support-dependency in the catalysis of gold. *Catalysis Today* **36,** 153–166 (1997).
19. Heiz, U., Sanchez, A., Abbet, S. & Schneider, W. D. Catalytic Oxidation of Carbon Monoxide on Monodispersed Platinum Clusters: Each Atom Counts. *Journal of the American Chemical Society* **121,** 3214–3217 (1999).
20. Tyo, E. C. & Vajda, S. Catalysis by clusters with precise numbers of atoms. *Nature Nanotechnology* **10,** 577–588 (2015).
21. Kaden, W. E., Wu, T., Kunkel, W. A. & Anderson, S. L. Electronic Structure Controls Reactivity of Size-Selected Pd Clusters Adsorbed on TiO_2 Surfaces. *Science* **326,** 826–829 (2009).

22. Zeng, C., Chen, Y., Iida, K., Nobusada, K., Kirschbaum, K., Lambright, K. J. & Jin, R. Gold Quantum Boxes: On the Periodicities and the Quantum Confinement in the Au_{28}, Au_{36}, Au_{44}, and Au_{52} Magic Series. *Journal of the American Chemical Society* **138,** 3950–3953 (2016).

23. Baxter, E. T., Ha, M.-A., Cass, A. C., Alexandrova, A. N. & Anderson, S. L. Ethylene Dehydrogenation on $Pt_{4,7,8}$ Clusters on Al_2O_3: Strong Cluster Size Dependence Linked to Preferred Catalyst Morphologies. *ACS Catalysis* **7,** 3322–3335 (2017).

24. Crampton, A. S., Rötzer, M. D., Ridge, C. J., Schweinberger, F. F., Heiz, U., Yoon, B. & Landman, U. Structure sensitivity in the nonscalable regime explored via catalysed ethylene hydrogenation on supported platinum nanoclusters. *Nature Communications* **7,** 10389 (2016).

25. Sanchez, A., Abbet, S., Heiz, U., Schneider, W. D., Häkkinen, H., Barnett, R. N. & Landman, U. When Gold Is Not Noble: Nanoscale Gold Catalysts. *The Journal of Physical Chemistry A* **103,** 9573–9578 (1999).

26. Liu, L. & Corma, A. Metal Catalysts for Heterogeneous Catalysis: From Single Atoms to Nanoclusters and Nanoparticles. *Chemical reviews* **118,** 4981–5079 (2018).

27. Gong, M. & Dai, H. A mini review of NiFe-based materials as highly active oxygen evolution reaction electrocatalysts. *Nano Research* **8,** 23–39 (2014).

28. Abbet, S., Sanchez, A., Heiz, U., Schneider, W. D., Ferrari, A. M., Pacchioni, G. & Rösch, N. Acetylene Cyclotrimerization on Supported Size-Selected Pdn Clusters ($1 \leq n \leq 30$): One Atom Is Enough! *Journal of the American Chemical Society* **122,** 3453–3457 (2000).

29. Abbet, S., Heiz, U., Häkkinen, H. & Landman, U. CO Oxidation on a Single Pd Atom Supported on Magnesia. *Physical Review Letters* **86,** 5950–5953 (2001).

30. Fu, Q., Saltsburg, H. & Flytzani-Stephanopoulos, M. Active Nonmetallic Au and Pt Species on Ceria-Based Water-Gas Shift Catalysts. *Science* **301,** 935–938 (2003).

31. Qiao, B., Wang, A., Yang, X., Allard, L. F., Jiang, Z., Cui, Y., Liu, J., Li, J. & Zhang, T. Single-atom catalysis of CO oxidation using Pt_1/FeO_x. *Nature Chem* **3,** 634–641 (July 2011).

32. Lu, Y., Wang, J., Yu, L., Kovarik, L., Zhang, X., Hoffman, A. S., Gallo, A., Bare, S. R., Sokaras, D., Kroll, T., *et al.* Identification of the active complex for CO oxidation over single-atom Ir-on-$MgAl_2O_4$ catalysts. *Nature Catalysis* **2,** 149–156 (2019).

33. Jones, J., Xiong, H., DeLaRiva, A. T., Peterson, E. J., Pham, H., Challa, S. R., Qi, G., Oh, S., Wiebenga, M. H., Pereira Hernández, X. I., *et al.* Thermally stable single-atom platinum-on-ceria catalysts via atom trapping. *Science* **353,** 150–154 (2016).
34. Wang, A., Li, J. & Zhang, T. Heterogeneous single-atom catalysis. *Nature Reviews Chemistry* **2,** 65–81 (2018).
35. Giannakakis, G., Flytzani-Stephanopoulos, M. & Sykes, E. C. H. Single-Atom Alloys as a Reductionist Approach to the Rational Design of Heterogeneous Catalysts. *Accounts of Chemical Research* **52,** 237–247 (2019).
36. Therrien, A. J., Hensley, A. J. R., Marcinkowski, M. D., Zhang, R., Lucci, F. R., Coughlin, B., Schilling, A. C., McEwen, J.-S. & Sykes, E. C. H. An atomic-scale view of single-site Pt catalysis for low-temperature CO oxidation. *Nature Catalysis* **1,** 192–198 (2018).
37. Thang, H. V., Pacchioni, G., DeRita, L. & Christopher, P. Nature of stable single atom Pt catalysts dispersed on anatase TiO_2. *Journal of Catalysis* **367,** 104–114 (2018).
38. DeRita, L., Resasco, J., Dai, S., Boubnov, A., Thang, H. V., Hoffman, A. S., Ro, I., Graham, G. W., Bare, S. R., Pacchioni, G., *et al.* Structural evolution of atomically dispersed Pt catalysts dictates reactivity. *Nature Materials* **18,** 746–751 (2019).
39. Parkinson, G. S. Single-Atom Catalysis: How Structure Influences Catalytic Performance. *Catalysis Letters* **149,** 1137–1146 (2019).
40. Mitchell, S., Vorobyeva, E. & Pérez-Ramírez, J. The Multifaceted Reactivity of Single-Atom Heterogeneous Catalysts. *Angewandte Chemie International Edition* **57,** 15316–15329 (2018).
41. Cui, X., Li, W., Ryabchuk, P., Junge, K. & Beller, M. Bridging homogeneous and heterogeneous catalysis by heterogeneous single-metal-site catalysts. *Nature Catalysis* **1,** 385–397 (2018).
42. Chen, Z., Vorobyeva, E., Mitchell, S., Fako, E., Ortuño, M. A., López, N., Collins, S. M., Midgley, P. A., Richard, S., Vilé, G., *et al.* A heterogeneous single-atom palladium catalyst surpassing homogeneous systems for Suzuki coupling. *Nature Nanotechnology* **13,** 702–707 (2018).
43. Lang, R., Li, T., Matsumura, D., Miao, S., Ren, Y., Cui, Y.-T., Tan, Y., Qiao, B., Li, L., Wang, A., *et al.* Hydroformylation of Olefins by a Rhodium Single-Atom Catalyst with Activity Comparable to $RhCl(PPh_3)_3$. *Angewandte Chemie International Edition* **55,** 16054–16058 (2016).

44. Wang, L., Zhang, W., Wang, S., Gao, Z., Luo, Z., Wang, X., Zeng, R., Li, A., Li, H., Wang, M., *et al.* Atomic-level insights in optimizing reaction paths for hydroformylation reaction over Rh/CoO single-atom catalyst. *Nature communications* **7,** 14036–14036 (2016).

45. Ding, K., Gulec, A., Johnson, A. M., Schweitzer, N. M., Stucky, G. D., Marks, L. D. & Stair, P. C. Identification of active sites in CO oxidation and water-gas shift over supported Pt catalysts. *Science* **350,** 189–192 (2015).

46. Fenter, P. & Sturchio, N. C. Mineral–water interfacial structures revealed by synchrotron X-ray scattering. *Progress in Surface Science* **77,** 171–258 (2004).

47. Balajka, J., Aschauer, U., Mertens, S. F. L., Selloni, A., Schmid, M. & Diebold, U. Surface Structure of TiO_2 Rutile (011) Exposed to Liquid Water. *The Journal of Physical Chemistry C* **121,** 26424–26431 (2017).

48. Björneholm, O., Hansen, M. H., Hodgson, A., Liu, L.-M., Limmer, D. T., Michaelides, A., Pedevilla, P., Rossmeisl, J., Shen, H., Tocci, G., *et al.* Water at Interfaces. *Chemical Reviews* **116,** 7698–7726 (2016).

49. Hodgson, A. & Haq, S. Water adsorption and the wetting of metal surfaces. *Surface Science Reports* **64,** 381–451 (2009).

50. Henderson, M. The interaction of water with solid surfaces: fundamental aspects revisited. *Surface Science Reports* **46,** 1–308 (2002).

51. Parkinson, G. S. Iron oxide surfaces. *Surface Science Reports* **71,** 272–365 (2016).

52. Wang, Y.-X. J., Hussain, S. M. & Krestin, G. P. Superparamagnetic iron oxide contrast agents: physicochemical characteristics and applications in MR imaging. *European Radiology* **11,** 2319–2331 (2001).

53. Dilnawaz, F., Singh, A., Mohanty, C. & Sahoo, S. K. Dual drug loaded superparamagnetic iron oxide nanoparticles for targeted cancer therapy. *Biomaterials* **31,** 3694–3706 (May 2010).

54. Sivula, K., Le Formal, F. & Grätzel, M. Solar Water Splitting: Progress Using Hematite (α-Fe_2O_3) Photoelectrodes. *ChemSusChem* **4,** 432–449 (2011).

55. Tartaj, P., Morales, M. P., Gonzalez-Carreno, T., Veintemillas-Verdaguer, S. & Serna, C. J. The Iron Oxides Strike Back: From Biomedical Applications to Energy Storage Devices and Photoelectrochemical Water Splitting. *Advanced Materials* **23,** 5243–5249 (July 2011).

56. Yensen, N. & Allen, P. B. Open source all-iron battery for renewable energy storage. *HardwareX* **6,** e00072 (2019).

57. Liu, J.-f., Zhao, Z.-s. & Jiang, G.-b. Coating Fe_3O_4 Magnetic Nanoparticles with Humic Acid for High Efficient Removal of Heavy Metals in Water. *Environ. Sci. Technol.* **42,** 6949–6954 (Sept. 2008).

58. Ketteler, G., Weiss, W., Ranke, W. & Schlögl, R. Bulk and surface phases of iron oxides in an oxygen and water atmosphere at low pressure. *Physical Chemistry Chemical Physics* **3,** 1114–1122 (2001).

59. Vervey, E. J. W. Electronic Conduction of Magnetite (Fe_3O_4) and its Transition Point at Low Temperatures. *Nature* **144,** 327–328 (Aug. 1939).

60. Smart, J. S. The Néel Theory of Ferrimagnetism. *American Journal of Physics* **23,** 356–370 (1955).

61. Zhao, L., Zhang, H., Xing, Y., Song, S., Yu, S., Shi, W., Guo, X., Yang, J., Lei, Y. & Cao, F. Morphology-Controlled Synthesis of Magnetites with Nanoporous Structures and Excellent Magnetic Properties. *Chem. Mater.* **20,** 198–204 (Jan. 2008).

62. Santos-Carballal, D., Roldan, A., Grau-Crespo, R. & de Leeuw, N. H. A DFT study of the structures, stabilities and redox behaviour of the major surfaces of magnetite Fe_3O_4. *Phys. Chem. Chem. Phys.* **16,** 21082–21097 (May 2014).

63. Yu, X., Huo, C.-F., Li, Y.-W., Wang, J. & Jiao, H. Fe_3O_4 surface electronic structures and stability from GGA+U. *Surface Science* **606,** 872–879 (May 2012).

64. Yamg, T., Wen, X.-D., Ren, J., LI, Y.-W., Wang, J.-G. & Huo, C.-F. Surface structures of Fe_3O_4 (111), (110), and (001): A density functional theory study. *Journal of Fuel Chemistry and Technology* **38,** 121–128 (Feb. 2010).

65. Parkinson, G. S., Lackner, P., Gamba, O., Maa , S., Gerhold, S., Riva, M., Bliem, R., Diebold, U. & Schmid, M. Fe_3O_4(110)-(1x3) revisited: Periodic (111) nanofacets. *Surface Science* **649,** 120–123 (July 2016).

66. Wiesendanger, R., Shvets, I. V., Bürgler, D., Tarrach, G., Güntherodt, H. J., Coey, J. M. D. & Gräser, S. Topographic and Magnetic-Sensitive Scanning Tunneling Microscope Study of Magnetite. *Science* **255,** 583–586 (1992).

67. Stanka, B., Hebenstreit, W., Diebold, U. & Chambers, S. A. Surface reconstruction of Fe_3O_4(001). *Surface Science* **448,** 49–63 (2000).

68. Pentcheva, R., Moritz, W., Rundgren, J., Frank, S., Schrupp, D. & Scheffler, M. A combined DFT/LEED-approach for complex oxide surface structure determination: Fe_3O_4(001). *Surface Science* **602,** 1299–1305 (Apr. 2008).

69. Novotný, Z., Argentero, G., Wang, Z., Schmid, M., Diebold, U. & Parkinson, G. S. Ordered Array of Single Adatoms with Remarkable Thermal Stability: Au/Fe_3O_4(001). *Physical Review Letters* **108,** 216103 (2012).

70. Bliem, R., Pavelec, J., Gamba, O., McDermott, E., Wang, Z., Gerhold, S., Wagner, M., Osiecki, J., Schulte, K., Schmid, M., *et al.* Adsorption and incorporation of transition metals at the magnetite Fe_3O_4(001) surface. *Physical Review B* **92,** 075440 (2015).

71. Ryan, P. T. P., Jakub, Z., Balajka, J., Hulva, J., Meier, M., Küchle, J. T., Blowey, P. J., Thakur, P. K., Franchini, C., Payne, D. J., *et al.* Direct measurement of Ni incorporation into Fe_3O_4(001). *Physical Chemistry Chemical Physics* **20,** 16469–16476 (2018).

72. Bliem, R., McDermott, E., Ferstl, P., Setvin, M., Gamba, O., Pavelec, J., Schneider, M. A., Schmid, M., Diebold, U., Blaha, P., *et al.* Subsurface cation vacancy stabilization of the magnetite (001) surface. *Science* **346,** 1215–1218 (2014).

73. Parkinson, G. S., Mulakaluri, N., Losovyj, Y., Jacobson, P., Pentcheva, R. & Diebold, U. Semiconductor-half metal transition at the Fe_3O_4 (001) surface upon hydrogen adsorption. *Physical Review B* **82,** 125413 (Sept. 2010).

74. Bliem, R. *Single Metal Adatoms at the Reconstructed Fe_3O_4(001) Surface* PhD thesis (TU Wien, 2016).

75. Parkinson, G. S., Novotný, Z., Jacobson, P., Schmid, M. & Diebold, U. Room Temperature Water Splitting at the Surface of Magnetite. *Journal of the American Chemical Society* **133,** 12650–12655 (2011).

76. Parkinson, G. S., Novotný, Z., Jacobson, P., Schmid, M. & Diebold, U. A metastable Fe(A) termination at the Fe_3O_4(001) surface. *Surface Science* **605,** L42–L45 (2011).

77. Parkinson, G. S., Novotny, Z., Argentero, G., Schmid, M., Pavelec, J., Kosak, R., Blaha, P. & Diebold, U. Carbon monoxide-induced adatom sintering in a Pd–Fe_3O_4 model catalyst. *Nature Materials* **12,** 724–728 (2013).

78. Bliem, R., Kosak, R., Perneczky, L., Novotny, Z., Gamba, O., Fobes, D., Mao, Z., Schmid, M., Blaha, P., Diebold, U., *et al.* Cluster nucleation and growth from a highly supersaturated adatom phase: silver on magnetite. *ACS Nano* **8,** 7531–7 (2014).

79. Bliem, R., van der Hoeven, J., Zavodny, A., Gamba, O., Pavelec, J., de Jongh, P. E., Schmid, M., Diebold, U. & Parkinson, G. S. An Atomic-Scale View of CO and H_2 Oxidation on a Pt/Fe_3O_4 Model Catalyst. *Angewandte Chemie-International Edition* **54,** 13999–14002 (2015).

80. Bliem, R., van der Hoeven, J. E. S., Hulva, J., Pavelec, J., Gamba, O., de Jongh, P. E., Schmid, M., Blaha, P., Diebold, U. & Parkinson, G. S. Dual role of CO in the stability of subnano Pt clusters at the Fe_3O_4(001) surface. *Proceedings of the National Academy of Sciences* **113,** 8921–8926 (2016).

81. Meier, M., Jakub, Z., Balajka, J., Hulva, J., Bliem, R., Thakur, P. K., Lee, T. L., Franchini, C., Schmid, M., Diebold, U., *et al.* Probing the geometry of copper and silver adatoms on magnetite: quantitative experiment versus theory. *Nanoscale* **10,** 2226–2230 (2018).

82. Gargallo-Caballero, R., Martin-Garcia, L., Quesada, A., Granados-Miralles, C., Foerster, M., Aballe, L., Bliem, R., Parkinson, G. S., Blaha, P., Marco, J. F., *et al.* Co on Fe_3O_4(001): Towards precise control of surface properties. *Journal of Chemical Physics* **144,** 094704 (2016).

83. Shaikhutdinov, S. K., Ritter, M., Wang, X. G., Over, H. & Weiss, W. Defect structures on epitaxial Fe_3O_4(111) films. *Physical Review B* **60,** 11062–11069 (1999).

84. Noh, J., Osman, O. I., Aziz, S. G., Winget, P. & Brédas, J.-L. Magnetite Fe_3O_4 (111) Surfaces: Impact of Defects on Structure, Stability, and Electronic Properties. *Chemistry of Materials* **27,** 5856–5867 (2015).

85. Zhu, L., Yao, K. L. & Liu, Z. L. First-principles study of the polar (111) surface of Fe_3O_4. *Physical Review B* **74,** 035409 (2006).

86. Dementyev, P., Dostert, K.-H., Ivars-Barceló, F., O'Brien, C. P., Mirabella, F., Schauermann, S., Li, X., Paier, J., Sauer, J. & Freund, H.-J. Water Interaction with Iron Oxides. *Angewandte Chemie International Edition* **54,** 13942–13946 (2015).

87. Sala, A., Marchetto, H., Qin, Z. H., Shaikhutdinov, S., Schmidt, T. & Freund, H. J. Defects and inhomogeneities in Fe_3O_4(111) thin film growth on Pt(111). *Physical Review B* **86,** 155430 (2012).

88. Li, X., Paier, J., Sauer, J., Mirabella, F., Zaki, E., Ivars-Barceló, F., Shaikhutdinov, S. & Freund, H. J. Surface Termination of Fe_3O_4(111) Films Studied by CO Adsorption Revisited. *The Journal of Physical Chemistry B* **122,** 527–533 (2017).

89. Mirabella, F., Zaki, E., Ivars-Barceló, F., Li, X., Paier, J., Sauer, J., Shaikhutdinov, S. & Freund, H.-J. Cooperative Formation of Long-Range Ordering in Water Ad-layers on Fe_3O_4 (111) Surfaces. *Angewandte Chemie International Edition* **57,** 1409–1413 (2018).

90. Shimizu, T. K., Jung, J., Kato, H. S., Kim, Y. & Kawai, M. Termination and Verwey transition of the (111) surface of magnetite studied by scanning tunneling microscopy and first-principles calculations. *Physical Review B* **81,** 235429 (2010).

91. Condon, N. G., Leibsle, F. M., Parker, T., Lennie, A. R., Vaughan, D. J. & Thornton, G. Biphase ordering on Fe_3O_4(111). *Physical Review B* **55,** 15885–15894 (1997).

92. Spiridis, N., Freindl, K., Wojas, J., Kwiatek, N., Madej, E., Wilgocka-Ślęzak, D., Dróżdż, P., Ślęzak, T. & Korecki, J. Superstructures on Epitaxial Fe_3O_4(111) Films: Biphase Formation versus the Degree of Reduction. *The Journal of Physical Chemistry C* **123,** 4204–4216 (2019).

93. Wojas, J., Kwiatek, N., Wilgocka-Ślęzak, D., Madej, E., Korecki, J. & Spiridis, N. CO adsorption on Fe_3O_4(111) with regular and biphase terminations. *Applied Surface Science* **507,** 145069 (2020).

94. Schalow, T., Brandt, B., Starr, D. E., Laurin, M., Shaikhutdinov, S. K., Schauermann, S., Libuda, J. & Freund, H.-J. Size-Dependent Oxidation Mechanism of Supported Pd Nanoparticles. *Angewandte Chemie International Edition* **45,** 3693–3697 (2006).

95. Schalow, T., Brandt, B., Starr, D. E., Laurin, M., Schauermann, S., Shaikhutdinov, S. K., Libuda, J. & Freund, H. J. Oxygen-induced Restructuring of a Pd/Fe_3O_4 Model Catalyst. *Catalysis Letters* **107,** 189–196 (2006).

96. Rim, K. T., Eom, D., Liu, L., Stolyarova, E., Raitano, J. M., Chan, S.-W., Flytzani-Stephanopoulos, M. & Flynn, G. W. Charging and Chemical Reactivity of Gold Nanoparticles and Adatoms on the (111) Surface of Single-Crystal Magnetite: A Scanning Tunneling Microscopy/Spectroscopy Study. *The Journal of Physical Chemistry C* **113,** 10198–10205 (2009).

97. Yu, X., Wang, S.-G., Li, Y.-W., Wang, J. & Jiao, H. Single Gold Atom Adsorption on the Fe_3O_4(111) Surface. *The Journal of Physical Chemistry C* **116,** 10632–10638 (2012).

98. Kiejna, A., Ossowski, T. & Pabisiak, T. Surface properties of the clean and Au/Pd covered Fe_3O_4(111): DFT and DFT+U study. *Physical Review B* **85,** 125414 (2012).

99. Meyer, R., Shaikhutdinov, S. & Freund, H.-J. CO Oxidation on a Pd/Fe_3O_4(111) Model Catalyst. *Zeitschrift für Physikalische Chemie* **218,** 905–914 (2004).

100. Qin, Z. H., Lewandowski, M., Sun, Y. N., Shaikhutdinov, S. & Freund, H. J. Morphology and CO adsorption on platinum supported on thin Fe_3O_4(111) films. *Journal of Physics: Condensed Matter* **21,** 134019 (2009).

101. Xue, P., Fu, Z. & Yang, Z. The density functional theory studies on the promoting effect of the Cu-modified Fe_3O_4 catalysts. *Physics Letters A* **379,** 607–612 (2015).

102. Tamirat, A. G., Rick, J., Dubale, A. A., Su, W.-N. & Hwang, B.-J. Using hematite for photoelectrochemical water splitting: a review of current progress and challenges. *Nanoscale Horiz.* **1,** 243–267 (2016).

103. Zboril, R., Mashlan, M. & Petridis, D. Iron(III) Oxides from Thermal Processes-Synthesis, Structural and Magnetic Properties, Mössbauer Spectroscopy Characterization, and Applications. *Chem. Mater.* **14,** 969–982 (Mar. 2002).

104. Morin, F. J. Electrical Properties of α-Fe_2O_3 and α-Fe_2O_3 Containing Titanium. *Physical Review* **83,** 1005–1010 (Sept. 1951).

105. Nakau, T. Electrical Conductivity of α-Fe_2O_3. *J. Phys. Soc. Jpn.* **15,** 727–727 (Apr. 1960).

106. Le Formal, F., Tetreault, N., Cornuz, M., Moehl, T., Gratzel, M. & Sivula, K. Passivating surface states on water splitting hematite photoanodes with alumina overlayers. *Chemical Science* **2,** 737–743 (2011).

107. Guo, H. & Barnard, A. S. Thermodynamic modelling of nanomorphologies of hematite and goethite. *J. Mater. Chem.* **21,** 11566–11577 (2011).

108. Kraushofer, F., Jakub, Z., Bichler, M., Hulva, J., Drmota, P., Weinold, M., Schmid, M., Setvin, M., Diebold, U., Blaha, P., *et al.* Atomic-Scale Structure of the Hematite α-$Fe_2O_3(1\bar{1}02)$ "R-Cut" Surface. *The Journal of Physical Chemistry C* **122,** 1657–1669 (2018).

109. Kuhlenbeck, H., Shaikhutdinov, S. & Freund, H. J. Well-Ordered Transition Metal Oxide Layers in Model Catalysis - A Series of Case Studies. *Chem. Rev.* **113,** 3986–4034 (June 2013).

110. Tang, Y., Qin, H., Wu, K., Guo, Q. & Guo, J. The reduction and oxidation of $Fe_2O_3(0001)$ surface investigated by scanning tunneling microscopy. *Surface Science* **609,** 67–72 (2013).

111. Lanier, C. H., Chiaramonti, A. N., Marks, L. D. & Poeppelmeier, K. R. The Fe_3O_4 origin of the "Biphase" reconstruction on α-$Fe_2O_3(0001)$. *Surface Science* **603,** 2574–2579 (2009).

112. Genuzio, F., Sala, A., Schmidt, T., Menzel, D. & Freund, H.-J. Interconversion of α-Fe_2O_3 and Fe_3O_4 Thin Films: Mechanisms, Morphology, and Evidence for Unexpected Substrate Participation. *The Journal of Physical Chemistry C* **118,** 29068–29076 (2014).

113. Shaikhutdinov, S. K. & Weiss, W. Oxygen pressure dependence of the α-$Fe_2O_3(0001)$ surface structure. *Surface Science* **432,** L627–L634 (1999).

114. Ketteler, G., Weiss, W. & Ranke, W. Surface Structures of α-$Fe_2O_3(0001)$ Phases Determined by LEED Crytallography. *Surface Review and Letters* **08,** 661–683 (2001).

115. Kim, C. Y., Escuadro, A. A., Bedzyk, M. J., Liu, L. & Stair, P. C. X-ray scattering study of the stoichiometric recovery of the α-Fe_2O_3 surface. *Surface Science* **572,** 239–246 (2004).

116. Walenta, C. A., Crampton, A. S., Xu, F., Heiz, U. & Friend, C. M. Chemistry of Methanol and Ethanol on Ozone-Prepared α-Fe_2O_3. *The Journal of Physical Chemistry C* **122,** 25404–25410 (2018).

117. Woodruff, D. P. Quantitative Structural Studies Of Corundum and Rocksalt Oxide Surfaces. *Chemical Reviews* **113,** 3863–3886 (2013).

118. Lad, R. J. & Henrich, V. E. Structure of α-Fe_2O_3 single crystal surfaces following Ar^+ ion bombardment and annealing in O_2. *Surface Science* **193,** 81–93 (1988).

119. Gautier-Soyer, M., Pollak, M., Henriot, M. & Guittet, M. The (1×2) reconstruction of the α-Fe_2O_3(012) surface. *Surface Science* **352-354,** 112–116 (May 1996).

120. Henderson, M. A., Joyce, S. A. & Rustad, J. R. Interaction of water with the (1×1) and (2×1) surfaces of α-Fe_2O_3(012). *Surface Science* **417,** 66–81 (Nov. 1998).

121. Henderson, M. A. Insights into the (1×1)-to-(2×1) phase transition of the α-Fe_2O_3(012) surface using EELS, LEED and water TPD. *Surface Science* **515,** 253–262 (2002).

122. Henderson, M. A. Surface stabilization of organics on hematite by conversion from terminal to bridging adsorption structures. *Geochimica et Cosmochimica Acta* **67,** 1055–1063 (2003).

123. Tanwar, K. S., Lo, C. S., Eng, P. J., Catalano, J. G., Walko, D. A., Brown, G. E., Waychunas, G. A., Chaka, A. M. & Trainor, T. P. Surface diffraction study of the hydrated hematite surface. *Surface Science* **601,** 460–474 (2007).

124. Tanwar, K. S., Catalano, J. G., Petitto, S. C., Ghose, S. K., Eng, P. J. & Trainor, T. P. Hydrated α-Fe_2O_3 surface structure: Role of surface preparation. *Surface Science* **601,** L59–L64 (2007).

125. Trainor, T. P., Eng, P. J., Chaka, A. M., Lo, C. S., Tanwar, K., Ghose, S. K., Brown, G. E., Catalano, J. G., Waychunas, G. A. & Tempelton, A. S. Structure and reactivity of hydroxylated hematite surfaces: Application of surface x-ray diffraction and spectroscopy. *Geochimica Et Cosmochimica Acta* **69,** A486–A486 (2005).

126. Lo, C. S., Tanwar, K. S., Chaka, A. M. & Trainor, T. P. Density functional theory study of the clean and hydrated hematite $(1\bar{1}02)$ surfaces. *Physical Review B* **75** (2007).

127. Tasker, P. The stability of ionic crystal surfaces. *Journal of Physics C: Solid State Physics* **12,** 4977–4984 (1979).

128. Wang, J. & Rustad, J. R. A simple model for the effect of hydration on the distribution of ferrous iron at reduced hematite (012) surfaces. *Geochimica et Cosmochimica Acta* **70,** 5285–5292 (2006).

129. Henderson, M. A. Low temperature oxidation of Fe^{2+} surface sites on the (2×1) reconstructed surface of alpha-$Fe_2O_3(01\bar{1}2)$. *Surface Science* **604,** 1197–1201 (July 2010).

130. Catalano, J. G., Zhang, Z., Park, C. Y., Fenter, P. & Bedzyk, M. J. Bridging arsenate surface complexes on the hematite (012) surface. *Geochimica Et Cosmochimica Acta* **71,** 1883–1897 (2007).

131. Kerisit, S. Water structure at hematite–water interfaces. *Geochimica et Cosmochimica Acta* **75,** 2043–2061 (2011).

132. Tanwar, K. S., Petitto, S. C., Ghose, S. K., Eng, P. J. & Trainor, T. P. Structural study of Fe(II) adsorption on hematite. *Geochimica et Cosmochimica Acta* **72,** 3311–3325 (2008).

133. Aboud, S., Wilcox, J. & Brown, G. E. Density functional theory investigation of the interaction of water with α-Al_2O_3 and α-Fe_2O_3 $(1\bar{1}02)$ surfaces: Implications for surface reactivity. *Physical Review B* **83,** 125407 (2011).

134. McBriarty, M. E., von Rudorff, G. F., Stubbs, J. E., Eng, P. J., Blumberger, J. & Rosso, K. M. Dynamic Stabilization of Metal Oxide–Water Interfaces. *Journal of the American Chemical Society* **139,** 2581–2584 (2017).

135. Binnig, G. & Rohrer, H. Scanning Tunneling Microscopy—from Birth to Adolescence (Nobel Lecture). *Angewandte Chemie International Edition in English* **26,** 606–614 (1987).

136. Tersoff, J. & Hamann, D. R. Theory of the scanning tunneling microscope. *Physical Review B* **31,** 805–813 (Jan. 1985).

137. Binnig, G., Quate, C. F. & Gerber, C. Atomic Force Microscope. *Phys. Rev. Lett.* **56,** 930–933 (9 Mar. 1986).

138. Gross, L., Mohn, F., Moll, N., Liljeroth, P. & Meyer, G. The Chemical Structure of a Molecule Resolved by Atomic Force Microscopy. *Science* **325,** 1110–1114 (2009).

139. Shiotari, A. & Sugimoto, Y. Ultrahigh-resolution imaging of water networks by atomic force microscopy. *Nature Communications* **8,** 14313 (2017).

140. Onoda, J., Ondráček, M., Jelínek, P. & Sugimoto, Y. Electronegativity determination of individual surface atoms by atomic force microscopy. *Nature Communications* **8,** 15155 (2017).

141. Sugimoto, Y., Pou, P., Abe, M., Jelinek, P., Pérez, R., Morita, S. & Custance, Ó. Chemical identification of individual surface atoms by atomic force microscopy. *Nature* **446,** 64–67 (2007).

142. Gross, L., Mohn, F., Moll, N., Schuler, B., Criado, A., Guitián, E., Peña, D., Gourdon, A. & Meyer, G. Bond-Order Discrimination by Atomic Force Microscopy. *Science* **337,** 1326–1329 (2012).

143. De Oteyza, D. G., Gorman, P., Chen, Y. C., Wickenburg, S., Riss, A., Mowbray, D. J., Etkin, G., Pedramrazi, Z., Tsai, H. Z., Rubio, A., *et al.* Direct Imaging of Covalent Bond Structure in Single-Molecule Chemical Reactions. *Science* **340,** 1434–1437 (2013).

144. Setvin, M., Hulva, J., Parkinson, G. S., Schmid, M. & Diebold, U. Electron transfer between anatase TiO_2 and an O_2 molecule directly observed by atomic force microscopy. *Proceedings of the National Academy of Sciences* **114,** E2556–E2562 (2017).

145. Patera, L. L., Queck, F., Scheuerer, P. & Repp, J. Mapping orbital changes upon electron transfer with tunnelling microscopy on insulators. *Nature* **566,** 245–248 (Feb. 2019).

146. Hofer, W. A., Foster, A. S. & Shluger, A. L. Theories of scanning probe microscopes at the atomic scale. *Rev. Mod. Phys.* **75,** 1287–1331 (4 Oct. 2003).

147. Giessibl, F. J. Forces and frequency shifts in atomic-resolution dynamic-force microscopy. *Phys. Rev. B* **56,** 16010–16015 (24 Dec. 1997).

148. Giessibl, F. J. The qPlus sensor, a powerful core for the atomic force microscope. *Review of Scientific Instruments* **90,** 011101 (2019).

149. Lauritsen, J. V. & Reichling, M. Atomic resolution non-contact atomic force microscopy of clean metal oxide surfaces. *Journal of Physics: Condensed Matter* **22,** 263001 (2010).

150. Hapala, P., Kichin, G., Wagner, C., Tautz, F. S., Temirov, R. & Jelínek, P. Mechanism of high-resolution STM/AFM imaging with functionalized tips. *Physical Review B* **90** (2014).

151. Lüth, H. *Solid Surfaces, Interfaces and Thin Films* (Springer Berlin Heidelberg, 2010).

152. Grosvenor, A. P., Kobe, B. A., Biesinger, M. C. & McIntyre, N. S. Investigation of multiplet splitting of Fe 2p XPS spectra and bonding in iron compounds. *Surface and Interface Analysis* **36,** 1564–1574 (2004).

153. Pavelec, J., Hulva, J., Halwidl, D., Bliem, R., Gamba, O., Jakub, Z., Brunbauer, F., Schmid, M., Diebold, U. & Parkinson, G. S. A multi-technique study of CO_2 adsorption on Fe_3O_4 magnetite. *The Journal of Chemical Physics* **146,** 014701 (2017).

154. De Jong, A. M. & Niemantsverdriet, J. W. Thermal desorption analysis: Comparative test of ten commonly applied procedures. *Surface Science* **233,** 355–365 (1990).

155. Ono, L. K. & Cuenya, B. R. Size Effects on the Desorption of O_2 from Au_2O_3/Au_0 Nanoparticles Supported on SiO_2: A TPD Study. *The Journal of Physical Chemistry C* **112,** 18543–18550 (2008).

156. Tait, S. L., Dohnálek, Z., Campbell, C. T. & Kay, B. D. n-alkanes on MgO(100). I. Coverage-dependent desorption kinetics of n-butane. *The Journal of Chemical Physics* **122,** 164707 (2005).

157. Redhead, P. A. Thermal desorption of gases. *Vacuum* **12,** 203–211 (1962).

158. Hapala, P., Temirov, R., Tautz, F. S. & Jelínek, P. Origin of High-Resolution IETS-STM Images of Organic Molecules with Functionalized Tips. *Physical Review Letters* **113,** 226101 (2014).

159. Meier, M., Hulva, J., Jakub, Z., Pavelec, J., Setvin, M., Bliem, R., Schmid, M., Diebold, U., Franchini, C. & Parkinson, G. S. Water agglomerates on Fe_3O_4(001). *Proceedings of the National Academy of Sciences* **115,** E5642–E5650 (2018).

160. Jakub, Z., Kraushofer, F., Bichler, M., Balajka, J., Hulva, J., Pavelec, J., Sokolović, I., Müllner, M., Setvin, M., Schmid, M., *et al.* Partially Dissociated Water Dimers at the Water–Hematite Interface. *ACS Energy Letters* **4,** 390–396 (2019).

161. Jakub, Z., Hulva, J., Meier, M., Bliem, R., Kraushofer, F., Setvin, M., Schmid, M., Diebold, U., Franchini, C. & Parkinson, G. S. Local Structure and Coordination Define Adsorption in a Model Ir_1/Fe_3O_4 Single-Atom Catalyst. *Angewandte Chemie Internation Edition* **58,** 13961–13968.

162. Choi, J. I. J., Mayr-Schmölzer, W., Mittendorfer, F., Redinger, J., Diebold, U. & Schmid, M. The growth of ultra-thin zirconia films on Pd_3Zr(0001). *Journal of Physics: Condensed Matter* **26,** 225003 (2014).

163. Huber, F. & Giessibl, F. J. Low noise current preamplifier for qPlus sensor deflection signal detection in atomic force microscopy at room and low temperatures. *Review of Scientific Instruments* **88,** 073702 (2017).

164. Setvín, M., Javorský, J., Turčinková, D., Matolínová, I., Sobotík, P., Kocán, P. & Ošťádal, I. Ultrasharp tungsten tips—characterization and nondestructive cleaning. *Ultramicroscopy* **113,** 152–157 (2012).

165. Pavelec, J. *Surface chemistry setup and adsorption of* CO_2 *on* Fe_3O_4*(001)* PhD thesis (TU Wien, 2019).

166. Halwidl, D. *Development of an Effusive Molecular Beam Apparatus* (Springer Fachmedien Wiesbaden, Wiesbaden, 2016).

167. Balajka, J., Pavelec, J., Komora, M., Schmid, M. & Diebold, U. Apparatus for dosing liquid water in ultrahigh vacuum. *Review of Scientific Instruments* **89,** 083906 (2018).

168. Balajka, J. *Interaction of Titanium Dioxide Surfaces with Liquid Water* PhD thesis (TU Wien, 2018).

169. Jakub, Z. *UHV-EC Transfer System for Electrochemical Surface Science Studies* MA thesis (Brno University of Technology, 2016).

170. Kraushofer, F. *The Hematite (012) Surface: Structure and Reactivity* MA thesis (TU Wien, 2017).

171. Iandolo, B., Wickman, B., Zorić, I. & Hellman, A. The rise of hematite: origin and strategies to reduce the high onset potential for the oxygen evolution reaction. *J. Mater. Chem. A* **3,** 16896–16912 (2015).

172. Koper, M. T. M. Thermodynamic theory of multi-electron transfer reactions: Implications for electrocatalysis. *Journal of Electroanalytical Chemistry* **660,** 254–260 (2011).

173. Man, I. C., Su, H.-Y., Calle-Vallejo, F., Hansen, H. A., Martínez, J. I., Inoglu, N. G., Kitchin, J., Jaramillo, T. F., Nørskov, J. K. & Rossmeisl, J. Universality in Oxygen Evolution Electrocatalysis on Oxide Surfaces. *ChemCatChem* **3,** 1159–1165 (2011).

174. Hong, W. T., Risch, M., Stoerzinger, K. A., Grimaud, A., Suntivich, J. & Shao-Horn, Y. Toward the rational design of non-precious transition metal oxides for oxygen electrocatalysis. *Energy & Environmental Science* **8,** 1404–1427 (2015).

175. Malherbe, J. B., Hofmann, S. & Sanz, J. M. Preferential sputtering of oxides: A comparison of model predictions with experimental data. *Applied Surface Science* **27,** 355–365 (1986).

176. Lee, J. & Han, S. Thermodynamics of native point defects in α-Fe_2O_3: an ab initio study. *Physical Chemistry Chemical Physics* **15,** 18906–18914 (2013).

177. Pielmeier, F. & Giessibl, F. J. Spin Resolution and Evidence for Superexchange on NiO(001) Observed by Force Microscopy. *Physical Review Letters* **110,** 266101 (2013).

178. Mu, R., Zhao, Z.-j., Dohnálek, Z. & Gong, J. Structural motifs of water on metal oxide surfaces. *Chem. Soc. Rev.* **46,** 1785–1806 (2017).

179. Kendelewicz, T., Kaya, S., Newberg, J. T., Bluhm, H., Mulakaluri, N., Moritz, W., Scheffler, M., Nilsson, A., Pentcheva, R. & Brown, G. E. X-ray Photoemission and Density Functional Theory Study of the Interaction of Water Vapor with the $Fe_3O_4(001)$ Surface at Near-Ambient Conditions. *The Journal of Physical Chemistry C* **117,** 2719–2733 (2013).

180. Mu, R., Cantu, D. C., Lin, X., Glezakou, V.-A., Wang, Z., Lyubinetsky, I., Rousseau, R. & Dohnálek, Z. Dimerization Induced Deprotonation of Water on $RuO_2(110)$. *The Journal of Physical Chemistry Letters* **5,** 3445–3450 (2014).

181. Mu, R., Cantu, D. C., Glezakou, V.-A., Lyubinetsky, I., Rousseau, R. & Dohnálek, Z. Deprotonated Water Dimers: The Building Blocks of Segmented Water Chains on Rutile $RuO_2(110)$. *The Journal of Physical Chemistry C* **119,** 23552–23558 (2015).

182. Kan, H. H., Colmyer, R. J., Asthagiri, A. & Weaver, J. F. Adsorption of Water on a PdO(101) Thin Film: Evidence of an Adsorbed $HO{-}H_2O$ Complex. *The Journal of Physical Chemistry C* **113,** 1495–1506 (2009).

183. Yang, W., Wei, D., Jin, X., Xu, C., Geng, Z., Guo, Q., Ma, Z., Dai, D., Fan, H. & Yang, X. Effect of the Hydrogen Bond in Photoinduced Water Dissociation: A Double-Edged Sword. *The Journal of Physical Chemistry Letters* **7,** 603–608 (2016).

184. Schiros, T., Ogasawara, H., Näslund, L. Å., Andersson, K. J., Ren, J., Meng, S., Karlberg, G. S., Odelius, M., Nilsson, A. & Pettersson, L. G. M. Cooperativity in Surface Bonding and Hydrogen Bonding of Water and Hydroxyl at Metal Surfaces. *The Journal of Physical Chemistry C* **114,** 10240–10248 (2010).

185. Yamamoto, S., Kendelewicz, T., Newberg, J. T., Ketteler, G., Starr, D. E., Mysak, E. R., Andersson, K. J., Ogasawara, H., Bluhm, H., Salmeron, M., *et al.* Water Adsorption on α-Fe_2O_3 at near Ambient Conditions. *The Journal of Physical Chemistry C* **114,** 2256–2266 (2010).

186. Ali, H., Seidel, R., Pohl, M. N. & Winter, B. Molecular species forming at the α-Fe_2O_3 nanoparticle–aqueous solution interface. *Chemical Science* **9,** 4511–4523 (2018).

187. Rustad, J. R. & Casey, W. H. Metastable structures and isotope exchange reactions in polyoxometalate ions provide a molecular view of oxide dissolution. *Nature Materials* **11,** 223–226 (2012).

188. Ohlin, C. A., Villa, E. M., Rustad, J. R. & Casey, W. H. Dissolution of insulating oxide materials at the molecular scale. *Nature Materials* **9,** 11–19 (2009).

189. Casey, W. H. & Rustad, J. R. Pathways for oxygen-isotope exchange in two model oxide clusters. *New Journal of Chemistry* **40,** 898–905 (2016).

190. Hellman, A. & Pala, R. G. S. First-Principles Study of Photoinduced Water-Splitting on Fe_2O_3. *The Journal of Physical Chemistry C* **115,** 12901–12907 (2011).

191. Elam, J. W., Nelson, C. E., Cameron, M. A., Tolbert, M. A. & George, S. M. Adsorption of H_2O on a Single-Crystal α-Al_2O_3(0001) Surface. *The Journal of Physical Chemistry B* **102,** 7008–7015 (1998).

192. Zaki, E., Jakub, Z., Mirabella, F., Parkinson, G. S., Shaikhutdinov, S. & Freund, H.-J. Water Ordering on the Magnetite Fe_3O_4 Surfaces. *The Journal of Physical Chemistry Letters* **10,** 2487–2492 (2019).

193. Salmeron, M., Bluhm, H., Tatarkhanov, M., Ketteler, G., Shimizu, T. K., Mugarza, A., Deng, X., Herranz, T., Yamamoto, S. & Nilsson, A. Water growth on metals and oxides: binding, dissociation and role of hydroxyl groups. *Faraday Discussions* **141,** 221–229 (2009).

194. Maier, S. & Salmeron, M. How Does Water Wet a Surface? *Accounts of Chemical Research* **48,** 2783–2790 (2015).

195. Önsten, A., Stoltz, D., Palmgren, P., Yu, S., Göthelid, M. & Karlsson, U. O. Water Adsorption on ZnO(0001): Transition from Triangular Surface Structures to a Disordered Hydroxyl Terminated phase. *The Journal of Physical Chemistry C* **114,** 11157–11161 (2010).

196. Wagner, M., Lackner, P., Seiler, S., Brunsch, A., Bliem, R., Gerhold, S., Wang, Z., Osiecki, J., Schulte, K., Boatner, L. A., *et al.* Resolving the Structure of a Well-Ordered Hydroxyl Overlayer on In_2O_3(111): Nanomanipulation and Theory. *ACS Nano* **11,** 11531–11541 (2017).

197. Duncan, D. A., Allegretti, F. & Woodruff, D. P. Water does partially dissociate on the perfect TiO_2(110) surface: A quantitative structure determination. *Physical Review B* **86,** 045411 (2012).

198. Walle, L. E., Borg, A., Uvdal, P. & Sandell, A. Experimental evidence for mixed dissociative and molecular adsorption of water on a rutile TiO_2(110) surface without oxygen vacancies. *Physical Review B* **80,** 235436 (2009).

199. Włodarczyk, R., Sierka, M., Kwapień, K., Sauer, J., Carrasco, E., Aumer, A., Gomes, J. F., Sterrer, M. & Freund, H.-J. Structures of the Ordered Water Monolayer on MgO(001). *The Journal of Physical Chemistry C* **115,** 6764–6774 (2011).

200. Peng, J., Guo, J., Hapala, P., Cao, D., Ma, R., Cheng, B., Xu, L., Ondráček, M., Jelínek, P., Wang, E., *et al.* Weakly perturbative imaging of interfacial water with submolecular resolution by atomic force microscopy. *Nature Communications* **9,** 122 (2018).

201. Bourgund, A., Lechner, B. A. J., Meier, M., Franchini, C., Parkinson, G. S., Heiz, U. & Esch, F. Influence of Local Defects on the Dynamics of O–H Bond Breaking and Formation on a Magnetite Surface. *The Journal of Physical Chemistry C* **123,** 19742–19747 (2019).

202. Gamba, O., Hulva, J., Pavelec, J., Bliem, R., Schmid, M., Diebold, U. & Parkinson, G. S. The Role of Surface Defects in the Adsorption of Methanol on Fe_3O_4(001). *Topics in Catalysis* **60,** 420–430 (2016).

203. Hulva, J. *Studies of Adsorption on Magnetite (001) Using Molecular Beams* PhD thesis (TU Wien, 2019).

204. Mulakaluri, N., Pentcheva, R., Wieland, M., Moritz, W. & Scheffler, M. Partial Dissociation of Water on Fe_3O_4(001): Adsorbate Induced Charge and Orbital Order. *Physical Review Letters* **103,** 176102 (2009).

205. Mulakaluri, N., Pentcheva, R. & Scheffler, M. Coverage-Dependent Adsorption Mode of Water on Fe_3O_4(001): Insights from First Principles Calculations. *The Journal of Physical Chemistry C* **114,** 11148–11156 (2010).

206. Liu, H., Bianchetti, E., Siani, P. & Di Valentin, C. Insight into the interface between Fe_3O_4 (001) surface and water overlayers through multiscale molecular dynamics simulations. *The Journal of Chemical Physics* **152,** 124711 (2020).

207. Zhang, K., Shaikhutdinov, S. & Freund, H.-J. Does the Surface Structure of Oxide Affect the Strong Metal–Support Interaction with Platinum? Platinum on Fe_3O_4(001) versus Fe_3O_4(111). *ChemCatChem* **7,** 3725–3730 (2015).

208. Hulva, J., Jakub, Z., Novotny, Z., Johansson, N., Knudsen, J., Schnadt, J., Schmid, M., Diebold, U. & Parkinson, G. S. Adsorption of CO on the Fe_3O_4(001) Surface. *The Journal of Physical Chemistry B* (2017).

209. Ralon, R. *Magnetite - Fe_3O_4(111)* (project thesis, TU Wien, 2018).

210. Zaki, E., Mirabella, F., Ivars-Barceló, F., Seifert, J., Carey, S., Shaikhutdinov, S., Freund, H.-J., Li, X., Paier, J. & Sauer, J. Water adsorption on the Fe_3O_4(111) surface: dissociation and network formation. *Physical Chemistry Chemical Physics* **20,** 15764–15774 (2018).

211. Jakub, Z., Hulva, J., Mirabella, F., Kraushofer, F., Meier, M., Bliem, R., Diebold, U. & Parkinson, G. S. Nickel Doping Enhances the Reactivity of Fe_3O_4(001) to Water. *The Journal of Physical Chemistry C* **123,** 15038–15045 (2019).

212. Jakub, Z., Hulva, J., Ryan, P. T. P., Duncan, D. A., Payne, D. J., Bliem, R., Ulreich, M., Hofegger, P., Kraushofer, F., Meier, M., *et al.* Adsorbate-induced structural evolution changes the mechanism of CO oxidation on a Rh/Fe_3O_4(001) model catalyst. *Nanoscale* **12,** 5866–5875 (2020).

213. Zhu, M. & Wachs, I. E. Iron-Based Catalysts for the High-Temperature Water–Gas Shift (HT-WGS) Reaction: A Review. *ACS Catalysis* **6,** 722–732 (2016).

214. Martos, C., Dufour, J. & Ruiz, A. Synthesis of Fe_3O_4-based catalysts for the high-temperature water gas shift reaction. *International Journal of Hydrogen Energy* **34,** 4475–4481 (2009).

215. Jeong, D.-W., Jang, W.-J., Shim, J.-O. & Roh, H.-S. High temperature water–gas shift without pre-reduction over spinel ferrite catalysts synthesized by glycine assisted sol–gel combustion method. *International Journal of Hydrogen Energy* **41,** 3870–3876 (2016).

216. Ashok, J., Wai, M. H. & Kawi, S. Nickel-based Catalysts for High-temperature Water Gas Shift Reaction-Methane Suppression. *ChemCatChem* **10,** 3927–3942 (2018).

217. Fu, Z., Wang, J., Zhang, N., An, Y. & Yang, Z. Effect of Cu doping on the catalytic activity of Fe_3O_4 in water-gas shift reactions. *International Journal of Hydrogen Energy* **40,** 2193–2198 (2015).

218. Trotochaud, L., Ranney, J. K., Williams, K. N. & Boettcher, S. W. Solution-Cast Metal Oxide Thin Film Electrocatalysts for Oxygen Evolution. *Journal of the American Chemical Society* **134,** 17253–17261 (2012).

219. Gong, M., Li, Y., Wang, H., Liang, Y., Wu, J. Z., Zhou, J., Wang, J., Regier, T., Wei, F. & Dai, H. An Advanced Ni–Fe Layered Double Hydroxide Electrocatalyst for Water Oxidation. *Journal of the American Chemical Society* **135,** 8452–8455 (2013).

220. Burke, M. S., Enman, L. J., Batchellor, A. S., Zou, S. & Boettcher, S. W. Oxygen Evolution Reaction Electrocatalysis on Transition Metal Oxides and (Oxy)hydroxides: Activity Trends and Design Principles. *Chemistry of Materials* **27,** 7549–7558 (2015).

221. Dionigi, F. & Strasser, P. NiFe-Based (Oxy)hydroxide Catalysts for Oxygen Evolution Reaction in Non-Acidic Electrolytes. *Advanced Energy Materials* **6,** 1600621 (2016).

222. Li, Y.-F. & Selloni, A. Mechanism and Activity of Water Oxidation on Selected Surfaces of Pure and Fe-Doped NiO_x. *ACS Catalysis* **4,** 1148–1153 (2014).

223. Wu, Z., Zou, Z., Huang, J. & Gao, F. $NiFe_2O_4$ Nanoparticles/NiFe Layered Double-Hydroxide Nanosheet Heterostructure Array for Efficient Overall Water Splitting at Large Current Densities. *ACS Applied Materials & Interfaces* **10,** 26283–26292 (2018).

224. Zhang, G., Li, Y., Zhou, Y. & Yang, F. NiFe Layered-Double-Hydroxide-Derived NiO-$NiFe_2O_4$/Reduced Graphene Oxide Architectures for Enhanced Electrocatalysis of Alkaline Water Splitting. *ChemElectroChem* **3,** 1927–1936 (2016).

225. Li, F., Li, Y., Zeng, X. C. & Chen, Z. Exploration of High-Performance Single-Atom Catalysts on Support M_1/FeO_x for CO Oxidation via Computational Study. *ACS Catalysis* **5,** 544–552 (2015).

226. Liang, J., Yu, Q., Yang, X., Zhang, T. & Li, J. A systematic theoretical study on FeO_x-supported single-atom catalysts: M_1/FeO_x for CO oxidation. *Nano Research* **11,** 1599–1611 (2018).

227. Lin, J., Wang, A., Qiao, B., Liu, X., Yang, X., Wang, X., Liang, J., Li, J., Liu, J. & Zhang, T. Remarkable Performance of Ir_1/FeO_x Single-Atom Catalyst in Water Gas Shift Reaction. *Journal of the American Chemical Society* **135,** 15314 15317 (Oct. 2013).

228. Tilley, S. D., Cornuz, M., Sivula, K. & Grätzel, M. Light-Induced Water Splitting with Hematite: Improved Nanostructure and Iridium Oxide Catalysis. *Angewandte Chemie International Edition* **49,** 6405–6408 (2010).

229. Matsumoto, Y. & Sato, E. Electrocatalytic properties of transition metal oxides for oxygen evolution reaction. *Materials Chemistry and Physics* **14,** 397–426 (1986).

230. Anic, K., Bukhtiyarov, A. V., Li, H., Rameshan, C. & Rupprechter, G. CO Adsorption on Reconstructed Ir(100) Surfaces from UHV to mbar Pressure: A LEED, TPD, and PM-IRAS Study. *The Journal of Physical Chemistry C* **120,** 10838–10848 (2016).

231. Hagen, D. I., Nieuwenhuys, B. E., Rovida, G. & Somorjai, G. A. Low-energy electron diffraction, Auger electron spectroscopy, and thermal desorption studies of chemisorbed CO and O_2 on the (111) and stepped [6(111)×(100)] iridium surfaces. *Surface Science* **57,** 632–650 (1976).

232. Sushchikh, M., Lauterbach, J. & Weinberg, W. H. Adsorption and desorption kinetics of CO on Ir(111): bridging the pressure gap. *Surface Science* **393,** 135–140 (1997).

233. Pfeifer, V., Jones, T. E., Velasco Vélez, J. J., Massué, C., Greiner, M. T., Arrigo, R., Teschner, D., Girgsdies, F., Scherzer, M., Allan, J., *et al.* The electronic structure of iridium oxide electrodes active in water splitting. *Physical Chemistry Chemical Physics* **18,** 2292–2296 (2016).

234. Duan, S., Wang, R. & Liu, J. Stability investigation of a high number density Pt_1/Fe_2O_3 single-atom catalyst under different gas environments by HAADF-STEM. *Nanotechnology* **29,** 204002 (2018).

235. Dessal, C., Len, T., Morfin, F., Rousset, J.-L., Aouine, M., Afanasiev, P. & Piccolo, L. Dynamics of Single Pt Atoms on Alumina during CO Oxidation Monitored by Operando X-ray and Infrared Spectroscopies. *ACS Catalysis,* 5752–5759 (2019).

236. Sterrer, M., Yulikov, M., Risse, T., Freund, H.-J., Carrasco, J., Illas, F., Di Valentin, C., Giordano, L. & Pacchioni, G. When the reporter induces the effect: unusual IR spectra of CO on $Au_1/MgO(001)/Mo(001)$. *Angewandte Chemie International Edition* **45,** 2633–2635 (2006).

237. Chen, Z., Vorobyeva, E., Mitchell, S., Fako, E., Ortuño, M. A., López, N., Collins, S. M., Midgley, P. A., Richard, S., Vilé, G., *et al.* A heterogeneous single-atom palladium catalyst surpassing homogeneous systems for Suzuki coupling. *Nature Nanotechnology* **13,** 702–707 (2018).

238. Guan, H., Lin, J., Qiao, B., Yang, X., Li, L., Miao, S., Liu, J., Wang, A., Wang, X. & Zhang, T. Catalytically Active Rh Sub-Nanoclusters on TiO_2 for CO Oxidation at Cryogenic Temperatures. *Angewandte Chemie International Edition* **55,** 2820–2824 (2016).

239. Matsubu, J. C., Zhang, S., DeRita, L., Marinkovic, N. S., Chen, J. G., Graham, G. W., Pan, X. & Christopher, P. Adsorbate-mediated strong metal–support interactions in oxide-supported Rh catalysts. *Nature Chemistry* **9,** 120 (2016).

240. Ghosh, T. K. & Nair, N. N. Rh_1/γ-Al_2O_3 Single-Atom Catalysis of O_2 Activation and CO Oxidation: Mechanism, Effects of Hydration, Oxidation State, and Cluster Size. *ChemCatChem* **5,** 1811–1821 (2013).

241. Gustafson, J., Balmes, O., Zhang, C., Shipilin, M., Schaefer, A., Hagman, B., Merte, L. R., Martin, N. M., Carlsson, P.-A., Jankowski, M., *et al.* The Role of Oxides in Catalytic CO Oxidation over Rhodium and Palladium. *ACS Catalysis* **8,** 4438–4445 (2018).

242. Freund, H.-J., Meijer, G., Scheffler, M., Schlögl, R. & Wolf, M. CO Oxidation as a Prototypical Reaction for Heterogeneous Processes. *Angewandte Chemie International Edition* **50,** 10064–10094 (2011).

243. Beniya, A. & Higashi, S. Towards dense single-atom catalysts for future automotive applications. *Nature Catalysis* **2,** 590–602 (2019).

244. Sinthika, S., Vala, S. T., Kawazoe, Y. & Thapa, R. CO Oxidation Prefers the Eley–Rideal or Langmuir–Hinshelwood Pathway: Monolayer vs Thin Film of SiC. *ACS Applied Materials & Interfaces* **8,** 5290–5299 (2016).

245. Newton, M. A., Ferri, D., Smolentsev, G., Marchionni, V. & Nachtegaal, M. Room-temperature carbon monoxide oxidation by oxygen over Pt/Al_2O_3 mediated by reactive platinum carbonates. *Nature Communications* **6,** 8675 (2015).

246. Pan, Q., Weng, X., Chen, M., Giordano, L., Pacchioni, G., Noguera, C., Goniakowski, J., Shaikhutdinov, S. & Freund, H.-J. Enhanced CO Oxidation on the Oxide/Metal Interface: From Ultra-High Vacuum to Near-Atmospheric Pressures. *ChemCatChem* **7,** 2620–2627 (2015).

247. Halder, A., Curtiss, L. A., Fortunelli, A. & Vajda, S. Perspective: Size selected clusters for catalysis and electrochemistry. *The Journal of Chemical Physics* **148,** 110901 (2018).

248. Zhao, K., Tang, H., Qiao, B., Li, L. & Wang, J. High Activity of Au/γ-Fe_2O_3 for CO Oxidation: Effect of Support Crystal Phase in Catalyst Design. *ACS Catalysis* **5,** 3528–3539 (2015).

249. Widmann, D. & Behm, R. J. Active Oxygen on a Au/TiO_2 Catalyst: Formation, Stability, and CO Oxidation Activity. *Angewandte Chemie International Edition* **50,** 10241–10245 (2011).

250. Halwidl, D., Mayr-Schmölzer, W., Setvin, M., Fobes, D., Peng, J., Mao, Z., Schmid, M., Mittendorfer, F., Redinger, J. & Diebold, U. A full monolayer of superoxide: oxygen activation on the unmodified $Ca_3Ru_2O_7$(001) surface. *Journal of Materials Chemistry A* **6,** 5703–5713 (2018).

251. Abe, Y., Kato, K., Kawamura, M. & Sasaki, K. Rhodium and Rhodium Oxide Thin Films Characterized by XPS. *Surface Science Spectra* **8,** 117–125 (2001).

252. Blomberg, S., Lundgren, E., Westerström, R., Erdogan, E., Martin, N. M., Mikkelsen, A., Andersen, J. N., Mittendorfer, F. & Gustafson, J. Structure of the Rh_2O_3(0001) surface. *Surface Science* **606,** 1416–1421 (2012).

253. Wovchko, E. A. & Yates, J. T. Activation of O_2 on a Photochemically Generated Rh^I Site on an Al_2O_3 Surface: Low-Temperature O_2 Dissociation and CO Oxidation. *Journal of the American Chemical Society* **120,** 10523–10527 (1998).

254. Moulder, J. F., Stickle, W. F., Sobol, P. E. & Bomben, K. D. *Handbook of X-Ray Photoelectron Spectroscopy: A Reference Book of Standard Spectra for Identification and Interpretation of XPS Data* (Physical Electronics Division, Perkin-Elmer Corporation, 1992).

List of Publications

This section provides a list of peer-reviewed research papers that I have co-authored during my PhD studies. The publications are listed in chronological order.

1. Pavelec, J., Hulva, J., Halwidl, D., Bliem, R., Gamba, O., Jakub, Z., Brunbauer, F., Schmid, M., Diebold, U. & Parkinson, G. S. **A multi-technique study of CO_2 adsorption on Fe_3O_4 magnetite**. *The Journal of Chemical Physics* **146**, 014701 (2017).

2. Hulva, J., Jakub, Z., Novotny, Z., Johansson, N., Knudsen, J., Schnadt, J., Schmid, M., Diebold, U. & Parkinson, G. S. **Adsorption of CO on the $Fe_3O_4(001)$ Surface**. *The Journal of Physical Chemistry B* **122**, 721-729 (2018).

3. Meier, M., Jakub, Z., Balajka, J., Hulva, J., Bliem, R., Thakur, P. K., Lee, T. L., Franchini, C., Schmid, M., Diebold, U., Allegretti, F., Duncan, D. A. & Parkinson, G. S. **Probing the geometry of copper and silver adatoms on magnetite: quantitative experiment versus theory**. *Nanoscale* **10**, 2226–2230 (2018).

4. Kraushofer, F., Jakub, Z., Bichler, M., Hulva, J., Drmota, P., Weinold, M., Schmid, M., Setvin, M., Diebold, U., Blaha, P. & Parkinson, G. S. **Atomic-Scale Structure of the Hematite α-$Fe_2O_3(1\bar{1}02)$ "R-Cut" Surface**. *The Journal of Physical Chemistry C* **122**, 1657–1669 (2018).

5. Ryan, P. T. P., Jakub, Z., Balajka, J., Hulva, J., Meier, M., Küchle, J. T., Blowey, P. J., Thakur, P. K., Franchini, C., Payne, D. J., Woodruff, D. P., Rochford L. A., Allegretti, F., Lee., T.-L., Parkinson, G. S. & Duncan D., A. **Direct measurement of Ni incorporation into $Fe_3O_4(001)$**. *Physical Chemistry Chemical Physics* **20**, 16469–16476 (2018).

6. Meier, M., Hulva, J., Jakub, Z., Pavelec, J., Setvin, M., Bliem, R., Schmid, M., Diebold, U., Franchini, C. & Parkinson, G. S. **Water agglomerates on $Fe_3O_4(001)$**. *Proceedings of the National Academy of Sciences* **115**, E5642–E5650 (2018).

7. Jakub, Z., Kraushofer, F., Bichler, M., Balajka, J., Hulva, J., Pavelec, J., Sokolović, I., Müllner, M., Setvin, M., Schmid, M., Diebold, U., Blaha, P. & Parkinson, G. S. **Partially Dissociated Water Dimers at the Water–Hematite Interface**. *ACS Energy Letters* **4**, 390–396 (2019).

8. Zaki, E., Jakub, Z., Mirabella, F., Parkinson, G. S., Shaikhutdinov, S. & Freund, H.-J. **Water Ordering on the Magnetite Fe_3O_4 Surfaces**. *The Journal of Physical Chemistry Letters* **10**, 2487–2492 (2019).

9. Jakub, Z., Hulva, J., Mirabella, F., Kraushofer, F., Meier, M., Bliem, R., Diebold, U. & Parkinson, G. S. **Nickel Doping Enhances the Reactivity of Fe_3O_4(001) to Water**. *The Journal of Physical Chemistry C* **123**, 15038–15045 (2019).

10. Jakub, Z., Hulva, J., Meier, M., Bliem, R., Kraushofer, F., Setvin, M., Schmid, M., Diebold, U., Franchini, C. & Parkinson, G. S. **Local Structure and Coordination Define Adsorption in a Model Ir_1/Fe_3O_4 Single-Atom Catalyst**. *Angewandte Chemie Internation Edition* **58**, 13961–13968 (2019).

11. Kraushofer, F., Mirabella, F., Xu, J., Pavelec, J., Balajka, J., Müllner, M., Resch, N., Jakub, Z., Hulva, J., Meier, M., Schmid, M., Diebold, U. & Parkinson, G. S. **Self-limited growth of an oxyhydroxide phase at the Fe_3O_4(001) surface in liquid and ambient pressure water**. *The Journal of Chemical Physics* **151**, 154702 (2019).

12. Jakub, Z., Hulva, J., Ryan, P. T. P., Duncan, D. A., Payne, D. J., Bliem, R., Ulreich, M., Hofegger, P., Kraushofer, F., Meier, M., Schmid, M., Diebold, U. & Parkinson, G. S. **Adsorbate-induced structural evolution changes the mechanism of CO oxidation on a Rh/Fe_3O_4(001) model catalyst**. *Nanoscale* **12**, 5866–5875 (2020).

13. Ryan, P. T. P., Meier, M., Jakub, Z., Balajka, J., Hulva, J., Payne, D. J., Lee, T.-L., Franchini, C., Allegretti, F., Parkinson, G. S. & Duncan, D. A. **Probing structural changes upon carbon monoxide coordination to single metal adatoms**. *The Journal of Chemical Physics* **152**, 051102 (2020).

Statement of Contributions

Many of the publications I have co-authored were a result of fruitful collaborations both within the research group and between different groups. Here I clarify my contributions to the listed papers.

As the first author of publications (7, 10), I carried out a significant part of experimental work and I did the majority of data analysis, I was also involved in the writing of these manuscripts. I'm also the first author of publications (9, 12), where I carried out some of the presented experiments, did the majority of data analysis and interpretation and I wrote the manuscripts. In these two papers (9, 12), a significant amount of experimental work was done by my predecessors in the group, Jan Hulva and Roland Bliem.

In publications (4, 6, 8) I carried out the majority of the imaging experiments, I analyzed and interpreted the STM and ncAFM data and I was involved in the writing of these manuscripts. I took and analyzed some experimental data published in papers (1, 2). In paper (11), I was involved in multiple preliminary experiments on the subject. Results published in papers (3, 5, 13) were acquired at synchrotrone facilites, I contributed by preparing the samples and assisting during the data acquisition.

Zdeněk Jakub

Phone: +420 732 579 390
Email: zdenek.jakub@tuwien.ac.at

EDUCATION

2016 - present

PhD in Surface Science
TU Wien, Austria
Supervisor: Gareth S. Parkinson
Title of the PhD Thesis: *Surface Science Studies of Iron Oxides as Model Catalyst supports*
Expected graduation 2020

2014 – 2016

Master’s degree in Physical Engineering
Brno University of Technology, Czech Republic
Title of the Master Thesis: *UHV-EC Transfer System for Electrochemical Surface Science Studies*

2011 – 2014

Bachelor’s degree in Physical Engineering
Brno University of Technology, Czech Republic
Title of the Bachelor Thesis: *Interaction of a SNOM Tip with the Electromagnetic Near-field Formed by the Interference of Surface Plasmon Polaritons*

PROFESSIONAL EXPERIENCE

2013 - 2014

Product Specialist, Moravia Europe, Brno
Responsibilities: Testing and documentation writing for educational experimental systems aimed at high school physics; presenting the products to customers

---

AWARDS & ACHIEVMENTS

2013 - 2014

GE Foundation Scholar-Leaders Program
Scholarship, leadership development and soft-skills training for outstanding undergraduate students

2010 - 2013

Scholarship Program for Excellent Students
Scholarship and soft-skills training awarded by the municipality of the South Moravian region

OUTREACH

2012 - 2013

NaturTech lecturer
Popularization of natural sciences at cultural events and festivals in the South Moravian region

---

PUBLICATIONS

Local Structure and Coordination Define Adsorption in a Model $Ir_1/Fe_3O_4(001)$ Single-Atom Catalyst
Z. Jakub, Hulva, J., Meier, M., Bliem, R., Kraushofer, F., Setvin, M., Schmid, M., Diebold, U., Cesare, P., and Parkinson, G. S. *Angewandte Chemie International Edition* **2019** *58*, 13961

Partially Dissociated Water Dimers at the Water–Hematite Interface
Z. Jakub, Kraushofer, F., Bichler, M., Balajka, J., Hulva, J., Pavelec, J, Sokolović, I., Müllner, M., Setvin, M., Schmid, M., Diebold, U., Blaha, P., and Parkinson, G. S. *ACS Energy Letters* **2019** *4*, 390-396

Adsorbate-induced Structural Evolution Changes the Mechanism of CO Oxidation on a $Rh/Fe_3O_4(001)$ Model Catalyst
Z. Jakub, Hulva, J., Ryan, P. T., Duncan, D. A., Payne, D. J., Bliem, R., Ulreich, M., Hofegger, P., Kraushofer, F., Meier, M., Schmid, M., Diebold., U., and Parkinson, G. S. *Nanoscale* **2020** *12*, 5866-5875

Nickel Doping Enhances the Reactivity of $Fe_3O_4(001)$ to Water
Z. Jakub, Hulva, J., Mirabella, F., Kraushofer, F., Meier, M., Bliem, R., Diebold, U., and Parkinson, G. S. *The Journal of Physical Chemistry C* **2019** *123,* 15038-15045

Water Ordering on the Magnetite Fe_3O_4 surfaces
E. Zaki, ***Jakub, Z.***, Mirabella, F., Parkinson, G. S., Shaikhutdinov, S. and Freund, H.-J., *The Journal of Physical Chemistry Letters* **2019** 10, 2478-2492

Probing the Geometry of Copper and Silver Adatoms on Magnetite: Quantitative Experiment versus Theory
M. Meier, ***Jakub, Z.***, Balajka, J., Hulva, J., Bliem, R., Thakur, P. K., Lee, T.-L., Franchini, C., Schmid, M., Diebold, U., Allegretti, F., Duncan, D. A. and Parkinson, G. S. *Nanoscale* **2018** 10, 2226-2230

Atomic-Scale Structure of the Hematite α-$Fe_2O_3(1\bar{1}02)$ "R-Cut" Surface
F. Kraushofer, ***Jakub, Z.****,* Bichler, M., Hulva, J., Drmota, P., Weinold, M., Schmid, M., Setvin, M., Diebold, U., Blaha, P. and Parkinson, G.S. *The Journal of Physical Chemistry C* **2018** *122*, 1657-1669

Water Agglomerates on $Fe_3O_4(001)$
M. Meier, Hulva, J., ***Jakub, Z.***, Pavelec, J., Setvin, M., Bliem, R., Schmid, M., Diebold, U., Franchini, C. and Parkinson, G. S. *Proceedings of the National Academy of Sciences* **2018**, 115, E5642-E5650

Adsorption of CO on the $Fe_3O_4(001)$ Surface
J. Hulva, ***Jakub, Z.***, Novotny, Z., Johansson, N., Knudsen, J., Schnadt, J., Schmid, M., Diebold, U., and Parkinson G. S. *The Journal of Physical Chemistry B* **2018** *122*, 721-729

CONFERENCE CONTRIBUTIONS

Local Environment Defines Reactivity of Model Single-Atom Catalysts: Ir and Rh on Fe_3O_4(001)
Symposium on Surface Science 2020, St. Christoph/Arlberg, Austria *(oral)*

Local Structure and Coordination Define Adsorption in a Model Ir_1/Fe_3O_4(001) Single-Atom Catalyst
American Vacuum Society Symposium 2019, Columbus, OH *(oral)*

Nickel Doping Enhances the Reactivity of Fe_3O_4(001) to Water
German Physics Society Spring Meeting 2019, Regensburg, Germany *(oral)*

Coverage-dependent Water Agglomerates on Iron Oxide Surfaces
American Vacuum Society Symposium 2018, Long Beach, CA *(oral)*

Coverage-dependent Water Agglomerates on Fe_3O_4(001)
International Conference on Nanoscience Technology 2018, Brno, Czech Republic *(poster)*

Coverage-dependent Water Agglomerates on Fe_3O_4(001): Insights from Experiments
German Physics Society Spring Meeting 2018, Berlin, Germany *(oral)*

Structure and Reactivity of the Hematite (012) surface
European Conference on Surface Science 2017, Szeged, Hungary *(oral)*

Atomic-scale STM and nc-AFM study of the Hematite (012) surface.
German Physics Society Spring Meeting 2017, Dresden, Germany *(oral)*

Vienna, May 2020